Water Waves, Fixed Cylinders, and Floating Spheres

Albert Ballast

Water Waves Fixed Cylinders and Floating Spheres

Fully nonlinear diffraction calculations compared to detailed experiments

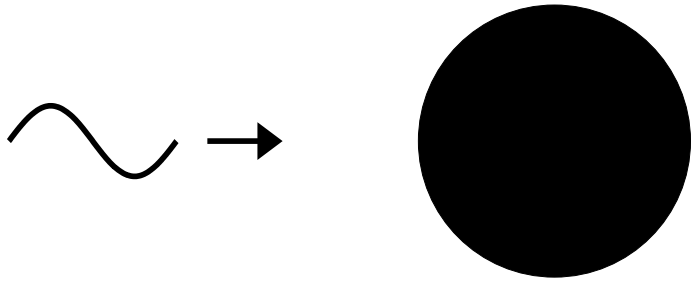

Albert Ballast

Water Waves
Fixed Cylinders
and Floating Spheres

This research was supported by the Technology Foundation STW, applied science division of NWO and the technology programme of the Ministry of Economic Affairs.

The use of the supercomputer facilities was sponsored by the Stichting Nationale Computerfaciliteiten (National Computing Facilities Foundation, NCF), with financial support from the Nederlandse Organisatie voor Wetenschappelijk Onderzoek (Netherlands Organization for Scientific Research, NWO).

ISBN 90-6464-895-6

Copyright © 2004 by Albert Ballast

Printed by Ponsen & Looijen BV, Wageningen, The Netherlands

WATER WAVES, FIXED CYLINDERS, AND FLOATING SPHERES

FULLY NONLINEAR DIFFRACTION CALCULATIONS COMPARED TO DETAILED EXPERIMENTS

PROEFSCHRIFT

ter verkrijging van
de graad van doctor aan de Universiteit Twente,
op gezag van de rector magnificus,
prof.dr. F.A. van Vught,
volgens besluit van het College voor Promoties
in het openbaar te verdedigen
op donderdag 7 oktober 2004 om 13.15 uur

door

Albert Ballast

geboren op 19 december 1973

te Groningen

Dit proefschrift is goedgekeurd door de promotor

Prof. dr. ir. P. J. Zandbergen

Summary

In designing offshore structures like oil rigs or FPSO's (Floating Production, Storage and Offloading units) one of the important aspects is the kind of waves that the structure will encounter and the kind of loads that they will cause. Nowadays this kind of questions is answered routinely by linear potential codes. Some of those codes apply higher-order corrections. In the final stages of the design the results are checked on model scale in hydrodynamic model test basins.

To increase the capabilities of the computer calculations a computer code for fully nonlinear potential calculations with water waves and floating bodies had been developed earlier. It uses a boundary integral equation formulation, which is discretized to give a higher order panel method. In the current thesis this computer code has been applied to diffraction calculations of regular waves of moderate steepness incident on fixed, surface piercing cylinders with circular and rectangular cross-sections. In addition it has also been applied to diffraction calculations of regular waves with small steepness incident on free floating spheres. For the fixed cylinders comparison was made with experimental values for the maximum wave elevation at several distances from and several angles to the cylinders. The agreement between the calculations and the experiments was fairly good. The absorbing boundary conditions will benefit from a larger domain size however, and the resolution in the calculations for the highest waves was not sufficient to make definite statements about the breaking behaviour. Details in the diffraction solution near the fixed cylinders were validated with laser-sheet measurements of the free surface. The calculations with the floating sphere were compared to linear theory: added mass and damping coefficients for the free decay tests, and amplitude and phase of the heave and surge motions together with the mean horizontal drift force for a range of incoming wave frequencies. Considering the difficulties in resolving the waves with the higher frequencies and the limited capabilities of the absorbing boundary conditions because of the small domain size, the results were satisfactory, although there remain some questions. Suggestions are given to widen the current bottlenecks. To be able to run these calculations on massively parallel processing computers, the computer code, which was originally optimised for vector computers, was parallelised using Open MP directives. This resulted in a maximum speed up of 40 using 60 processors on a Silicon Graphics Origin 3800 for a problem with a grid consisting of 9000 panels.

Samenvatting

Voor het ontwerp van offshore installaties zoals boorplatformen en FPSO's (Floating Production, Storage and Offloading units, oftewel drijvende productie, opslag en afvoer eenheden) is een van de belangrijke aspecten het soort golven dat de installatie zal tegenkomen en de belastingen die deze zullen veroorzaken. Tegenwoordig worden dit soort vragen routinematig beantwoord met behulp van computerprogramma's gebaseerd op lineaire potentiaal theorie. Een aantal van deze programma's past hogere orde correcties op de lineaire theorie toe. In de eindfase van het ontwerp worden de resultaten gecontroleerd op modelschaal in grote "zwembaden" met golfslag, bijvoorbeeld bij het MARIN.

Om de mogelijkheden van deze computerberekeningen te vergroten was al eerder een computerprogramma ontwikkeld gebaseerd op de volledig niet-lineaire potentiaal theorie voor berekeningen aan watergolven en drijvende lichamen. Dit programma gebruikt een randintegraal formulering die zodanig is gediscretiseerd dat een hogere orde panelenmethode ontstond. In dit proefschrift is dit computerprogramma, genaamd HYPAN, toegepast op diffractie berekeningen voor reguliere golven van gematigde steilheid invallend op vaste, wateroppervlak doorsnijdende cilinders met cirkelvormige en met rechthoekige dwarsdoorsnedes. Bovendien is het toegepast op diffractie berekeningen voor reguliere golven van lage steilheid invallend op vrij drijvende bollen. De resultaten voor de vaste cilinders zijn vergeleken met metingen van de maximale golfhoogte op verschillende afstanden en hoeken ten opzichte van de cilinders. De overeenkomst tussen de berekeningen en de metingen is gunstig, hoewel de absorberende randvoorwaarden zouden kunnen profiteren van een groter domein en de resolutie van de berekeningen voor de hoogste golven niet voldoende was om definitieve uitspraken te doen over het al dan niet breken van de golven. Enige details in het golfpatroon rond de vaste cilinders zijn gevalideerd met metingen aan het wateroppervlak door middel van laser belichting van verticale dwarsdoorsnedes. De berekeningen aan de drijvende bol zijn vergeleken met de lineaire theorie: de toegevoegde massa en demping coëfficiënten voor de uitdemp testen, en de amplitude en de fase van de verticale en van de horizontale bewegingen samen met de gemiddelde horizontale driftkracht voor een reeks van inkomende golffrequenties. Rekening houdend met de moeilijkheden om de golven met de hogere frequenties met voldoende resolutie weer te geven en de beperkte prestaties van de absorberende randvoorwaarden als gevolg van de kleine domein grootte, zijn de resultaten bevredigend, alhoewel er nog enige vragen overblijven. Suggesties om de grootste beperkingen uit de weg te ruimen worden gegeven. Om deze berekeningen op massief parallelle computers te kunnen doen, is de computercode, die oorspronkelijk was geoptimaliseerd voor vector

supercomputers, geparallelliseerd, gebruikmakend van de Open MP methode. Dit heeft geresulteerd in een maximale versnelling met een factor 40 wanneer er 60 processoren van een Silicon Graphics Origin 3800 supercomputer worden gebruikt voor een probleem met een rekenrooster bestaand uit 9000 panelen.

Contents

Summary v

Samenvatting vii

1 Introduction 1
- 1.1 The motivation for the project . . . 1
- 1.2 The history of the project . . . 2
- 1.3 The current sub-project . . . 3
- 1.4 A glimpse of the alternatives . . . 3
- 1.5 The current thesis . . . 4

2 Physics, mathematics and numerics 5
- 2.1 Basic presentation of the method . . . 5
  - 2.1.1 Flow field . . . 5
  - 2.1.2 Time dependence . . . 6
  - 2.1.3 Floating body boundary condition . . . 7
  - 2.1.4 Discretisation . . . 10
- 2.2 Grid topology . . . 11
- 2.3 Grid motion . . . 11
  - 2.3.1 Free surface . . . 12
  - 2.3.2 Free surface with a body . . . 13
- 2.4 Incoming wave fields . . . 14
- 2.5 Absorbing outgoing waves . . . 15
  - 2.5.1 Sommerfeld radiation condition . . . 15
  - 2.5.2 Pressure damping . . . 16
  - 2.5.3 Selecting the beach parameters . . . 17

3 Three-dimensional diffraction calculations 19
- 3.1 Setup . . . 19
  - 3.1.1 Grid . . . 21
  - 3.1.2 Start up . . . 22
  - 3.1.3 Grid motion . . . 26
  - 3.1.4 Beaches . . . 28
- 3.2 Testing . . . 28
  - 3.2.1 Rienecker & Fenton wave with open cylinder . . . 29
  - 3.2.2 Comparison with linear diffraction theory . . . 35

3.3 Comparison with experimental data . . . 40
3.3.1 ISSC comparative study . . . 40
3.3.2 EXPRO-CFD wave profile measurements . . . 76
3.4 Conclusion . . . 87

4 Three-dimensional diffraction calculations with a free-floating body 89
4.1 Setup . . . 89
4.1.1 Start up . . . 90
4.1.2 Grid motion . . . 90
4.1.3 Mooring system . . . 90
4.1.4 Beaches . . . 91
4.2 Testing . . . 91
4.2.1 Grid motion without mooring . . . 91
4.2.2 Damping experiments . . . 94
4.2.3 Comparison with linear diffraction theory, including second order drift effects 100
4.3 Conclusion . . . 140

5 Parallelisation and other computational aspects 141
5.1 Computational work . . . 141
5.2 How to speed things up . . . 143
5.3 Parallelisation . . . 144
5.3.1 Open MP or MPI? . . . 144
5.3.2 Principles and problems . . . 145
5.3.3 Implementation . . . 146
5.3.4 Results . . . 147
5.4 Conclusion . . . 148

6 The future 157
6.1 Solving only for the difference with the incoming wave . . . 158
6.2 Lowering the computational complexity of the problem . . . 159
6.3 Dealing with irregular waves . . . 159
6.4 Conclusion . . . 160

A 161
A.1 Broeze's equation 6.22 . . . 161
A.2 Calculation of α and β from free decay tests . . . 161
A.3 Implementation of the mooring system . . . 162
A.4 Components of the mean horizontal drift force . . . 163

Bibliography 165

Acknowledgements 169

Nawoord 171

Curriculum vitae 173

Chapter 1

Introduction

1.1 The motivation for the project

In designing offshore structures like oil rigs or FPSO's (Floating Production, Storage and Offloading units) one of the important aspects is the kind of waves that the structure will encounter and the kind of loads that they will cause. Given the incoming wave field, a consequence of a certain sea state, you can try to simulate it in a wave basin or you can try to calculate it with numerical methods. Unlike computations, the equipment and the setup of model experiments is very expensive and not very well-suited for trial and error. Especially in the early design phase, it is very important to have a rapid trial and error cycle. For numerical methods the most widely used at the moment are linear models, potential theory but with a linearised free surface condition and body conditions, working in the frequency domain. More advanced codes include higher-order corrections. These linear calculations in the frequency domain are often referred to as diffraction calculations: an incoming wave is diffracted or scattered by an object in all directions. The same terminology is used for the nonlinear variants in the time domain.

Especially for large body motions and frequency interactions linear theory is not very accurate or applicable. An example of a practical application that needs non-linear theory is the mooring of vessels in sea states containing both long and smaller wavelengths. Near the oilfields at the coast of West Africa there are no harbours. To get the oil into tankers to move it elsewhere, there are offloading units placed offshore. So the tanker has to be moored at open sea. The slowly oscillating wave drift forces associated with the incoming wave groups can excite the mooring system at its resonant frequency.

A second example is a semi submersible. The pillars connecting the super structure to the subsea structure are exposed to the incoming waves. Relevant questions include: will the resulting wave pattern reach the super structure and what are the impact loads on the pillars.

A third example is an FPSO in survival conditions. An FPSO is a ship like structure floating above an oil well to pump up the oil while storing it until it can be transferred to a shuttle tanker. The station keeping is done by using mooring lines or by using dynamic positioning using thrusters. An FPSO cannot run away

from a storm, so it has to withstand even the most extreme ones. In the most severe conditions it can stop producing oil but it at least has to survive. In those survival conditions you typically have waves that are large compared to the ship giving rise to large ship motions. Although the waves are very high they do not need to be very steep because of their long wavelengths. The most interesting cases are where part of the ship comes out of the water, for example the bow. These scenarios will almost certainly include local wave breaking phenomena.

The frequency effects and the large ship motions can be dealt with by going to fully nonlinear potential theory. Potential theory however, cannot handle re-entrant breaking phenomena. For that one needs a more complete formulation that can describe rotational flow with very good free surface tracking. This means a Navier-Stokes model with for example a volume of fluid approach to capture the free surface. But even when the wildest scenarios cannot be calculated with codes based on fully nonlinear potential theory, such codes can still be used to validate the more exotic codes in their milder regions. Potential theory is relatively well understood, it can be a valuable reference for Navier-Stokes codes who need a number of not so well understood approximations (turbulent models and the like). And very important: potential theory is much less computational intensive. A higher order fully nonlinear potential code is very suitable for very accurate calculations. For Navier-Stokes codes being robust is not so big a problem, being accurate is. The window of application between linear methods and breaking waves is relatively small, the usefulness is largely determined by the relative computational cost. The two dimensional potential theory codes have already proven their value.

There was, and still is, a clear need for better nonlinear tools for three-dimensional problems. In the middle of the 1980s Zandbergen started the current project to create a three-dimensional fully nonlinear potential code.

1.2 The history of the project

In 1984 Romate started the development of a three-dimensional fully nonlinear panel method to calculate water waves. In 1989 he finished his PhD. HYPAN (HYdrodynamic PANel method), as he called his computer program, was able to accurately calculate linear and moderately nonlinear waves. It was one of the first three-dimensional fully nonlinear methods for calculating water waves. He did the work at Delft Hydraulics. He was succeeded by two new PhD students: Van Daalen and Broeze. Broeze continued the work at Delft Hydraulics, especially focusing on the calculation of very high nonlinear waves. Van Daalen started his work at MARIN, where he was supposed to implement floating bodies. In 1993 both finished their thesis. Broeze had been able to calculate very high regular waves and also a very large part of the breaking process of a wave. Van Daalen worked out the algorithm for the free-floating body and implemented a two-dimensional version of it. He did damping and radiation problems. Their successors were De Haas at Delft Hydraulics and Berkvens at MARIN. De Haas concentrated his work on domain decomposition in order to make very large calculations feasible. When he finished his PhD in 1997 he had implemented the domain decomposition in two and in three dimensions. This algorithm worked very efficiently but because of the way HYPAN handles the network intersections between the domains the accuracy was less than we were used to. Berkvens

had to extend the two-dimensional floating body algorithm of Van Daalen to three dimensions. He succeeded in calculating the damping and radiation problems of a sphere in three dimensions. His PhD was finished in 1998.

1.3 The current sub-project

The current phase of the project started in 1998 when the current author and Eggermont started their PhD project at MARIN and Delft Hydraulics respectively. After the two diverted versions at MARIN and Delft Hydraulics were merged together there was one code which could handle both domain decomposition and freely floating bodies. Eggermont then took up the problem of the intersections, to make domain decomposition a more useful tool and to enhance the flexibility in constructing grids. The current author, together with Eggermont, worked on practical diffraction calculations. First on some two-dimensional problem, and after that a three-dimensional cylinder in waves was considered as part of a comparative study. The acquired know-how was then used to put the desired freely floating object into waves.

1.4 A glimpse of the alternatives

One can look at water at many different levels of sophistication. If one assumes incompressible water and rotational flow, the flow field can be obtained by solving the Laplace equation. For waves on the free surface one can linearise with respect to the amplitude. Within this linear approach it is possible to write a frequency domain code which only uses unknowns on the surface of the object, for example a ship in deep water. These codes are the workhorse of shipbuilding related hydrodynamic codes. Practical ship simulations can be run on a desktop PC. Classically these frequency domain codes are programmed using constant panel strengths. This gives a lot of flexibility in the construction of a grid: one can use an unstructured approach where ever that is considered to be convenient. The main disadvantage is the accuracy: it is not a consistent discretisation scheme. Instead of a frequency domain code one can also write a time domain code. It is possible to include the free surface condition in the Green function. Such a time domain approach is more general, but also less convenient than a frequency domain approach.

In an attempt to include some of the nonlinear effects associated with large motions, a so-called Froude-Krylov technique is introduced, see e.g. [6]. Instead of holding the body fixed as appropriate in a completely linear method, one takes the instantaneous position of the object in the instantaneous position of the free surface to calculate the undisturbed excitation forces. The diffraction forces are still calculated for the mean body position as in standard linear theory. For an attempt to quantify the effect of instead calculating the diffraction for the instantaneous body position see [17]. The linear frequency domain codes can be extended to include some of the nonlinear frequency interactions. Instead of making a linear approximation to the free surface and the body boundary conditions in time domain codes, one can also make a higher order approximation, with a relatively small increase in computational effort. Within the potential theory framework the most sophisticated approach is to use the fully nonlinear boundary conditions. This means that you have to track the

free surface and update your geometry related influence coefficients every time step, which is very computationally intensive. This is the approach used in the current thesis.

If one wants to allow for viscous effects or irrotational flow, potential theory is no longer applicable. Then the Navier-Stokes equations are needed. Again these equations can be used at different levels of sophistication. On the one end there is the complete direct numerical simulation of the Navier-Stokes equations which is very, very computationally intensive, and on the other end there is a very rough discretisation with emphasis on inertial effects which still takes a lot of computation time. One of the issues is how to capture the free surface. One of the promising methods is the so-called volume of fluid method, see for example [7]. For green water simulations, where the effects of waves plunging on the deck of the ship are investigated, you really need a method that can capture an arbitrary free surface such as the VOF methods. The disadvantage of methods that can deal with an arbitrary free surface is that they often have a relatively high dissipation.

Nowadays several researchers have developed fully nonlinear potential methods for three-dimensional calculations with fixed or floating bodies. The computational demands and the proper treatment of the nonlinear instabilities are problematic for all of them. Ferrant was the first one to do precise calculations for a vertical cylinder in waves [8, 9, 10]. He used a boundary element method with triangular linear elements and has paid a lot of attention to be able to run it on a workstation. Because of the triangular elements his code is a little bit more flexible in the choice of the grid. He has worked on more or less unstructured grids, but the accuracy proved to be a problem [11]. Tanizawa [28] proposed a three-dimensional fully nonlinear boundary element method that included a proper treatment of a freely floating body using the body boundary condition presented in chapter 2, but he only presented results of a two-dimensional version. A three-dimensional version was presented by him and two others in [27]. Their calculations included damping and forced oscillation tests, but the fully nonlinear description of the free surface was only validated for linear waves.

1.5 The current thesis

The main emphasis of this PhD project was to get a practical diffraction calculation running of a (free) floating object. Because of available validation material we started with a cylinder kept fixed in regular waves. This is described in chapter 3. After we gained confidence in that setup we could apply it to a floating object. With this setup improvements on results obtained by Berkvens for the free damping case were possible. And of course, now excitation calculations were possible. These subjects are described in chapter 4. Halfway the PhD project the supercomputer that we used was upgraded from a vector machine to a massively parallel machine. Our porting efforts are described in chapter 5, together with some related issues. The bottlenecks we encountered during the whole project gave us valuable insight in the future prospects of this approach. This is put to paper in chapter 6.

But before all that, we first introduce, in the next chapter, the physics, the mathematics, and the numerics of the problem at hand. This ends the first chapter.

Chapter 2

Physics, mathematics and numerics

HYPAN has already been described in five different PhD theses [25, 3, 5, 16, 2]. The following description will therefore first focus on creating a basic understanding, for the details the reader should consult either the previous theses or the program source code. Following that, the aspects most relevant to the current thesis are given a more complete treatment. There is a section on the grid topology to illustrate the resulting constraints. Another section explains the new grid motion around the floating body. The pressure damping zone that is new to HYPAN is treated in a section about the absorbing boundary conditions.

2.1 Basic presentation of the method

2.1.1 Flow field

We only consider irrotational motion of the water, the velocity field can therefore be written as the gradient of a potential:

$$\vec{v} = \vec{\nabla}\phi \tag{2.1}$$

In addition we consider the water to be incompressible, this implies that the divergence of the flow field vanishes. Combining that with the previous equation we get a Laplace equation for the velocity potential:

$$\nabla^2\phi = 0 \tag{2.2}$$

Such a Laplace equation can be transformed into a boundary integral equation:

$$\frac{\Omega}{4\pi}\,\phi(\vec{x}) = \oint_S \left[\frac{\partial\phi}{\partial n}(\vec{x}\,')\,G(\vec{x},\vec{x}\,') - \phi(\vec{x}\,')\,\frac{\partial}{\partial n}G(\vec{x},\vec{x}\,')\right] dS_{x'} \tag{2.3}$$

with

$$G(\vec{x},\vec{x}\,') = \frac{1}{4\pi\,\|\,\vec{x}-\vec{x}\,'\|} \tag{2.4}$$

and

$$\Omega = \text{solid angle} = \begin{cases} 4\pi & \vec{x} \text{ inside } S \\ 2\pi & \vec{x} \text{ on smooth part of } S \\ 0 & \vec{x} \text{ outside } S \end{cases} \tag{2.5}$$

Using this boundary integral equation we can determine ϕ everywhere when given ϕ and ϕ_n on S. Even better, we have for all $\vec{x}$ on S one equation and two unknowns. This means that if we know the position of S and on any part of S either ϕ or ϕ_n, we can solve for the remaining ϕ_n's and ϕ 's. For the different parts of S we can have the following boundary conditions. The position of the bottom of the domain is known and stationary. On this known surface S_{bot} we prescribe a zero normal velocity, $\phi_n = 0$, to state that the bottom is impenetrable. If the domain is surrounded by walls, the same is true for the lateral boundaries. When some of those walls are moving, the position and the normal velocity of that wall are prescribed as a function of time. When the lateral boundaries are artificial we call them input output boundaries, S_{IO}. The position of these boundaries is arbitrary and a convenient choice is made. On these boundaries ϕ or ϕ_n can be prescribed, depending on whether there are incoming waves and/or absorbing boundary conditions like a Sommerfeld radiation condition. The most important boundary is the free surface. Its position and the value of the velocity potential on it depend on the dynamics of the problem.

2.1.2 Time dependence

It is time to write down the dynamics of the problem. The material time derivative of the momentum of a water particle is determined by the local pressure gradient together with the gravitational force:

$$\frac{D(\rho\vec{v})}{Dt} = -\vec{\nabla}p - \rho g\hat{z} \tag{2.6}$$

For an incompressible fluid in irrotational motion satisfying this equation everywhere in fluid is equivalent to satisfying

$$\vec{\nabla}\left(\phi_t + \frac{1}{2}(\nabla\phi)^2 + \frac{p}{\rho} + gz\right) = 0 \tag{2.7}$$

and this is again equivalent to

$$\phi_t + \frac{1}{2}(\nabla\phi)^2 + \frac{p - p_0}{\rho} + g(z - z_0) = B(t) \tag{2.8}$$

Here $B(t)$ is an arbitrary constant that does not need to be constant in time. By putting $B(t)$ to 0 for all t we make sure that if the water stays at rest ϕ_t will vanish for all t. The dynamics represented by this Bernoulli equation determines ϕ_t on the free surface. Integration in time of the position of and the potential in all the points on the free surface gives us then the new positions on and the new values of the potential on the free surface at the next time level. Next we solve the Laplace equation to give us ϕ_n on the free surface, which gives us, together with ϕ for the tangential velocities, the total velocity in all points on the free surface. This enables us to calculate the new ϕ_t and to go for another round.

2.1.3 Floating body boundary condition

A body in forced motion is just like a moving wall from a boundary condition point of view. If a body is free to negotiate its movements with the water with only external forces like gravitation and perhaps a mooring prescribed, we call it a floating body. As the word negotiate suggests, the boundary condition for a floating body is not so much a prescription as more a set of constraints to which one has to find a solution. Let us have a look at those constraints. First we have the equation of translational motion of the centre of mass of the body

$$\frac{d}{dt}(\vec{P}) = \vec{F} \tag{2.9}$$

$$m\dot{\vec{v}}_b = \vec{F} \tag{2.10}$$

$$\vec{a}_b = m^{-1}\vec{F} \tag{2.11}$$

and the equation of rotational motion around that centre of mass

$$\frac{d}{dt}(\vec{L}) = \vec{N} \tag{2.12}$$

$$\frac{d}{dt}(\bar{I}\cdot\vec{\omega}) = \vec{N} \tag{2.13}$$

$$= \bar{I}\cdot\dot{\vec{\omega}} + \vec{\omega}\times(\bar{I}\cdot\vec{\omega}) = \vec{N} \tag{2.14}$$

$$\dot{\vec{\omega}} = \bar{I}^{-1}(\vec{N} - \vec{\omega}\times(\bar{I}\cdot\vec{\omega})) \tag{2.15}$$

The forces and the moments in the right-hand sides of the previous equations follow from

$$\vec{F} = -\int_S \hat{n}p\,dS - mg\hat{z} + \vec{F}_{ext} \tag{2.16}$$

and

$$\vec{N} = -\int_S \vec{r}\times\hat{n}p\,dS \tag{2.17}$$

The normal to the body surface $\hat{n}$ is pointing into the fluid and the pressure is given by

$$p = p_0 - \rho\left(\phi_t + \frac{1}{2}(\nabla\phi)^2 + g(z - z_0)\right) \tag{2.18}$$

The partial time derivative of the potential in this expression for the pressure, needed to calculate the forces and thus the accelerations of the body, is unknown. Using backward finite differences of ϕ is unstable, see [2] or [5] for references.

Now we have to look for relations involving ϕ_t and the accelerations $\vec{a}_b$ and $\dot{\vec{\omega}}$. For a water particle anywhere in the fluid the acceleration in terms of the velocity potential is (from the derivation of Bernoulli, just $\frac{D}{Dt}(\vec{\nabla}\phi)$)

$$\vec{a}_w = \vec{\nabla}\left(\phi_t + \frac{1}{2}(\nabla\phi)^2\right) \tag{2.19}$$

And thus the acceleration of a water particle somewhere on the body boundary in the direction of the local normal $\hat{n}$ is

$$\hat{n}\cdot\vec{a}_w = \phi_{tn} + \partial_n\left(\frac{1}{2}(\nabla\phi)^2\right) \tag{2.20}$$

Now we have the accelerations of the body $\vec{a}_b$ and $\dot{\vec{\omega}}$ as a function of ϕ_t from (2.9) till (2.18) and the perpendicular component of the acceleration of a water particle on the body boundary $\hat{n} \cdot \vec{a}_w$ as a function of ϕ_{tn} from (2.20). We therefore need a relation between $\vec{a}_b$, $\dot{\vec{\omega}}$ and $\hat{n} \cdot \vec{a}_w$ and we need a relation between ϕ_t and ϕ_{tn}. That second relation is easy, we just use

$$\nabla^2 \phi_t = 0 \tag{2.21}$$

which shares most of the computational effort with the Laplace problem for ϕ. To relate the acceleration of the body to the acceleration of the water in a point on the body boundary we separate the acceleration into the accelerations of the body itself and into the accelerations relative to the body:

$$\begin{aligned}
\vec{a}_w = \vec{a}_b + \dot{\vec{\omega}} \times \vec{r} \quad & \text{(translational plus angular acceleration of body)} \\
+ \vec{a}\,'_w \quad & \text{(translational acceleration relative to body fixed coordinates)} \\
+ \vec{\omega} \times (\vec{\omega} \times \vec{r}) \quad & \text{(centrifugal, ``}\omega^2 r\text{'')} \\
+ 2\vec{\omega} \times \vec{v}\,'_w \quad & \text{(coriolis)}
\end{aligned} \tag{2.22}$$

For a water particle moving on the body surface

$$\vec{a}\,'_w = \vec{a}\,'_{w,\parallel} + \vec{a}\,'_{w,\perp} \tag{2.23}$$

the component parallel to the body surface, $\vec{a}\,'_{w,\parallel}$, is free, but the component perpendicular to the body surface, $\vec{a}\,'_{w,\perp}$, must be such that the motion follows the shape of the body. Or better: $\vec{a}\,'_{w,\perp}$ must be such that the motion has the same curvature as the surface has in the direction of $\vec{v}\,'_w$:

$$\vec{a}\,'_{w,\perp} = \frac{v'^2_w}{R_{\hat{v}'_w}} \hat{n} \tag{2.24}$$

Thus

$$\hat{n} \cdot \vec{a}\,'_w = \frac{v'^2_w}{R_{\hat{v}'_w}} \tag{2.25}$$

For a water particle in a point on the body boundary the acceleration in the direction of the local body normal is therefore determined by the motions of the body and the velocity of the water particle:

$$\hat{n} \cdot \vec{a}_w = \hat{n} \cdot \left\{ \vec{a}_b + \dot{\vec{\omega}} \times \vec{r} + \vec{\omega} \times (\vec{\omega} \times \vec{r}) + \frac{v'^2_w}{R_{\hat{v}'_w}} \hat{n} + \; 2\vec{\omega} \times \vec{v}\,'_w \right\} \tag{2.26}$$

where

$$\vec{v}\,'_w = \vec{v}_w - \vec{v}_b - \vec{\omega} \times \vec{r} \tag{2.27}$$

$$= \vec{\nabla}\phi - \vec{v}_b - \vec{\omega} \times \vec{r} \tag{2.28}$$

Use the equations of motion to fill in equation (2.26):

$$\begin{aligned}
\hat{n}\cdot\vec{a}_w &= \hat{n}\cdot\Big\{m^{-1}\vec{F}+(\bar{I}^{-1}\cdot(\vec{N}-\vec{\omega}\times(\bar{I}\cdot\vec{\omega})))\times\vec{r}+\dots\Big\}\\
&= \hat{n}\cdot\Big\{-m^{-1}\int_S \hat{n}p\,dS - g\hat{z}+m^{-1}\vec{F}_{ext}\\
&\qquad +(\bar{I}^{-1}\cdot(-\int_S \vec{r}'\times\hat{n}'p\;dS'-\vec{\omega}\times(\bar{I}\cdot\vec{\omega})))\times\vec{r}+\dots\Big\}\\
&= \hat{n}\cdot\Big\{-\int_S\big[m^{-1}\hat{n}'+(\bar{I}^{-1}\cdot(\vec{r}'\times\hat{n}'))\times\vec{r}\big]p\,dS'\\
&\qquad -(\bar{I}^{-1}\cdot(\omega\times(\bar{I}\cdot\omega)))\times\vec{r}\\
&\qquad -g\hat{z}+m^{-1}\vec{F}_{ext}+\dots\Big\}
\end{aligned}\tag{2.29}$$

Use (2.20) and (2.18) to get:

$$\begin{aligned}
&\phi_{tn}+\partial_n\left(\frac{1}{2}(\nabla\phi)^2\right)=\\
&\hat{n}\cdot\Big\{-\int_S\big[m^{-1}\hat{n}'+(\bar{I}^{-1}\cdot(\vec{r}'\times\hat{n}'))\times\vec{r}\big]\big[p_0-\rho\big(\phi_t+\frac{1}{2}(\nabla\phi)^2+g(z-z_0)\big)\big]\,dS'+\dots\Big\}
\end{aligned}\tag{2.30}$$

Put the unknowns ϕ_t and ϕ_{tn} to the left and the rest to the right

$$\begin{aligned}
&\phi_{tn}-\hat{n}\cdot\int_S\big[m^{-1}\hat{n}'+(\bar{I}^{-1}\cdot(\vec{r}'\times\hat{n}'))\times\vec{r}\big]\big[\rho\phi_t\big]\,dS'=\\
&\hat{n}\cdot\Big\{\int_S\big[m^{-1}\hat{n}'+(\bar{I}^{-1}\cdot(\vec{r}'\times\hat{n}'))\times\vec{r}\big]\big[\frac{1}{2}\rho(\nabla\phi)^2+\rho g(z-z_0)-p_0\big]\,dS'+\dots\Big\}\\
&\qquad -\partial_n\left(\frac{1}{2}(\nabla\phi)^2\right)
\end{aligned}\tag{2.31}$$

and write out the dots explicitly:

$$\begin{aligned}
&\phi_{tn}-\hat{n}\cdot\int_S\big[m^{-1}\hat{n}'+(\bar{I}^{-1}\cdot(\vec{r}'\times\hat{n}'))\times\vec{r}\big]\big[\rho\phi_t\big]\,dS'=\\
&\quad\hat{n}\cdot\Big\{\int_S\big[m^{-1}\hat{n}'+(\bar{I}^{-1}\cdot(\vec{r}'\times\hat{n}'))\times\vec{r}\big]\big[\frac{1}{2}\rho(\nabla\phi)^2+\rho g(z-z_0)-p_0\big]\,dS'\\
&\qquad -(\bar{I}^{-1}\cdot(\omega\times(\bar{I}\cdot\omega)))\times\vec{r}-g\hat{z}+m^{-1}\vec{F}_{ext}\\
&\quad+\vec{\omega}\times(\vec{\omega}\times\vec{r})+\frac{(\vec{\nabla}\phi-\vec{v}_b-\vec{\omega}\times\vec{r})^2}{R_{(\dots)}}\,\hat{n}+\;2\vec{\omega}\times(\vec{\nabla}\phi-\vec{v}_b-\vec{\omega}\times\vec{r})\Big\}\\
&\qquad -\partial_n\left(\frac{1}{2}(\nabla\phi)^2\right)
\end{aligned}\tag{2.32}$$

Here we have (using the Laplace equation in general orthogonal curvilinear coordinates)

$$\partial_n \left(\frac{1}{2} (\nabla\phi)^2 \right) = \phi_{s_1}\phi_{s_1 n} + \phi_{s_2}\phi_{s_2 n} + R_1^{-1}\phi_{s_1}^2 + R_2^{-1}\phi_{s_2}^2 + (R_1^{-1} + R_1^{-1})\phi_n^2 - (\phi_{s_1 s_1} + \phi_{s_2 s_2})\phi_n \quad (2.33)$$

with $s_{1,2}$ the local orthogonal tangential coordinates and $R_{1,2}$ the respective local curvature radii.

Let us summarize using

$$j(\vec{r}, \vec{r}\,') \equiv m^{-1}\hat{n}\cdot\hat{n}' + \hat{n}\cdot\left[(\bar{I}^{-1}\cdot(\vec{r}\,'\times\hat{n}'))\times\vec{r}\right] \quad (2.34)$$

the contribution of the body gyro moment

$$B(\vec{r}) \equiv -\hat{n}\cdot\left[(\bar{I}^{-1}\cdot(\omega\times(\bar{I}\cdot\omega)))\times\vec{r}\right] \quad (2.35)$$

and the remaining known quantities

$$W(\vec{r}) \equiv \hat{n}\cdot\left[\vec{\omega}\times(\vec{\omega}\times\vec{r}) + \frac{(\vec{\nabla}\phi - \vec{v}_b - \vec{\omega}\times\vec{r})^2}{R_{(\ldots)}}\hat{n} + 2\vec{\omega}\times(\vec{\nabla}\phi - \vec{v}_b - \vec{\omega}\times\vec{r})\right] - \partial_n\left(\frac{1}{2}(\nabla\phi)^2\right) \quad (2.36)$$

to get

$$\phi_{tn}(\vec{r}) - \int_S \rho\phi_t j(\vec{r}, \vec{r}\,')\,dS' = \int_S \left[\frac{1}{2}\rho(\nabla\phi)^2 + \rho g(z - z_0) - p_0\right] j(\vec{r}, \vec{r}\,')\,dS' - g(\hat{n}\cdot\hat{z}) + m^{-1}(\hat{n}\cdot\vec{F}_{ext}) + B(\vec{r}) + W(\vec{r}) \quad (2.37)$$

Combining these relations expressing the body boundary conditions with the integral equation for $\nabla^2\phi_t = 0$ both can be solved simultaneously. The resulting ϕ_t on the body boundary can be used to calculate the fluid forces on the body which in turn can be used to calculate the accelerations $\vec{a}_b$ and $\dot{\vec{\omega}}$ of the body. From these the normal velocity ϕ_n on the body boundary follows, which is used to solve the next $\nabla^2\phi = 0$ problem.

2.1.4 Discretisation

The whole water boundary is represented by a finite number of points on that boundary. They are called collocation points and are grouped together into several patches with a rectangular topology. This gives us a structured grid of collocation points. The eight neighbours around a collocation point define a local quadratic surface element called a panel. All panels together represent the boundary surface of the water. These eight neighbours are also used to calculate any tangential derivatives in the central point using finite differences. Now the boundary integral (2.3) can be written as a sum of integrals over the individual panels, considering as field points only the collocation points, at positions $\vec{x}_i$:

$$\frac{\Omega}{4\pi}\phi(\vec{x}_i) = \sum_{j=1}^{N} \oint_{\Delta S_j} \left[\frac{\partial\phi}{\partial n}(\vec{x}\,')\,G(\vec{x_j}, \vec{x}\,') - \phi(\vec{x}\,')\,\frac{\partial}{\partial n}G(\vec{x_j}, \vec{x}\,')\right] dS_{x'} \quad (2.38)$$

On each panel ϕ_n and ϕ are approximated with a Taylor expansion around the collocation point of the panel, ϕ_n up to first order and ϕ up to second order (inclusive). The tangential derivatives in these expansions are evaluated using finite differences with neighbouring values. These $\phi_n(\vec{x}_i)$ and $\phi(\vec{x}_i)$ in the collocation points $\vec{x}_i$ do not depend on the local coordinates and can therefore be taken out of the integration of each term. Collecting all terms depending on $\phi_n(\vec{x}_i)$ and $\phi(\vec{x}_i)$ results in the following system of equations

$$\sum_{j=1}^{N} \left[C_s(i,j) \frac{\partial \phi}{\partial n}(\vec{x}_j) + C_d(i,j) \phi(\vec{x}_j) \right] = 0 \tag{2.39}$$

The C_s are called the source influence coefficients and the C_d are called the dipole influence coefficients. These N equations include $2N$ unknowns. However, on each patch or network of collocation points either ϕ_n or ϕ is given. Putting these known terms on the other side we get a standard linear system $Ax = b$. In general the matrix A is full and neither symmetric nor positive definite. This linear system is solved by an iterative method called Conjugate Gradients Squared (CGS).

Romate [25] showed that when using a quadratic representation of the panel geometry, a quadratic representation of the potential on the panel, and a linear representation of the normal derivative of the potential on the panel, the local asymptotic truncation error would be of order Δ^3 on smooth boundaries, and of order Δ^2 on non-smooth boundaries in the current method. This resulted in a global asymptotic error of order Δ^2 for practical geometries.

To integrate ϕ and $\vec{x}$ in time (using ϕ_t and $\vec{v}$) a classical fourth order Runge-Kutta method is used. This means that the linear system has to be constructed and solved four times per time step.

2.2 Grid topology

The panels are organised in groups, called networks, with a rectangular topology. These rectangular collections of panels can be connected to each other to form a grid on the boundary surface of the water domain. Every edge of the network can be divided into several edge parts, with a minimum length per edge part of four panels. Each edge part can be connected to another edge part. To connect edge parts the number of panels in both edge parts needs to be the same. Edge parts can connect smoothly or under an angle, both cases have their own intersection algorithm. The discretisation stencils on both sides of the intersection are one-sided, even when it is a smooth connection. Since these one-sided discretisations present a discontinuity to the passing waves, the number of network intersections on the free surface should be minimised. The current intersection algorithms are described in Broeze [3].

2.3 Grid motion

Using fully nonlinear free surface boundary conditions means that you have to track the free surface. The grid cannot be kept fixed, it needs at least one degree of freedom

for every collocation point. Only motions perpendicular to the water domain boundary are physically relevant. If the tangential motions are relevant, it is only because of the numerics. On boundaries where the boundary condition does not depend on the value of the previous time level, the boundary can be regridded arbitrarily without causing numerical problems. Examples are a solid wall condition or prescribed body movement. On boundaries where the boundary condition does depend on the value of the previous time level, like on the free surface, one has to be more careful. To exploit the tangential freedom for maintaining a nice grid distribution the tangential velocities should be adjusted just a little bit in every time step. The transport of the previous value to the new position is then already taken care of by the material derivative, which is already used for the standard motion.

2.3.1 Free surface

The time evolution of a volume of incompressible water in irrotational motion is completely determined by the normal velocities at the boundary. We are therefore free to manipulate the tangential velocities of the collocation points to enforce a favourable grid distribution or to restrain the degrees of freedom of the collocation points.

Lagrangian grid motion

Lagrangian grid motion means that the collocation points basically move with the local water velocity. Tangential correction velocities are only applied to guarantee a reasonable grid distribution. The vertical networks at the open boundaries move like a curtain: the top follows the lagrangian motion of the free surface and the rest moves with the same horizontal velocity to prevent large deformations of the network. This does change the normal velocity at the boundary, but this is not important as it is an artificial boundary. Broeze found in his thesis that this lagrangian motion was necessary for doing stable calculations of highly nonlinear waves, because of the hyperbolic character of the free surface condition.

Eulerian grid motion

Eulerian grid motion means that the freedom to choose the tangential velocities is used to keep the horizontal velocities of the collocation points zero:

$$\vec{v} = \vec{v}_\perp + \vec{v}_\parallel, \text{ with } \vec{v}_\parallel \text{ such that } \hat{v} \cdot \hat{z} = 1. \tag{2.40}$$

This implies that an overturning free surface is no longer allowed. All collocation points have now a fixed horizontal position, so although the grid distribution is always reasonable it is no longer possible to increase the local grid density in difficult spots, for example near the crest of a wave. At the open boundaries the characteristics go in and out of the domain. This can cause instabilities, as mentioned above.

Mixed lagrangian and eulerian grid motion

When there is a vertical cylinder penetrating the free surface, the collocation points near the cylinder somehow have to stay in the neighbourhood of that cylinder. It is

possible to use a mix of lagrangian and eulerian motion for this. Near the cylinder the motion can be completely eulerian and in the far field completely lagrangian:

$$\vec{v}_{\parallel} = (1+\epsilon)\vec{v}_{\parallel,\text{eul}} + \epsilon\vec{v}_{\parallel,\text{lagr}} \tag{2.41}$$

with ϵ changing smoothly from 0 near the cylinder to 1 further away.

2.3.2 Free surface with a body

The collocation points nearest to the body should keep a more or less constant distance from it. They could move along the circumference of the body as long as the grid density remains reasonable. For bodies with a more or less circular horizontal cross-section this would be a good way to deal with rotations of the body, for bodies with a longer horizontal cross-section this would be difficult. The collocation points a little further away from the body should move more or less the same as the collocation points more closer to the body to maintain a reasonable grid distribution. Moving further and further away from the body the requirement to follow the motions of the body can be gradually relaxed. In the far field the collocation points can then move either lagrangian or eulerian.

We have therefore a mix between two behaviours, one is to follow the body and the other is to ignore the body. We need to specify what we mean by following the body for arbitrary collocation points. First consider the body but now enlarged with such a factor that the collocation point under consideration is on its surface. This we will call the virtual body. Following the body means moving parallel to the tangent plane B of the virtual body in the collocation point. Now consider the tangent plane W of the free surface in the collocation point. We are free to add correction velocities to the motion of the collocation point as long as they are parallel to the tangent plane W. Combining these two constraints leaves us free to move along the virtual waterline.

We will make this more precise now. The velocity of the collocation points can be written as follows

$$\vec{v}_{cp} = \vec{v}_{water} + \vec{v}_{corr} \tag{2.42}$$

It is more convenient however to split the correction velocity up into two parts, one part that is also applied at infinity, and one part that has to do with the motion of the body. Then we can write

$$\vec{v}_{cp} = \vec{v}_{\infty} + \epsilon\vec{w} \tag{2.43}$$

where

$$\vec{v}_{\infty} = \vec{v}_{water} + \vec{v}_{corr,\infty} \tag{2.44}$$

and $\vec{w} \in W$ is the correction velocity that tries to follow the body. Again ϵ should vary smoothly from one near the body to zero at infinity. We try to determine $\vec{w}$, so in the remainder of this section $\epsilon = 1$. To move parallel to the body we must have the following

$$\vec{v}_{cp} \cdot \hat{n}_B = \vec{v}_{body} \cdot \hat{n}_B \tag{2.45}$$

where $\vec{v}_{body}$ is the velocity of the virtual body surface in the collocation point and $\hat{n}_B$ the unit normal to the tangent plane B. Using (2.43) this implies that

$$\vec{w} \cdot \hat{n}_B = \vec{v}_{body} \cdot \hat{n}_B - \vec{v}_{\infty} \cdot \hat{n}_B \tag{2.46}$$

We can also put it differently by considering the tangent to the virtual waterline

$$WL = W \cap B \tag{2.47}$$

Now we span W by the orthonormal basis vectors $\hat{w}_{\parallel}$ and $\hat{w}_{\perp}$. The first one also spans WL. This enables us to write

$$\vec{w} = c\,\hat{w}_{\perp} + d\,\hat{w}_{\parallel} \tag{2.48}$$

where c is determined by eq. (2.46) and d is free. This freedom along the waterline can be used to limit the motion of the collocation points to certain trajectories on the (virtual) body. This can be used to control the grid on the body, which could be very useful for difficult shapes, for example shapes with relatively sharp edges. As an example we take the meridians on a sphere, assuming both poles to be near the top and the bottom respectively. To follow the meridians (φ_B is constant) we can chose d such that

$$d = \frac{\vec{v}_{body} \cdot \hat{\varphi}_B - \vec{v}_{\infty} \cdot \hat{\varphi}_B}{\hat{w}_{\parallel} \cdot \hat{\varphi}_B} \tag{2.49}$$

2.4 Incoming wave fields

On the artificial lateral boundaries of the water domain an incoming wave field can be specified if either ϕ or ϕ_n is known as a function of time and position. For non-linear regular[1] waves a Rienecker & Fenton description is used [23]. It is a superposition of linear solutions with wave numbers jk ($j = 1..N$), all moving with the same velocity. Given a period T, a wave height H, and a water depth h, all coefficients are determined such that the superposition satisfies the fully non-linear boundary conditions. The wave elevation is written as

$$\eta(x,t) = \frac{a_0}{2} + \sum_{j=1}^{N} a_j \cos(jk(x - x_0 - ct)) \tag{2.50}$$

and the potential as

$$\phi(x,z,t) = (c+B_0)(x-x_0) + \sum_{j=1}^{N} B_j \frac{\cosh(jk(z+h))}{\cosh(jkh)} \sin(jk(x-x_0-ct)) + b(t) \tag{2.51}$$

with

$$b(t) = -(g(R-h) - \frac{1}{2}c^2)t \tag{2.52}$$

following from the choice of $B(t) = 0$ in the Bernoulli equation. For deep water this term is very small.

[1] A stationary wave profile with a certain wavelength and period, the closest thing to a monochromatic wave.

2.5 Absorbing outgoing waves

On the artificial lateral boundaries of the water domain not only the incoming waves have to be put in, but also the outgoing waves have to be allowed to go out. In our case the external wave field is prescribed on the whole outer lateral boundary, coming and leaving. With the outgoing waves we then mean the waves resulting from the diffraction of the external wave field by the body inside of the domain. There are two ways to let these diffracted waves go out of the domain. First we can modify the boundary conditions on the lateral boundaries such that outward moving waves are anticipated for in the boundary condition. This can be done by using a Sommerfeld radiation condition. Secondly, we can modify the boundary conditions on the free surface such that any wave motions are damped. This is called an artificial beach. It is obvious that both these modifications need to be made such that they only apply to the difference with the external wave field. A combination of these two methods proves to be the most effective. Both the artificial beach itself as the combination of that beach with a Sommerfeld radiation condition is called the beach in the present thesis, but that should be clear from the context.

2.5.1 Sommerfeld radiation condition

Every function $f(x,t) \equiv \tilde{f}(x-ct)$ is constant for $x(t) = x_0 + ct$ or

$$\frac{df}{dt} = \frac{\partial f}{\partial x}c + \frac{\partial f}{\partial t} = 0 \tag{2.53}$$

Applying this Sommerfeld radiation condition to the difference with the incoming Rienecker & Fenton wave we get

$$\phi_t = \phi_t^{RF} - c\big[(\phi_r - \phi_r^{RF}) + \frac{1}{2r}(\phi - \phi^{RF})\big] \tag{2.54}$$

The $1/2r$ term results because in 3D the diffracted amplitude gets smaller to keep the radiated energy constant. The reflection coefficient is

$$|r| = \left|\frac{c_s - c_{wave}}{c_s + c_{wave}}\right| \tag{2.55}$$

Using the deep water limit of the linear dispersion relation, $\omega = \sqrt{gk}$, we get

$$|r| = \left|\frac{1 - \omega_{SRC}/\omega_{wave}}{1 + \omega_{SRC}/\omega_{wave}}\right| \tag{2.56}$$

Or more compact:

$$|r| = \left|\frac{1 - \frac{\omega_s}{\omega}}{1 + \frac{\omega_s}{\omega}}\right| \tag{2.57}$$

This reflection coefficient only vanishes when the outgoing wave has the same frequency as the tuning frequency of the Sommerfeld radiation condition. To absorb outgoing waves of several frequencies we need a dissipative zone on the free surface.

2.5.2 Pressure damping

Instead of doing something smart at the outflow boundary, one can also add dissipative terms to a piece of the free surface. This takes more grid points, but is effective for a broader range of frequencies. Most ideal is the combination with a Sommerfeld radiation condition, because the absorption of the lower frequencies takes a longer stretch of beach. We implemented the method used by Westhuis [30] and Meskers [20], which has been proven to be very effective. In the pressure damping zone an extra term is added to the dynamic free surface boundary condition:

$$\phi_{t,damp} = \frac{p_{damp}}{\rho} \tag{2.58}$$

where

$$p_{damp} = b \cdot (r - r_0) \cdot (\phi_n - \phi_n^{RF}) \tag{2.59}$$

with r the horizontal radius and b a constant.

Meskers derived in his master thesis some expressions for the reflection coefficient of such a beach. His two dimensional derivation gives, with some small modifications, the same results for a circular damping zone in three dimensions absorbing waves from a point source in the middle. The reflection is the sum of the immediate reflection on the beginning of the beach, because of the discontinuity in the medium, and of the reflection of the transmitted wave at the end of the beach. When the beachs ends in a Sommerfeld radiation condition this last reflection equals

$$r_t = t \cdot r_{src} \cdot t \tag{2.60}$$

where t is the transmission coefficient for the beach:

$$t = e^{-\frac{1}{2}\frac{b}{b_0}(kL)^2} \tag{2.61}$$

with

$$b_0 = \frac{\rho g}{c} = \frac{\rho g k}{\omega} \overset{\text{deep}}{=} \rho\omega \tag{2.62}$$

for the linear deep water limit. Then the total reflection is given by

$$r_{tot} = t \cdot r_{src} \cdot t + r_b \tag{2.63}$$

The bounce reflection r_b depends on the discontinuity introduced by the beach and thus on the beach characteristics:

$$r_b = f(\frac{b}{b_0}) = 0 + f' \cdot \frac{b}{b_0} + \ldots \tag{2.64}$$

Two-dimensional numerical experiments of Meskers proofed this first order approximation to be sufficient and determined f' to be 0.2. This brings us to a total reflection coefficient of

$$r_{tot} = \left| \frac{1 - \frac{\omega_s}{\omega}}{1 + \frac{\omega_s}{\omega}} \right| \cdot e^{-\frac{b}{b_0}(kL)^2} + 0.2 \cdot \frac{b}{b_0} \tag{2.65}$$

2.5.3 Selecting the beach parameters

We want a convenient graph to select the beach parameters. We therefore rewrite (2.65) to

$$r_{tot}(r_b, \frac{L}{\lambda}) = \left|\frac{1-\frac{\omega_s}{\omega}}{1+\frac{\omega_s}{\omega}}\right| \cdot e^{-\frac{r_b}{0.2}(2\pi(\frac{L}{\lambda}))^2} + r_b \tag{2.66}$$

Using r_b instead of $\frac{b}{b_0}$ enables us to use the same axis for r_b and r_{tot}. To find the smallest beach length that gives a certain amount of reflection we also plot the zero contour of the partial derivative of r_{tot} with respect to r_b. The points on this contour have the smallest beach length for a certain r_{tot}. For the calculations presented later in this thesis there was not a lot of room for a beach. The length of the beach was therefore more or less fixed. The parameter that remained to be determined was the slope of the beach, b.

For the calculations with the cylinder in chapter 3 the Sommerfeld radiation condition is tuned to the incoming wave frequency. This guarantees that the first order components of the diffraction, that have the same frequency as incoming wave, are absorbed completely if there is no beach. The higher components of the diffraction need a beach, but this will introduce a bounce reflection for the first order components. The second order components of the diffraction have a frequency that is twice the frequency of the incoming wave and have thus a wavelength that is a quarter of that of the incoming wave. Figure 2.1(a) is here appropriate.

For the calculations with the sphere in chapter 4 the Sommerfeld radiation condition is also tuned on the incoming wave frequency to absorb the first order diffraction. To absorb the radiated waves from the sphere because of its heave motion a beach is used. The initial transients will include lower frequencies then the heave eigen frequency. In these calculations the largest difference in frequency between the incoming wave and the heave eigenfrequency gives a ω_s/ω of around 0.75. See figure 2.1(b).

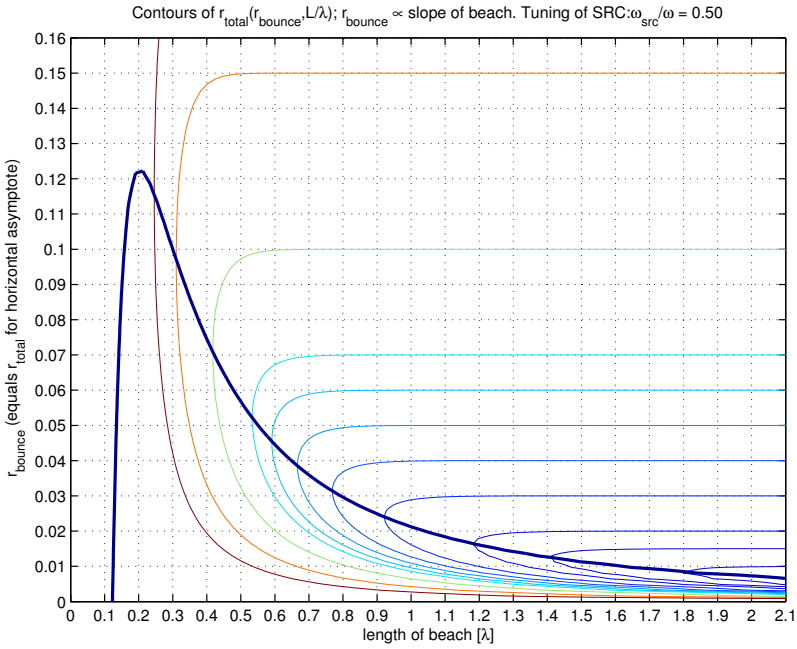

(a) For the cylinder the SRC is tuned on the incoming wave. For the 2ω components ω_s/ω is then 0.5. For the ω components the reflection only depends on r_b.

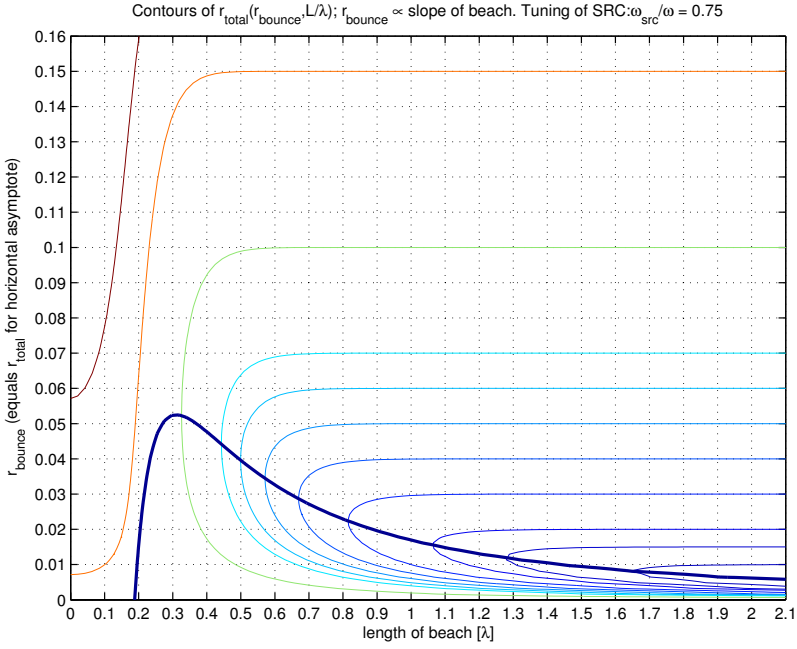

(b) For the sphere the SRC is also tuned on the incoming wave. The radiated waves resulting from the heave motions will then be out of tune in most cases, the maximum value for ω_s/ω is about 0.75.

Figure 2.1: Two graphs of eq.(2.66) for convenient values of ω_s/ω.

Chapter 3

Three-dimensional diffraction calculations

We want to get a practical diffraction calculation running and we want to validate it. For a circular vertical cylinder kept fixed in regular waves there is a lot of data available and because of its simple form arbitrary grid generation problems can be postponed until later. We concentrated our efforts on the regular wave cases of the ISSC comparative study. These included the little less simple form of a rounded square cylinder. In this study only measurements of the wave height were considered, not of forces or pressures. If you already know the free surface, forces or pressures do not give any really new information in potential theory. They are also less sensitive. So we too put our focus on the wave height around the cylinder. Preliminary results were presented in [1]. In a later stage we also took the opportunity to compare our calculations with the wave profile measurements performed by the EXPRO-CFD project for a similar situation.

3.1 Setup

In a time domain code it is tempting to mimic the diffraction experiments as done in the wave basin by including a wave maker. However, this is not necessary and not efficient. When a wave flap is used for creating the wave field one has to start from a basin in rest. From there it takes time for the wave field to settle down and to reach the object. The alternative, the analytical description of an incoming regular wave field, is more flexible.[1] Such an inflow condition puts no requirements on the shape of the outer boundary. This freedom can be used to please the outflow conditions. Those outflow conditions have to deal with the diffracted waves spreading from the object out to infinity. This is an essentially spherical symmetric situation, that can be handled best by a grid having the same property. If the object is then also almost spherical symmetric, the grid generation turns out to be really simple. Hence, it is natural to have an outer domain boundary that is cylindrical.

[1] Similar tricks should be possible for an irregular wave field, see chapter 6.

In HYPAN panels are organised in patches with a rectangular topology called networks. The intersections between networks are problematic. This makes it desirable to have the free surface made up out of one network. For a cylindrical setup the free surface network will then be laid around the object and connected to itself. Because of the rectangular network structure panels close to the object will be relatively small and panels far away will be relatively large. This gives a larger resolution in the vicinity of the object, where it is appreciated. On the other hand, one cannot control the circumferential resolution as it becomes less and less moving away from the object. This causes problems when trying to resolve the incoming wave, effectively putting a limit on the domain radius depending on the required resolution and the number of panels in the circumferential direction.

Using one network for the free surface in such a way still leaves us with one network intersection in that free surface. This is not optimal. Because we have a left-to-right symmetry in all cases that we are going to consider, we can use a simple work around. The intersection is put at right angles with the incoming wave in, say, the right half of the free surface. The disturbing effects of that intersection will be largely contained within that right half of the free surface. We can then replace the solution[2] in that half with the values coming from the other half, effectively removing the intersection at the cost of needing symmetry without being able to use it for bringing down the computational cost. Certainly, it would be better to introduce networks that can attach to themselves without having to use one-sided discretisations. However, this would involve a lot of small logistic changes in the core of the code, without providing a general solution. This was considered a waste, since Eggermont was already working on a more fundamental solution.

The purpose of the outflow boundary is to absorb the outgoing diffracted waves instead of reflecting them. This can be achieved by the applying absorbing techniques to the difference with the (analytical) incoming wave. The lowest frequencies can be absorbed best by a Sommerfeld radiation condition tuned to the lowest frequency. The higher frequencies can then be absorbed by a relatively short pressure damping zone.

A time domain program has to start up from some known situation to the situation you are interested in. On a circular outer boundary one cannot prescribe an arbitrary start-up function on an incoming wave, because the value at the sides must correspond with the physical evolution. So instead of bringing the wave carefully onto the object we bring the object carefully into the wave. Using the analytical description for the incoming wave we have a continuous path from prescribing the normal velocity of the full incoming wave on the object to prescribing a normal velocity of 0 on the object. See also Ferrant [8].

Using lagrangian grid motion, calculations remain stable even for very high waves. When the orbital motion of the water particles is large compared to the object, however, lagrangian grid motion is no option. As a compromise, one can use fully eulerian grid motion near the object, fully lagrangian motion (far) away from the object, and a varying linear combination of them in between. However, lagrangian motion needs some corrections to guarantee an acceptable grid distribution. When the positions of the grid points form a rectangular array in physical space these algorithms are more or less straightforward. When the positions of the grid points form a curved array

[2]This is done each time a new solution is calculated.

they are not. Therefore we tried to get away with eulerian motion.

For the moment the diffracting object is defined by its depth, its horizontal coordinates, and vertical freedom of motion. This fits (truncated) vertical cylinders of arbitrary cross-section. The standard intersection algorithms in HYPAN can handle this. Grid points on the cylinder mantle move with a fraction of the motion of the intersection point above them. The bottom networks of the cylinder are kept fixed in time.

3.1.1 Grid

The domain is cylindrical, with a truncated vertical cylinder in the middle. The bottom of the cylinder is flat, because there was no need to make it nicely rounded. The cylinder and the domain boundary are therefore similar in shape. For their circular bottoms we use five networks: one square in the middle, with a width half the diameter of the bottom, and four networks around the square each connected to one of its sides. The cylinder mantle consists of one network connected to itself. The same is true for the free surface and for the outer domain boundary.

All HYPAN networks are collections of panels with a rectangular structure.[3] Connecting networks have to be connected panel by panel, but not necessarily with all panels: a network edge can be divided into segments, each connecting to a fitting segment of another network. This rectangular structure means that by choosing the number of panels on the free surface around the cylinder the number of panels in the circumferential direction of the other networks will also be fixed. For example, on the cylinder mantle one cannot change the number of panels in the circumferential direction, especially not as a function of depth, whereas one certainly would like this possibility to bring down the total number of panels.

Because the circular free surface is covered by one network with a rectangular topology connected to itself, the width of the panels in the circumferential direction is determined by the number of panels on the circumference of the cylinder and the distance to that cylinder (constant angle). To resolve the incoming wave a minimum number of panels per wavelength is required at the outside of the domain. Given the number of panels in the circumference, the maximum radius is then determined by

$$R = \frac{M}{2\pi n}\lambda, \tag{3.1}$$

with M the number of panels in the circumference, and n the required number of panels per wavelength. At a minimum resolution of 25 panels per wavelength, 40 panels in the circumference give a radius of half a wavelength, 80 panels a radius of one wavelength, and 160 panels a radius of two wavelengths.

On the free surface the resolution should preferably be the same in all directions. This is impossible, because the circumferential width of the panels has to span a fixed horizontal angle. For waves originating in the centre of the domain a constant radial width would be sufficient. But for waves moving in any other direction the differences in resolution, especially near the outer boundary, would be very high in such a situation and would probably influence the propagation. Originally, we therefore choose to use approximately square panels on the free surface. In a later stage we kept the

[3] See also chapter 2.

panels square up to a certain radius, after which the radial width remained constant. Any deviations from the incoming wave should be damped by the beach anyway.

Given the exponentially decaying amplitude of the wave solutions while going deeper into the water, the need for resolution is higher near the free surface and lower away from the free surface. Because of the large differences in size between the smallest and the largest panels it was preferred, from a numerical accuracy point of view, to make the largest panels, the ones on the outer boundary, not unnecessary large. At the bottom of the outer boundary this meant not making the panels higher than their width in order to have less panels. To resolve the incoming wave on the outer boundary it did not seem to be necessary to have the height of the panels close to the free surface be less than their width (at the expense of more panels and a less than ideal aspect ratio). On the outer boundary we therefore have square panels. On the cylinder mantle the panels close to the free surface should be close to being square. However, to provide some extra manoeuvring margin for the grid motion, the height of those upper panels was taken to be twice their width. For simplicity, all the other panels on the cylinder mantle were given the same size. At the time it was not considered worth the effort to try to minimise the number of panels as much as possible by letting the panel height grow as much as possible going deeper and deeper. The gain that could be expected reasonably was at most 1000 panels less (of 9000 panels), including the effect of a similar policy on the outer boundary. This would have given a decrease in calculation time of around 30 percent.

The previous considerations result in the following panel configuration. For all calculations there are 80 panels in the circumference. For the mixed grid there are 30 panels in the radial direction of the free surface. Along the vertical direction of the cylinder mantle there are 20 panels, along the vertical direction of the domain mantle there are 25 panels. This results in a total number of panels of 7760.

3.1.2 Start up

Typically, a time domain diffraction calculation consists of the following phases: start from rest, create a sea state, and look at the resulting behaviour of the object (for some time). Starting from rest and creating a sea state takes time. You want the fastest route to that sea state. In general one knows this sea state more or less analytically: either one has an explicit formula, or one can interpolate between numerical wave tank data. The sea state including the object is not known of course. Normally, one starts from rest and introduces the wave gently on to the object. If, however, one has an analytical description for the incoming wave, one can gently introduce the object into the wave: start with prescribing the wave solution on the object and then slowly bring the normal velocity on the object down to zero.

Bringing the wave in gently has another downside in our case. Having an analytical description for the incoming sea state but no analytical description for the evolution from rest to that sea state, an arbitrary start-up function has to be used. It should start at 0 and change sufficiently smoothly to 1. Multiplied with the incoming sea state we get an analytical description that starts with no waves at all and which then changes to the full incoming sea state in a smooth way. However, when applied on a circular boundary the waves that travel through the middle will be different from the waves that are prescribed on the boundary further to the outside. Unless, of course,

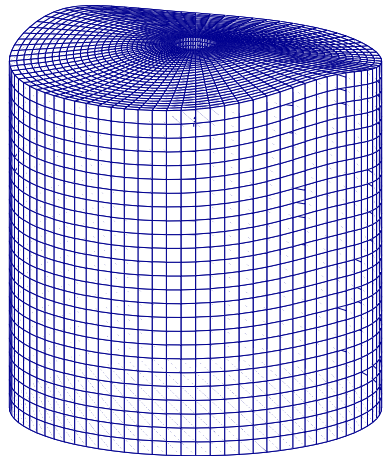

(a) complete grid of mixed grid at $t = 0$

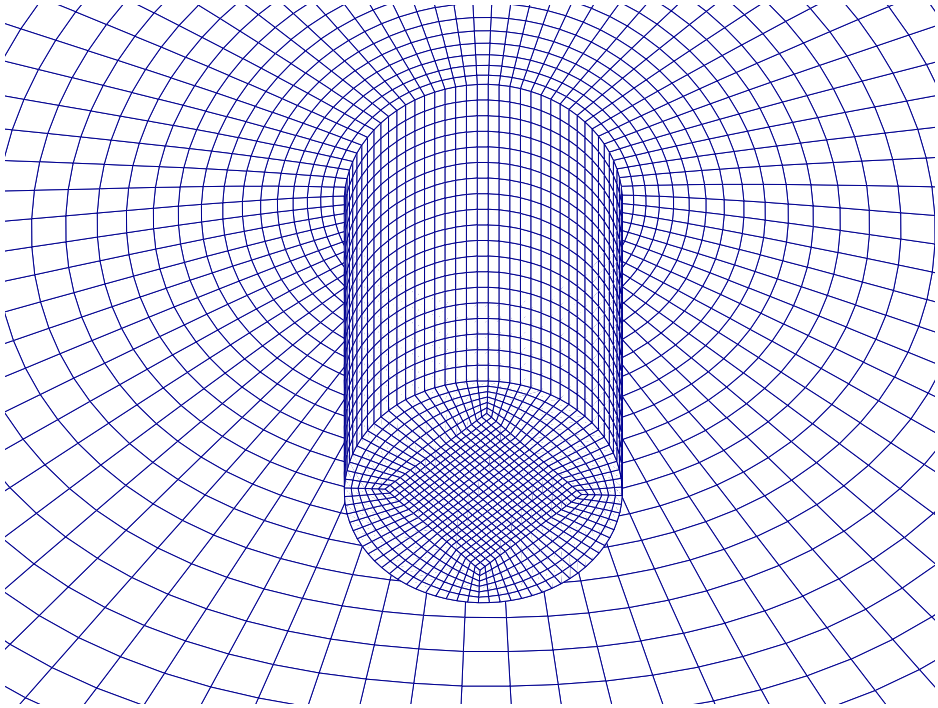

(b) cylinder grid viewed from below at $t = 0$

Figure 3.1: Two different views on the grid used.

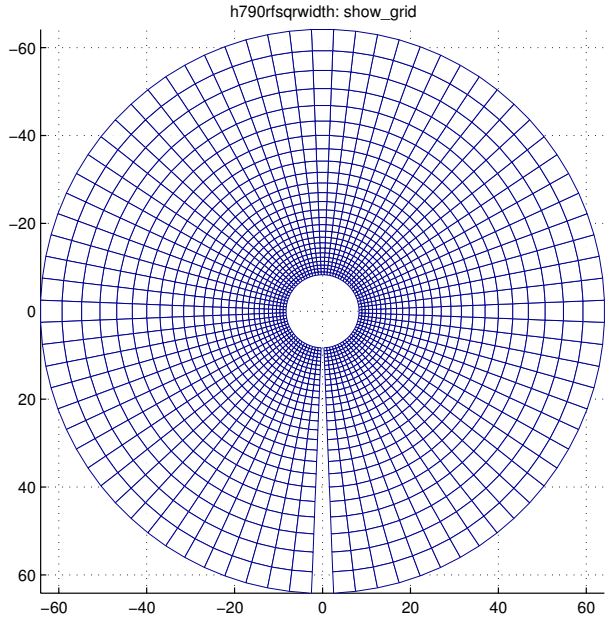

(a) square grid for circular cylinder

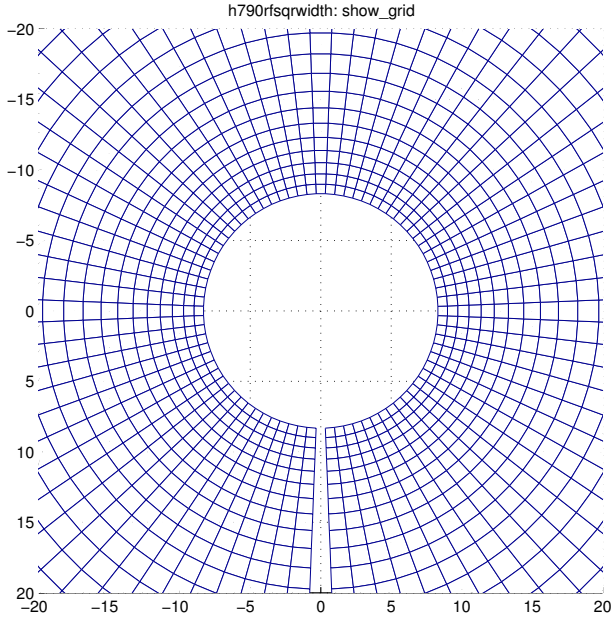

(b) square and mixed grid: near circular cylinder

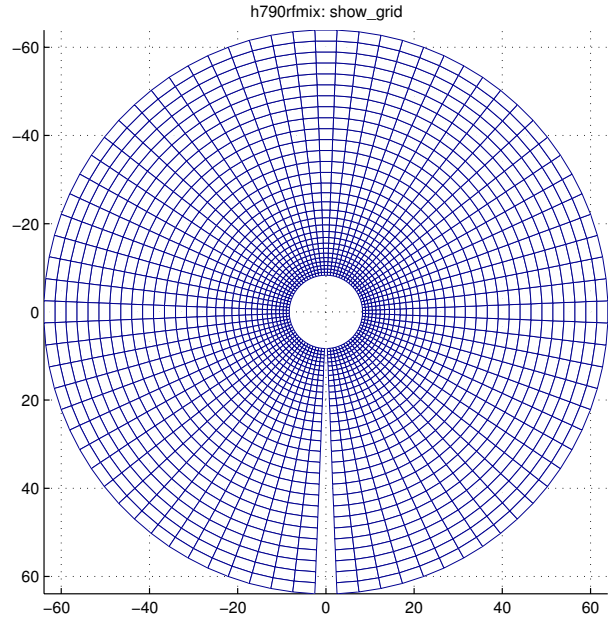

(c) mixed grid for circular cylinder

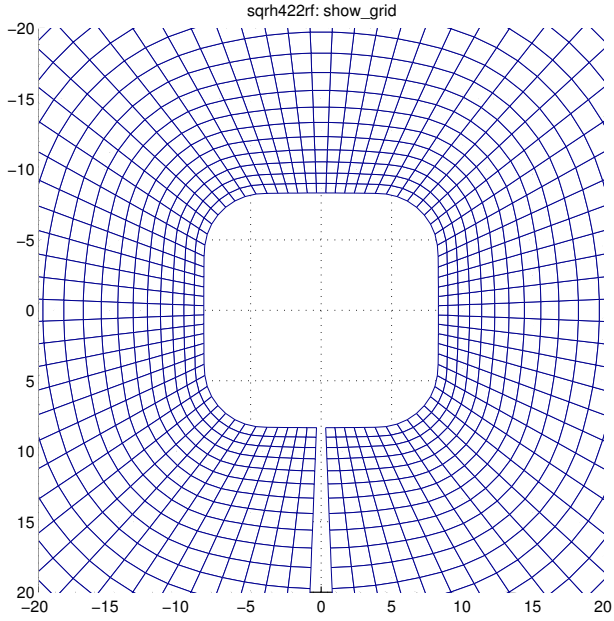

(d) square and mixed grid: near square cylinder

Figure 3.2: Free surface grids for the circular and square cylinders.

the start-up function has a physical time evolution (dispersion relation). With a very good beach this should not be a big problem, one could just wait until all the start-up phenomena would have been absorbed, but for our current beaches the statement "What you don't put in you don't have to take out" is very applicable.

As said before, we start with the incoming wave field prescribed in the whole domain. This means for example that the free surface is initialised with the appropriate wave elevation and the appropriate potential, both derived from the Rienecker & Fenton description of the incoming wave.

For the boundary condition on the cylinder we take the following:

$$\phi_n = \epsilon \phi_n^{\mathrm{RF}}, \text{ with } \epsilon = \begin{cases} 1 & \text{if } t \leq 0 \\ \text{see (3.3)} & \text{if } 0 < t < \tau,\ \tau = T \text{ or } 2T \\ 0 & \text{if } t \geq \tau \end{cases} \tag{3.2}$$

$$\epsilon = \frac{1}{2} \tanh\left(\tan\left(\frac{\pi}{2}\left(1 - 2\frac{t}{\tau}\right)\right)\right) \tag{3.3}$$

Here τ is the start-up time and T is the period of the incoming wave. The superscript RF refers to the semi-analytical Rienecker & Fenton description.

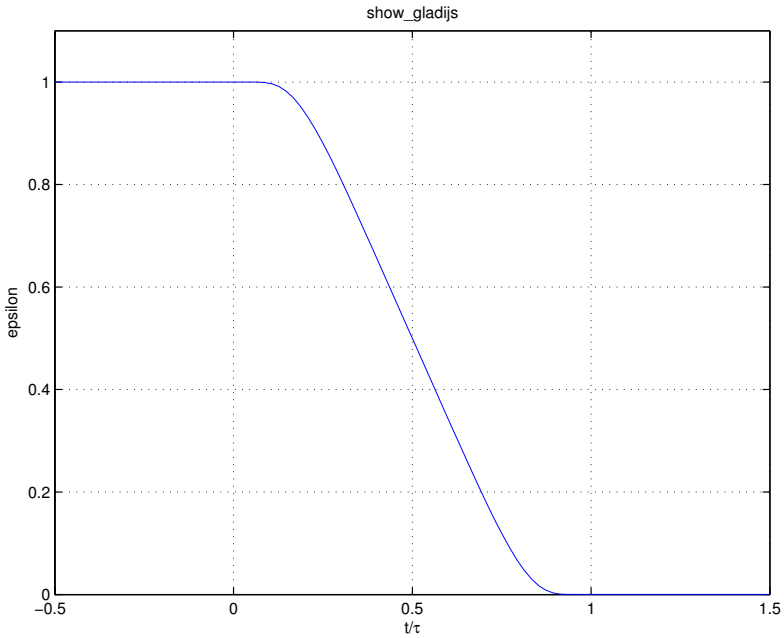

Figure 3.3: Graph of ϵ (see (3.2)) as a function of t/τ.

3.1.3 Grid motion

The basic theory concerning the motion of the grid has already been presented in the theory chapter. This section is meant to give an explanation of what we did and why

we did not do it otherwise.

Free surface

The motion of the free surface grid can be implemented in several ways. As described in the theory chapter, Broeze showed in his PhD thesis that a lagrangian treatment of the free surface was the most stable one. For the current problem this has some drawbacks however. Because the orbital motion of the incoming wave is comparable to the size of the object, the grid points around the object go from the front to the back, and back again, causing large changes in the resolution. With even larger orbital motions the grid points would like to leave the cylinder, which is of course impossible. From this it is obvious that the grid points around the cylinder should be fixed relative to the cylinder, at least to some degree. The other drawback is less fundamental, but still significant. When applying lagrangian motion some attention should be given to the distribution of the grid. This can be accomplished with the use of correction velocities. In the case of rectangular grids the algorithms for the correction of the velocities are relatively straightforward, because it is just a matter of keeping things straight. For nonrectangular grids the situation is more difficult: the difference between good non-straight and bad non-straight is very difficult to put in an algorithm.

The first drawback necessitates the use of at least a mix of eulerian and lagrangian motion. The second drawback makes it attractive to first try fully eulerian motion. A fixed grid is of course always convenient. To judge whether eulerian motion is acceptable a Rienecker & Fenton wave is also prescribed on the cylinder to see whether the grid causes any unacceptable deviations from the prescription. See the testing section. The eulerian motion proved to be sufficient, so we kept using it.

Cylinder

With eulerian motion close to the cylinder, the motion of the grid on the wetted surface of the cylinder becomes trivial. The horizontal positions specified at start up for the points on the cylinder mantle define the mantle shape. During the simulation only the vertical coordinates will be modified. The collocation points move with a fraction of the vertical velocity of the fluid: no movement on the bottom of the cylinder and proportional to position in between. In addition, the collocation points get a small correction velocity towards the centre of their panel, which is half way its vertical neighbours. When using square panels, this simple algorithm allows the topmost collocation point to come too close to the free surface for the highest waves. Taking the vertical width as twice the size of the horizontal width gives enough space for buffer.

Other surfaces

The motion of the other surfaces, the bottom and the outer boundary of the domain, depends on the motion of the free surface. In case of eulerian motion the vertical network that forms the outer boundary only has to move in the vertical direction to follow the intersection with the free surface. The bottom networks can then remain at their initial positions. The collocation points of the outer boundary network get a

vertical velocity equal to that of the fluid, together with a small correction velocity towards the centre of their panel. For the large panel sizes at the outer boundary this algorithm is subtle enough.

3.1.4 Beaches

The incoming wave is prescribed both at inflow and at the outflow. Or in other words, around the entire outer boundary. The diffracted waves reaching the outer boundary have to be absorbed. Or, to be more precise, everything that reaches the outer boundary other than the incoming wave that should be there and is prescribed already, should be absorbed. We therefore apply absorbing techniques to the difference with the incoming wave.

Because we will be looking at regular wave cases, the diffracted waves will consist mainly of contributions at the incoming wave frequency supplemented by contributions at multiples of that frequency. This makes the Sommerfeld radiation condition the ideal starting point for a beach setup. A Sommerfeld radiation condition tuned on the incoming wave frequency takes out the first order diffraction and the higher diffraction affects can then be removed by a relatively short pressure damping zone.

There is not a lot of room for a beach. Coming too close to the object will disturb the diffraction field in its neighbourhood. Having a beach of 32 m seemed to be a good compromise. This is one wavelength of the first higher harmonic. With a domain radius of 64 m there remains an area of 32 m radius with an unmodified free surface boundary condition. The cylinder has a radius of 8 m. We chose three different beach strengths, see section 2.5.3: a beach slope parameter b of $0.10 \cdot 10^3$, referred to as *full* beach, a value of b of $0.05 \cdot 10^3$, referred to as *half* beach, and a value of b of $0.025 \cdot 10^3$, referred to as *quarter* beach. The dimensions of b are $[\rho\omega] = \mathrm{kg} \cdot \mathrm{m}^{-3} \cdot \mathrm{rad} \cdot \mathrm{s}^{-1}$. The full beach has a bounce reflection for the first order component of the diffraction of around 3% and a total reflection for the second order component of again around 3%. The quarter beach has a bounce reflection for the first order component of the diffraction of around 1% and a total reflection for the second order component of around 17%. The relative performance of the beaches therefore depends on the relative importance of the higher order components in the diffraction.

3.2 Testing

First we want to know whether our grid can resolve the incoming wave. For that, we prescribe the incoming Rienecker & Fenton wave also on the cylinder. Now, ideally, there should be nothing else than the incoming wave in our domain and any deviations are spotted easily by looking at the difference with the prescribed incoming wave.

Secondly, we want to get confidence in the rest of the setup. For this we have to compare to some known data. Experimental data is not ideal for bug hunting. There is a limited number of data points and the accuracy is relatively small and not certain. Ideally, one would like to have analytical expressions to compare with. In that case one can have a very detailed look at what goes wrong where. Of course, we do not have such expressions for the cases we are really interested in. However, we can compare with linear diffraction theory in some simple situations. In this case,

the linear diffraction solution for an infinite vertical cylinder from McCamy & Fuchs [19] can be used.

3.2.1 Rienecker & Fenton wave with open cylinder

How well do we resolve the incoming wave? To answer that question we prescribe the incoming wave solution also on the cylinder, while retaining the beach and the Sommerfeld radiation condition. Subtracting the incoming wave solution from the resulting solution shows any deviations from the ideal situation. As said before in section 3.1.1, we originally used more or less square panels on the free surface. In a later stage we made the radial width of the further out lying panels smaller[4] in an effort to minimise the inaccuracies. We refer to this grid as *mixed grid* and to the original one as *square grid*.

Looking at the maximum deviations from the incoming wave elevation as a function of time, one notices the following. For the 4 m high wave, figure 3.4, the deviations remain at approximately 1% for four periods. The difference between the two different grids is perhaps a factor of 1.2. These results are more or less independent of whether the cylinder is circular or square, as is shown by figure 3.7. For the 8 m high wave, figure 3.5, the difference between the two different grids is larger: the peaks in the deviations of the square grid are 1.6 times higher than those in the mixed grid. For the mixed grid the deviations in the collocation points near the cylinder[5] are around 1% after three periods. For the square grid this is 1.5%. Animations of the deviations on the free surface show that most of the deviations near the cylinder have their origin in the outer half of the domain, as was to be expected considering the low resolution of the grid in that part of the domain. We conclude that the deviations from the incoming wave are around 1% in our calculations. For the 8 m high wave we need the mixed grid for that.

To obtain these results for the 8 m high wave with the circular cylinder and for the 4 m high wave with the square cylinder, we had to use equation 6.22 from Broeze (A.1). The 4 m high wave with the circular cylinder did not have such problems. For the 8 m high wave there is on the back of the cylinder a little bump going up and down spreading around the cylinder and backwards. The little wave spreading around the cylinder could be a cross wave instability as described in Broeze, having the backwards spreading wave as a consequence. That it only occurs at the backside of the cylinder suggests that the prescription of the incoming wave on the cylinder mantle has at least something to do with it. On the other hand, the peak of the wave is moving from the front side to the backside of the cylinder, encountering their one-sided finite differences in opposite directions. This gives a possible reason for the observed asymmetry. To prevent any cross wave instabilities, Broeze used equation 6.22 in his thesis. It applies a small amount of damping depending on a measure of the discretisation error at the first row of collocation points on the network. We did the same: for the results see figure 3.8(a) and figure 3.8(b). As can be seen, this procedure does not prevent the occurrence of the cross wave entirely, but it does prevent it from getting out of hand.

[4] By making the radial width constant after a certain radius.
[5] Near means the inner 15 rows.

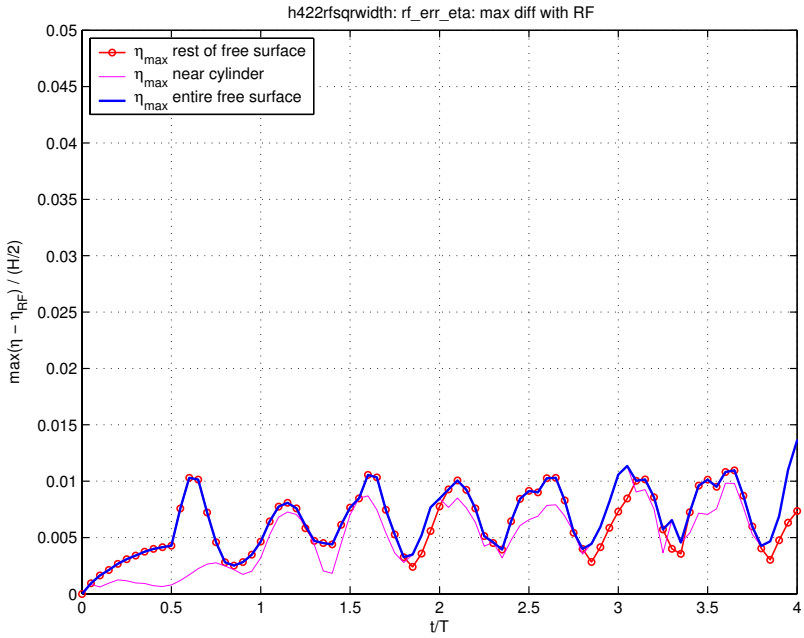

(a) Square grid

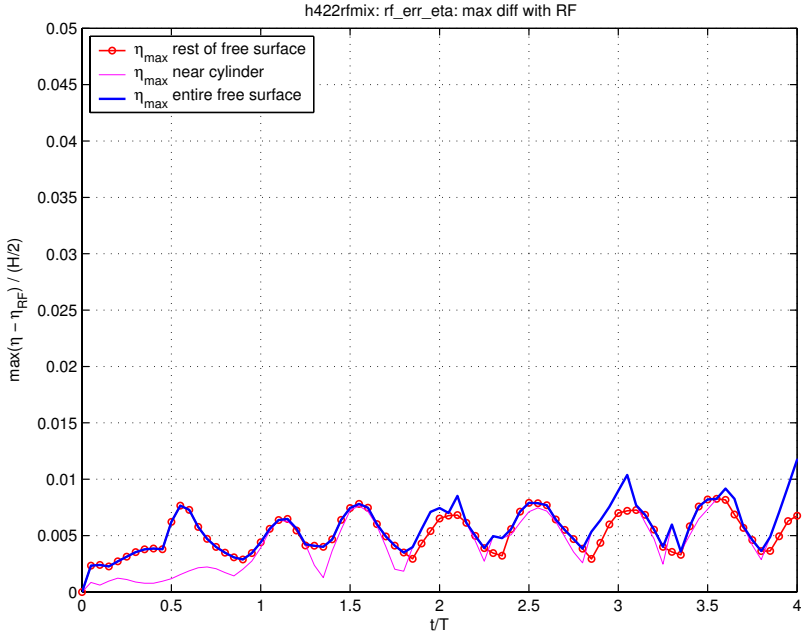

(b) Mixed grid

Figure 3.4: Maximum elevation error as function of time for the 4 m high wave.

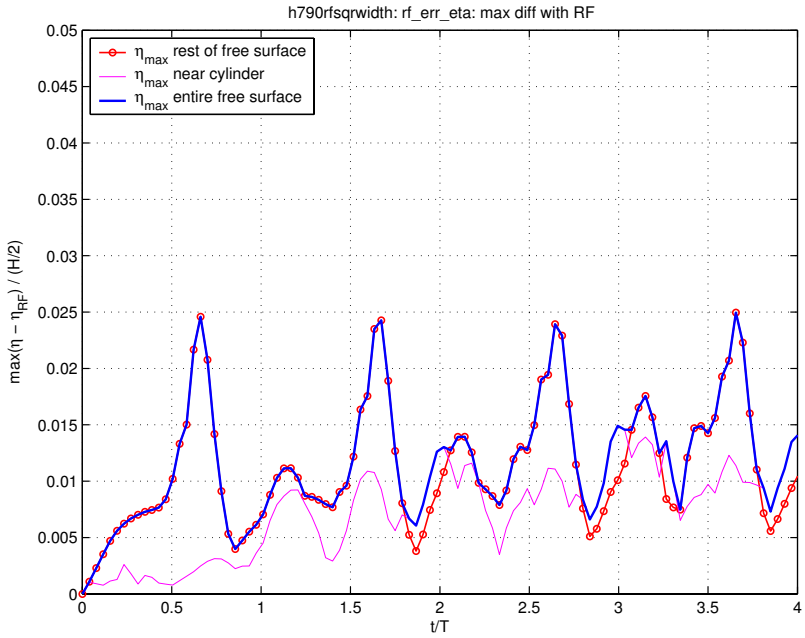

(a) Square grid

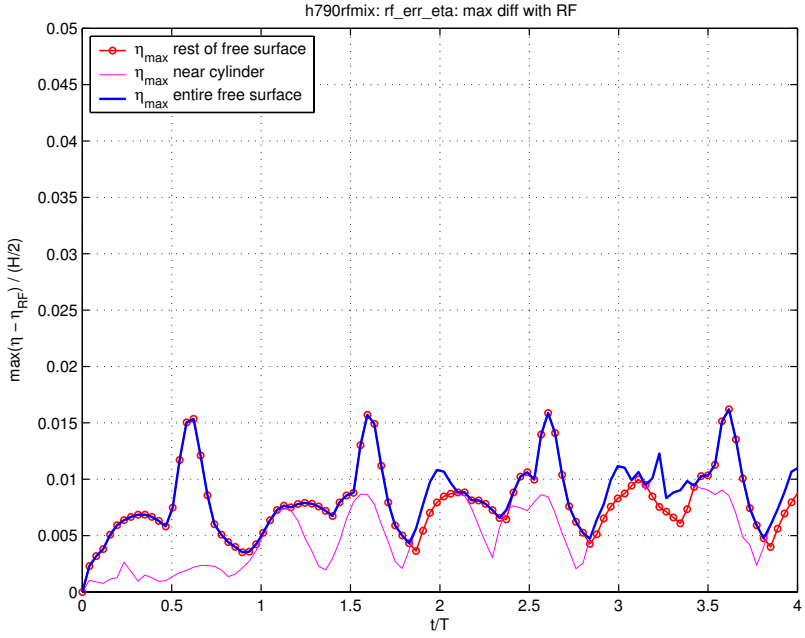

(b) Mixed grid

Figure 3.5: Maximum elevation error as function of time for the 8 m high wave.

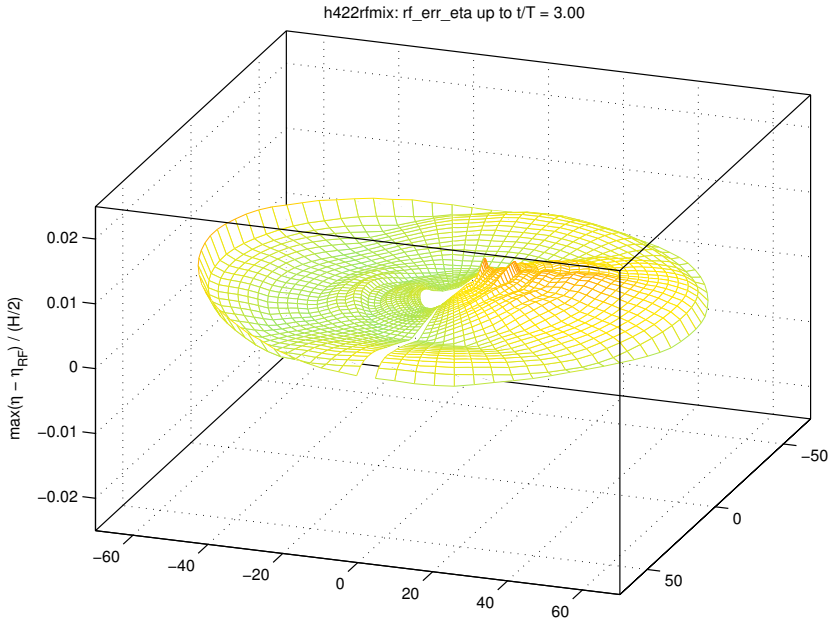

(a) The 4 m high wave with mixed grid

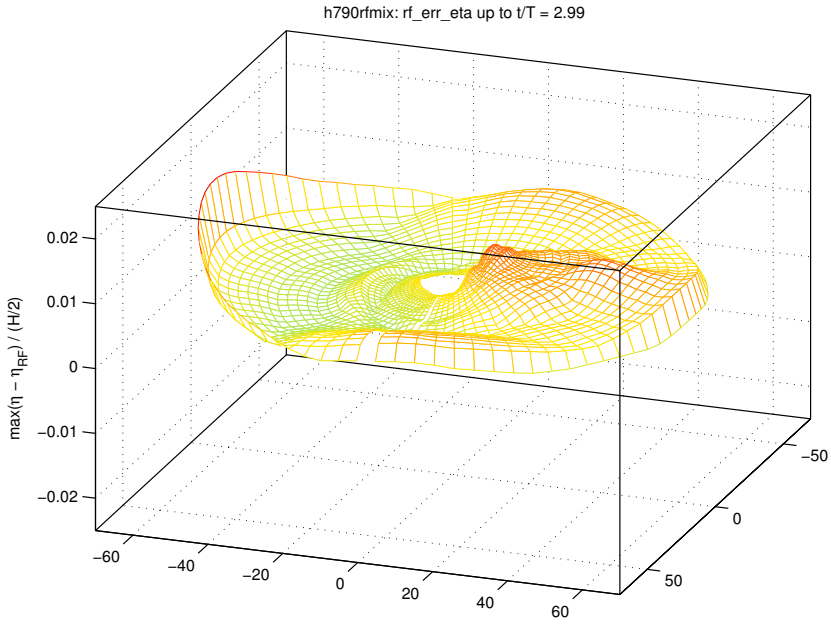

(b) The 8 m high wave with mixed grid

Figure 3.6: Maximum elevation error up till $t/T = 3$.

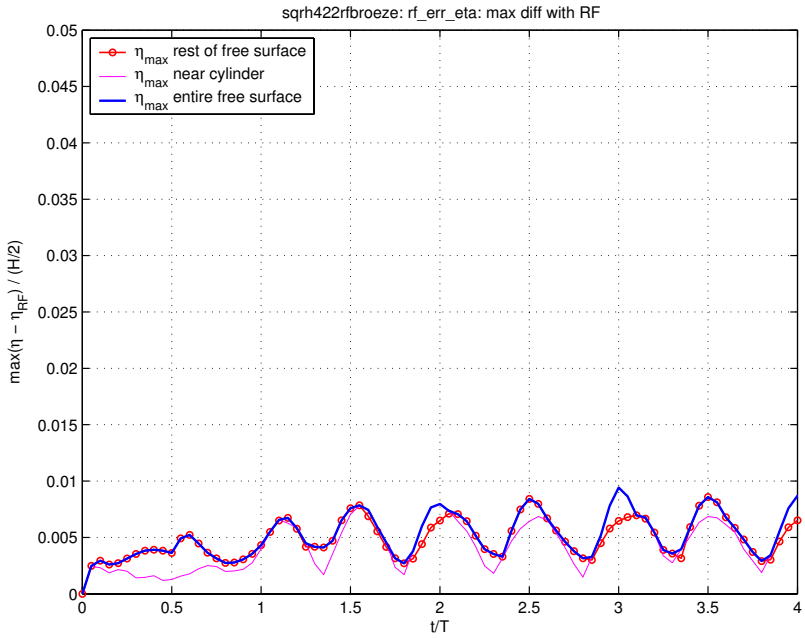

(a) Mixed grid

(b)

Figure 3.7: Maximum elevation error as function of time for the 4 m high wave with the square cylinder.

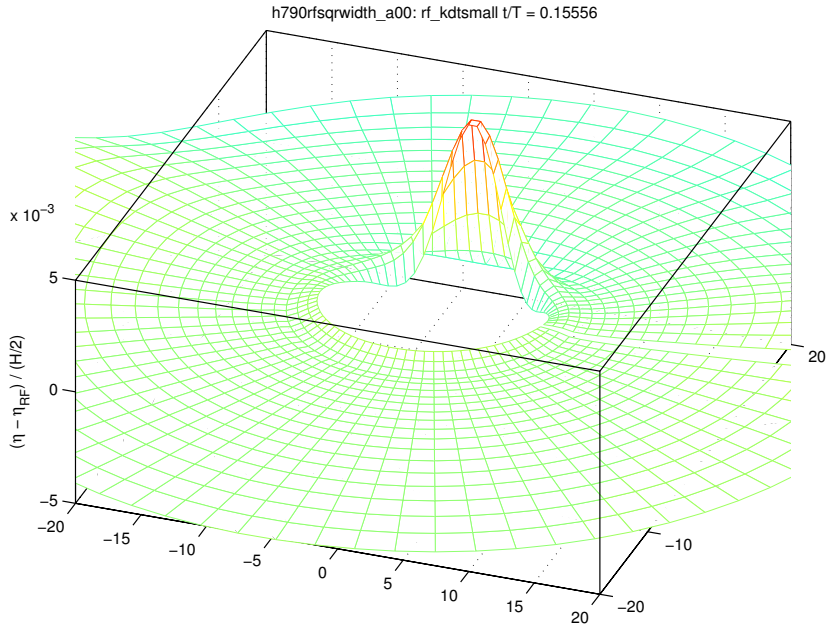

(a) $a = 0.0$

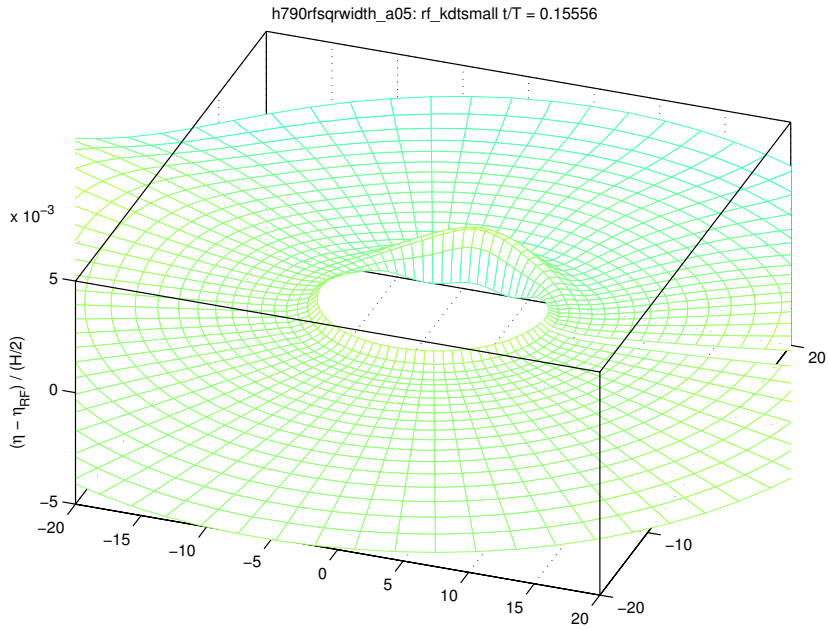

(b) $a = 0.5$

Figure 3.8: Deviation in elevation after 20 time steps of 0.07 seconds for the 8 m high wave near the cylinder.

3.2.2 Comparison with linear diffraction theory

In this section the whole setup is tested by comparing with the linear diffraction solution by McCamy and Fuchs for an infinite, vertical cylinder diffracting a regular wave on deep water. Instead of an infinite cylinder we double the depth of our cylinder from 24 m to 48 m. To ensure that that is close enough to a cylinder of infinite depth we double the depth again and look at the difference. See figure 3.9. As one can see the difference between the two is negligible, so we consider the infinite solution to be appropriate reference material for the 48 m deep cylinder.[6] For the amplitude of our linear wave calculated in our non-linear diffraction code, we take a value of 0.10 m on a wavelength of 126 m. This corresponds to a steepness of $a/\lambda = 0.001$.

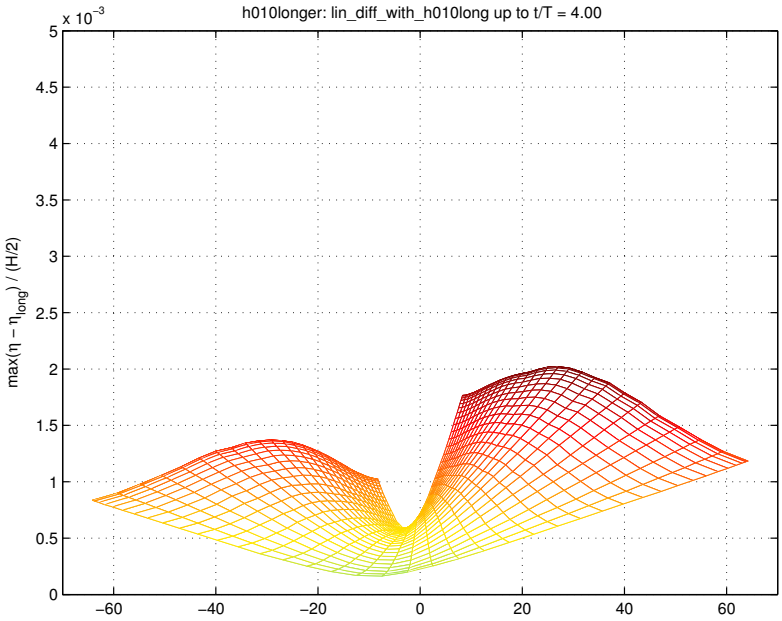

Figure 3.9: Maximum difference between the 48 m deep and the 96 m deep cylinder up till $t/T = 4$. Please note the exponent in the top left corner.

Start up from complete linear solution

We take out the start-up part of the setup, and directly start from the complete linear diffraction solution. The beach turns out to have a large effect. This is shown by considering four different beach strengths including no beach. Note that for a linear diffraction calculation the Sommerfeld radiation condition should be sufficient (as long as it is applied in the far field).

The calculation without a beach but with a Sommerfeld radiation condition has after four periods an error of two percent. Half of that has the shape of a wave with the

[6] The orbital motions of a wave with a wavelength of 128 m have at a depth of 48 m a magnitude that is nine percent of their magnitude on the free surface. At a depth of 96 m it is one percent.

same wavelength of the incoming wave. We do not understand this. The calculation with a full beach has after four periods an error of 5 percent. In figure 3.11(f) one can see that the difference with the linear diffraction solution has an edge at the start of the beach. It then does not come as a surprise that the beach has a significant influence. The half beach has an error of three percent, and the quarter beach has an error of two percent, which is comparable with the calculation without a beach. Looking at the snapshots of the error at $t/T = 3.25$, one can see that the shape of the error is more like the other beaches then like the calculation without a beach.

This section showed that without disturbing transients from the start-up procedure we can simulate the linear diffraction solution with 2 till 5 percent accuracy depending on the strength of the beach. See also section 3.3.1.

Linear incoming wave

Here we look at the complete setup: again a normal (closed) cylinder, now combined with the start-up procedure. We look at two calculations: one without a beach and one with the full beach. The question is how long the transients associated with the start-up procedure will spoil the stationary diffraction solution and whether a beach is needed to absorb them.

The maximum error of the two calculations is the same up till the first quarter of the first period. Both have then reached an error level of 5 percent. The calculation without a beach then goes up and down between two and 5 percent for two more periods, before settling down towards an error level of 1 percent. The calculation with a full beach settles after four periods on an error level that fluctuates between 3 and 5 percent.

The conclusion is that the calculation with the full beach has lost its transients after 2 1/2 periods and that the Sommerfeld radiation condition is capable of absorbing the transients in the linear case.

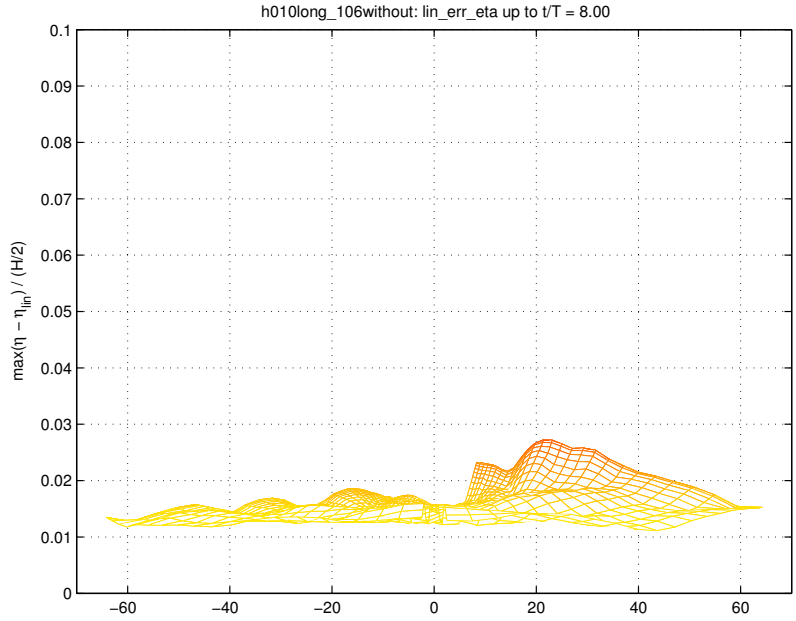

(a) Maximum elevation error up till $t/T = 4$.

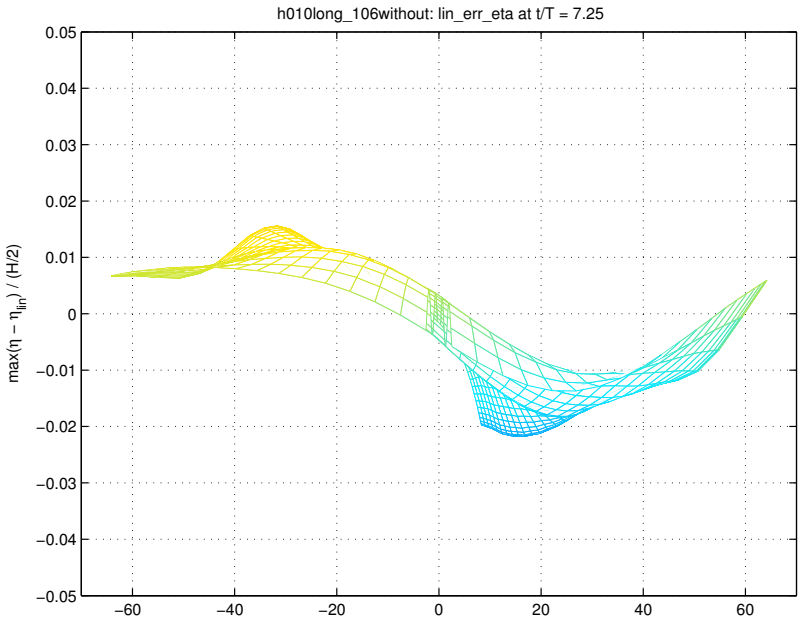

(b) Difference with the linear solution at $t/T = 3.25$.

Figure 3.10: Start up from complete linear diffraction solution, with a Sommerfeld radiation condition and without a beach.

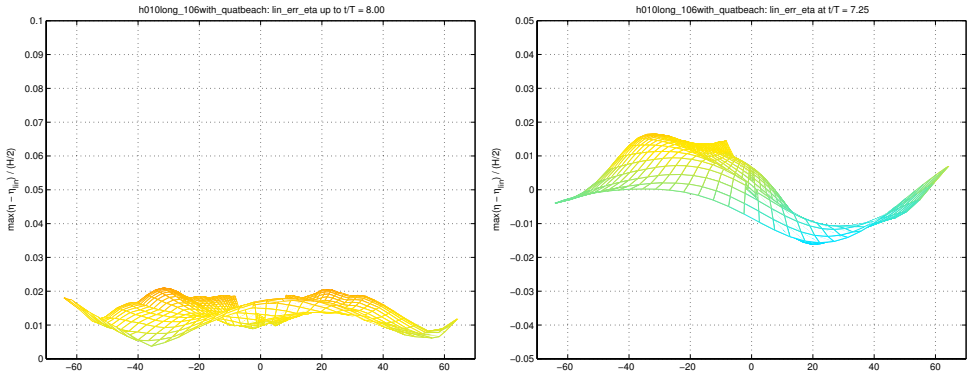

(a) quarter beach

(b) quarter beach

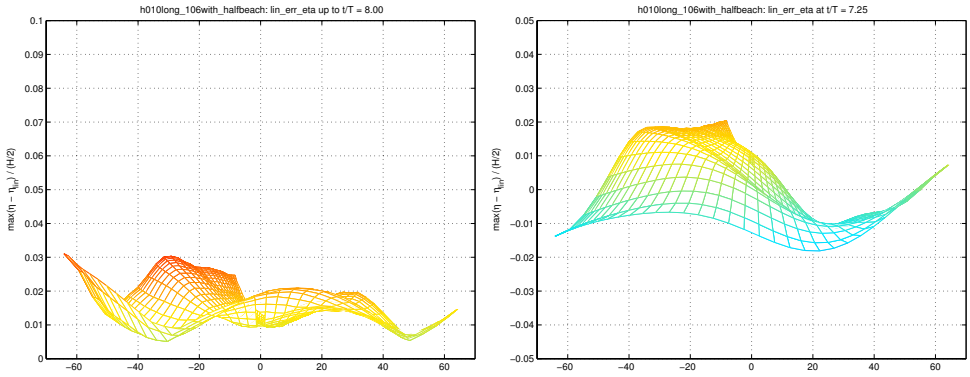

(c) half beach

(d) half beach

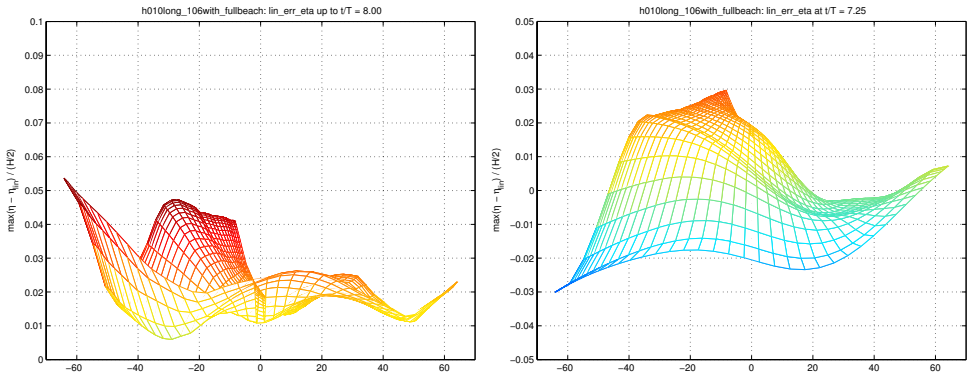

(e) full beach

(f) full beach

Figure 3.11: Start up from complete linear diffraction solution, with a Sommerfeld radiation condition and with a beach. On the left side: maximum elevation error up till $t/T = 4$. On the right side: difference with the linear solution at $t/T = 3.25$.

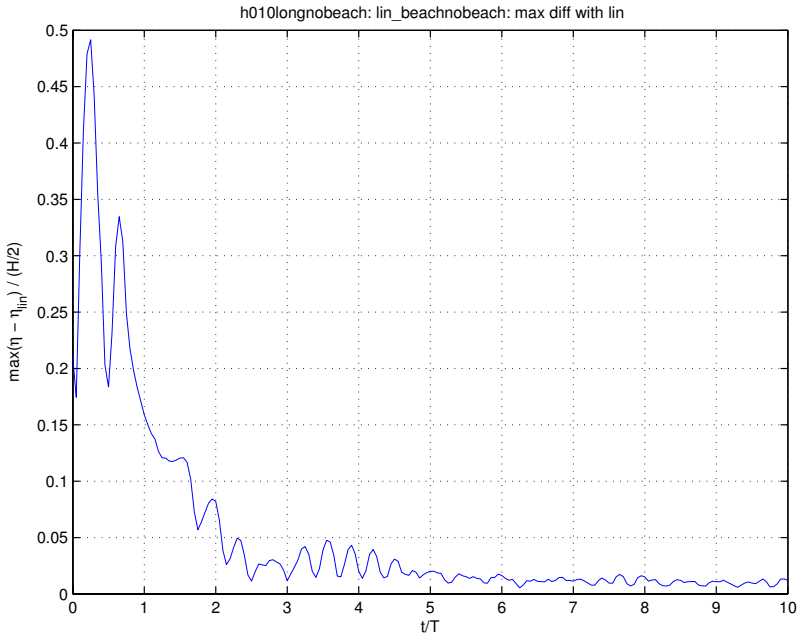

(a) without a beach

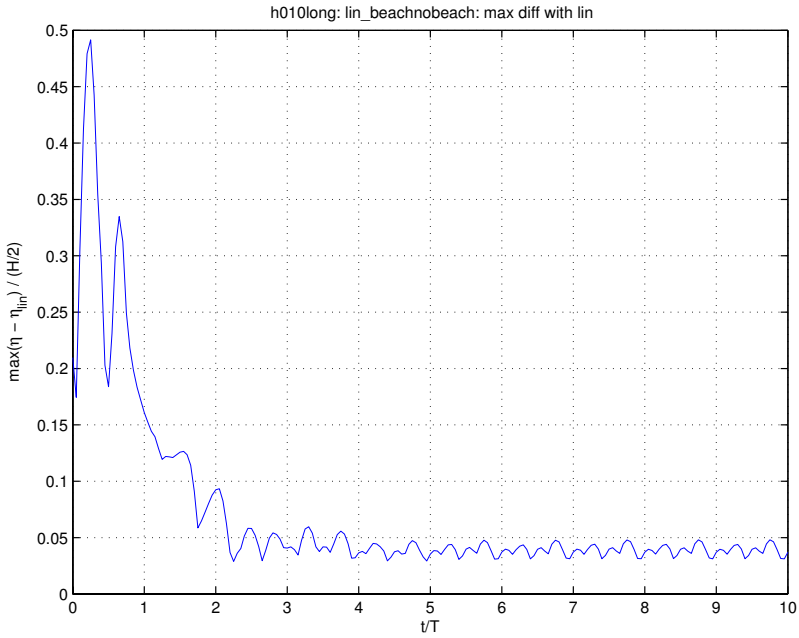

(b) with a full beach

Figure 3.12: Maximum deviation in the elevation as function of time. Start up from open cylinder to closed cylinder in one period.

3.3 Comparison with experimental data

The main comparison is with the ISSC comparative study, as presented in the next subsection. This study also determined the specifics of our set up. The EXPRO-CFD wave profile measurements presented in section 3.3.2 happened to come along and needed little adjustment to the ISSC setup.

3.3.1 ISSC comparative study

The ISSC[7] 2000 Load Committee, Committee 1.2, identified computation of airgap under platforms and runup along platform columns as important issues and they initiated a comparative study: "Comparative Study of Airgap on Floating Platforms and Runup on Platform Columns" [21]. A large number of organisations with a recognised expertise in hydrodynamic modelling were approached for this study. Only six organisations submitted results to the study. Of those there were only two computer codes that implemented the fully nonlinear boundary conditions: HYPAN and the code from Ferrant. Our calculations broke off quite soon then and were not included in the results. Since these calculations were a very good starting point for practical diffraction calculations with a floating body we did continue to work on it.

The comparative study defines three separate cases to be calculated. The first case is a rigid vertical truncated circular cylinder. The cylinder is fixed and exposed to monochromatic, bichromatic as well as irregular waves. The second case is identical to the first case except for the cylinder. In this case the cylinder has a square cross-section with rounded corners. The third case is a complete semisubmersible free to respond to the waves and exposed to regular waves of various steepnesses. For all these cases experimental data existed which was used in the final comparison. Of these cases, only the first two were realistic to try and calculate with our method and for those two only the monochromatic waves that would not break.

The diameter of the circular cylinder is 16.0 m and the draft of both the cylinders is 24.0 m. The width of the square cylinder 16.0 m, the radius of the corners is 4.0 m, and the width of the plane section between the corners on each side is 8 m. One side is facing the waves. All incoming monochromatic waves have a period of 9.0 seconds, which implies a linear wavelength of 126 m (the water depth can be considered to be infinite). This gives a wavelength over diameter ratio of about 8. There are three different wave heights: 4.22 m, 7.90 m, and 12.65 m. With steepnesses of respectively: 1/30, 1/16, and 1/10. The last one will certainly break and was not considered. The other two waves will be referred to as the 4 m high wave and the 8 m high wave.

The experimental data consists of wave elevation measurements at a number of points, grouped in rows radiating outward from the cylinder. In the experiments there were only wave probe rows in the front half of the cylinder, for the calculations those positions were mirrored to the back half of the cylinder. This resulted in the following wave probe configurations, see also figure 3.13. For the circular cylinder there are seven rows of wave probes going radially outwards from centre of the cylinder: at 0 degrees with respect to the origin of the incoming wave, at 22.5 degrees, at 45 degrees, at 90 degrees, at 135 degrees, at 157.5 degrees, and at 180 degrees. Within a row the radial distances are: 8.05 m, 9.47 m, 12.75 m, 16.00 m. For the square

[7] International Ship and offshore Structure Congress

cylinder there are five rows of wave probes: at 0 degrees, at 45 degrees, at 90 degrees, at 135 degrees, and at 180 degrees. The radial distances are the same as for the circular cylinder except for the rows at 45 degrees and at 135 degrees. Here the radial distances are: 9.707 m, 11.127 m, 14.407 m, and 17.657 m.

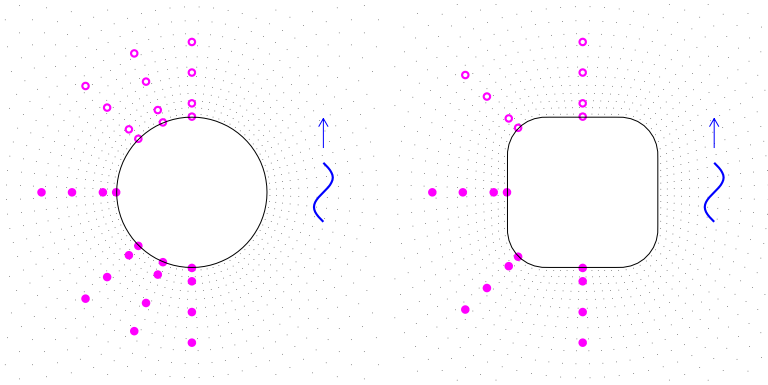

(a) near the circular cylinder (b) near the square cylinder

Figure 3.13: The positions of the wave probes near the cylinders. The closed circles are the original ISSC positions; the open circles are the extra positions.

To give an overview of what the experiments are about we show 7 snapshots of the 8 m high wave in figure 3.23. In the first three snapshots the wave crest is moving towards the front of the cylinder, creating a bump in front of it, which then splits up into two. In the fourth one the two bumps go around the cylinder and in the fifth one they collide together into a peak at the backside of the cylinder. In the last two pictures that peak collapses, creating some small waves.

The results of the experiments done for the comparative study are presented as the maximum elevation in the wave probes for each wave case. The ISSC measurements were only done for four angles in the front half of the cylinder. We mirrored those wave probe positions to the back half. All seven angles are put together in one figure showing for each angle the dependence on the radius.

The 4 m high wave with the circular cylinder

First we give the results of the 4 m high wave together with some comparison material including the ISSC measurements. After that we present in the same format a range of slightly different calculations to show the effect of those changes. This includes the maximum per period (to show when the start-up procedure has lost its influence), some grid modifications, and a number of different beach strengths.

In figure 3.14 we present our results together with the experimental results of the ISSC study, some experimental results from a paper by Contento [4], the calculations of Ferrant done for the ISSC study, and as a reference the linear diffraction results of McCamy & Fuchs [19]. For each wave probe row there is a subfigure with the maximum elevation as function of the radius. The angle that the row is making with

the origin of the incoming wave is given in the title of the subfigure. The elevation is normalised with respect to half of the incoming wave height, and the radius is normalised with respect to the radius of the cylinder. Be warned that the vertical axis does not start at 0! One of the first things that one notices is that the ISSC results at the second row lie way above the others. They have confirmed that it should be considered to be wrong. We kept them in, because for the 8 m high wave there is a similar, although less severe problem. In this way the trustworthiness of those measurements can be judged better. At the other rows their results agree nicely with our results and those of Ferrant. Near the cylinder there is no difference between the calculations from HYPAN and the calculations from Ferrant. One cylinder radius away from the cylinder the difference is less than 5 percent, with HYPAN lying closer to the experiments. Compared to the experimental results of the ISSC study the HYPAN calculations differ by 5 percent or less. The results from Contento are too high, especially in the first three rows. They do however more or less confirm the behaviour at the back of the cylinder. For the HYPAN calculations one start up period is used and less than two periods later the results do not change any more from period to period, see figure 3.15.

In the next figure, figure 3.16, one can see that changing the grid from a square grid (*beach*) to a mixed grid (*mixed*) makes only a very small difference: at the front the results are one or two percent smaller. The calculations referred to as *broeze* and *mixbr* are the same as the other two, only now using equation 6.22 from Broeze (A.1). It did not have a significant effect. The strength of the beach has a much stronger influence: around 5 percent at the front, see figure 3.17. These calculations used a mixed grid. One can see that taking half or a quarter of the strength of the beach will lower the results at the front of the cylinder. At an angle of 45 degrees it then even coincides with the linear result for the weakest beach (but that linear result is for an infinite cylinder, see section 3.3.1). At angles of 90 degrees and higher, the results are almost independent of the strength of the beach. In section 3.2.2 it was shown that the beach can have an effect of a few percent, which is compatible with the present results. One cannot say however that the weakest beach is the best beach for the current incoming waves, since in this case the steepness is not negligible and therefore there are higher order effects that do not move with the velocity at which the Sommerfeld radiation condition is tuned. The experimental results do not suggest that the weaker beaches are better, as was suggested by figure 3.11, but the results from Ferrant do.

Figure 3.18 shows the time evolution of the waterline on the cylinder. When the crest of the wave reaches the cylinder two small bumps are split off that move around the cylinder meeting each other at the back to form a peak and then move back again. This behaviour is not shown by the linear solution. It is interesting to see that the linear solution looks like a sort of average to the fully nonlinear solution.

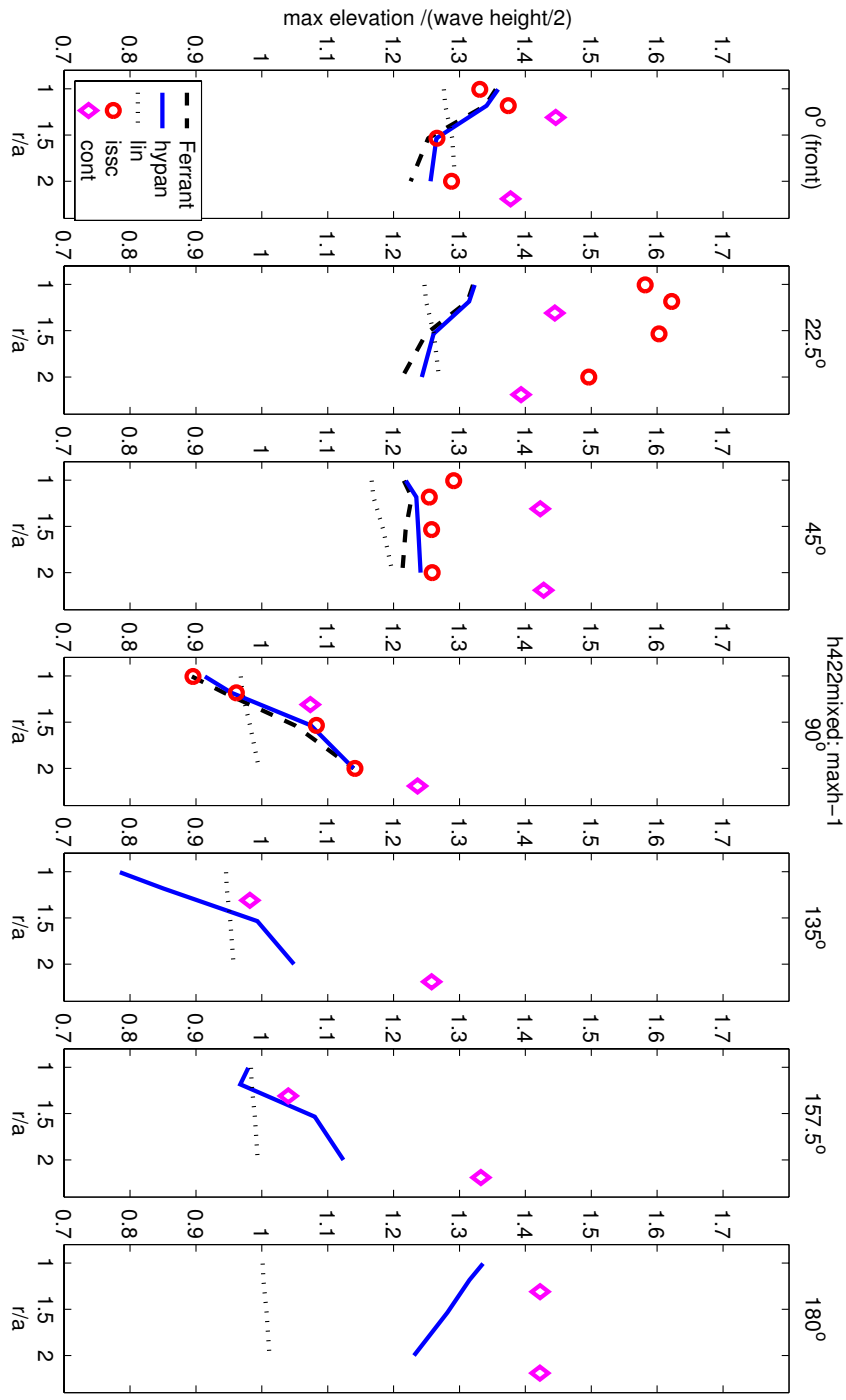

Figure 3.14: The 4 m high wave with the circular cylinder. Maximum wave elevation at the extended ISSC wave probe positions. Comparison with experimental data and the other calculations.

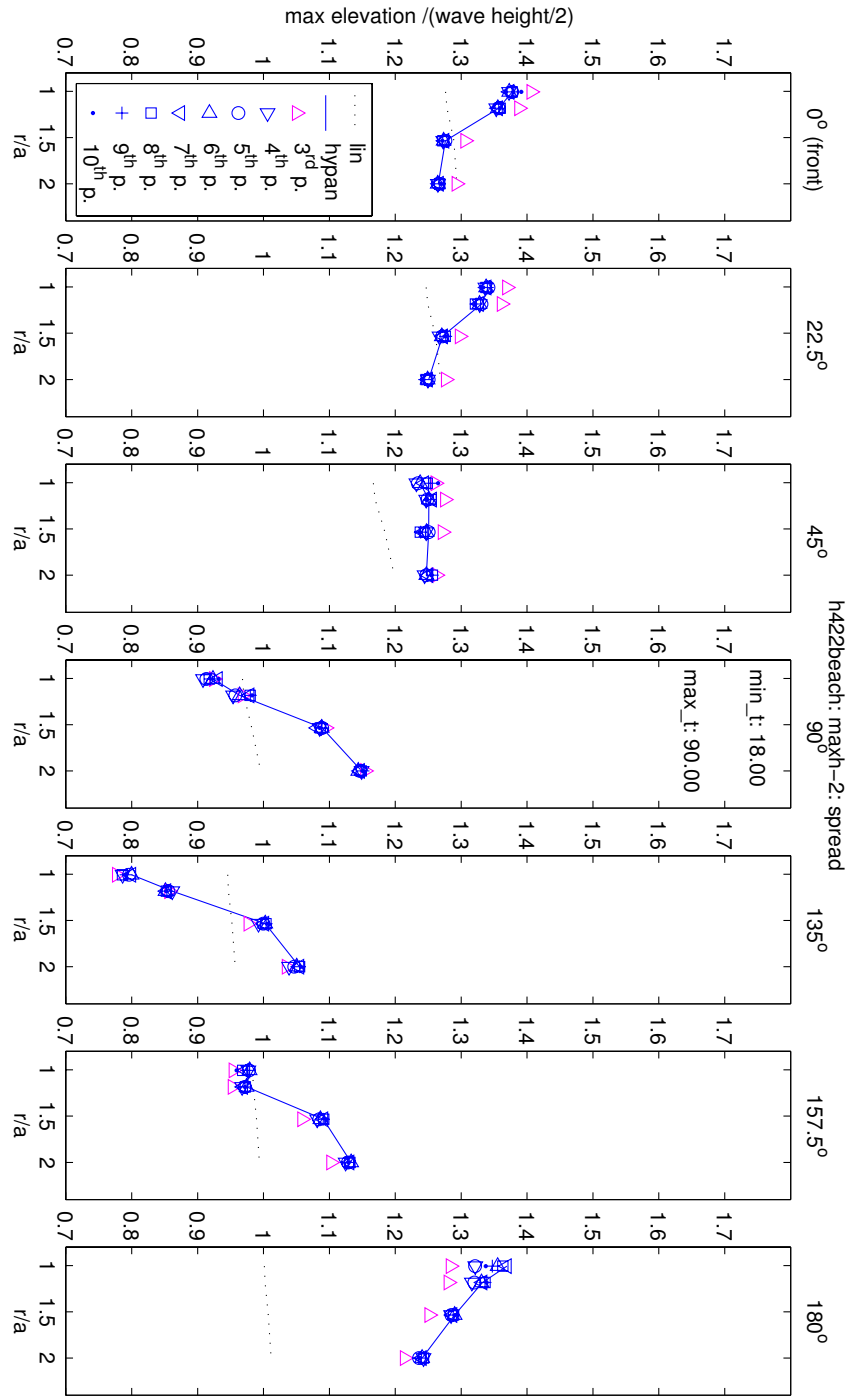

Figure 3.15: The 4 m high wave with the circular cylinder. Maximum wave elevation at the extended ISSC wave probe positions. Maximum per wave period starting at period 3.

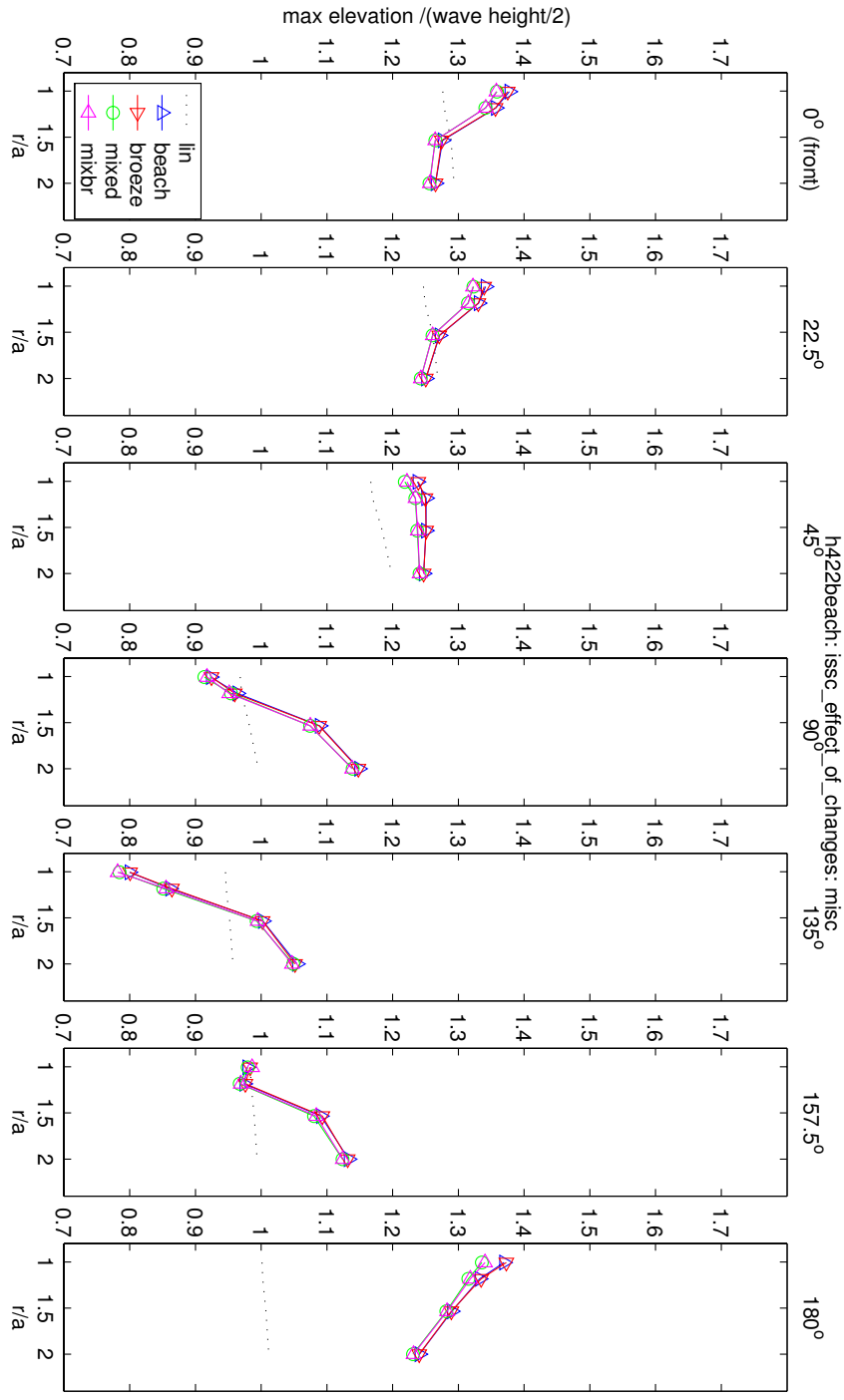

Figure 3.16: The 4 m high wave with the circular cylinder. Maximum wave elevation at the extended ISSC wave probe positions. Miscellaneous changes.

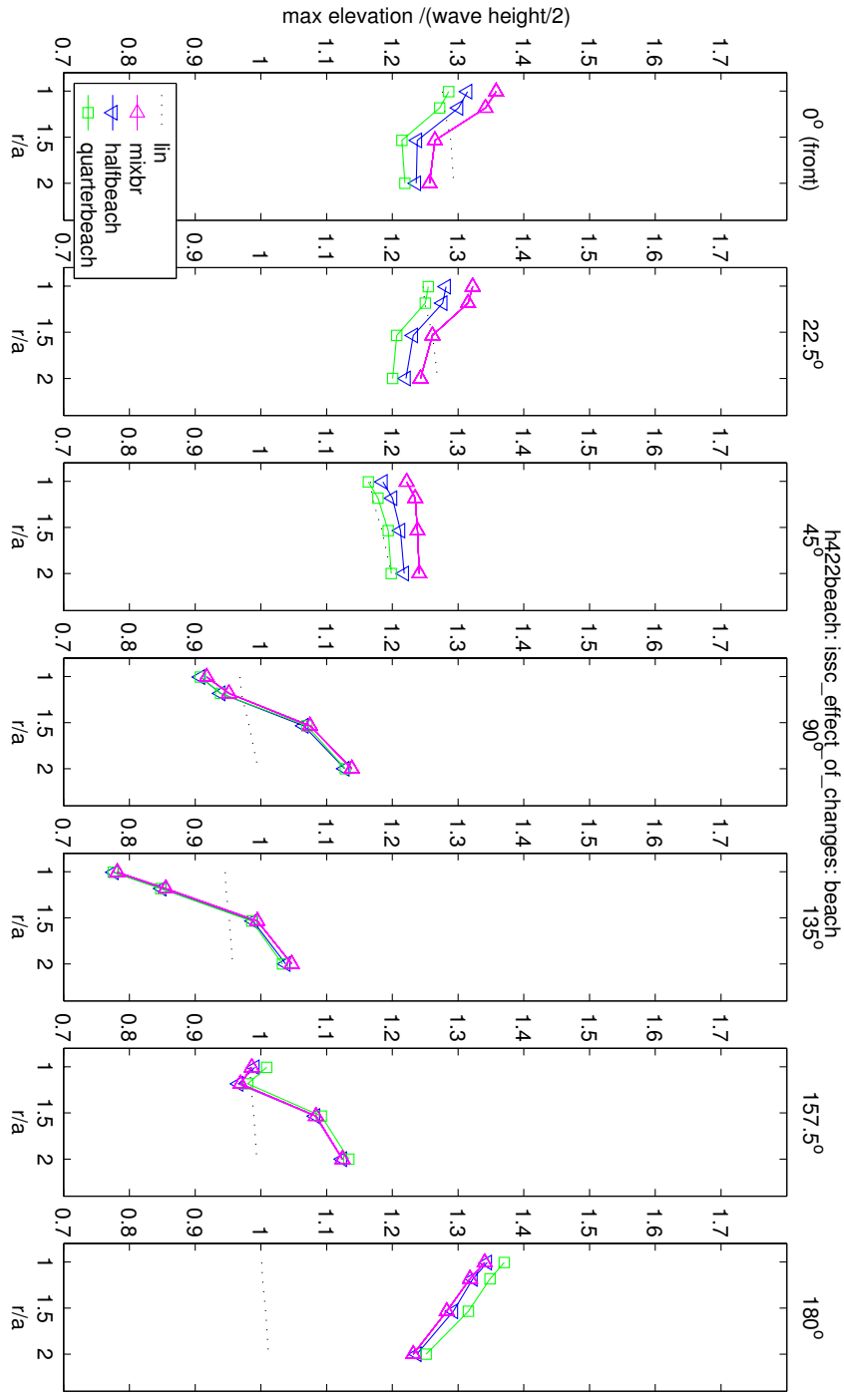

Figure 3.17: The 4 m high wave with the circular cylinder. Maximum wave elevation at the extended ISSC wave probe positions. Different beach strengths

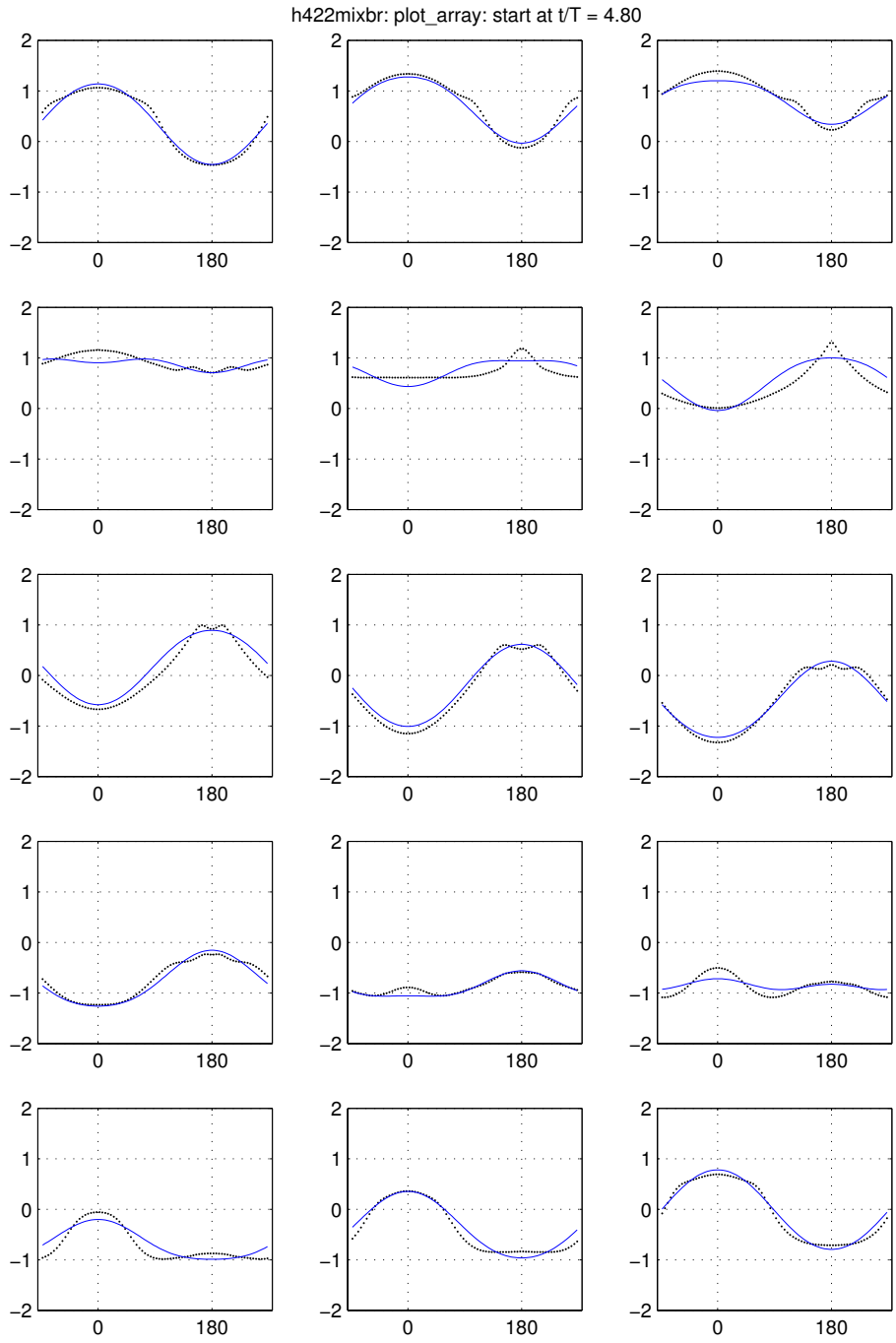

Figure 3.18: Surface elevation on the circular cylinder in the 4 m high wave given in 15 frames from one period. Normalised elevation versus angle in degrees. Front at 0 degrees, back at 180 degrees. The dots are the collocation points nearest to the cylinder, at 1.04 times the radius. The thin line is the linear solution.

The 8 m high wave with the circular cylinder

Figure 3.19 is the same as figure 3.14, but now for the 8 m high wave. The first thing one notices is the remarkable behaviour of the calculations done by Ferrant for the wave probe row at 45 degrees. Most probably this is an error in the handling of the data and not of the calculation itself. For the 4 m high wave the ISSC measurements were far too high for the row at 22.5 degrees. Also for the 8 m high wave their results for that row are quite high. It is less extreme than with the 4 m high wave and they did not mention anything about it in their report. One probably should be a little bit careful in trusting these values, however. The other ISSC measurements agree reasonably well with the numerical calculations, although they lie a little bit higher in certain places, the deviations are less than 10 percent. The Contento measurements in this picture are not for a 7.90 m high wave, but for a 8.4 m high wave. We did put them in to have at least some reference values at the back of the cylinder. The values agree quite well with those of the calculations and those of the other experiments, whereas for the case of the 4 m high wave the values are systematically too high. For the last four rows near the back of the cylinder the differences between the Contento measurements and the HYPAN calculations are 5 percent or less.

The problem with our calculations for this case is that they break down. After two start up periods we can calculate another 2.8 periods using equation (A.1). Looking at the 4 m case, where after one start up period the first two periods are still influenced by start-up transients and the rest are stationary, one would expect a stationary solution in the third period after start-up. At the backside of the cylinder the maxima are reached in the first half of the period. This means that for the rows at 90 degrees up till 180 degrees we can hope that there are no start-up transients any more in the last period. The maxima at the frontside however are reached in the last fifth of the period. This means that for the rows at 0 degrees up till 45 degrees the values in the last period still include start up transients. Looking again at the 4 m case for guidance, one should anticipate for a decrease of 2 till 3 percent before reaching stationary values.

As with the 4 m case we had a look at the effects that certain changes in the setup had on the outcome. The effects of changing the grid from a mixed grid to a square grid are very small and comparable to the effects in the 4 m case. Changing the strength of the beach has a larger effect, but again the effect is comparable to what we see for the 4 m case: almost 7 percent.

A 3D overview of what happens around the cylinder during a period is given in figure 3.23. It combines well with the 2D overview of figure 3.24. They do not start at the same position in the period however: the first 3D picture is approximately the eleventh 2D picture. To further complicate things: the first 3D snapshot is in time the last one, but for the storyline of the period it was better to put it first. At $t/T = 0, 1, 2, \ldots$ the wave crest is halfway the cylinder, at $t/T = \frac{1}{2}, 1\frac{1}{2}, 2\frac{1}{2}, \ldots$ the wave trough is halfway the cylinder. The wave direction is from left to right. In figure 3.23 the meshes connect the collocation points on the free surface. The hole in the centre is the position of the cylinder and the cut from the cylinder to the outside is the intersection of the free surface network with itself.

Now we describe what is happening in all the subfigures of figure 3.23. Figure 3.23(a): the wave trough is halfway the cylinder, the first run-up is starting. Figure 3.23(b): the wave crest is coming. A bump is forming in front. Figure 3.23(c): the

bump is splitting into two little bumps, one on each side of cylinder. Figure 3.23(d): the wave crest is now halfway the cylinder. The two little bumps have gone around the cylinder and are now approaching each other at the back. Figure 3.23(e): the two bumps bump into each other to produce a peak. At approximately the same time the wave crest is also at the back of cylinder. Figure 3.23(f): the wave crest is moving away from the cylinder. The peak has collapsed and has produced some secondary waves, including two bumps going around the cylinder in the other way. Could be considered to be the original bumps. Figure 3.23(g): the two bumps are returning to the front, but go sideways away from the cylinder. The wave trough is approaching the cylinder.

In figure 3.24 there are 15 two-dimensional snapshots from 1 period, starting at $t/T = 2.80$. They have the wave elevation on the cylinder plotted as a function of the horizontal angle. An angle of 0 degrees is at the front of the cylinder, and an angle of 180 degrees is at the back of the cylinder. The wave elevation is normalised with respect to half of the incoming wave height. For reference the linear solution of an infinite cylinder is included, see the thin line. The dots are the collocation points on the first row on the free surface near the cylinder. The time, t/T, of the first picture in each row is respectively: 2.8, 3.0, 3.2, 3.4, and 3.6. Thus the wave crest is halfway the cylinder at picture four, the wave trough is there between pictures 10 and 11. In these snapshots the time evolution of the two bumps is easily seen. In the first snapshot they have just been created and are heading towards the back of the cylinder. In the fifth snapshot they have collapsed together to one peak at the back. It is clear that the grid resolution is very low for this kind of event. The peak collapses in the seventh snapshot, creating again two outgoing waves. Those two bumps move back towards the front of the cylinder. Before they reach the front they go sideways. In the eleventh snapshot we can see the last remains of the bumps and the start of a new cycle. It is obvious that there are clear differences between the fully nonlinear computation and the linear diffraction solution, however, as a kind of average that linear solution is not too bad.

The question is, of course, why does the calculation break? Figure 3.25 shows a number of snapshots of the waterline on the cylinder. The snapshots have a true aspect ratio, and the angle and the position of the steepest slope are indicated. There are a few things worth noticing. First, when the wave crest moves to the back of the cylinder, there is a maximum slope with an angle of almost 50 degrees. Secondly, the peak at the back of the cylinder, created when the two bumps bumped into each other, has an even steeper angle of almost 70 degrees, whereas there are only grid points at the bottom and at the top of the peak. As a last thing we notice that in the last snapshot before the crash we have a steep slope with an angle of more than 50 degrees with some wiggles behind it.

Related to figure 3.25, is figure 3.26. Here we see the maximum slope in the waterline around the cylinder as a function of time. For comparison, figure 3.27 shows the same for the 4 m high wave. Note that changes of the maximum slope in time do not imply that they occur for the same physical "bump": they only show the evolution of one particular slope for the time it is the steepest. In the case of the 8 m high wave the crest to trough part of the periods (e.g. $t/T = 3.0$ till 3.5) show comparable steepness as the trough to crest part of the periods (e.g. $t/T = 2.5$ till 3.0), except for the very high peak associated with the peak at the back of the

cylinder. For the 4 m high wave on the other hand, the crest to trough periods have much lower steepness then the trough to crest periods, only the peak can keep up. The 4 m high wave case is also much smoother, probably because the 8 m high wave case has not enough resolution to deal nicely with the peak at the back and the resulting secondary waves. The 8 m high wave case gets less and less smooth in time, until it breaks down. The figures suggest that this breakdown is not because of a steady steepening of the largest slope, but because the current slope cannot be dealt with properly, resulting in a kind of wiggles that get very steep locally. It is not strange that we have problems dealing with these steep slopes, given the low resolution and the eulerian grid motion. This does not exclude the possibility that these wiggles are a sign of physical instabilities that cause breaking in the real world too. Ferrant, however, claims that he can calculate these kind of waves in this situation and that he has seen experimental data that confirms the no breaking behaviour[8].

[8]Source: personal communication

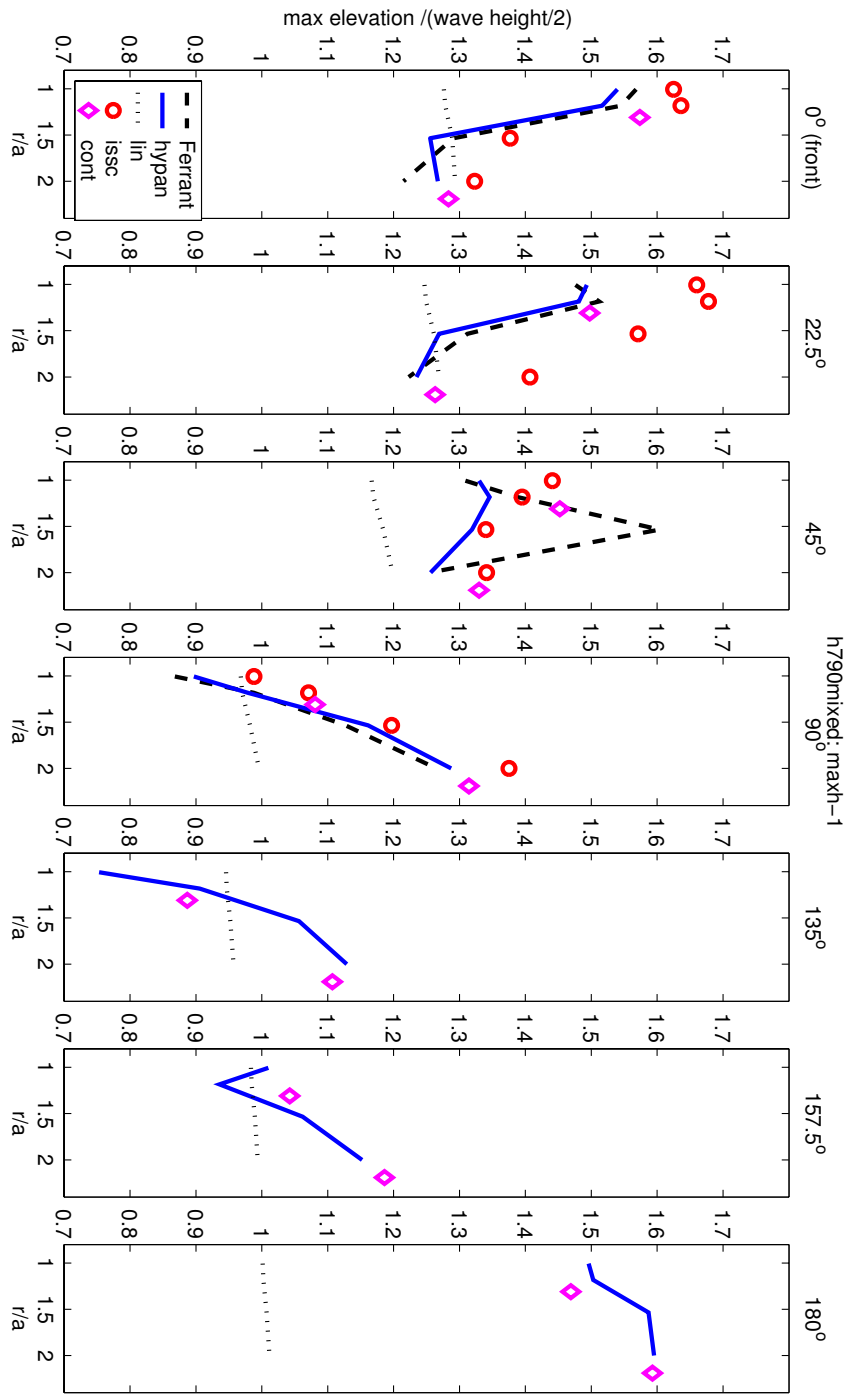

Figure 3.19: The 8 m high wave with the circular cylinder. Maximum wave elevation at the extended ISSC wave probe positions. Comparison with experimental data and the other calculations.

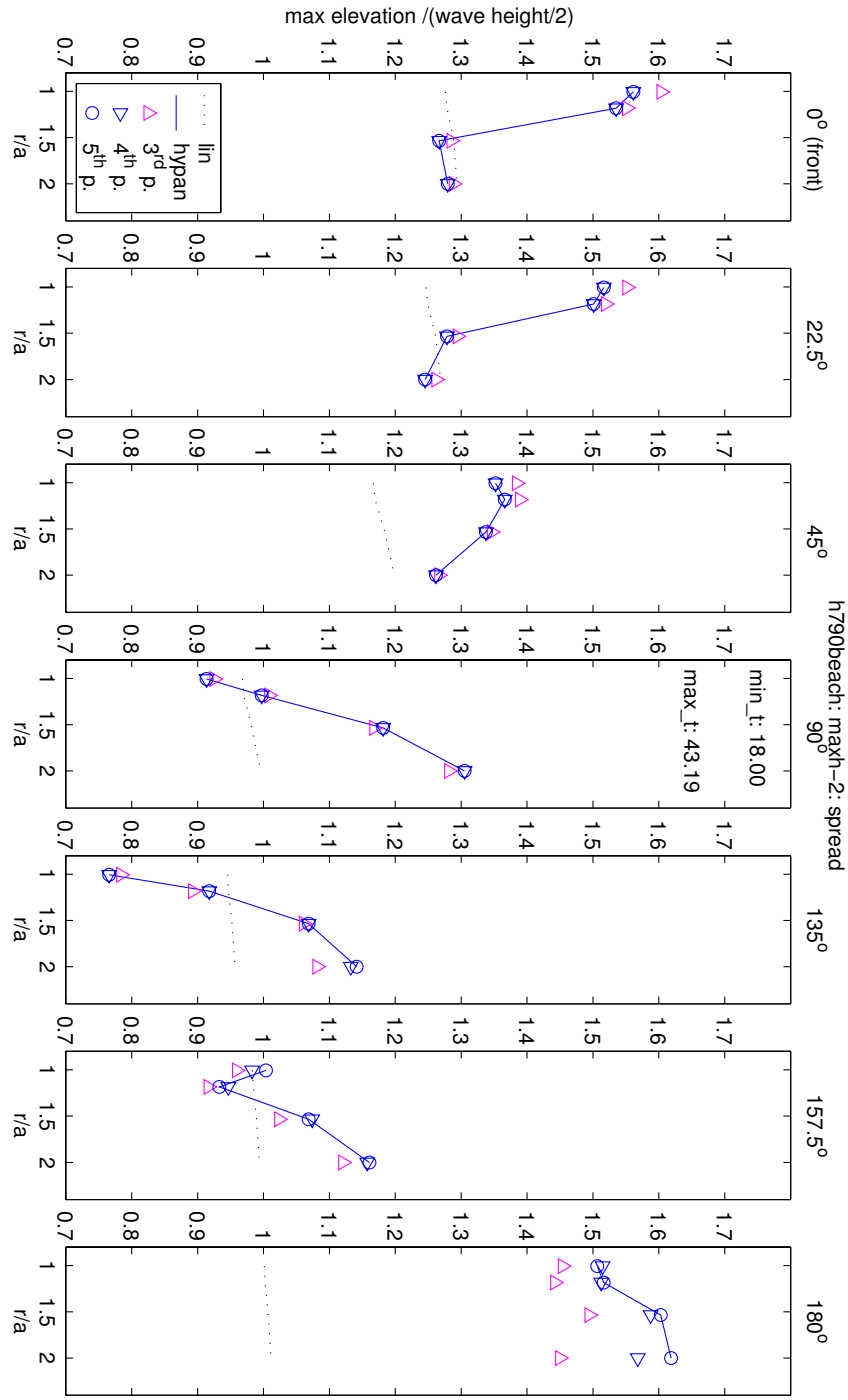

Figure 3.20: The 8 m high wave with the circular cylinder. Maximum wave elevation at the extended ISSC wave probe positions. Maximum per wave period starting at period 3.

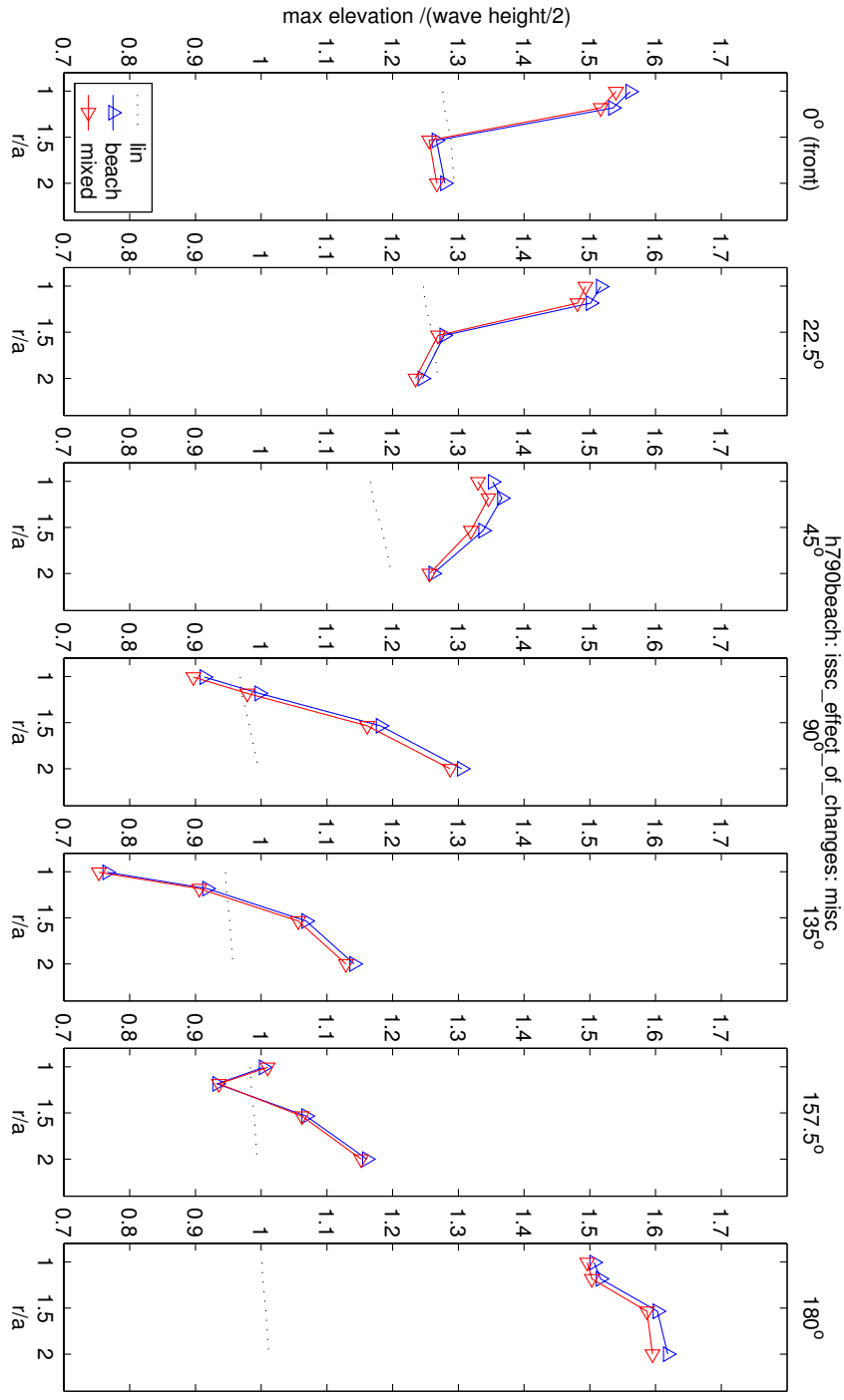

Figure 3.21: The 8 m high wave with the circular cylinder. Maximum wave elevation at the extended ISSC wave probe positions. Miscellaneous changes.

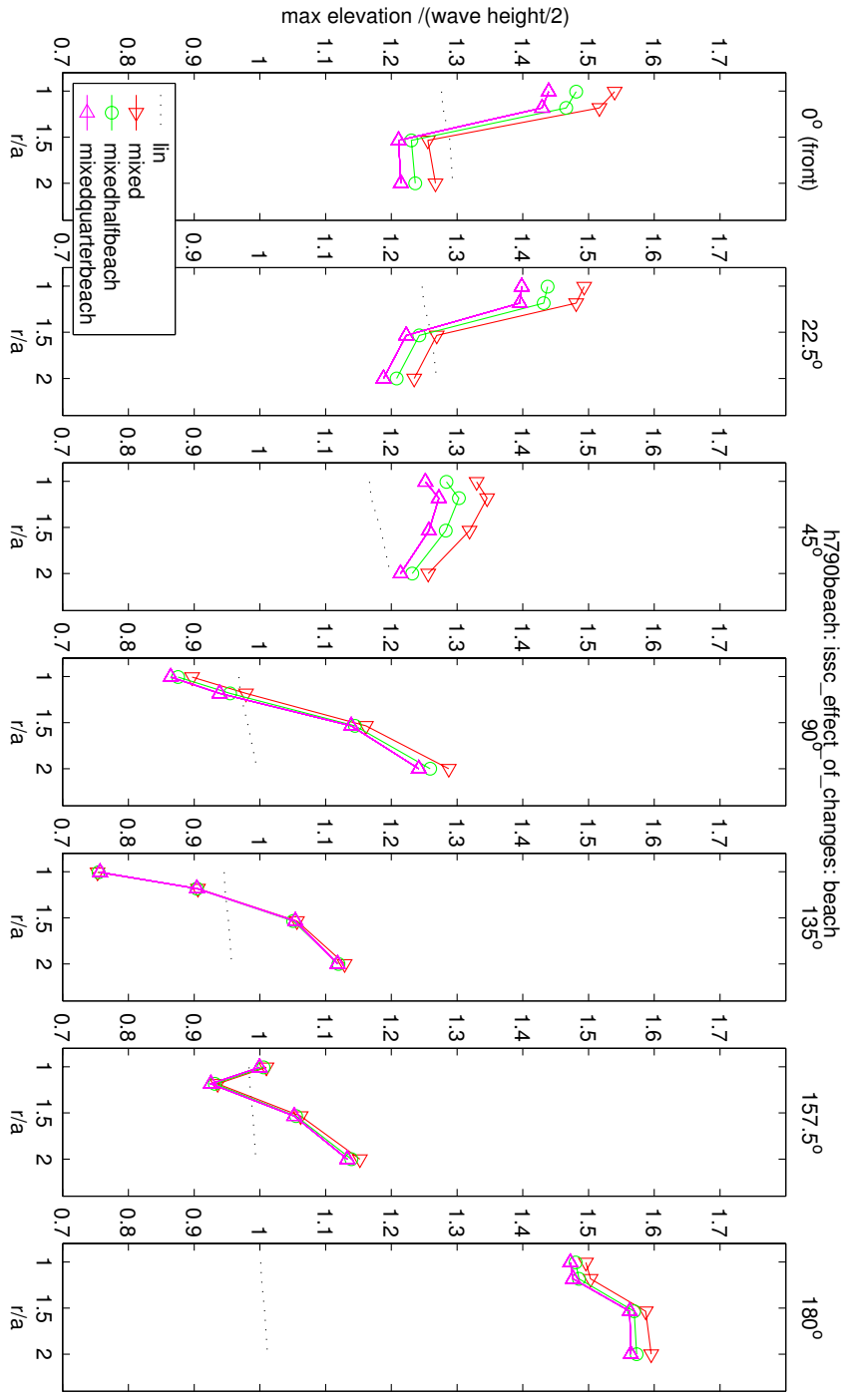

Figure 3.22: The 8 m high wave with the circular cylinder. Maximum wave elevation at the extended ISSC wave probe positions. Different beach strengths

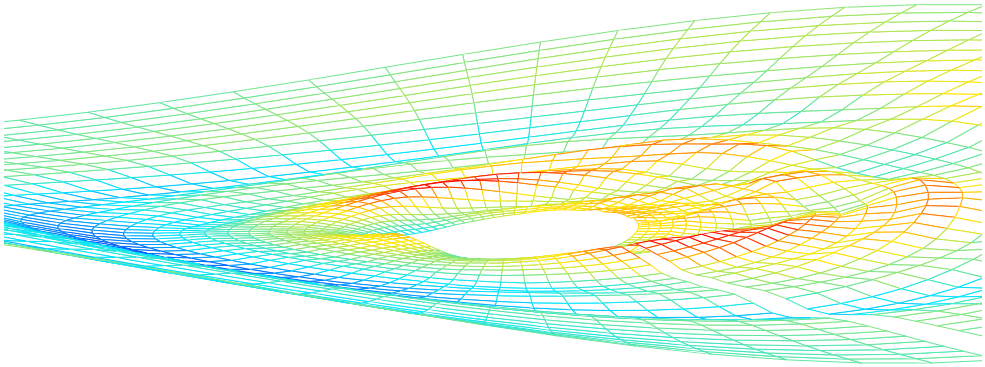

(a) $t/T = 3.50$

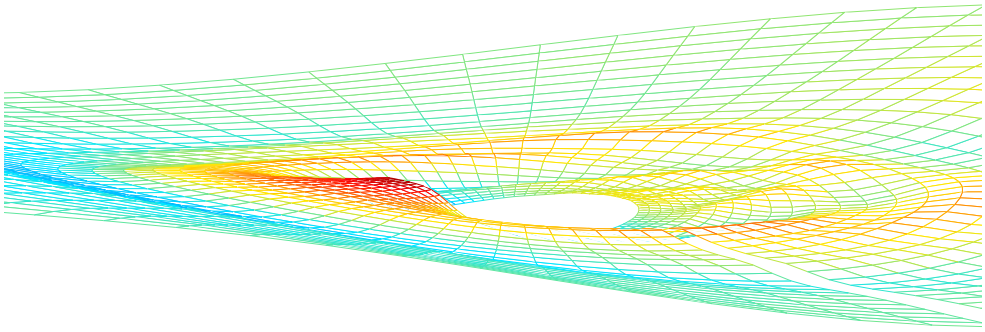

(b) $t/T = 2.58$

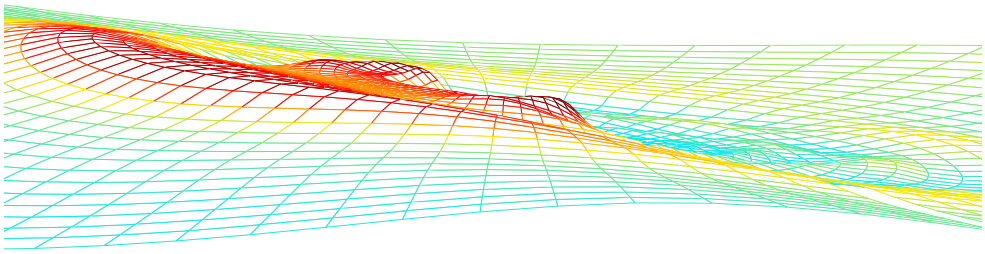

(c) $t/T = 2.80$

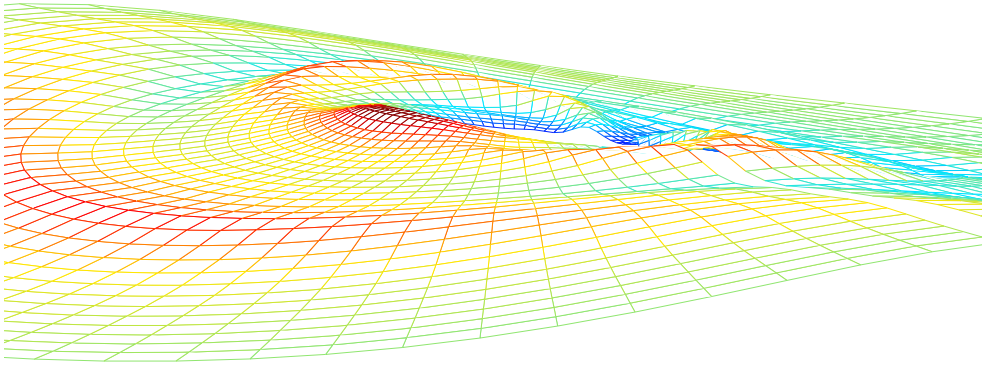

(d) $t/T = 3.00$

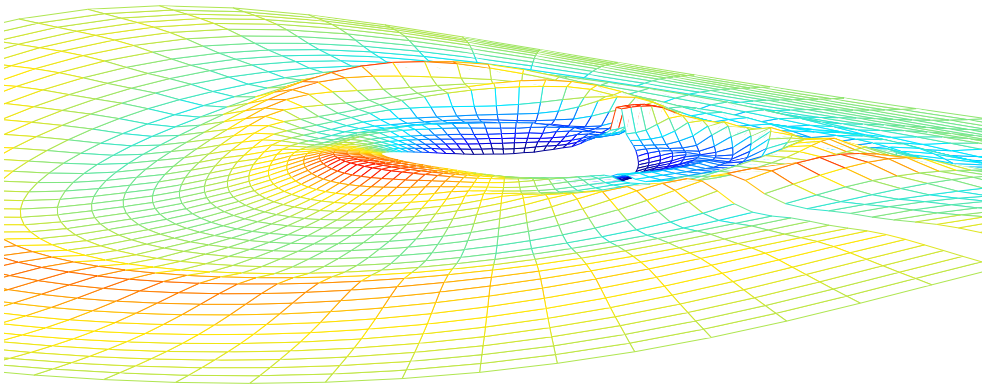

(e) $t/T = 3.08$

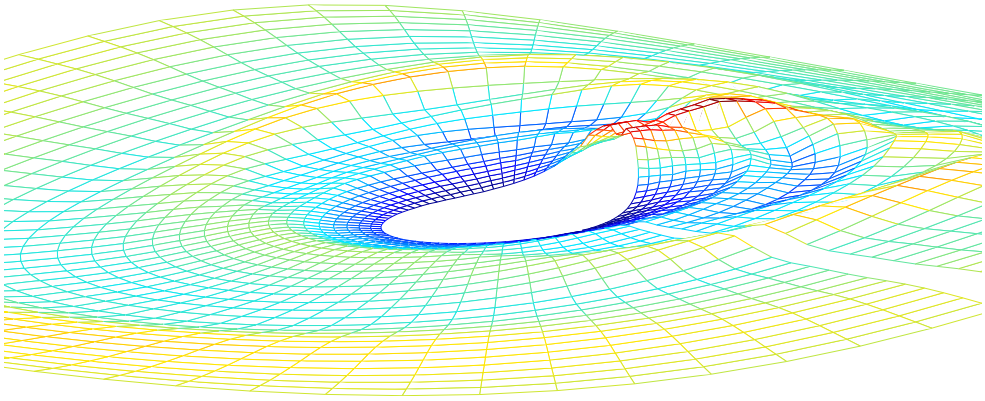

(f) $t/T = 3.18$

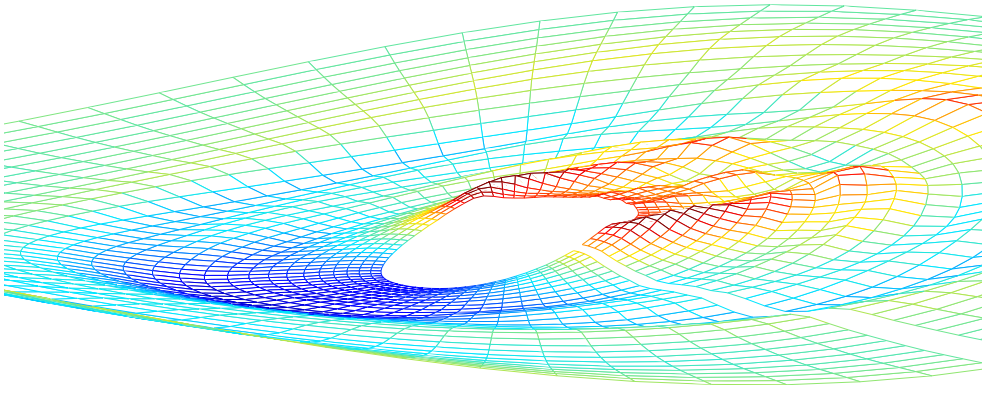

(g) $t/T = 3.40$

Figure 3.23: The 8 m high wave with the circular cylinder: 7 snapshots of the free surface from one period. The vertical direction is in true ratio with the horizontal directions. The colours are a measure of the difference with the incoming wave.

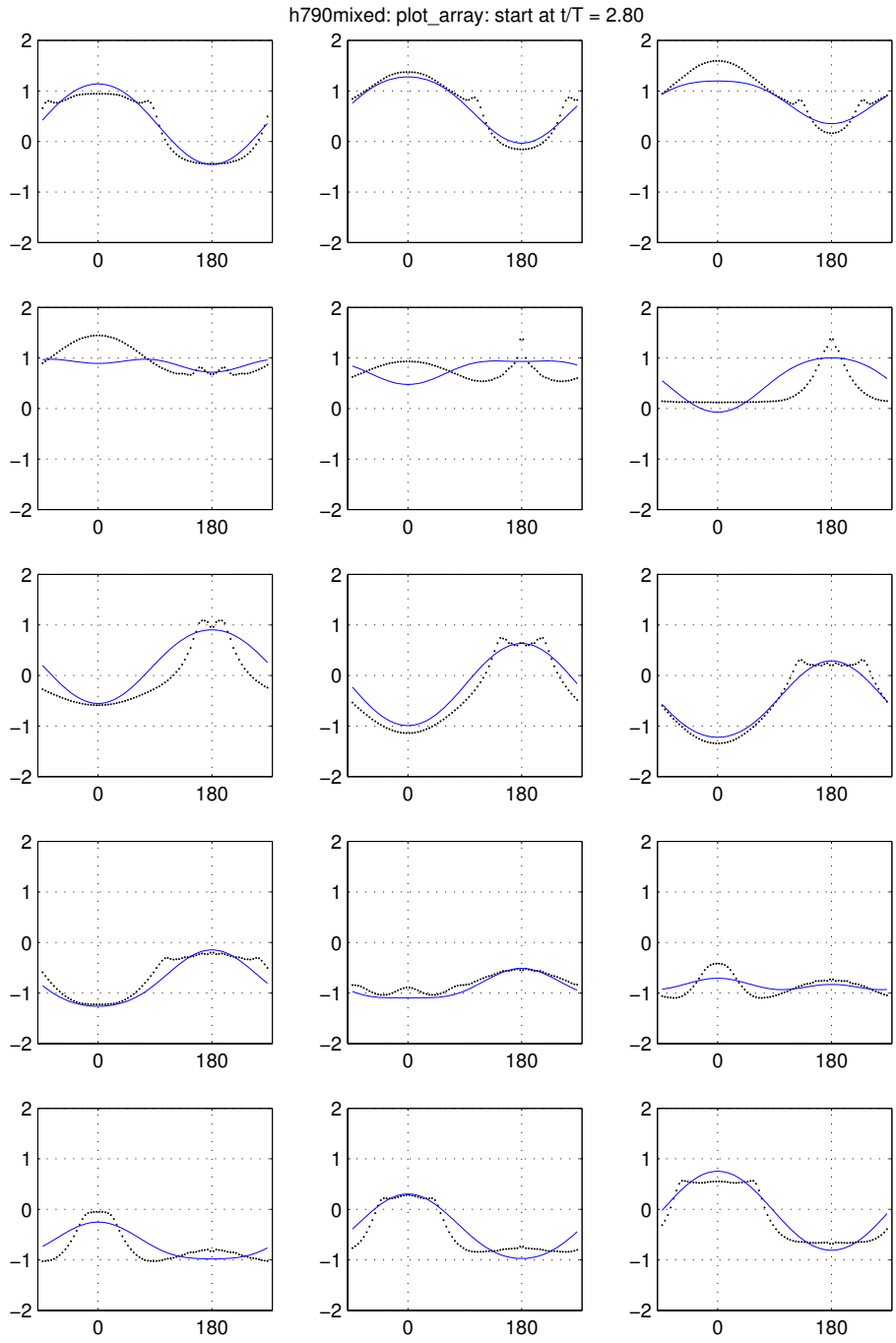

Figure 3.24: Surface elevation on the circular cylinder in the 8 m high wave given in 15 frames from one period. Normalised elevation versus angle in degrees. Front at 0 degrees, back at 180 degrees. The dots are the collocation points nearest to the cylinder, at 1.04 times the radius. The thin line is the linear solution.

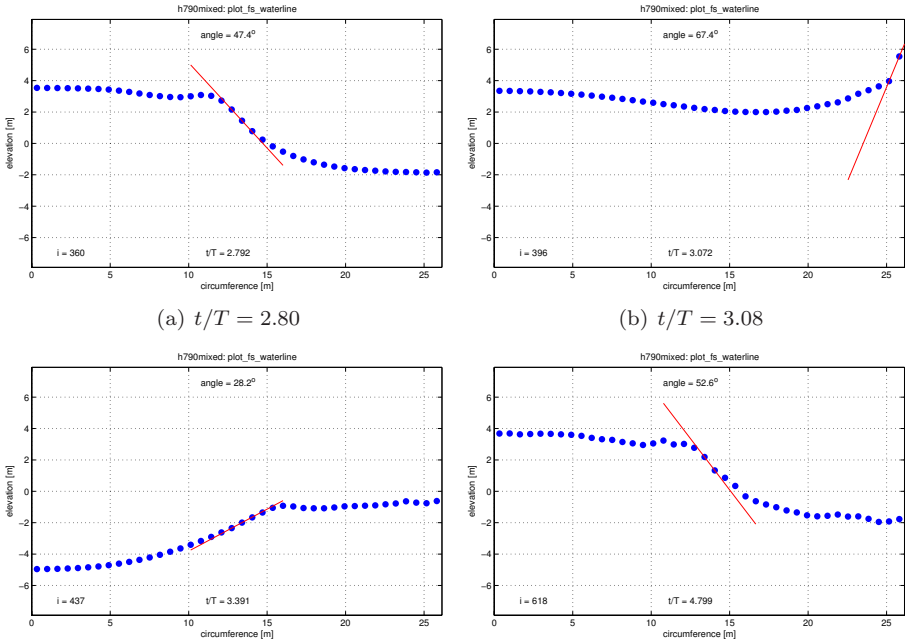

(a) $t/T = 2.80$ (b) $t/T = 3.08$

(c) $t/T = 3.40$ (d) $t/T = 4.80$, last before crash

Figure 3.25: Four snapshots of the waterline with true aspect ratio and maximum slope with angle indicated. On the left of the figures is the front of the cylinder, on the right is the back of cylinder.

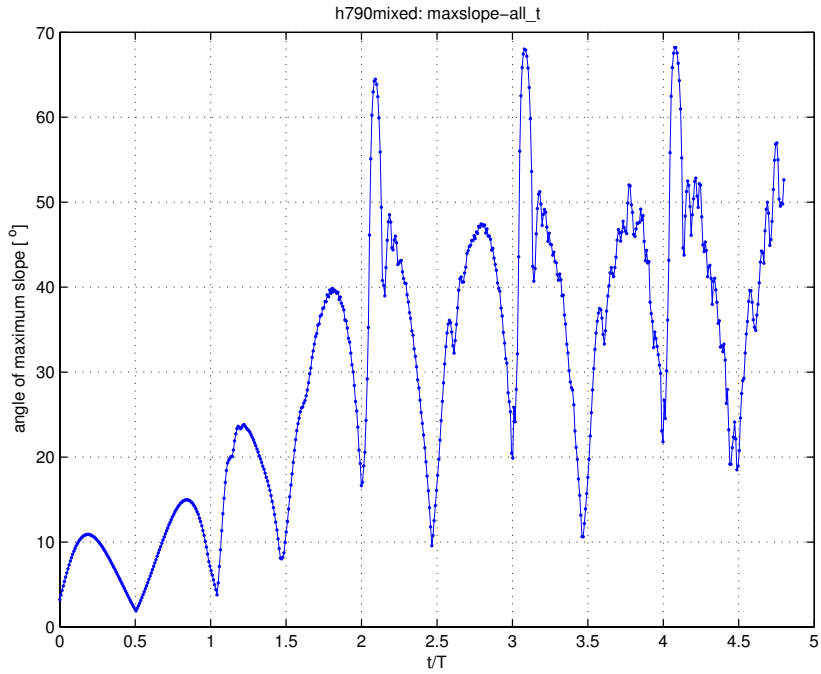

(a) From start till breakdown of calculation.

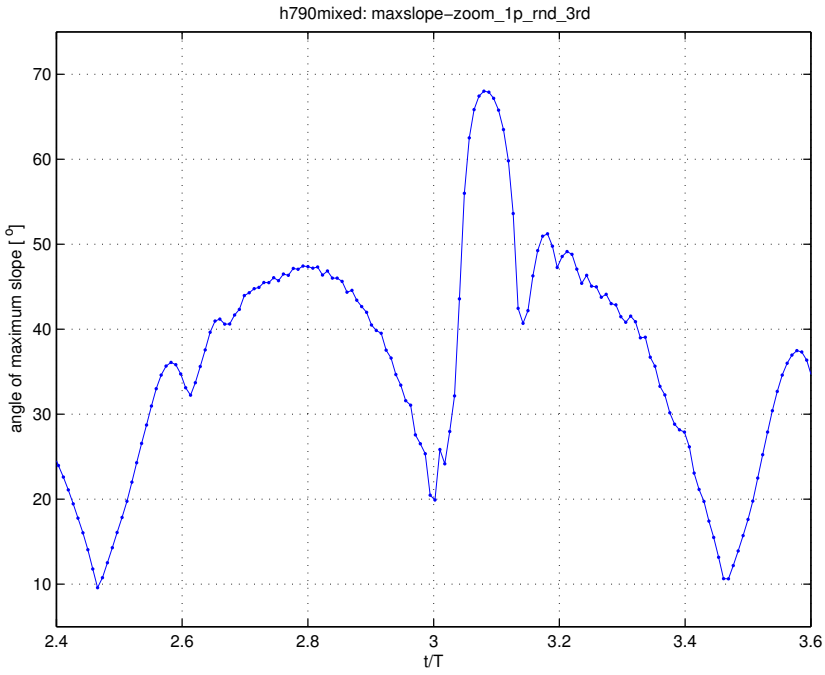

(b) Zoomed in on one period.

Figure 3.26: The maximum slope on the waterline as a function of time for the circular cylinder in the 8 m high wave.

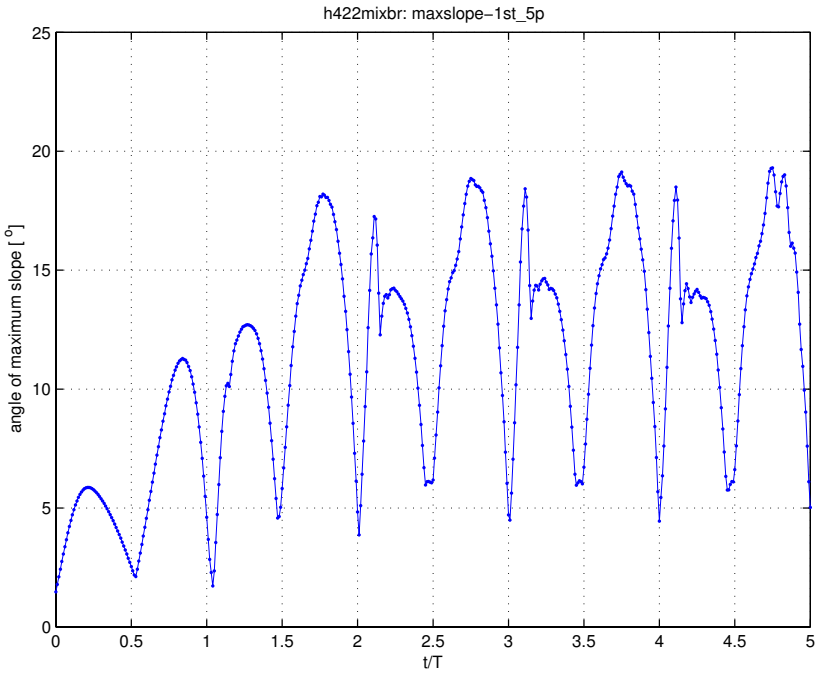

(a) Periods 1 till 5.

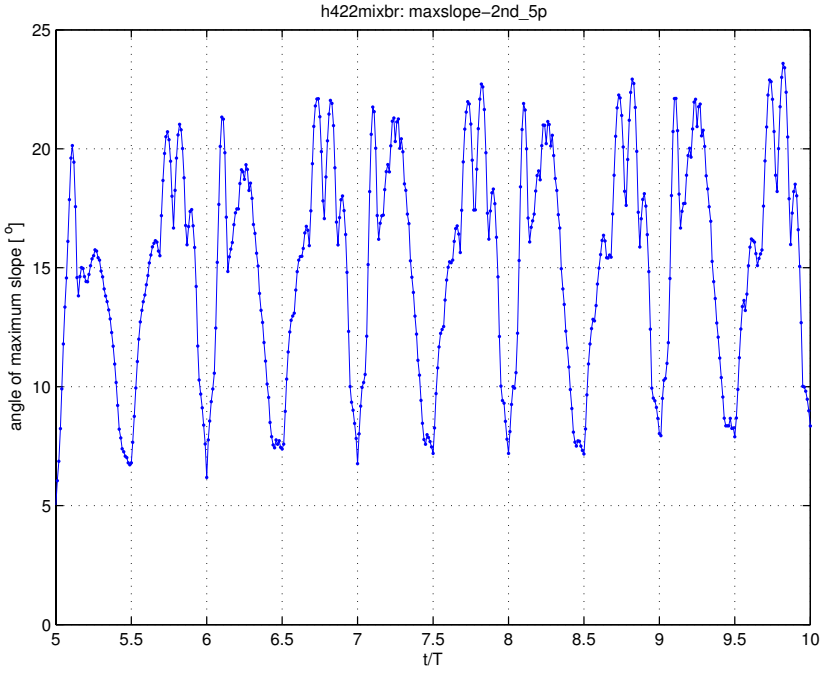

(b) Periods 6 till 10.

Figure 3.27: The maximum slope on the waterline as a function of time for the circular cylinder in the 4 m high wave.

The 4 m high wave with the square cylinder

For the square cylinder case there are five rows of wave probes instead of the 7 rows for the circular cylinder. The angles of those rows are the same, except for the two that are missing. We use the same figure format, leaving the subfigures for the missing rows empty. The linear solution is for the infinite circular cylinder. It is put in here as a rough reference.

The calculation breaks down after 39.3 seconds or 4.37 periods. When using equation 6.22 from Broeze (A.1), the calculation can be continued for at least ten periods. The results are given in figure 3.28 (mixed grid). The ISSC measurements are higher than the HYPAN calculations, as was the case for the circular cylinder cases. For all rows the deviations are 10 percent or less. The calculations from Ferrant are clearly lower than the HYPAN calculations in this case. It would be nice to have some data for comparison at the back of the cylinder. The results at the front and at the back are not the same for every period, and this dependends on the choice of grid. The calculation without using Broeze has not yet converged and can therefore hardly be used for comparison. Figures 3.29 and 3.30 give the maximum per period for the calculations using a square and a mixed grid respectively. At the wave probe closest to the front of the cylinder the maximum per period rises from 1.4 to 1.6 while going from period number 4 till period number 10. There is no sign of convergence. The other wave probes at the front remain approximately stable. At the back of the cylinder the two calculations differ. The calculation with a mixed grid starts out with values around 1.3, but jumps to 1.4 in period No 7, settling down around 1.45. The calculation with the square grid on the other hand, also starts out at around 1.3, but in period number seven the values drop towards 1.25. In both cases the second wave probe more or less joins the behaviour of the first wave probe (counting from the cylinder). This is clearly dubious behaviour. At the back it seems to be stable, at the front it looks unstable. Looking at the animations of the calculations no clear reason or mechanism can be found.

Figure 3.32 is the same as figure 3.23 but now for the 4 m high wave on the square cylinder. Because this calculation runs longer we took the snapshots at time points that were exactly two periods later. It is probably best to look at it together with figure 3.33, which is the equivalent of figure 3.24. The extra grid lines denote the beginning and the ending of the curved corners. The horizontal axis is in degrees and is therefore not one-to-one to distance for the square. The line is again the linear solution for the infinite circular cylinder. We see that there is more detail in this case. In the first picture we now have two bumps instead of one for example. It is also clear that we have quite a low resolution for the things that are happening. Notice that the position of the corner areas is also indicated by the behaviour of the waterline.

The maximum slope as a function of time is given in figure 3.34 for the calculation without Broeze (eq. (A.1)) and in figure 3.35 for the calculation with Broeze. Without Broeze we see from $t/T = 3.5$ till 4 much more peaks than from $t/T = 2.5$ till 3. However, breakdown at $t/T = 4.4$ seems to be at a relative quiet moment. Notice also the large minimum at $t/T = 4$. With Broeze on the other hand we do see an increase in peaks from the fifth period onwards, but the calculation does not break. A little later the minimum slope starts to go up and up, together with some clear peaks in the last three periods. For the same calculation but with a square grid the same three peaks are there but now in the other half of the period. The amount of

peaks in these pictures is much higher than for the 4 m high wave on the circular cylinder, as shown in figure 3.27. It indicates that there are much more small waves running around. This was to be expected: more small structure in the shape of the object should cause more small structure in its diffraction pattern. With the current resolution around the cylinder we have trouble dealing with that.

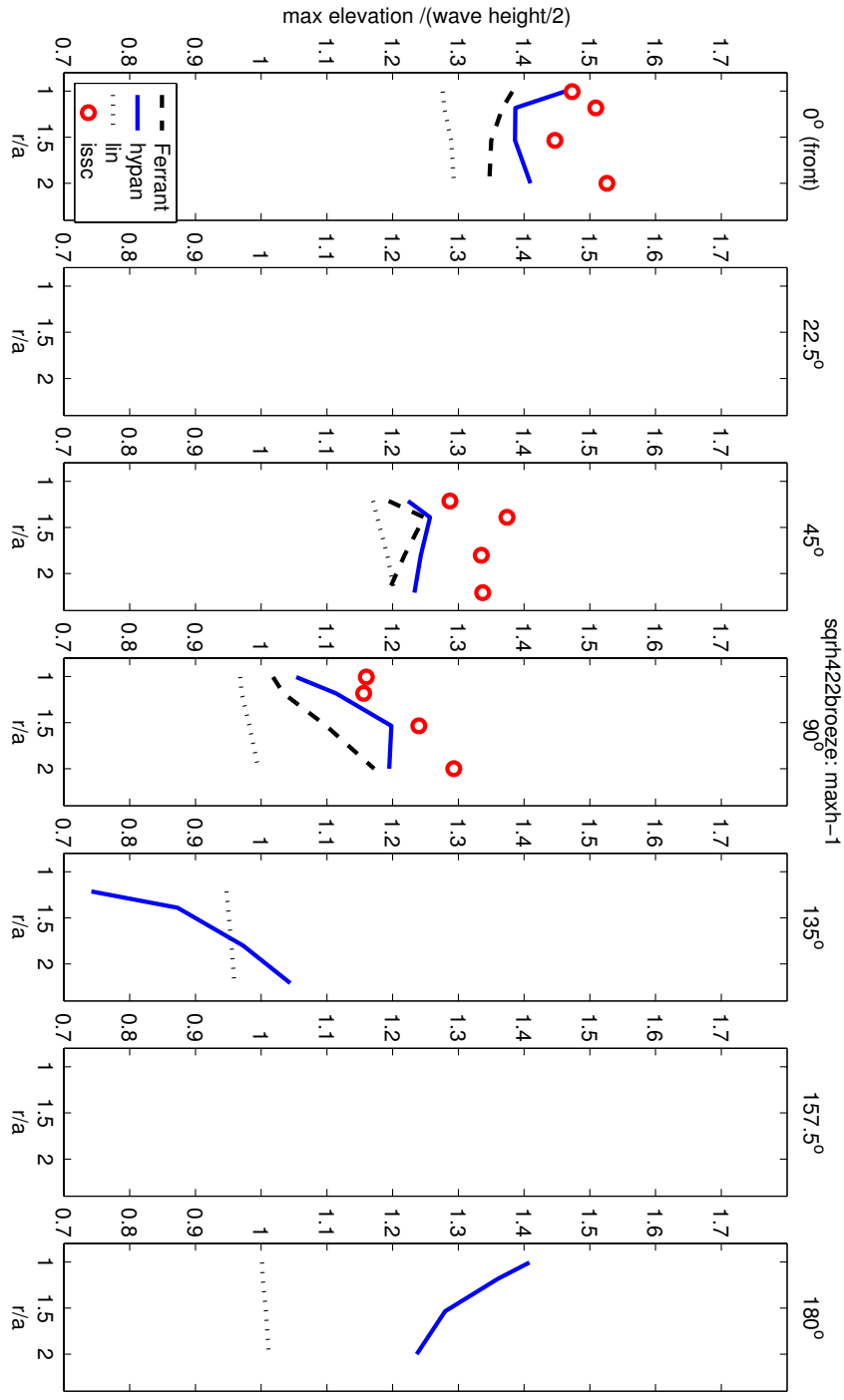

Figure 3.28: The 4 m high wave with the square cylinder using the mixed grid. Maximum wave elevation at the extended ISSC wave probe positions. Comparison with experimental data and the other calculations.

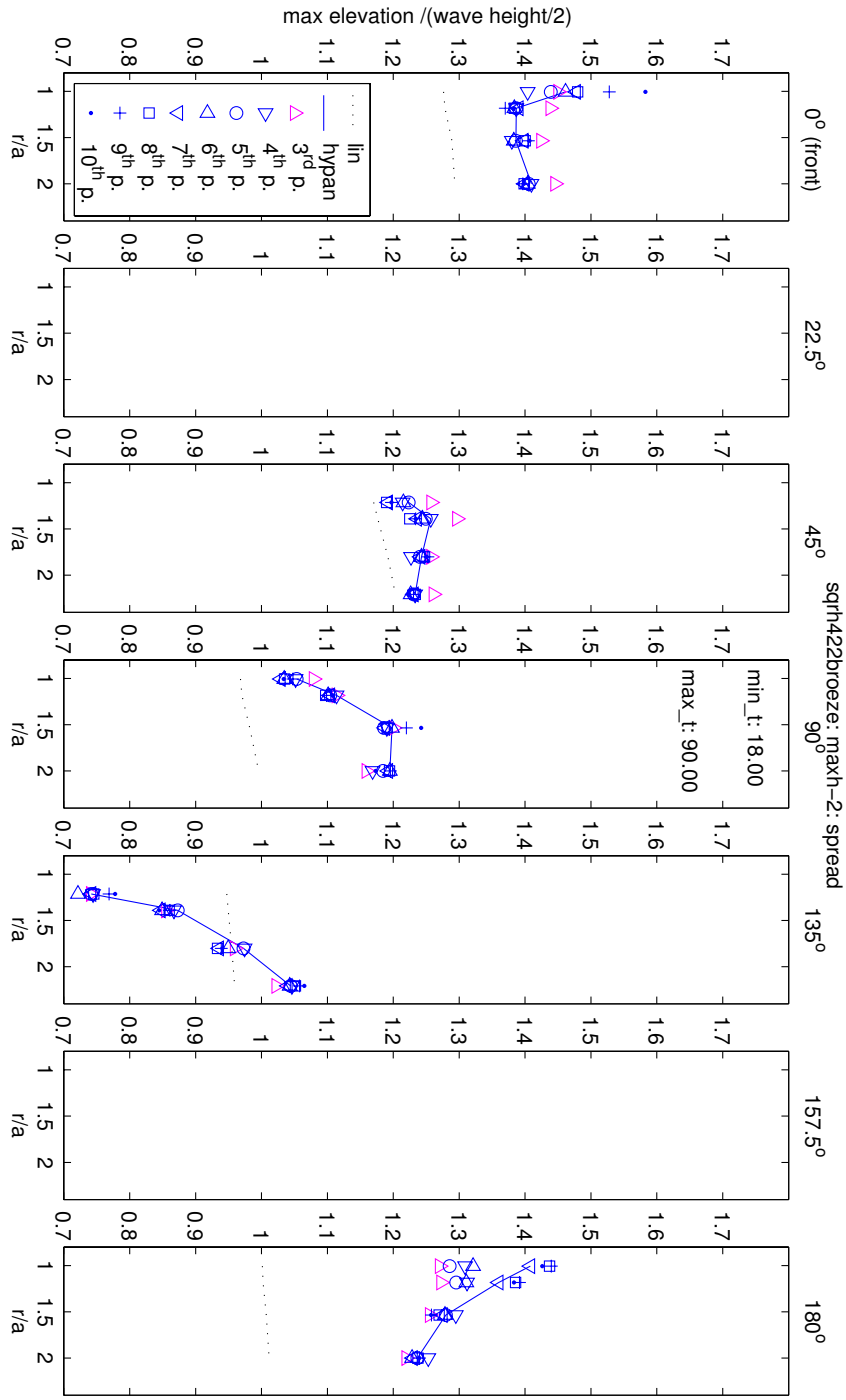

Figure 3.29: The 4 m high wave with the square cylinder using the mixed grid. Maximum wave elevation at the extended ISSC wave probe positions. Maximum per wave period starting at period 3.

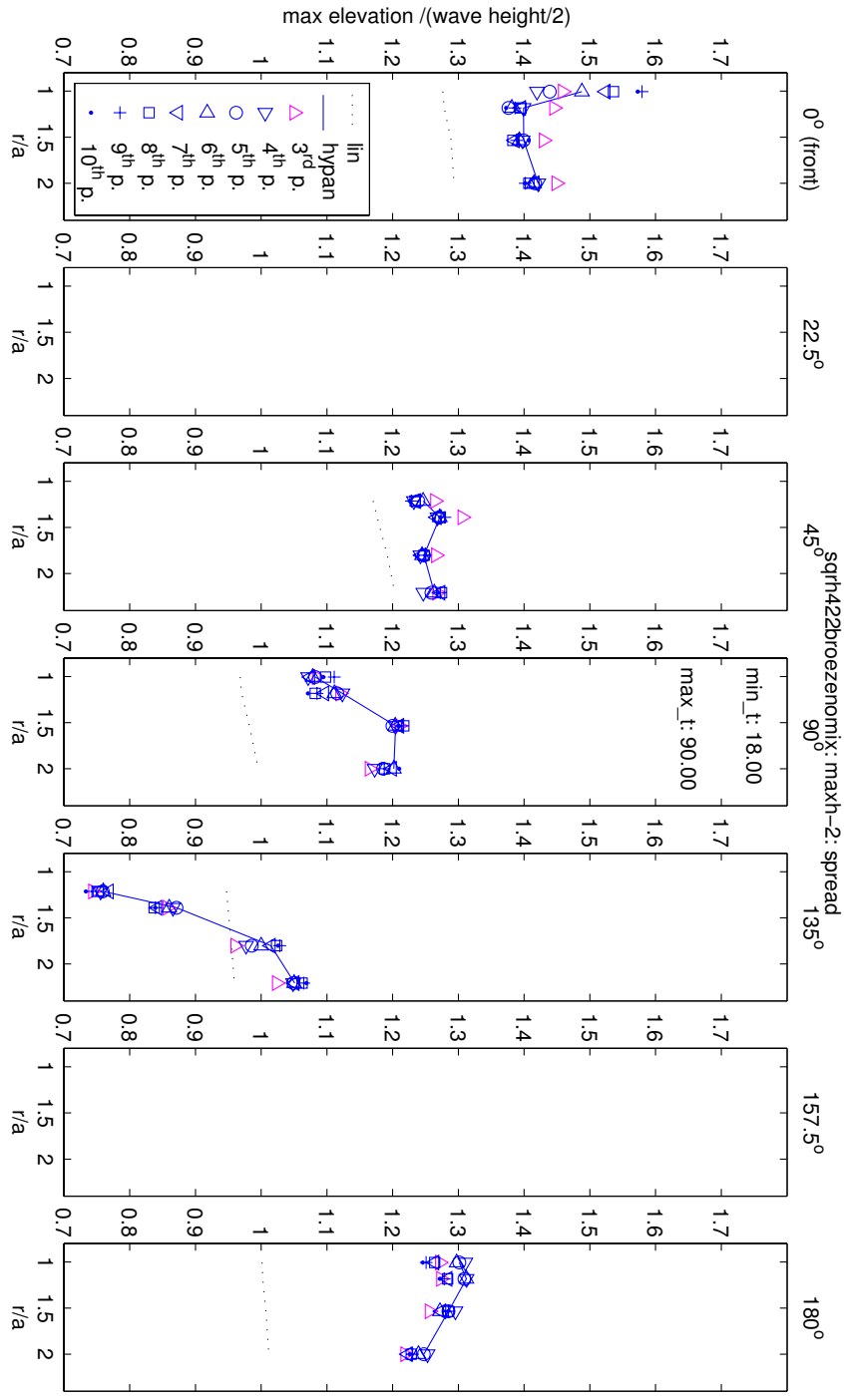

Figure 3.30: The 4 m high wave with the square cylinder using the square grid. Maximum wave elevation at the extended ISSC wave probe positions. Maximum per wave period starting at period 3.

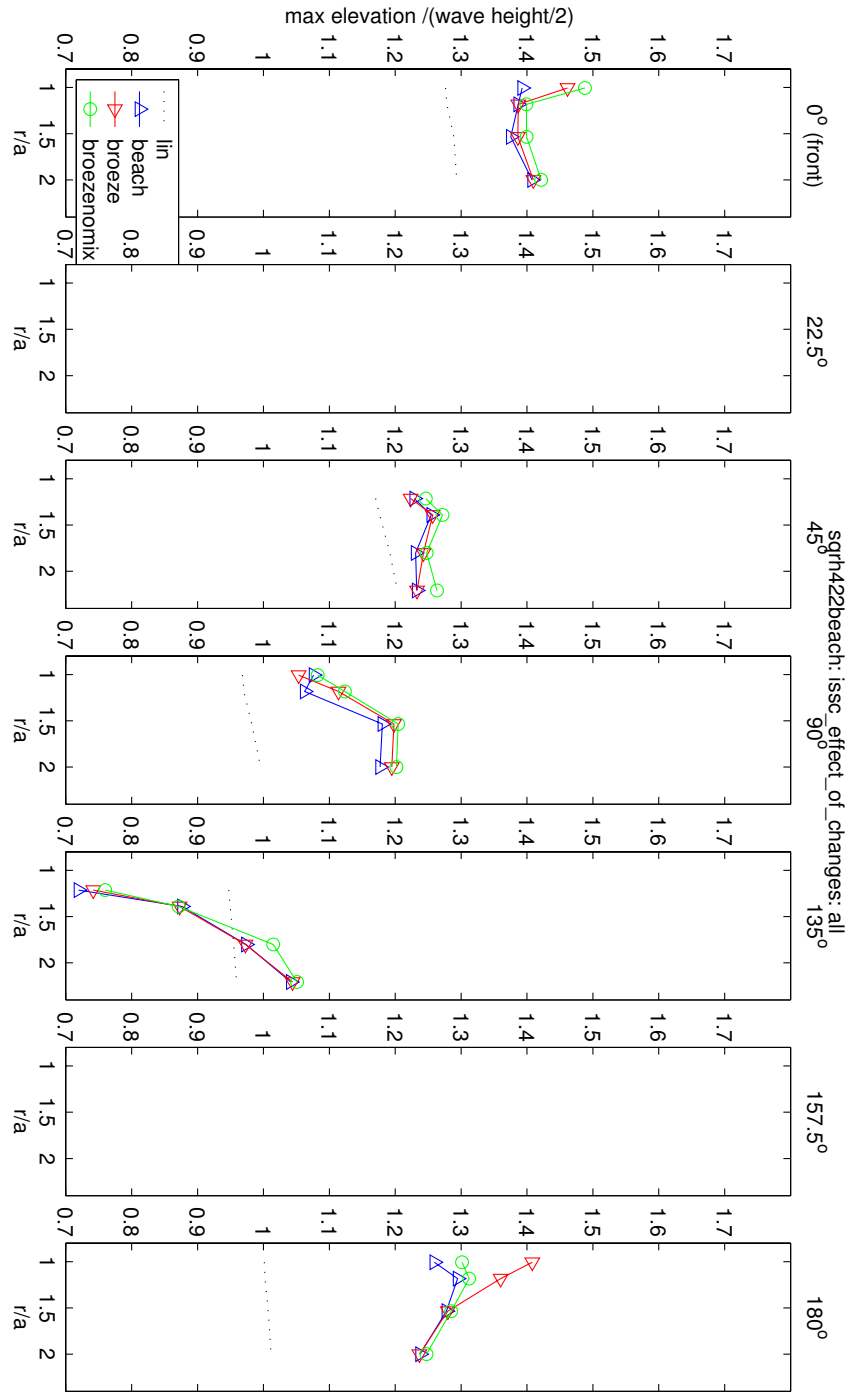

Figure 3.31: The 4 m high wave with the square cylinder. Maximum wave elevation at the extended ISSC wave probe positions. Miscellaneous changes.

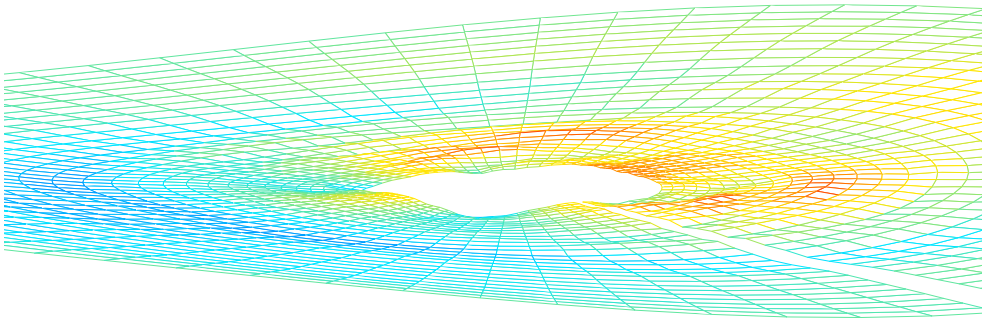

(a) $t/T = 5.50$

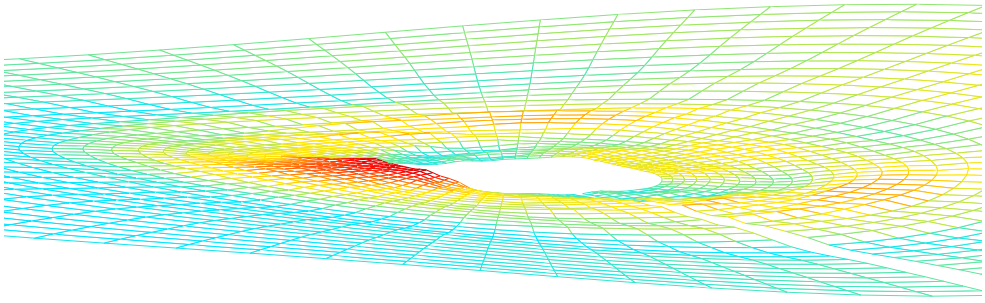

(b) $t/T = 4.58$

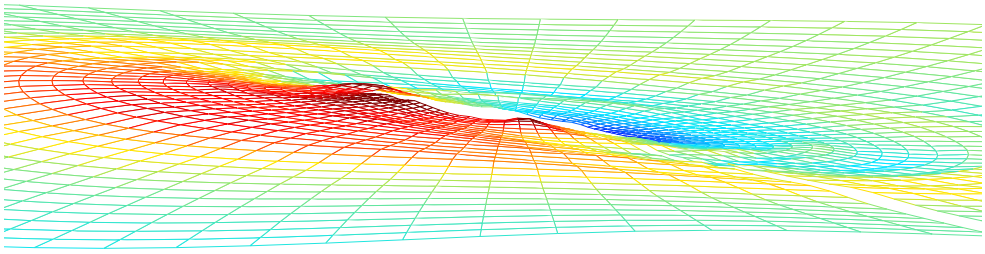

(c) $t/T = 4.80$

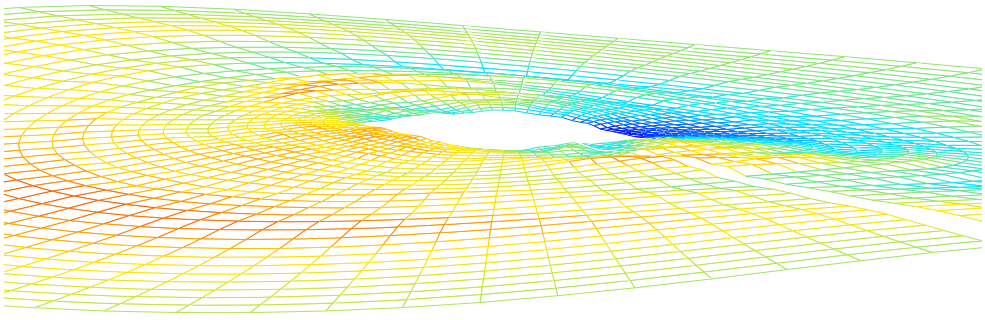

(d) $t/T = 5.00$

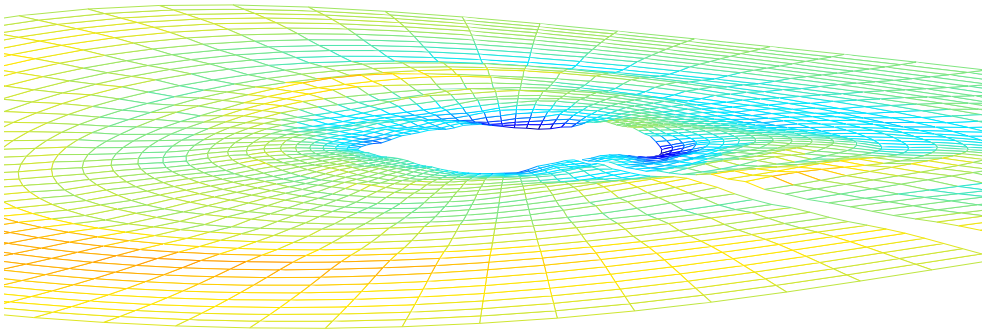

(e) $t/T = 5.08$

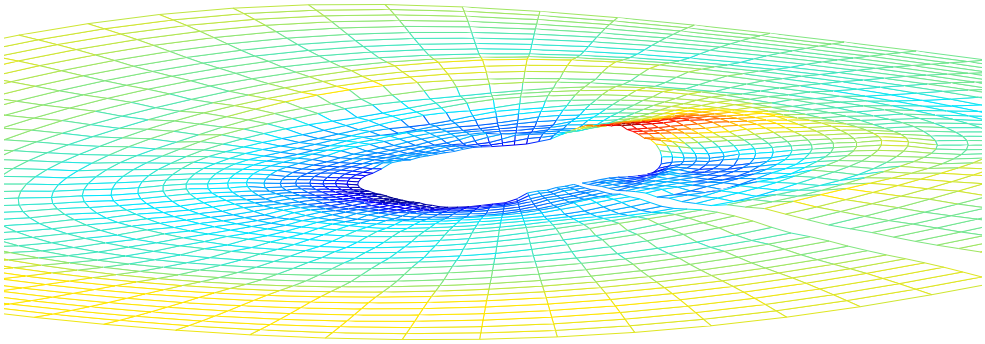

(f) $t/T = 5.18$

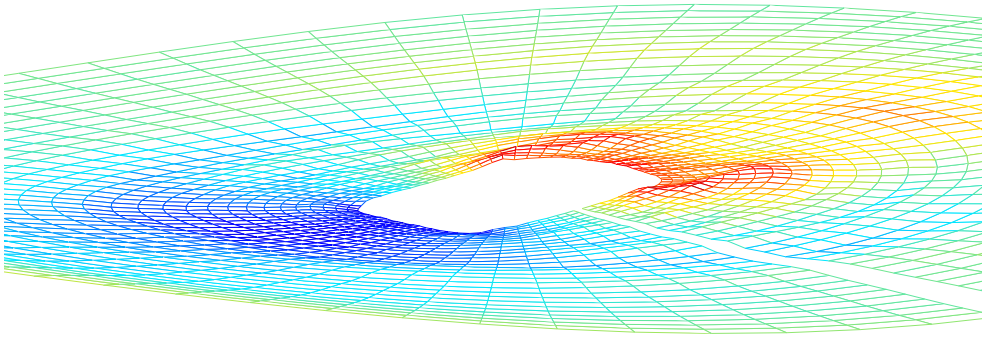

(g) $t/T = 5.40$

Figure 3.32: The 4 m high wave with the square cylinder: 7 snapshots of the free surface from one period. The vertical direction is in true ratio with the horizontal directions. The colours are a measure of the difference with the incoming wave.

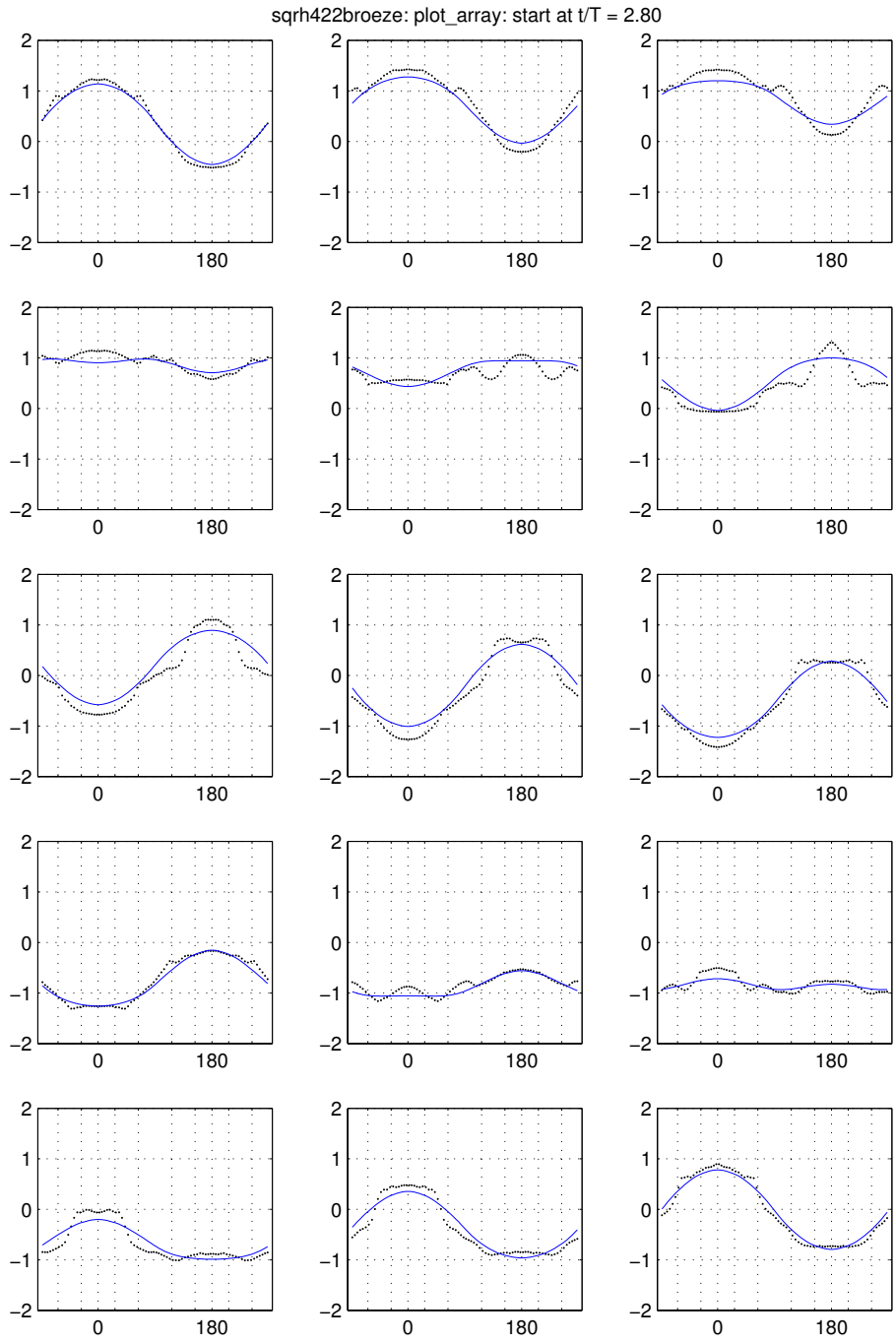

Figure 3.33: Surface elevation on the square cylinder in the 4 m high wave given in 15 frames from one period. Normalised elevation versus angle in degrees. Front at 0 degrees, back at 180 degrees. The dots are the collocation points nearest to the cylinder, at 1.04 times the radius. The thin line is the linear solution for an infinite circular cylinder.

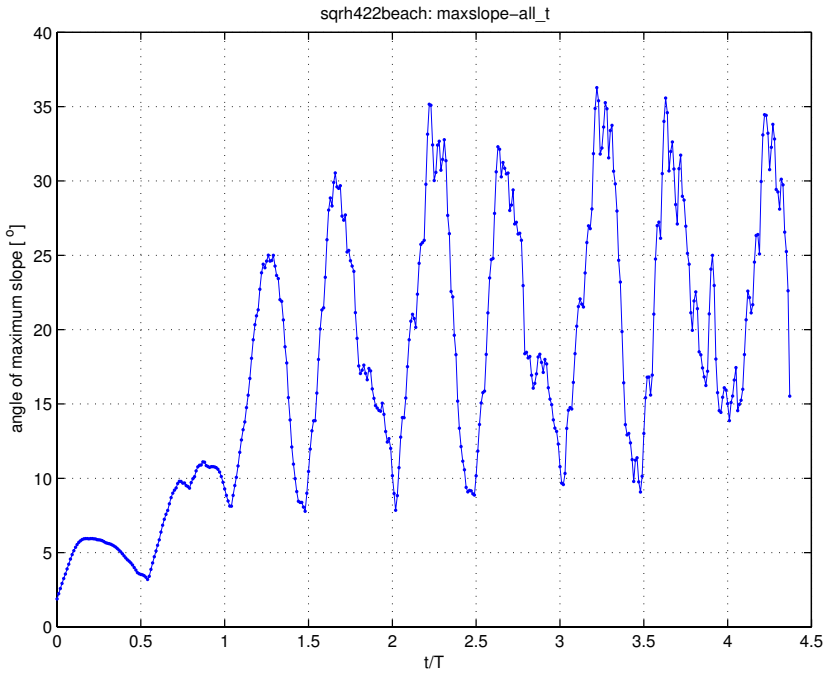

(a) From start till breakdown of calculation.

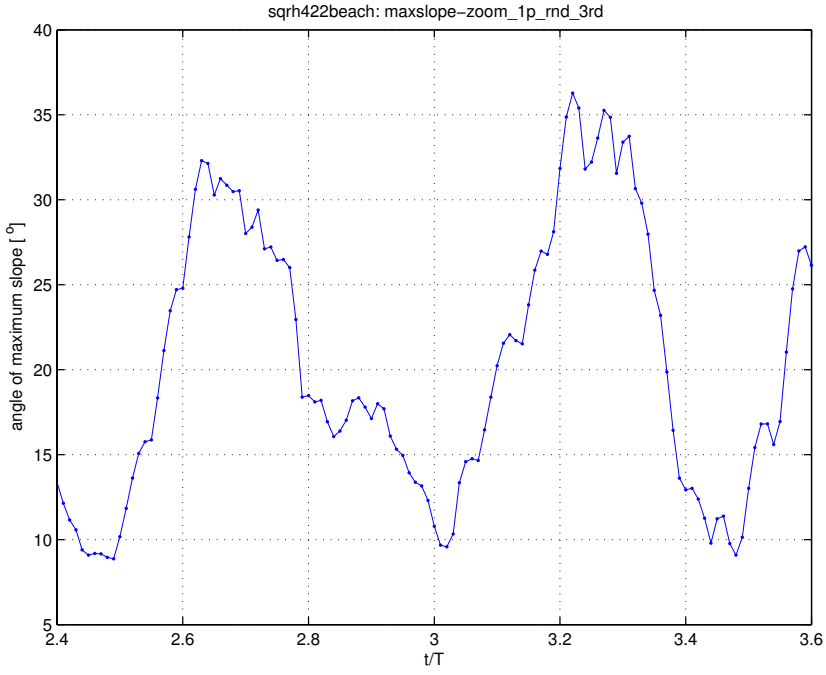

(b) Zoomed in on one period.

Figure 3.34: The maximum slope on the waterline as a function of time for the square cylinder in the 4 m high wave. Without Broeze.

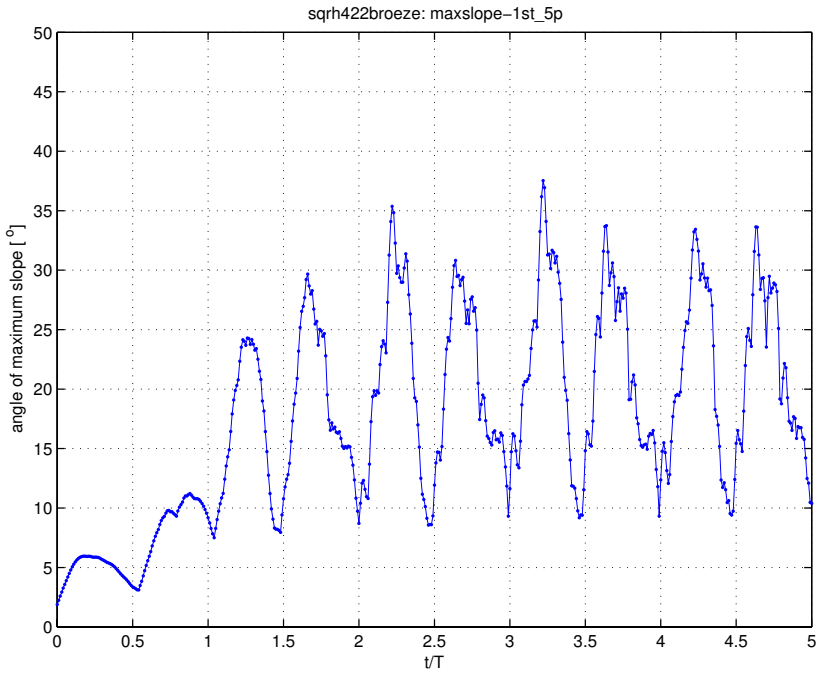

(a) Periods 1 till 5.

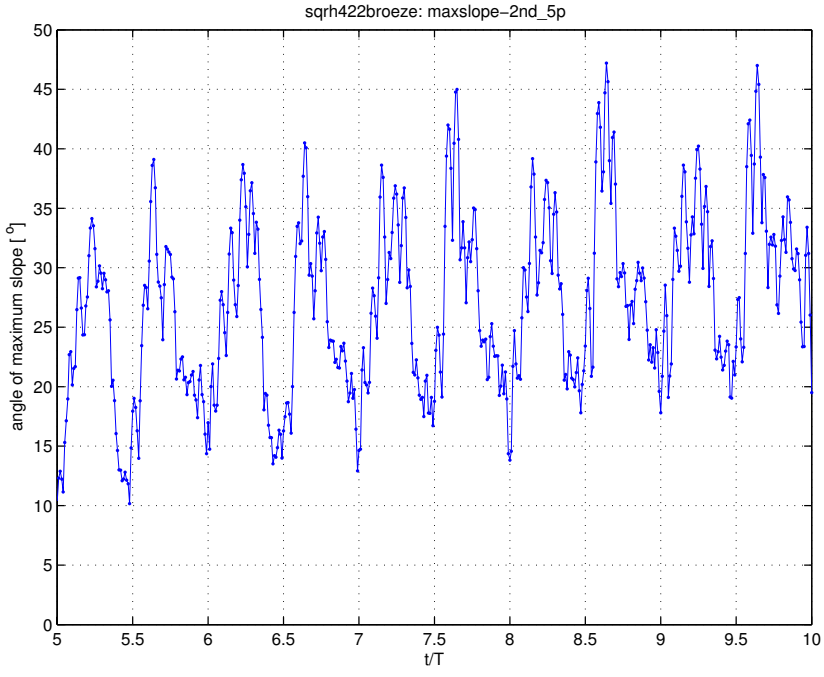

(b) Periods 6 till 10.

Figure 3.35: The maximum slope on the waterline as a function of time for the square cylinder in the 4 m high wave. With Broeze.

A range of amplitudes put together

In figure 3.36 four different heights of the incoming wave are plotted together. As a linear starting point we take a wave height of 0.1 m. The other wave heights are 1 m, 2 m, 4 m, and 8 m, for a wavelength of approximately 128 m. All these calculations use the cylinder length of the ISSC study: 24 m. They use a mixed grid and a full beach. As a reference again the linear solution for the infinite cylinder is included. In the first three rows at the front of the cylinder only the 4 m and especially the 8 m high wave deviate significantly from the linear solution. In the last four rows even the 1 m wave deviates clearly from the linear case. For the row at an angle of 157.5 degrees the results for the 4 m and 8 m wave are almost the same. For the rest of the rows there is a large difference between them. Near the front of the cylinder the 4 m wave deviates not too much from the linear case, but near the back it does. Especially at the back where the difference is around 30 percent.

To have a better look at the difference between the linear solution and the calculation with a wave height of 0.1 m see figures 3.37 and 3.38. In the last figure the vertical axis is stretched to have a more detailed view. There are two major and two minor factors involved. The most important are the length of the cylinder and the presence or absence of a beach. The two less important factors are the choice of grid and the start-up procedure. In the legend *lin* stands for the analytical linear solution, *long* for the 48 m long cylinder, *longer* for the 96 m long cylinder (which gives almost exactly the same results as the long one, see figure 3.9), *mixed* for the mixed grid, *nobeach* and *without* for no beach but with a Sommerfeld radiation condition, and *106* for starting up with the linear solution. Figure 3.38 shows that having a short cylinder instead of a long one and having a beach instead of no beach both have a large effect but of opposite sign. For some of the rows the effect of the length of the cylinder is small or even absent. The beach has an effect everywhere. The start-up procedure only has a significant effect at the front two rows. The effect of the grid depends on the other factors, but is everywhere quite small. An interesting effect is seen in the last two rows for the calculations using the linear start-up procedure: the mixed grid deviates about 1 percent at the third measurement point.

Returning to the question of how close our calculation with the 0.1 m wave is to the linear solution: when taking a long enough cylinder while leaving out the beach the result of our calculation is within almost 1 percent of the linear solution.

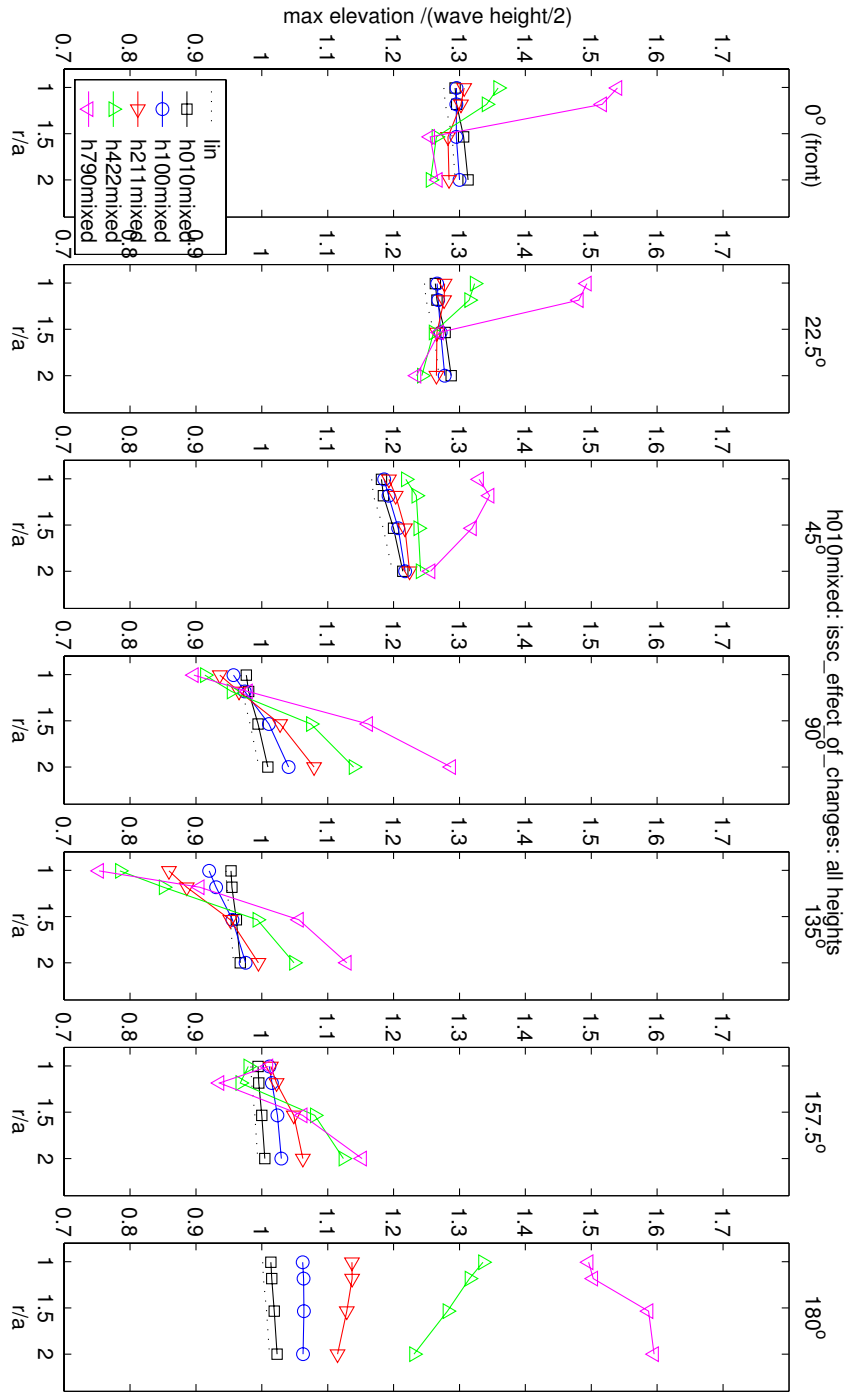

Figure 3.36: A range of different wave heights with the circular cylinder. Maximum wave elevation at the extended ISSC wave probe positions.

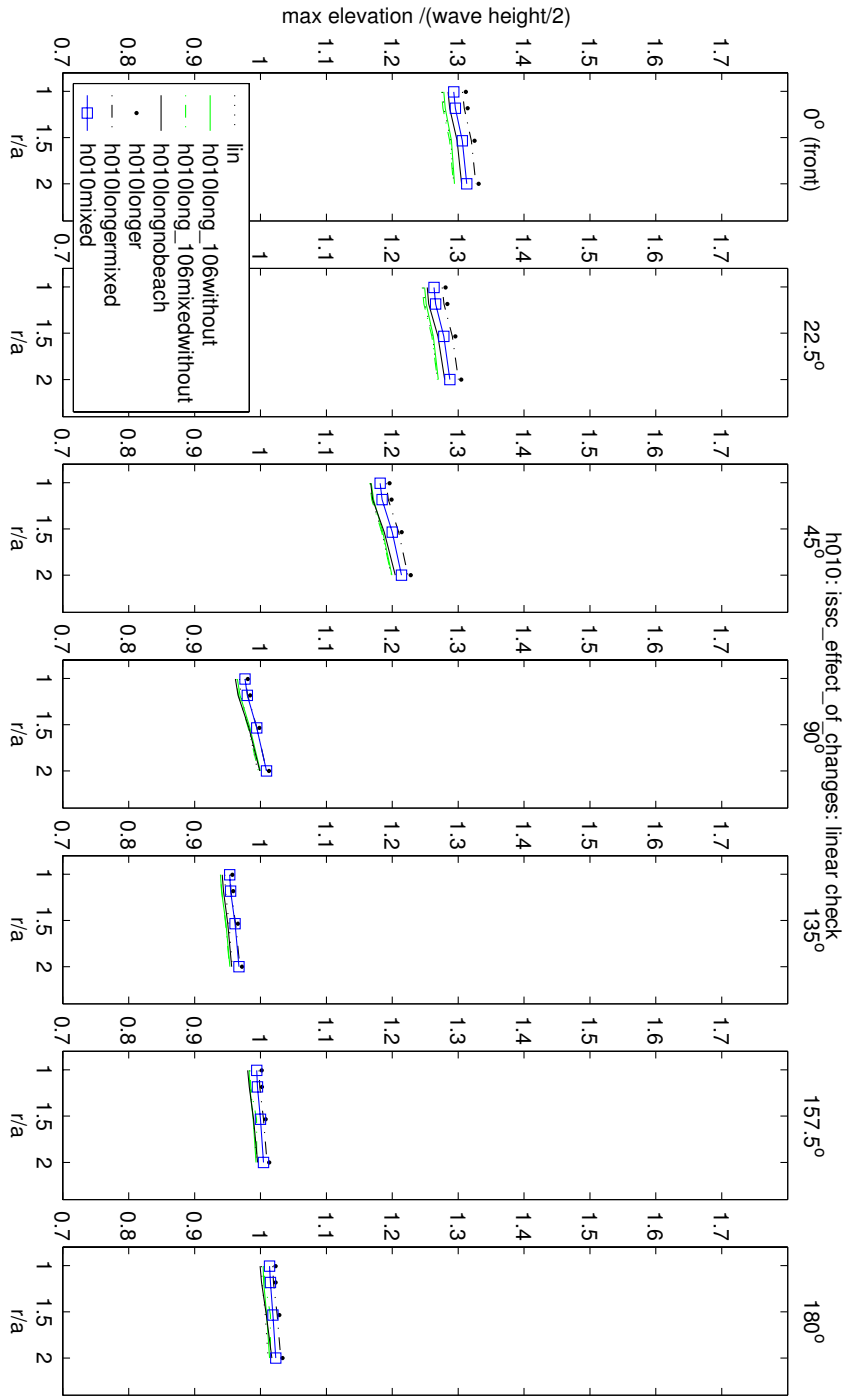

Figure 3.37: A look at how the different attempts to mimic the linear diffraction solution are doing.

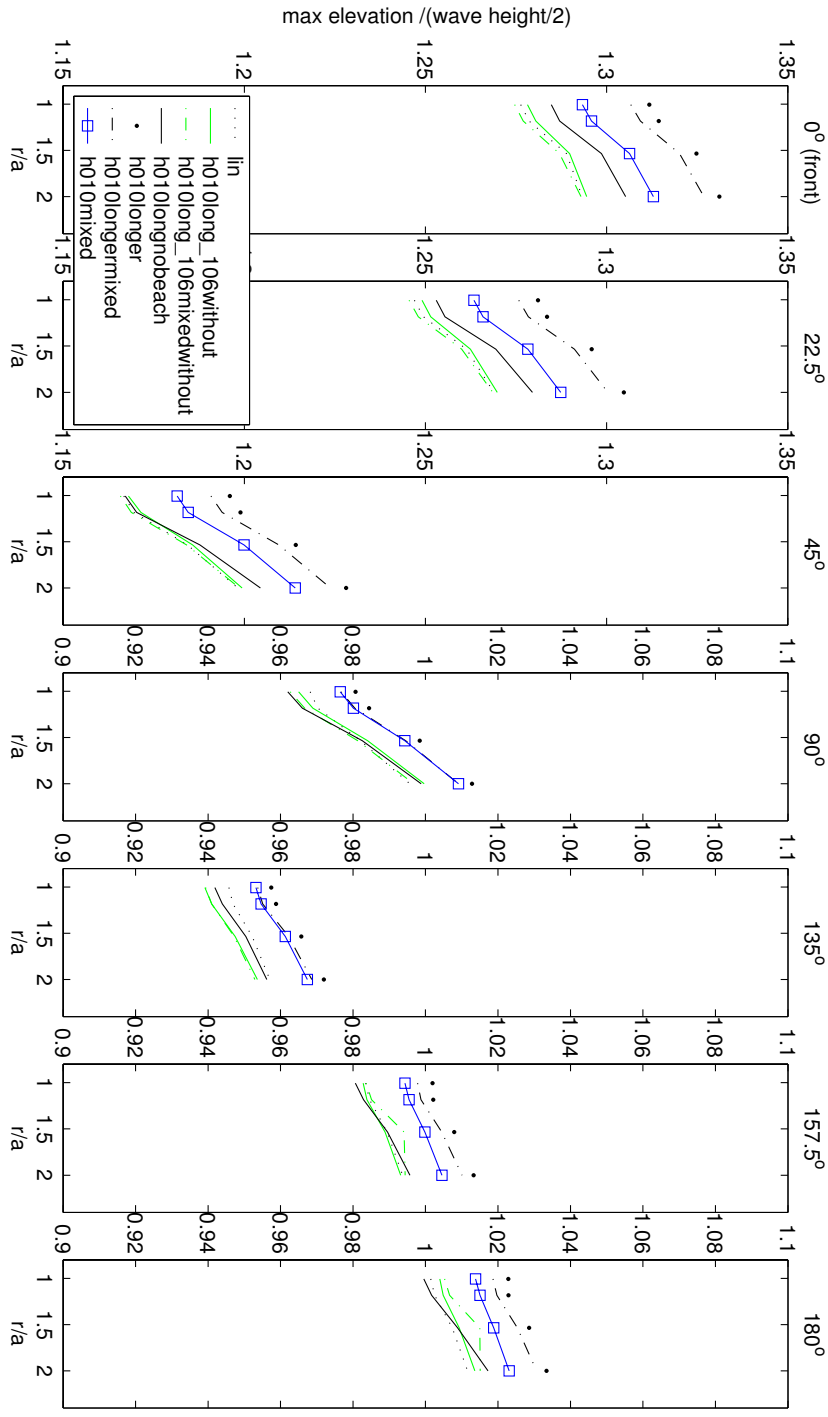

Figure 3.38: A look at how the different attempts to mimic the linear diffraction solution are doing. ZOOMED

3.3.2 EXPRO-CFD wave profile measurements

The EXPRO-CFD project is a collaborative project aimed at making substantial improvements to techniques for the prediction of non-linear and extreme wave loads and responses of offshore floating production systems. The three-year project started in February 2001 and is supported by the European Commission as part of its Fifth Framework programme Growth 2000. Within that project wave profile measurements were carried out around a cylinder in regular waves. Some of their wave cases were appropriate for the setup developed for the ISSC calculations.

We chose the regular wave case with $L/D = 10$ and $L/2a = 20$, here L is the wavelength, D the diameter of the cylinder, and $2a$ the wave height. When the wavelength is 128 m, the diameter is 12.8 m, and the wave height will be 6.40 m. For the incoming wave we took a Rienecker & Fenton wave with a period of 9.00 seconds and a wave height of 6.40 m. This gives a wavelength of 129.6 m. The diameter of the cylinder was taken to be 12.8 m. The water depth could be considered to be infinite. The wave profiles were measured in two radial planes: one at the front, at an angle of 0 degrees with the incoming wave, and the other one at an angle of 45 degrees with the incoming wave. The free surface was illuminated by a laser sheet in the radial plane to be measured. This was then recorded by two video cameras placed next to each other and looking to the side of the radial plane. Each camera covered its own piece of the illuminated free surface. The free surface was then extracted using image analysis software. The two cameras together covered a radial width of approximately one cylinder diameter outside of the cylinder.

Compared to the setup of the ISSC calculations, only the diameter and the length of the cylinder are changed. The length of the cylinder was taken to be 48 m to mimic an infinite cylinder since the cylinder in the measurements extended to the bottom of the basin.

Figures 3.39 till 3.44 show for both the radial planes at 6 different radial positions the wave elevation as function of time as obtained from the wave profiles and as obtained from the HYPAN calculations. From the time series of a wave probe at the same wave phase as the cylinder the first decent maximum and the period of the experimental incoming wave are established, see figure 3.46. The plotted time series run from that first decent maximum till the last profile taken. The period of the incoming wave in the experiments is 5 percent longer than it is in the calculations. In the figures the period of the calculations is enlarged with the same factor to correct for this. From the wave profile at each time step the elevation in six radial positions is taken: $r/D = 0.503, 0.596, 0.767, 1.000, 1.250$, and 1.500. This gives the six time series for each profile angle. The best[9] period from the calculations is synchronised with the incoming wave and repeated to compare with the different experimental periods. The synchronisation depends on the determination of the first decent maximum. In order to put the calculations nicely in sync with the experiments a shift of 5 frames to earlier times was needed on top of the calculated synchronisation. This correction is the same for both wave profile angles. The incoming waves stay nicely in sync with each other, with no sign of changing periods. The reason for the above deviation is unclear. The not so accurate determination of the position in time of the first decent maximum could be the cause, but then one would expect a different deviation for

[9]The fourth period, after two start-up periods. The calculation breaks at $t/T = 4.8$.

both profile angles.

For the radial plane at an angle of 0 degrees there is a difference in the amplitudes of the measurements and the calculations in figures 3.42, 3.43, and 3.44 that can be traced back to the different alignment of the two cameras in that case, as suggested by figure 3.45(a).

The difference in the shape and the timing of the bumps in the wave profiles at 90 degrees can probably be traced back to the sharp (in space) experimental bump and the low resolution in the calculated bump, see figure 3.45(b). Figure 3.47 shows that it is not likely that this problem is caused by a lack of convergence: in a time series modulo one period all periods are plotted on top of each other and after start-up the position of the bump does not change significantly.

The noise or snow in the experimental results is caused by bad wave profiles. With this we mean that the data representing a wave profile at a certain point in time is often partially or completely nonsense. It seems that getting reliable wave profiles is not that easy yet.

All in all the HYPAN calculations compare very well with the measurements. Where they disagree it can be either traced back to inaccuracies in the experimental setup or to the limited resolution of the calculations. The greatest point of concern is the breaking down of the calculations. Whether this can be attributed to physical instabilities, lack of resolution, or something else, remains yet to be determined. Some kind of video material of the experiments could be helpful in establishing whether the wave is already showing signs of breaking.

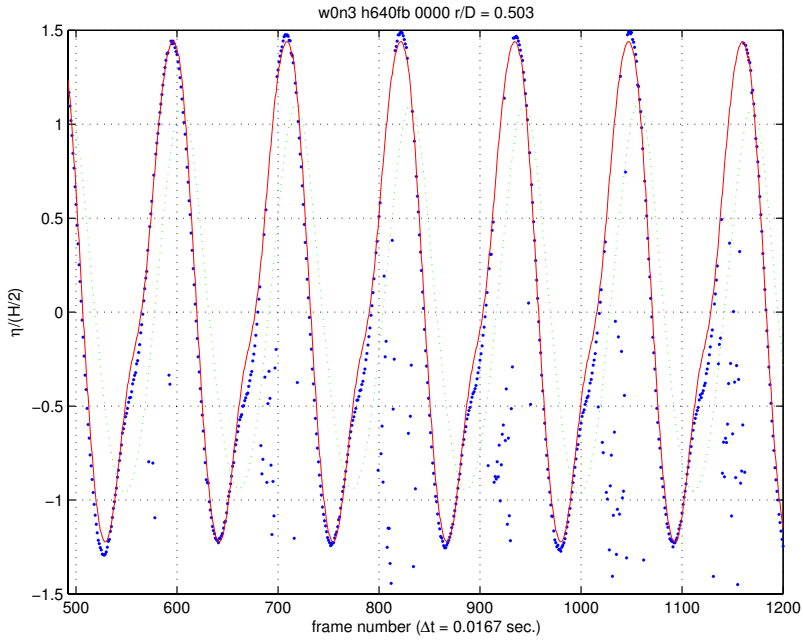

(a) 0 degrees

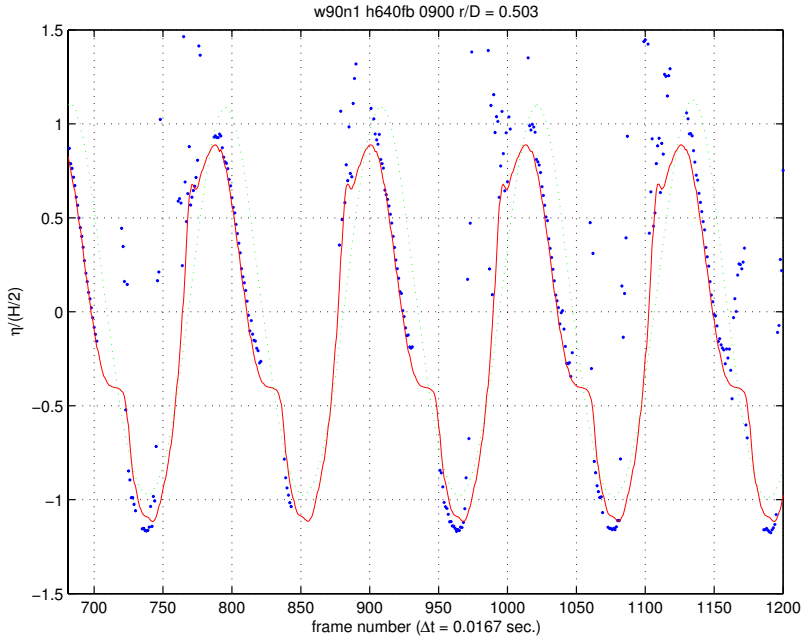

(b) 90 degrees

Figure 3.39: Time series at a radius of $r/D = 0.503$; EXPRO-CFD wave profile data (dots) and HYPAN calculation (line). The small dots with the same size as the gridline dots are the incoming R&F wave.

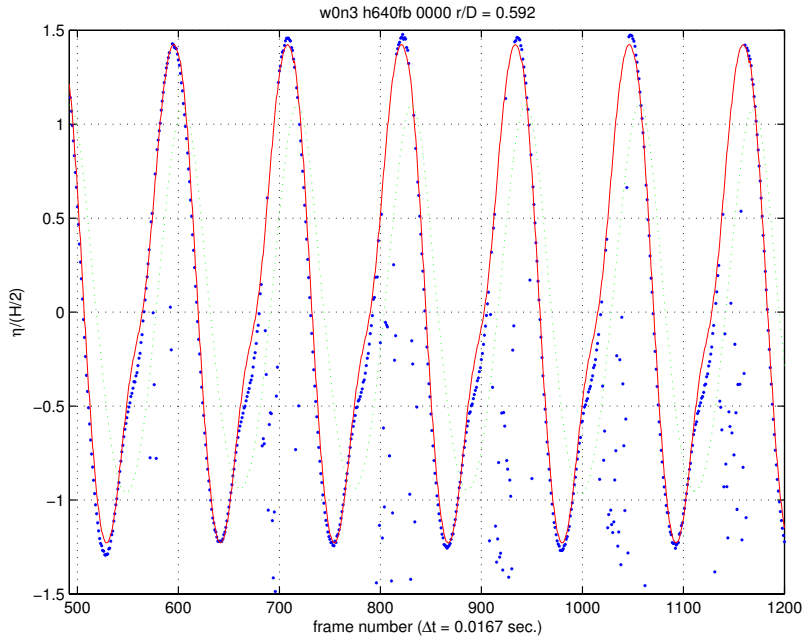

(a) 0 degrees

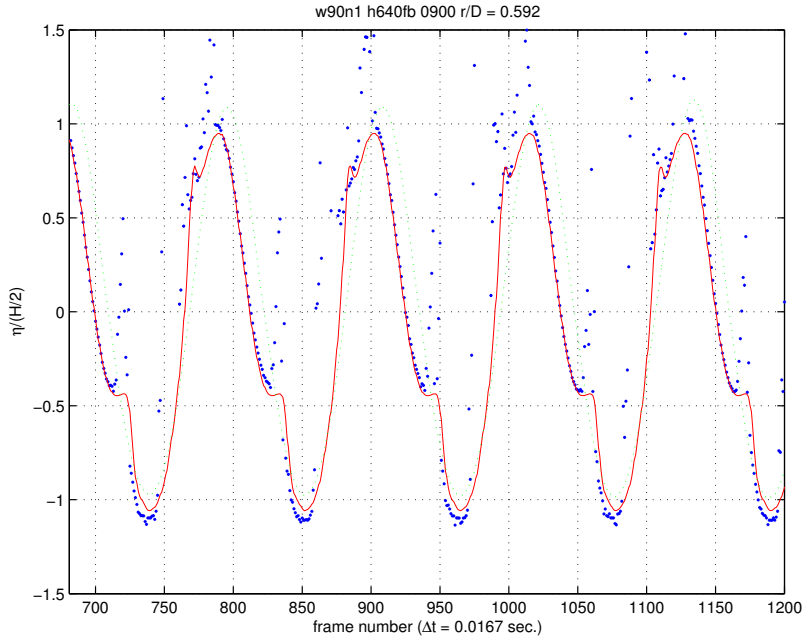

(b) 90 degrees

Figure 3.40: Time series at a radius of $r/D = 0.592$; EXPRO-CFD wave profile data (dots) and HYPAN calculation (line). The small dots with the same size as the gridline dots are the incoming R&F wave.

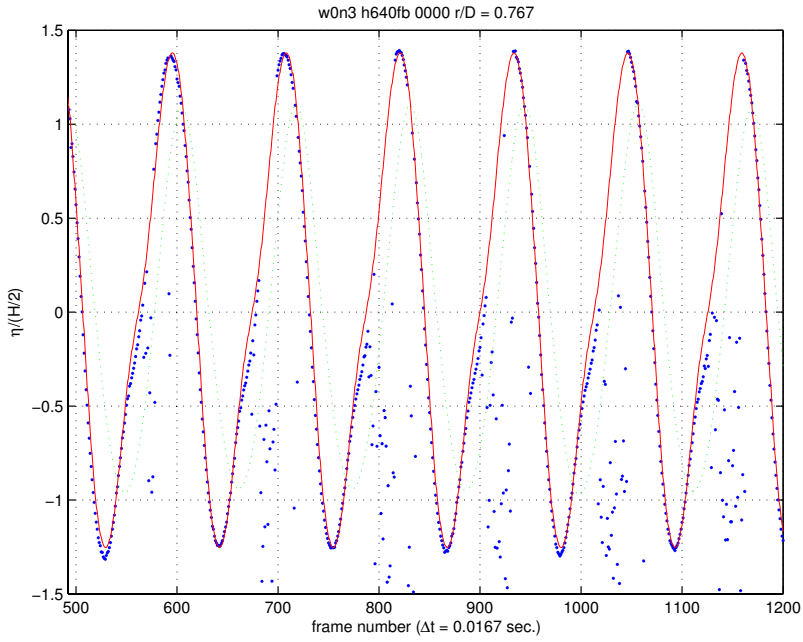

(a) 0 degrees

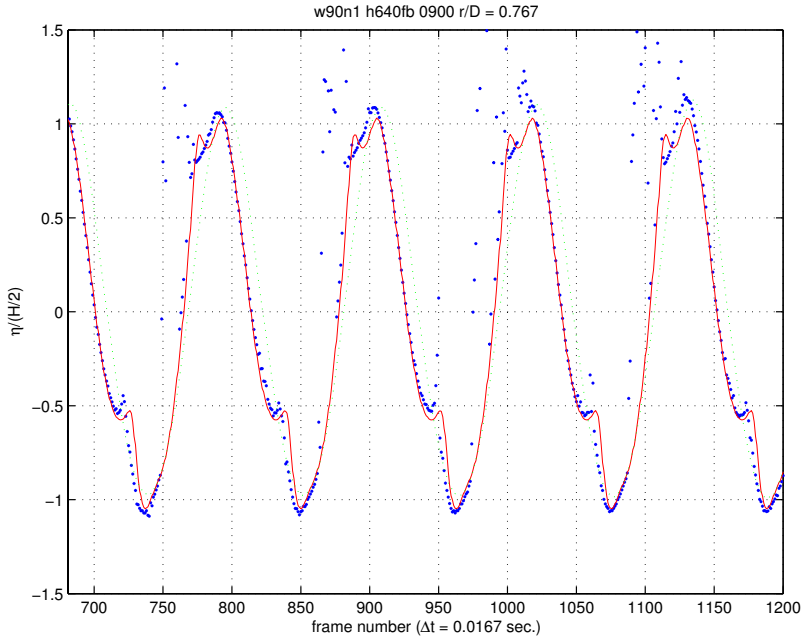

(b) 90 degrees

Figure 3.41: Time series at a radius of $r/D = 0.767$; EXPRO-CFD wave profile data (dots) and HYPAN calculation (line). The small dots with the same size as the gridline dots are the incoming R&F wave.

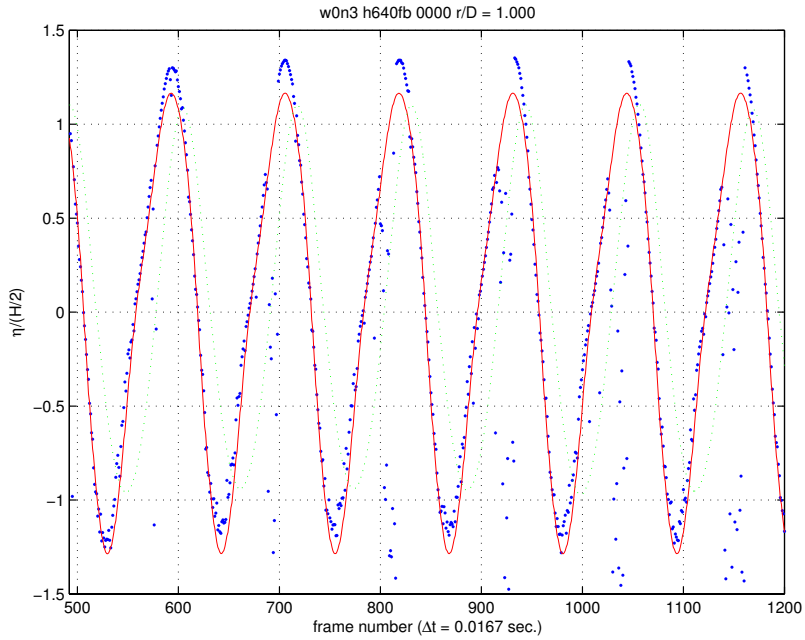

(a) 0 degrees

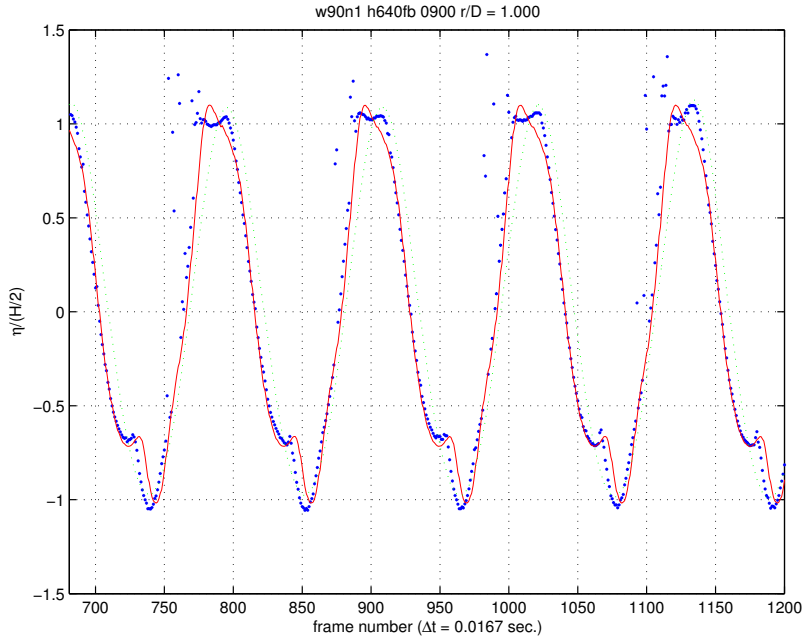

(b) 90 degrees

Figure 3.42: Time series at a radius of $r/D = 1.000$; EXPRO-CFD wave profile data (dots) and HYPAN calculation (line). The small dots with the same size as the gridline dots are the incoming R&F wave.

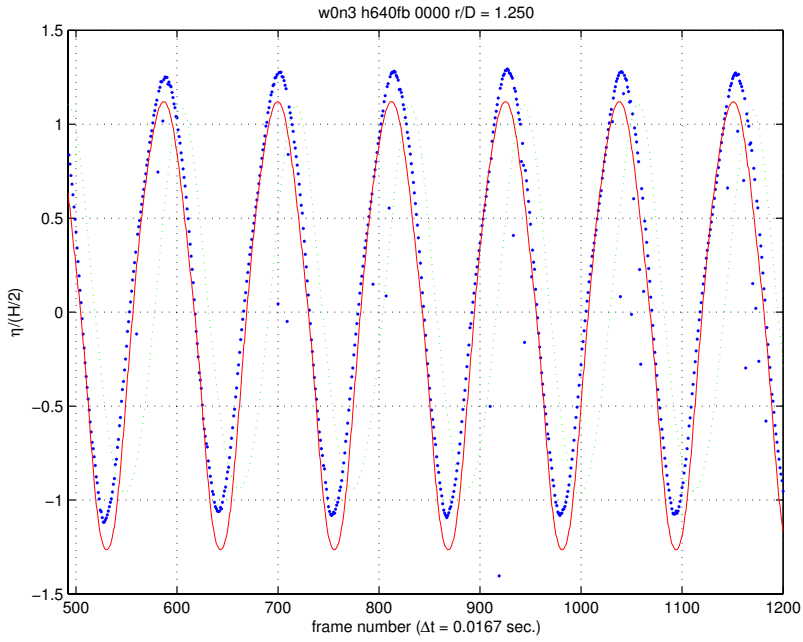

(a) 0 degrees

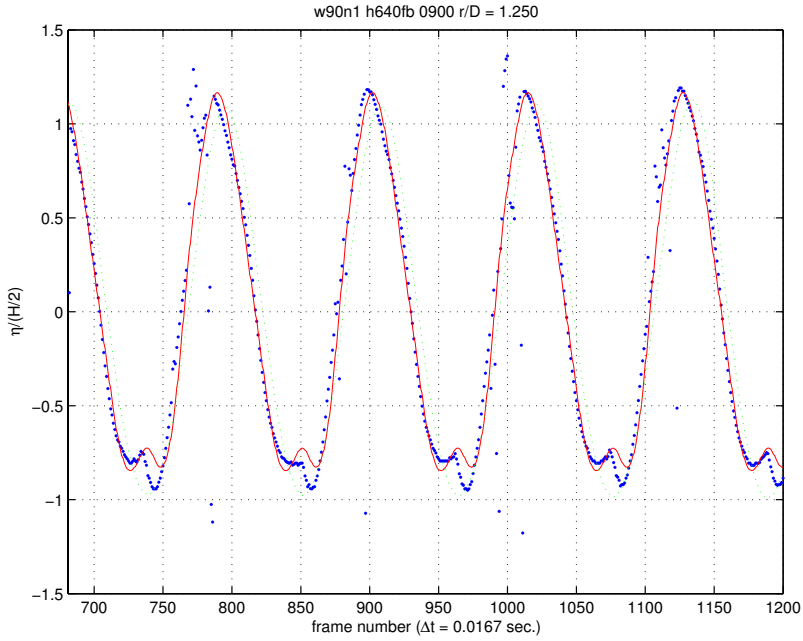

(b) 90 degrees

Figure 3.43: Time series at a radius of $r/D = 1.250$; EXPRO-CFD wave profile data (dots) and HYPAN calculation (line). The small dots with the same size as the gridline dots are the incoming R&F wave.

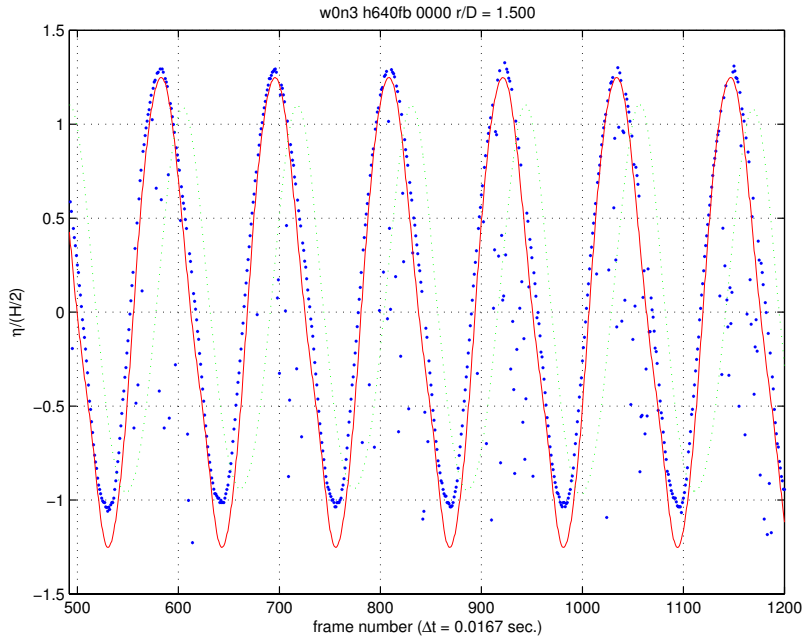

(a) 0 degrees

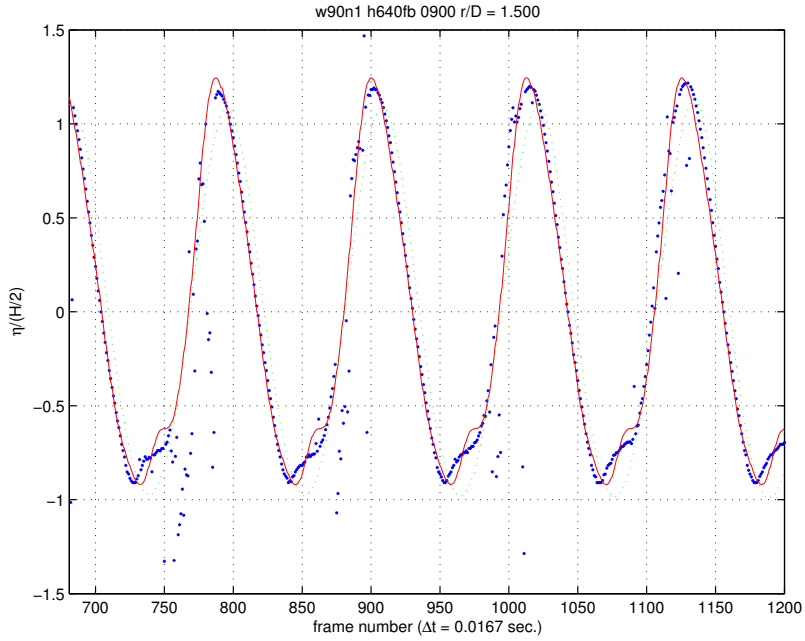

(b) 90 degrees

Figure 3.44: Time series at a radius of $r/D = 1.500$; EXPRO-CFD wave profile data (dots) and HYPAN calculation (line). The small dots with the same size as the gridline dots are the incoming R&F wave.

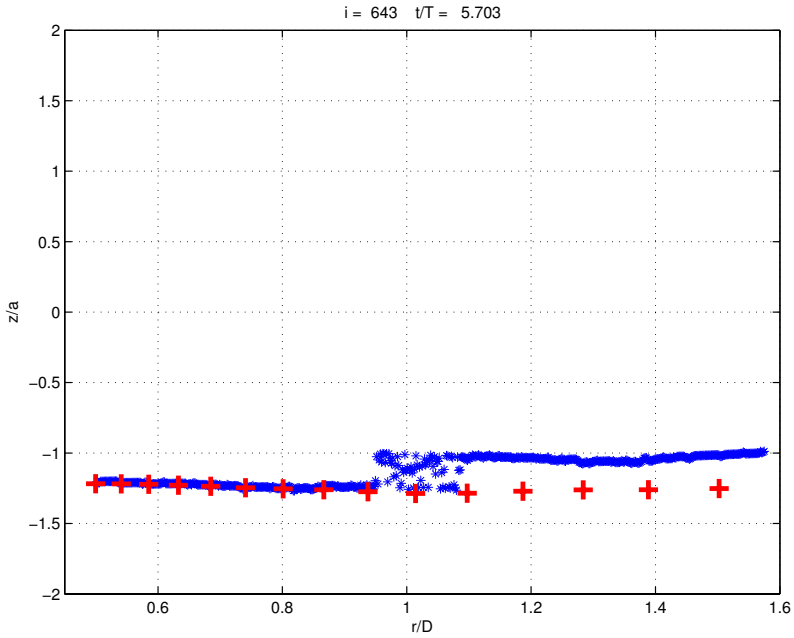

(a) 0 degrees

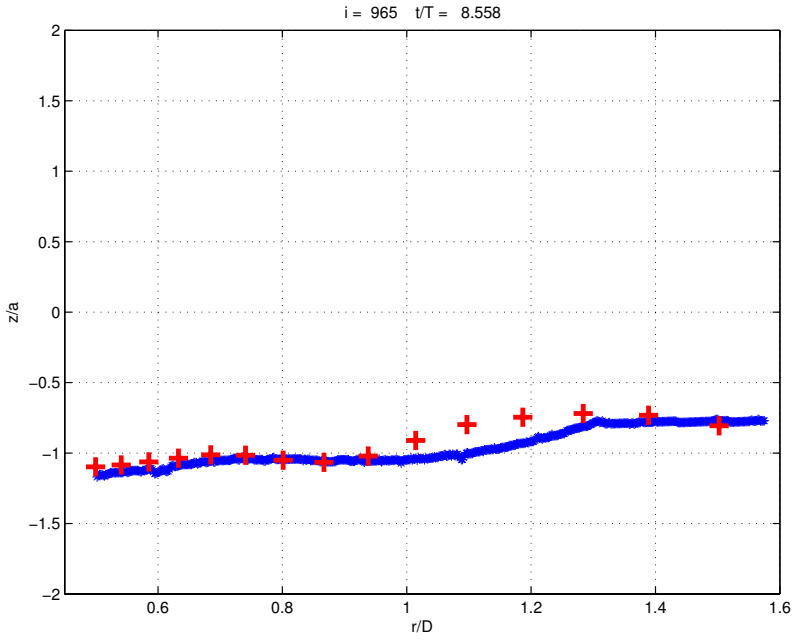

(b) 90 degrees

Figure 3.45: Two snapshots of a wave profile to indicate the quality of the EXPRO-CFD measurements (line of stars) and the resolution of the HYPAN calculations (crosses).

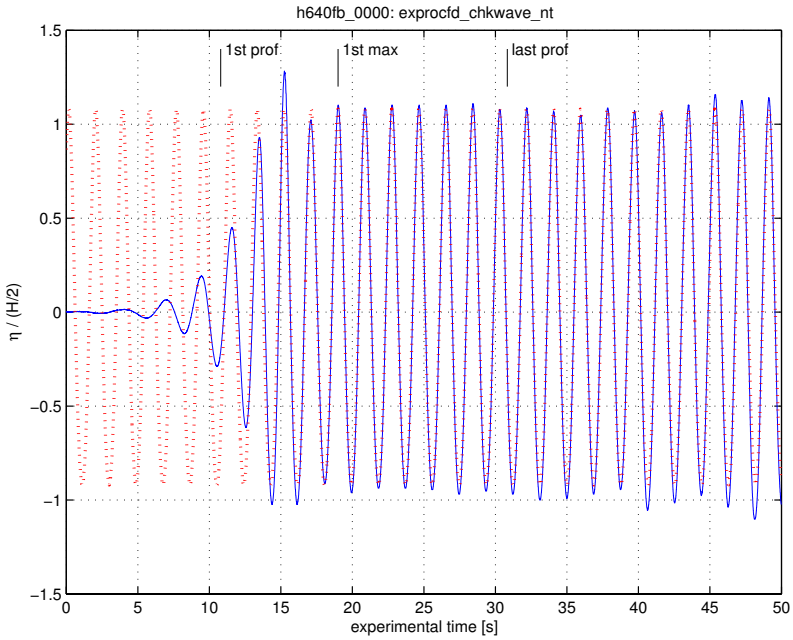

(a) 0 degrees

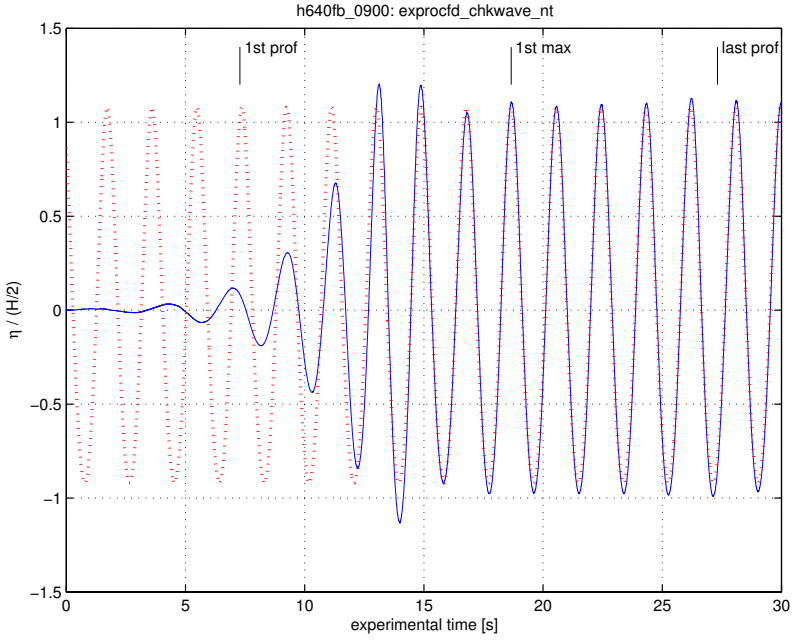

(b) 90 degrees

Figure 3.46: The incoming experimental wave, as measured by a wave probe at the same phase as the cylinder, compared to the incoming Rienecker & Fenton wave of the calculations. The time periods in which the wave profiles were obtained are indicated.

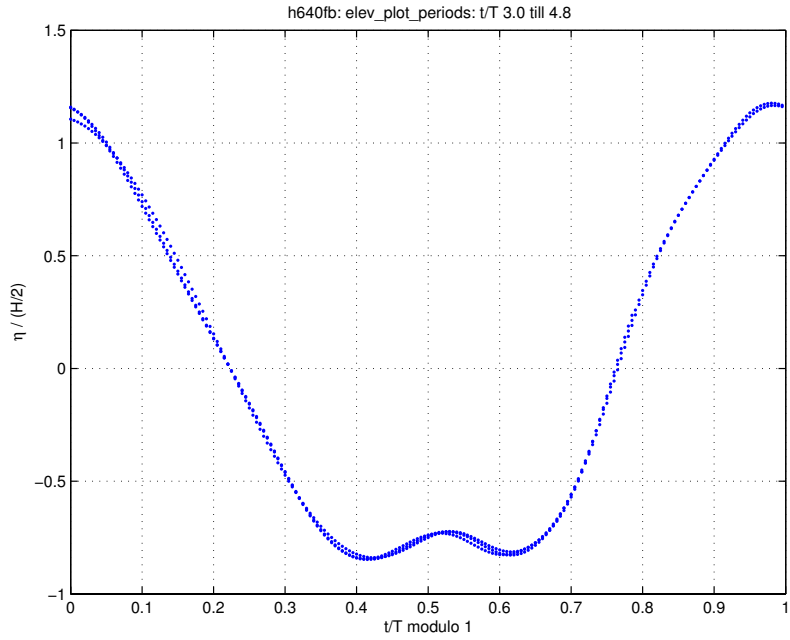

(a) The last three periods.

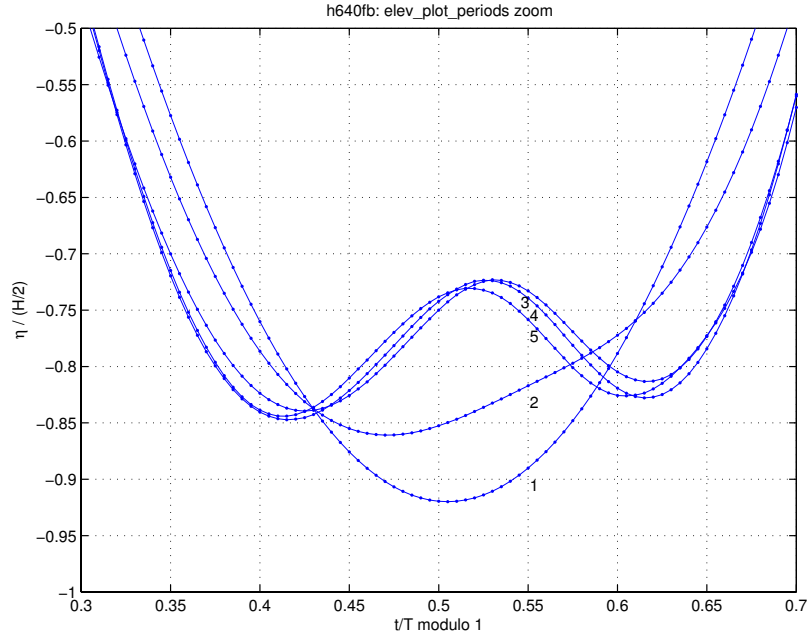

(b) All five periods, zoomed.

Figure 3.47: Dependence of the numerical results on which period one chooses to use for the figures comparing the numerical and the experimental time series.

3.4 Conclusion

We can reproduce the linear solution. Almost perfectly when looking only at the maximum wave elevation at the extended ISSC wave probe positions, and with deviations of around 2 percent when looking at the maximum error. This uses the Sommerfeld radiation condition as absorbing condition and the linear solution as start-up procedure. Changing the grid has a very small effect. In practical calculations we need a different start-up procedure and a beach. This start-up procedure, starting with the incoming wave and an open cylinder that changes slowly to a normal closed one, has a small effect on the maximum wave elevation at the extended ISSC wave probe positions. The beach has an effect of around 2 percent and changing the grid still has a small effect.

Also for the more practical wave heights of moderate and high steepness the results are good. The HYPAN calculations are within 10 till 5 percent of the measurements for the ISSC study. The details in the experiments for the EXPRO-CFD study are reproduced very well, especially considering the relatively low resolution of the calculations. There are some problems of course, mainly related to the limited computational resources. The strength of the beach, for example, has a significant influence, most probably because the beach is too close and too short. Another problem is that the very large wave heights break after a number of periods. A lack of resolution prevents us from making definitive statements about this.

The conclusion is therefore that the current setup is satisfactory. However, for real practical calculations there is a need for more resolution and larger domain sizes. For example, when considering irregular waves both the large wavelengths and the short wavelengths have to fit onto the grid, putting demands on both the minimum domain size and on the minimum resolution. For thoughts on how to deal with this see chapter 6.

Chapter 4

Three-dimensional diffraction calculations with a free-floating body

Using the results of the previous chapter we can now extend that work to free-floating bodies. Berkvens already had a free-floating sphere. He did not have an incoming wave yet. He did damping calculations and forced motion calculations both using only the Sommerfeld radiation condition as an absorbing boundary condition. We will set up the diffraction calculations for such a sphere. While checking our absorbing boundary conditions we can improve Berkvens' damping calculations of a sphere with the help of a beach and a larger domain.

4.1 Setup

The basic setup for these diffraction calculations with a free-floating body is the same as for those with a fixed body. There are some extensions needed however. Starting up, for example, is a little bit more complicated, because a free-floating body does not have a Neumann boundary condition, prescribing the normal velocity on the boundary. Also the motion of the grid needs some attention. As the position and the orientation of the object are no longer fixed, the grid points around the object cannot be kept fixed either. They should, in some way, move along with the object. Of course, when the object is moving over large distances one can either move the whole grid along with it, or you can restrain the position of the object somewhat. Because our prime interest is in moored offshore structures, the latter is the natural thing to do. A last point of attention are the absorbing boundary conditions. In the case of a fixed object we had an incoming wave and the diffracted wave, both with the same basic frequency. With a free-floating object we still have those waves, but also the radiated waves caused by the motions of the object. This has to be taken into account when tuning the beaches.

4.1.1 Start up

For the fixed cylinder we introduced the cylinder slowly into the wave instead of introducing the wave slowly on to the cylinder. This was done by prescribing as a normal velocity on the cylinder a fraction of the appropriate velocity component of the incoming wave, the fraction decreasing slowly from one to zero. For a free-floating object however, the velocity follows from the acceleration which is calculated using $\nabla^2\phi_t = 0$. To adjust the above procedure to this case is not trivial and whether it is worth doing so is questionable. Instead, we use a simple practical solution: first we keep the sphere fixed and use the procedure for a fixed object, and then when having the sphere introduced slowly into the wave we let it go free by prescribing the free-floating body boundary condition.

4.1.2 Grid motion

With respect to the fixed cylinder only the grid motion on the object and the grid motion on the free surface change. A more elaborate and more general treatment of the grid motion is presented in chapter 2.

Sphere

The boundary between the wetted and the dry part of an object is called the waterline. The waterline follows from the intersection of the free surface with the object. The grid on the sphere is generated from the waterline at every geometry update.

Free surface

For the motion of the grid on the free surface we use a mixed eulerian lagrangian approach with respect to the sphere. Near the sphere a point moves along a meridian of a virtual sphere obtained from the original sphere by scaling such that the point lies on the new sphere. Further away it shows a fraction of that behaviour, and far away it moves eulerian: it only moves in the vertical direction. The freedom of motion along the intersection line of the water tangent plane and the body tangent plane is used to implement this.

4.1.3 Mooring system

In the offshore business free-floating objects mostly need to be at a specific stationary position. For example, an FPSO above an oilwell or a shuttle tanker near an offloading unit. This is accomplished by a mooring system, a dynamic positioning system or a combination of the two. From a calculation point of view this is also a good idea. If an object is cut loose in a fully developed wave it will get an average speed depending on where in the period of the wave it was free to go. This speed is arbitrary and inconvenient: the object will flow out of the domain or the domain has to move with the object. It therefore is both realistic and convenient to keep the position of the object somewhat constrained. We mimic a soft spring by prescribing a linear restoring force to the middle of the domain. To be able to determine the equilibrium position of the mooring system in a reasonable number of periods, an extra damping of 0.33 times the critical damping is applied in addition to the wave damping already there.

The choice of the eigenfrequency of the mooring system of 0.10 rad/s satisfies the criterium mentioned by Pinkster: $\omega_{inc}/\omega_{0,m} > 5$ for all incoming wave frequencies ω_{inc}. Using the amplitude response function of the mooring system, the effect of the mooring system on the first order surge motions is estimated to be less than 1% for all cases with $ka \geq 0.8$. In the implementation of this mooring used for the calculations in this chapter a small error was made. The effect on the results is considered to be negligible, see the appendix, section A.3.

4.1.4 Beaches

In these calculations we not only have to absorb the incoming wave and the diffracted waves, but also the waves radiating from the sphere going up and down. Because the sphere is free-floating the frequency of the radiated waves will be more or less at the resonance frequency. The length of the beach is again 32 m.

The first damping experiments of section 4.2.2 called `big-beach` were originally meant to check the performance of the beach for the cylinder setup of chapter 3. The Sommerfeld radiation condition is therefore tuned to the wave frequency of the incoming wave used in those calculations: $\omega_s = 0.70$ rad/s. Together with a heave eigenfrequency of 1.1 rad/s for the sphere with the 8 m radius, $\omega_s/\omega = 0.64$. The strength or slope of the beach b was chosen to be $0.25 \cdot 10^3$ kg $\cdot$ m^{-3} $\cdot$ rad $\cdot$ s^{-1}. This results in a bounce reflection for the waves radiated at the heave eigenfrequency of about 5% and a total reflection that is a little bit higher, but still 5%.

The other damping experiments of section 4.2.2 called `chk-damp` were originally meant to check the performance of the beach for the calculations of section 4.2.3 and especially the calculations at heave resonance. The strength of the beach b was put to $0.10 \cdot 10^3$ kg $\cdot$ m^{-3} $\cdot$ rad $\cdot$ s^{-1}. The Sommerfeld radiation condition is tuned to the incoming wave frequency $\omega = 1.1$ rad/s. At a heave eigenfrequency of 1.14 the relative tuning $\omega_s/\omega = 0.96$. This results in a bounce reflection and a total reflection of about 2%. This is near optimal considering the slight mis-tuning. The bounce reflection gives a good indication for the reflection of the diffracted waves for the calculations in section 4.2.3, because the Sommerfeld radiation condition is for each calculation tuned to the incoming wave frequency.

4.2 Testing

4.2.1 Grid motion without mooring

First we test the capabilities of the new grid motion algorithm that implements a mixed eulerian lagrangian approach with respect to the sphere. For that we take the setup used for the 4 m high wave of the ISSC study and replace the cylinder with a sphere of the same diameter. It turns out that the average speed obtained by the sphere is very dependent on the moment in time at which the sphere is free to go: if the acceleration $a = -\omega^2 A \sin(\omega t + \phi)$ then the velocity $v = \omega A \cos(\omega t + \phi) + C$, with C such that $v(t = 0) = 0$. The average velocity is equal to the integration constant C, which is not necessarily equal to the initial velocity.

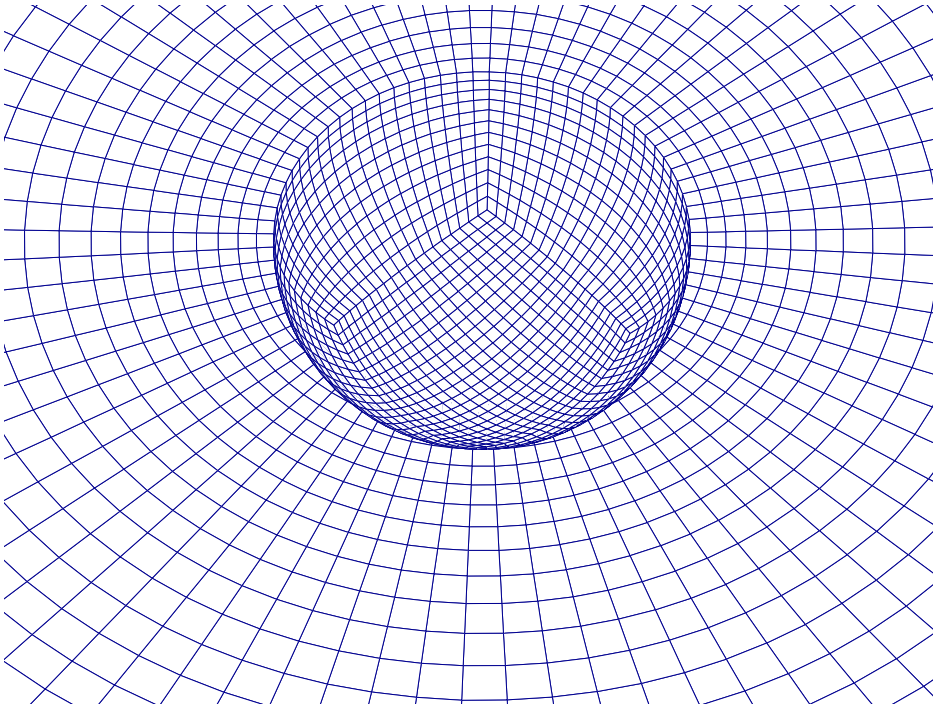

(a) Close up of the grid around the sphere. The radius of the sphere is 12 m, the grid as used in "drift-new".

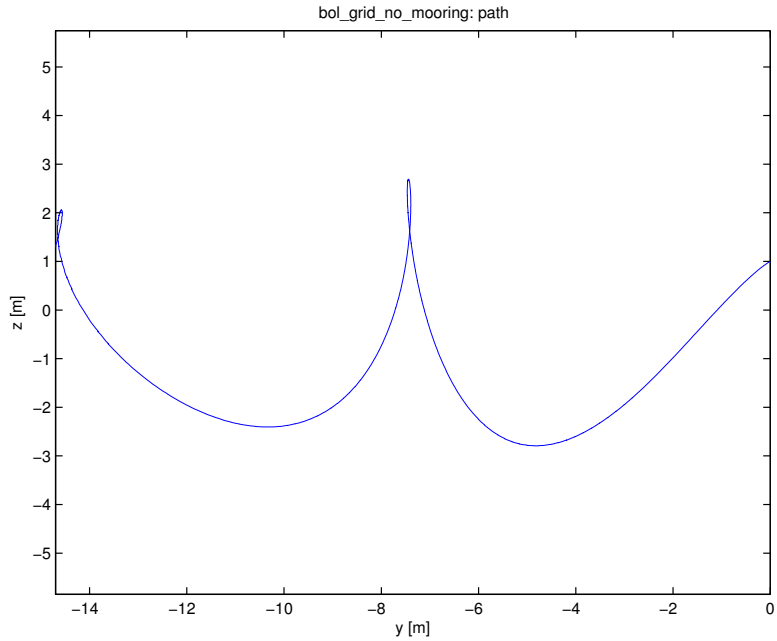

(b) Trajectory of the centre of the sphere, no mooring. Radius of the sphere is 8 m, wave height is 4 m, wave period is 9 seconds.

Figure 4.1: See captions above

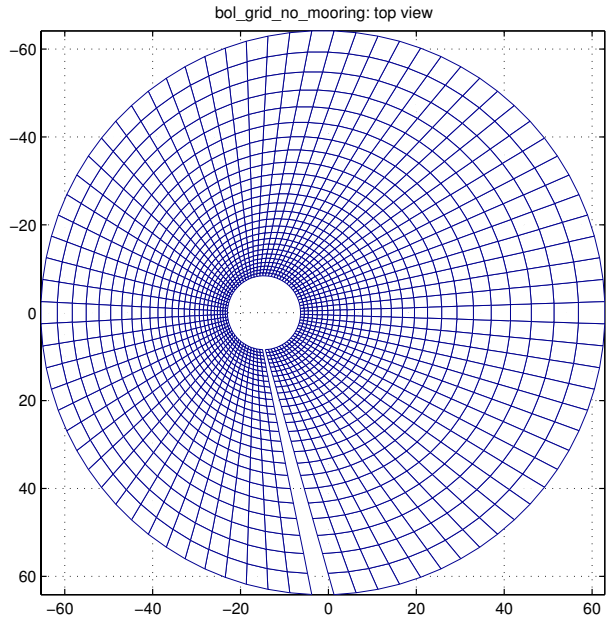

(a) A deformed grid when the sphere is not restrained by a mooring system.

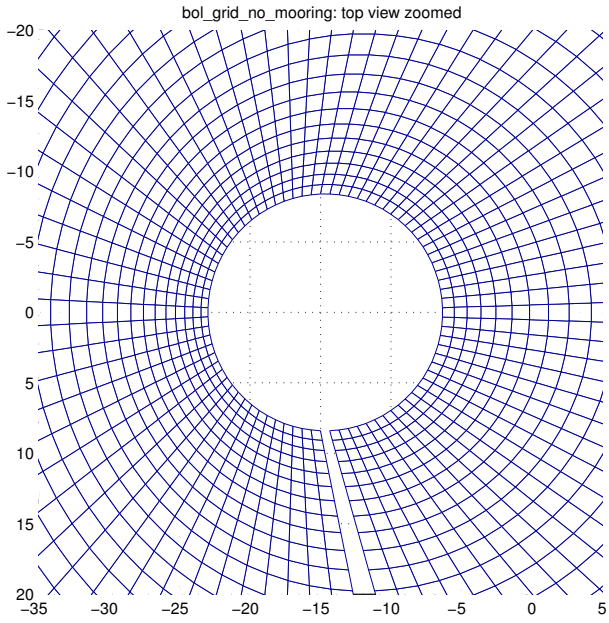

(b) Close up of the same situation.

Figure 4.2: The grid movement algorithm can handle grid motions like this without problems.

4.2.2 Damping experiments

By performing a few damping experiments the performance of the beach can be checked together with the quality of the floating body algorithm. Berkvens already did some damping calculations, but as an absorbing condition he only used a Sommerfeld radiation condition, which has problems absorbing the front of the wave train coming from the sphere because of dispersion. See for example his figure 6.6. There the decay is not monotonic, at around $t = 40$ the amplitude rises again for a moment, which is an obvious sign of reflection. In his section 6.4.2 he compares the added mass and damping coefficients calculated from his experiments to those obtained by Pinkster, and gets a deviation of a factor of two. This is a calculation error however: he mixed up the dimensionless values. From the results given in his thesis the calculation can be repeated and the correct values are: $\alpha = 0.400$ and $\beta = 0.275$. The deviations for these values are respectively -6% and +12%.

For our calculations we first took a standard grid (square) and a sphere with a radius of 8 m. The beach setup was described in section 4.1.4. The grid on the sphere had 6 panels in the height of the side networks. For comparison we use the linear results from the thesis of Pinkster. There are two cases: one with no special care[1] taken for the pressure integration around the waterline, figure 4.3(b), and one with that special care taken, figure 4.3(a). The one without the special care had an initial displacement of 1 m. The one with the special care had an initial displacement of 0.1 m. Only in the end of the decay there is a difference between the two: for the one without, the equilibrium position is not exactly 0, but that is only after the amplitude has decayed to less than one-hundredth of its starting value. Changing the equilibrium position in the calculations to the new value, as done in figure 4.3(b), helps. To completely correct for it one needs a linear function from 0 to a fraction of the final position. After this correction the two graphs are right on top of each other.

It is very clear that we have three different regions in the decay. None of which agrees completely with the results from Pinkster: Pinkster is somewhere in between. This behaviour can be related to the following: in the beginning the sphere has still to create the wave system, later on reflections return from the beach and in the end the movements are so small that they are sensitive to anything.

In the legends we give the values of α and β for the four different lines: first the line through all points, then the other lines starting from the left. The three values per line are the lower bound, the average, and the upper bound. The Pinkster values are given for the four different frequencies coming from the different lines. The difference between those frequencies is small compared to the error in those frequencies. The effect is therefore small. To explain the large error bounds we look at the line through all points from figure 4.3(a). The relative error in α is about 20 percent and the relative error in β is around 10 percent. The sources of those errors are the frequency, with a relative error of around 3 percent, and the slope, with for this case also a relative error of around 3 percent. It is obvious that the error in the slope will be less for the other lines. α depends on the squares of those two quantities, multiplying their relative errors by a factor of two. Because α is formed by the subtraction of two similar quantities, the relative error is multiplied even more: for the current values with a

[1] Calculate only the difference with the equilibrium situation. This means that most of the large hydrostatic contribution can be calculated analytically. See the thesis of Berkvens.

factor of around 3.5. The total error in α resulting from the error in the frequency is then around 20 percent. β depends on the third power of the frequency and on the square of the slope and has no subtraction of two terms. The total error in β resulting from the error in the frequency is then around 10 percent. For an indication of where the error in the frequency is coming from, see figure 4.5(a) and later on in this section.

We also did two damping experiments with the setup as used for the calculations in section 4.2.3. This means that the grid is mixed, that there are 12 panels in the height of the side networks on the sphere, that the strength of the beach is $0.10 \cdot 10^3$ instead of $0.25 \cdot 10^3$, and that special care is taken for the pressure integration around the waterline. The Sommerfeld radiation condition is tuned to the incoming wave. Since we were especially interested in the situation at heave resonance, we took the setup for $ka = 1.0$, which means that the Sommerfeld radiation condition is (approximately) tuned to the resonance frequency of the sphere. At $ka = 1.0$ we have two geometry setups: one for a sphere with a radius of 8 m and one for a sphere with a radius of 12 m. The domain size and the length of the beach are the same in both cases. Both spheres get an initial displacement of 1 m. The results are presented in figure 4.4. The format is the same as used in figure 4.3.

First we notice that there are no problems with the equilibrium position. This means that the problem as mentioned above is related to the choice of pressure integration and not to the initial displacement of the sphere. Then there is the strange behaviour of regions with different slope. For the 8 m sphere we see something similar in the beginning. For the 12 m sphere we hardly see anything. It should be noticed that the 12 m sphere is both absolutely and relatively closer to the start of the beach and that the beach is relatively shorter. It is clear from these experiments that the sphere is decaying monotonically all the way down to amplitudes a factor of 100,000 smaller then the initial displacement. But also in these cases we have error bounds that are quite large. We will concentrate on the lines through all points here. For the 8 m sphere we then have an α of 0.428 and a β of 0.19. The 12 m sphere gives an α of 0.450 and a β of 0.20. The reference data from Pinkster gives an α of 0.426 and a β of 0.245. This implies for the 8 m sphere a deviation of 0.5 percent for α and a deviation of 20 percent for β. For the 12 m sphere the deviation is 5 percent for α and 20 percent for β. Giving a similar comparison for figure 4.3 is problematic, because of the arbitrary choice of which region one should take. α for the 8 m sphere would be somewhere between 0.40 and 0.44. β would be somewhere around 0.29. This would mean a deviation of less than 5 percent for α and a deviation of around 20 percent for β. In this case β is larger however instead of smaller. Therefore it is reasonable to say that the added mass coefficient deviates less than 5 percent from the value given by Pinkster, which is reasonable. The situation for the damping coefficient is less reasonable however: we get both values of 20 percent less and of 20 percent more than the value given by Pinkster. For the 12 m sphere we do get a more or less consistent value for the damping coefficient of 0.20 plus or minus 5 percent. This could explain the deviation of 10 percent in the heave amplitude at resonance, see section 4.2.3.

Figures 4.5(a) and 4.5(b) give an indication of the raw data for the determination of the frequency. In these figures the time between zero-crossings (in terms of time steps) is plotted as a function of the period number. Figure 4.5(a) is for the 8 m sphere and the mixed grid, but it gives also a good indication for the situation in

figures 4.3(a) and 4.3(b). The time of the zero-crossing is determined by a straight line through the two points nearest to that crossing, but even then there is a periodic deviation with an amplitude of approximately half a time step. Figure 4.5(b) however shows that that does not need to be. Further investigation should show whether this behaviour is caused by reflections or by something else.

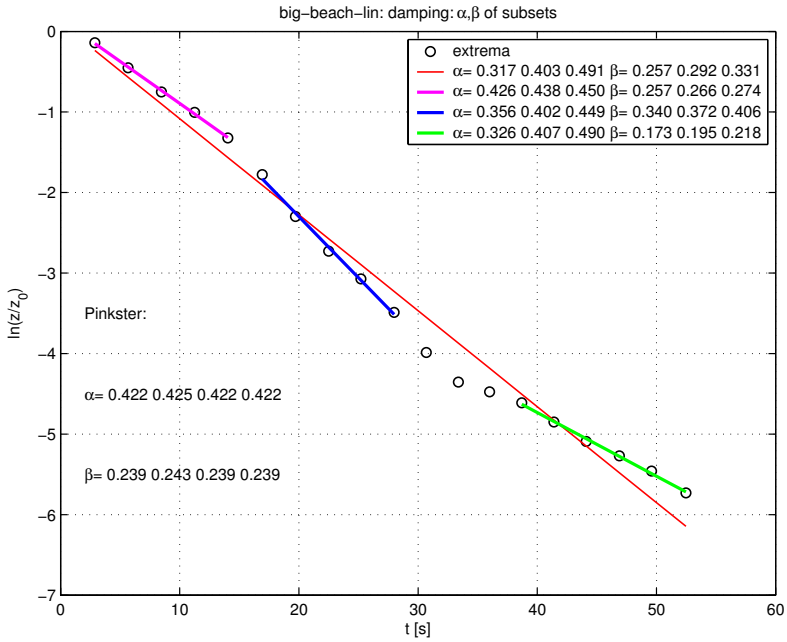

(a) Starting with a small deviation from equilibrium of 0.1 m. IGRAV=0.

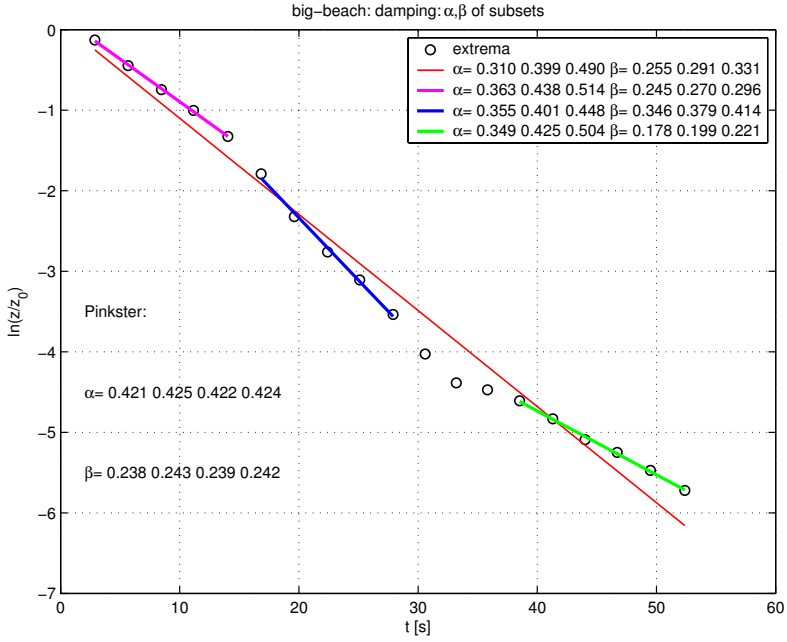

(b) Starting with a larger deviation from equilibrium of 1 m. IGRAV=1.

Figure 4.3: Free damping experiments with a sphere with a radius of 8 m. The logarithm of both the maximum and the minimum values as a function of time.

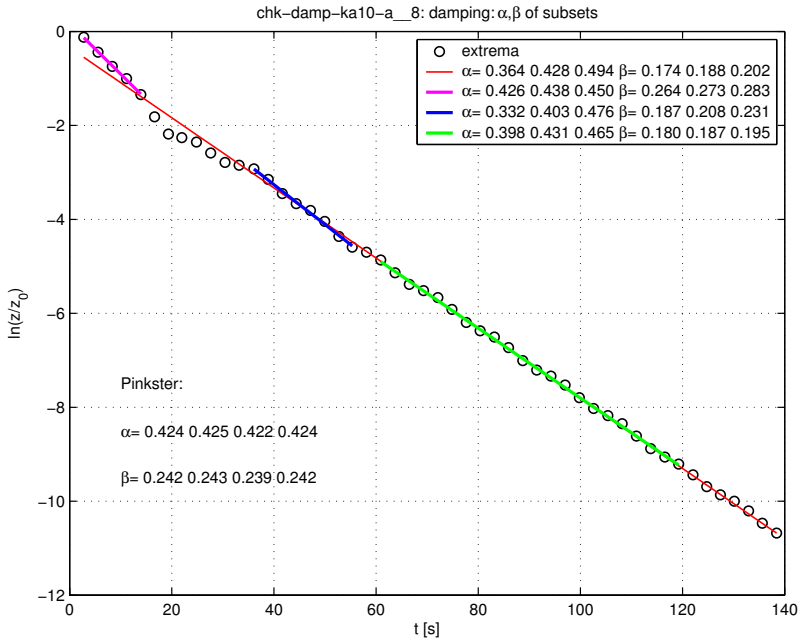

(a) Sphere with a radius of 8 m.

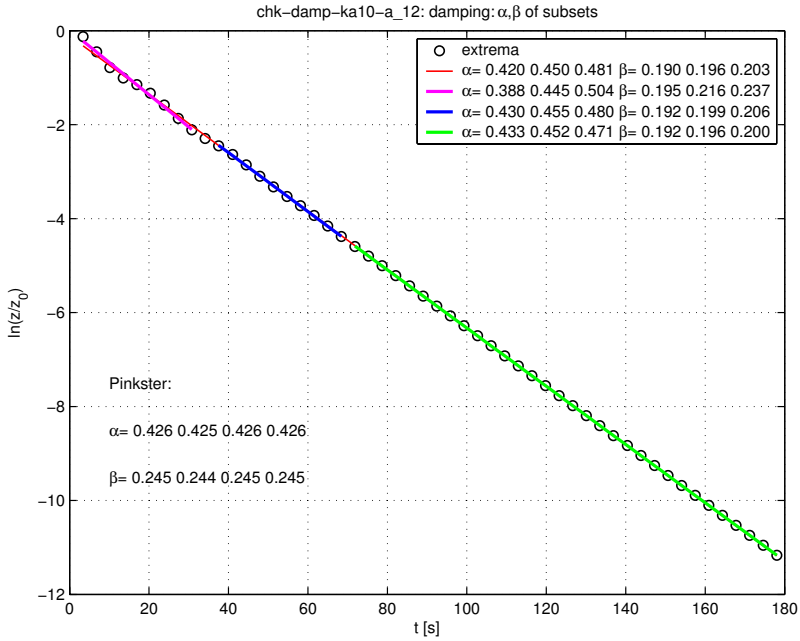

(b) Sphere with a radius of 12 m.

Figure 4.4: Free damping experiments with the same set up as used for the "drift-new" calculations at $ka = 1.0$. The logarithm of both the maximum and the minimum values as a function of time.

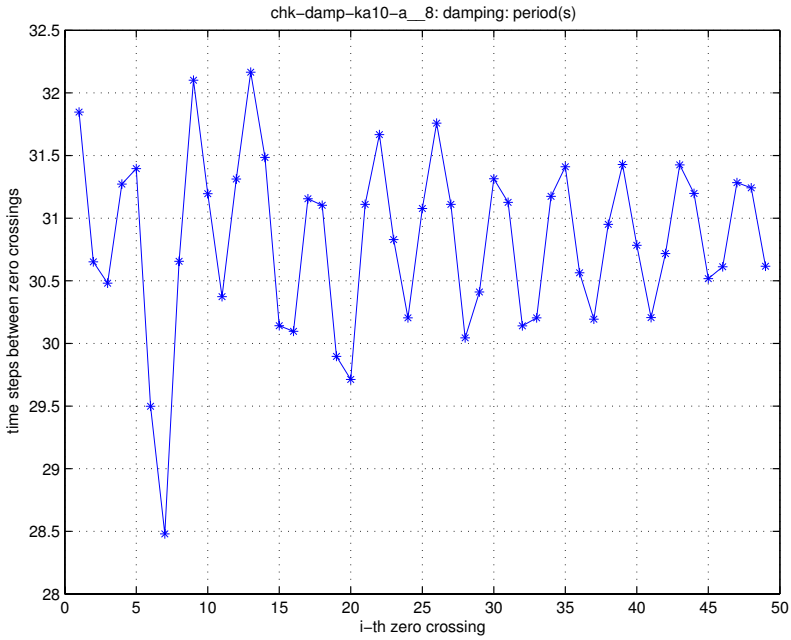

(a) Sphere with a radius of 8 m.

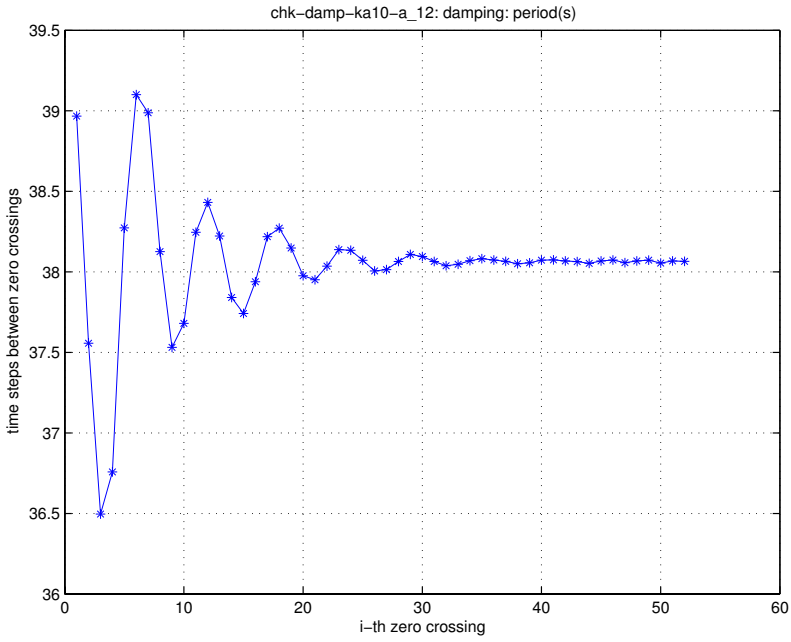

(b) Sphere with a radius of 12 m.

Figure 4.5: Determination of frequency: time in timesteps between zerocrossings plotted as function of the period number.

4.2.3 Comparison with linear diffraction theory, including second order drift effects

Now that we have tested the setup of the absorbing boundary conditions, the complete setup for doing diffraction calculations with a floating sphere can be tested. For this we compare with linear diffraction results from the thesis of Pinkster. We have a look at all the relevant RAO's (Response Amplitude Operator): for surge and for heave, both the amplitude and the phase. Pinkster also computed the low-frequency part of the horizontal drift force, which only depends on the first order quantities.

For this comparison we need to do calculations for a range of frequencies. This causes problems because of our limited resolution and domain size. The relevant range of wave numbers goes from $ka = 0.4$ up till $ka = 1.5$, where a is the radius of the cylinder and k the wave number of the incoming wave. The $ka = 0.4$ case corresponds to the wave cylinder combination of the ISSC study. By allowing for less panels per wavelength on the outer boundary, 10 instead of 25, we can get to about $ka = 1.0$. By taking a larger sphere of 12 m instead of 8 m, values of $ka = 1.0$ up till $ka = 1.5$ become possible. This at the cost of effectively reducing the domain size and thus putting a smaller beach closer to the sphere. The $ka = 1.0$ case is calculated for both the two radii of the sphere to assess the inaccuracies involved. To get an idea of the possible nonlinearities up to four different wave heights have been calculated for some wave numbers. See table 4.1. The smallest wave height of $H = 0.25$ m has a steepness H/λ of 0.003 for $ka = 1.0$ and $a = 12$ m.

To quantify the effect of the lack of resolution we have included calculations for an open fixed sphere with an incoming Rienecker & Fenton wave for each frequency. The results are presented in figures 4.29 till 4.38. For each figure there are three subfigures. The first one shows the maximum deviation from the prescribed incoming wave after three periods. The second one shows a snapshot of the deviation from the incoming wave at $t/T = 3.25$. The third subfigure gives the maximum deviation from the incoming wave as a function of time for the whole free surface, for the part near the sphere, and for the rest of the free surface. The format of these figures is similar to the ones presented in chapter 3. These figures clearly show that the low resolution at higher frequencies is a problem, but the maximum error near the sphere remains less than around 3.5 percent except for $ka = 1.5$ where it is 4.5 percent.

The drift force on the sphere is determined in two different ways. In the first method we determine the equilibrium position of the mooring system from the time series of the horizontal coordinate of the centre of mass. This can be done in a reasonable number of periods, because we added some damping to the mooring system. In the second method we calculate the average of the horizontal force. Both give approximately the same answer, except for the calculation at $ka = 1.5$.

The results for the RAO's and for the horizontal drift are presented in figures 4.6 up till 4.9(a) and in tables 4.1 and 4.2. Most results are as close to the linear solution as can be expected from the quality of the incoming waves and it is nice to see the convergence towards the/a linear solution with decreasing wave heights. The heave amplitude and the mean horizontal drift force show differences however. At heave resonance the heave amplitude is significantly larger for the big sphere. For the small sphere the deviation from the linear results is 2.5 percent, which is acceptable given the error in the representation of the incoming wave near the sphere of around 3

percent. For the big sphere four different wave heights were calculated: 0.25 m, 0.50 m, 1.00 m, and 2.00 m; at a wavelength of about 75 m. The smallest two wave heights give a heave amplitude that is 9 percent larger than the linear result. The larger wave heights deviate more and more, here the nonlinearities begin to have their effect. The higher resonance amplitude found for the big sphere is compatible with the low damping found for that sphere. But if that is true then the relevant part of figure 4.3(a) for the small sphere is the line through the first five or six points. This line gives similar results for all three damping calculations for the 8 m sphere. The points further on represent very small amplitudes and are therefore very sensitive to reflections even when those reflections are not large enough to destroy the monotonic decay. There are also large deviations for $ka = 1.2$ (-8%) and $ka = 1.4$ (+8%).

The other exceptions are in the drift results, presented in figure 4.9(a). The stars represent the results from the HYPAN calculations obtained from the equilibrium position of the mooring system and the open squares are the results from the HYPAN calculations obtained from the average horizontal force on the sphere. They do not give the same results everywhere, at $ka = 1.5$ the difference is even 8 percent. The reason for this is unclear, but the determination of the equilibrium position is a bit difficult and indirect. The deviations from the linear results, represented by the line, follow from table 4.1. Most deviations are between -15% and -20%. The difference between the small and the big sphere at $ka = 1.0$ is 10%, with the 12 m sphere closer to the linear result, but the deviation for the 8 m sphere is consistent with the deviations for higher ka.

Let us investigate the above differences. At $ka = 1.1$, where the horizontal drift force reaches a maximum, changing the wave height has hardly any influence on the result (normalised with the amplitude squared). Furthermore, the representation of the incoming wave is still quite good at $ka = 1.1$: near the cylinder the deviation with the incoming wave is less than about 2 percent. When we put the damping in the mooring system to 0, it had no significant effect. In the following we will have a closer look to the contributions that make up the "linear" drift.

This horizontal drift is a combination of 4 terms, see figure 4.10(a): the largest contribution comes from the relative wave height and is easy to calculate given the relative wave height amplitude on the waterline, see equation A.19. The second contribution is an integration of the velocity squared term over the mean wetted surface, see equation A.20. It has the opposite sign of the first contribution. The third contribution involves a product of the first order motions and a pressure gradient. The sign depends on the phase angles of both quantities. In this case it will be directed into the waves. The fourth contribution depends on the angular motions and is 0 in our case. Figure 4.10(a) shows both the components as presented by Pinkster in his thesis and the components as calculated by the current version of the linear diffraction program DIFFRAC from MARIN.[2] The second component of Pinkster deviates from the second component of DIFFRAC. The contributions of Pinkster do not add up to his total given, but that total is equal to that of DIFFRAC. Pinkster did compare his total to exact second order analytical results, but had no analytical expressions available for the components seperately, so the drawing error went unnoticed.

Figure 4.9(b) shows several versions of the first contribution to the horizontal drift. The line is the line given by Pinkster in his thesis and the open squares are the points

[2]Pinkster used the then current version of the same program.

carrying that line in his thesis. The crosses are calculated from the relative wave amplitudes obtained by DIFFRAC. The circles are calculated from the relative wave amplitudes obtained by HYPAN. For $ka = 0.8$ and $ka = 0.9$ the difference is again around 20 percent, as was the case for the total drift, but the sign is now opposite for $ka = 0.8$. These are very small drifts where the accuracy could be a problem. At $ka = 1.0$ the results have kind of shifted compared to the total drift: the small sphere now has a deviation of -7 percent instead of -17 percent, and the big sphere now has a deviation of +7 percent instead of -8 percent. From $ka = 1.1$ onwards the deviations are four percent or less, which is compatible with the wave accuracy. Because the other two contributions are subtracted from the first contribution the relative errors will be magnified. At maximum drift this means that a relative error of four percent in the first contribution results in a relative error of 9 percent in the total drift. If the other contributions would have a similar relative error and if those errors would not cancel, we could get at a total relative error in the total drift that would approach the 20 percent. This is not a very likely scenario however. And besides, for the first contribution the deviations are both positive and negative, whereas for the total drift the deviations are all negative for ka higher than 0.8.

In HYPAN the total hydrodynamic force `ft` on the sphere is build up from the following components: a linear term `fl` coming from $\rho\phi_t$, the dynamic contribution `fd` coming from $\frac{1}{2}\rho(\nabla\phi)^2$, and the hydrostatic contribution `fs` coming from ρgz. Because the hydrostatic contribution is already very large in equilibrium, it is better for the accuracy to separate it in a contribution `fs` without the equilibrium value for ρgz and a contribution `fpb` that corrects for the equilibrium values that were corrected too much above the equilibrium waterline and that were not enough corrected for below the equilibrium waterline, see the thesis of Berkvens [2]. In table 4.2 the amplitude and the average are given for all these contributions. Table 4.3 gives an indication of the accuracy of those values by giving their standard deviation. In figure 4.10(b) the second component of the drift is plotted. The agreement between the results from HYPAN (the average of `fd`) and from DIFFRAC is very good. The third (and first) components cannot be calculated so easily from these HYPAN force components.

Finally, we have a more detailed look at the difference of the HYPAN solution with the linear solution of the current problems, because the basic ingredients in all the linear drift components are the solution on and the motion of the sphere. If two potential methods calculate approximately the same wave elevation on the sphere for a number of periods, then the rest of their solutions will also be approximately the same[3]. Therefore the wave elevation on the waterline as function of time together with the motions of the sphere itself provide a complete summary of the solution. It was clear from animations of the whole waterline as a function of time that the only major differences between the HYPAN calculations and the linear diffraction calculations were an overall factor for the amplitudes and an overall phase difference. To quantify the differences between the two calculations it was therefore sufficient to have a look at the time series of the wave elevation at the front and at the back of the sphere together with the time series of the motion of the sphere. In figures 4.11 up till 4.28 these time series are plotted for one period, the upper subfigure gives the absolute wave elevation together with the motion of the centre of mass of the sphere, the lower subfigure gives the relative wave elevation together with the position of the

[3]Think of the e^{-kz} dependence of linear waves.

mean free surface level. The solid lines are the HYPAN calculations and the dashed lines are the linear diffraction results from DIFFRAC. Looking at these figures we come to the following conclusions.

There are no obvious higher frequency components. For the low frequencies the results are very nice, for the higher frequencies there are significant differences, see the RAO's. The phase differences with the linear calculations are quite large, but the relative phase differences between the components is smaller. The deviations of several percent in the RAO's are understandable considering the representation of the incoming wave and the limited beach. The relative wave motions on the sphere are close enough to the linear values to calculate the first linear drift component within 10% of the linear result. But that is of course not how the mean drift force is calculated in HYPAN. The correspondence between the second linear component of the drift force and the average of the $\frac{1}{2}\rho(\nabla\phi)^2$ contribution to the total hydrodynamic force is very good. A direct calculation of the first and the third linear drift components from the hydrodynamic force contributions in HYPAN is difficult, but could be worthwhile if possible.

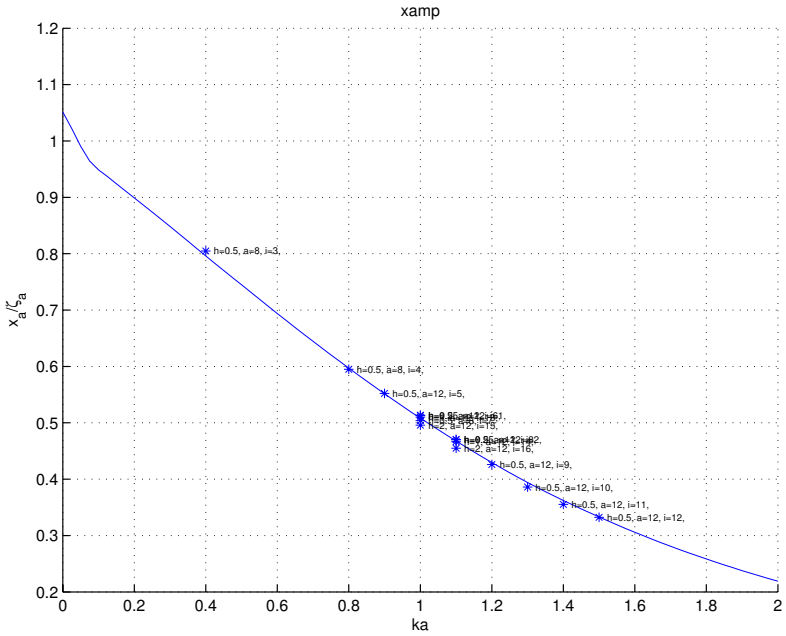

(a) Amplitude

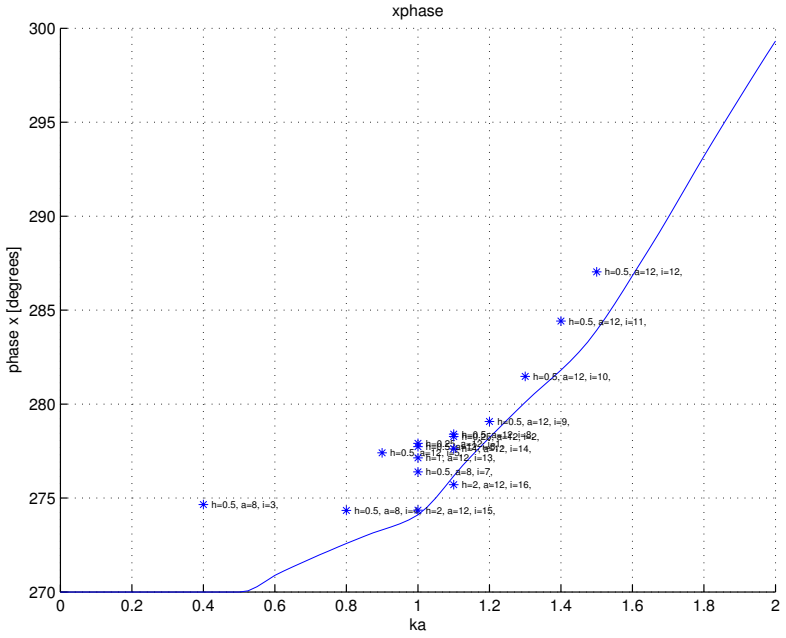

(b) Phase

Figure 4.6: RAO for surge motion.

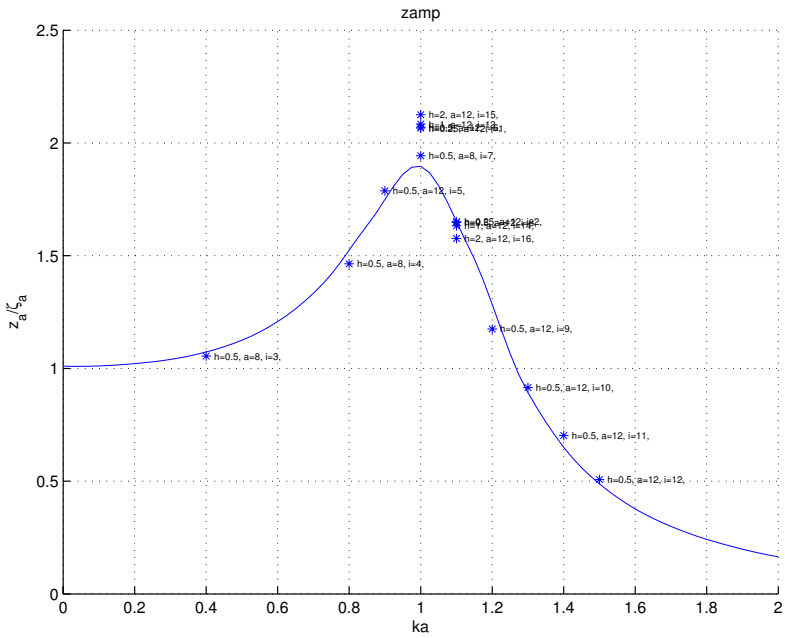

(a) Amplitude

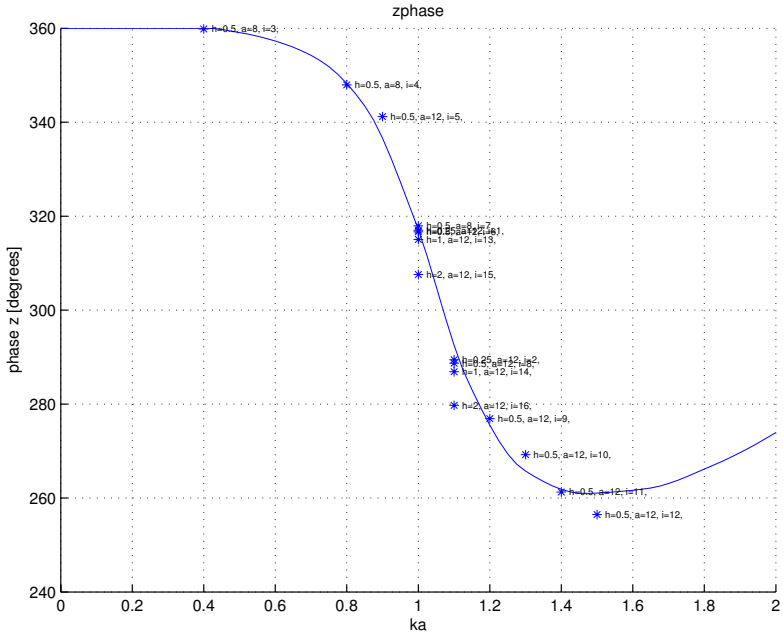

(b) Phase

Figure 4.7: RAO for heave motion

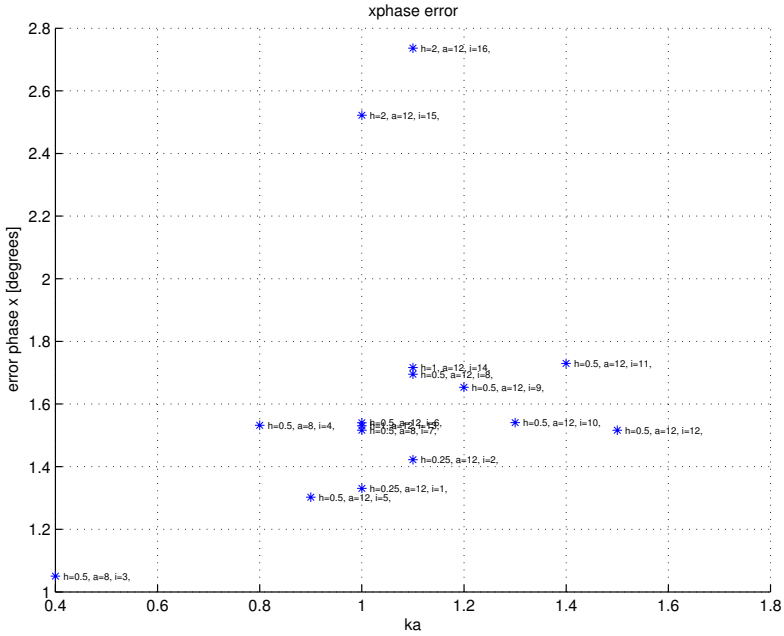

(a) Surge motion.

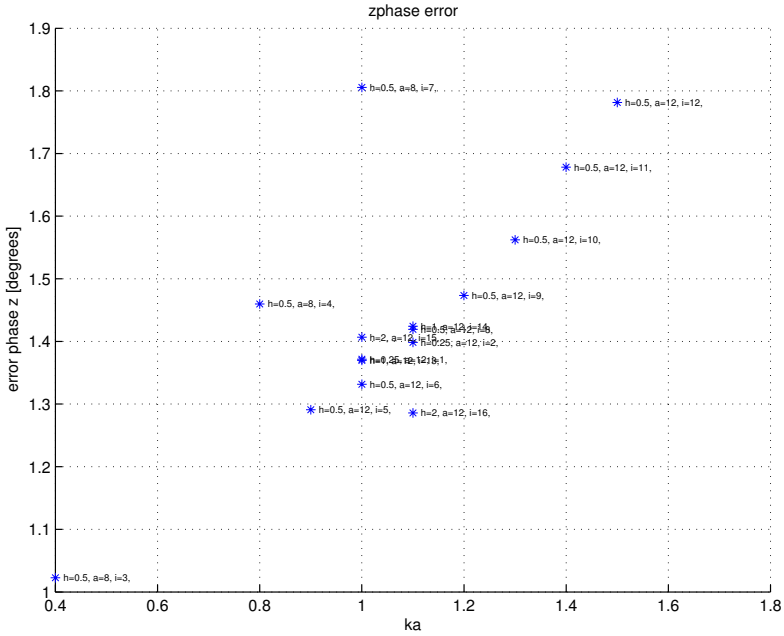

(b) Heave motion.

Figure 4.8: Error in the phase part of the RAO, in degrees.

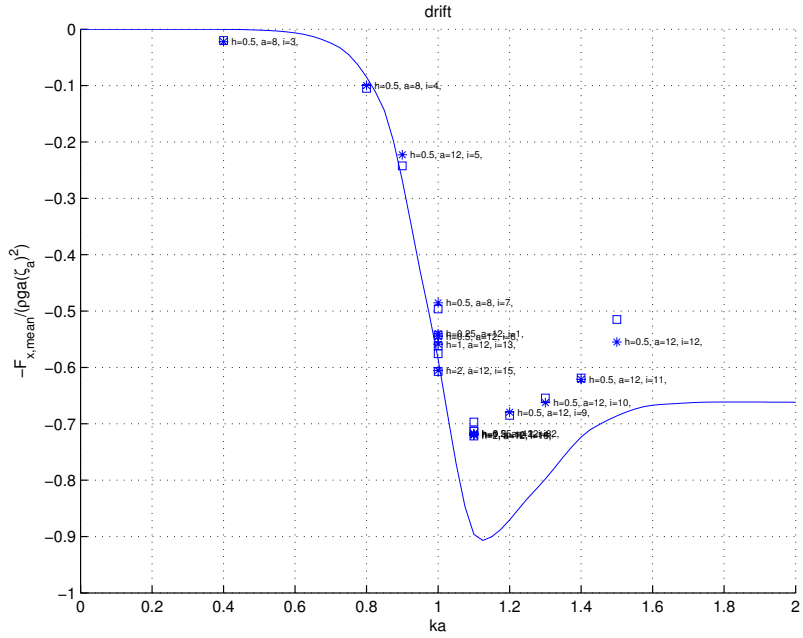

(a) The total drift.

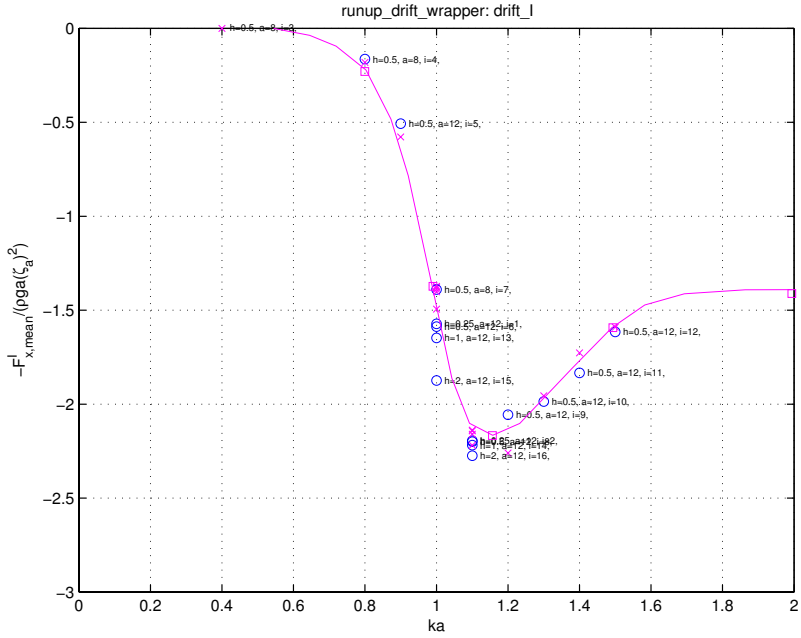

(b) Component I in the thesis of Pinkster. The term depending on the relative wave motions.

Figure 4.9: The drift in the horizontal direction.

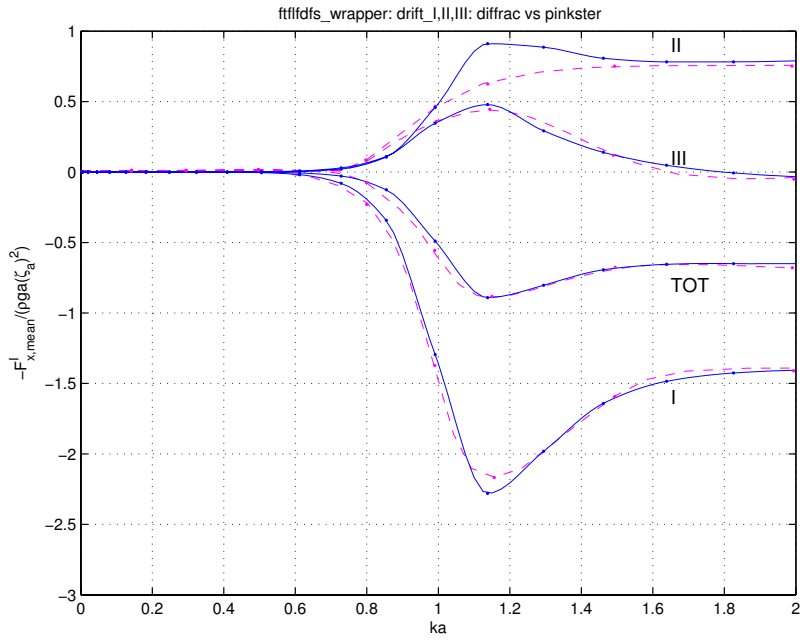

(a) The total drift and all components for Pinkster and DIFFRAC.

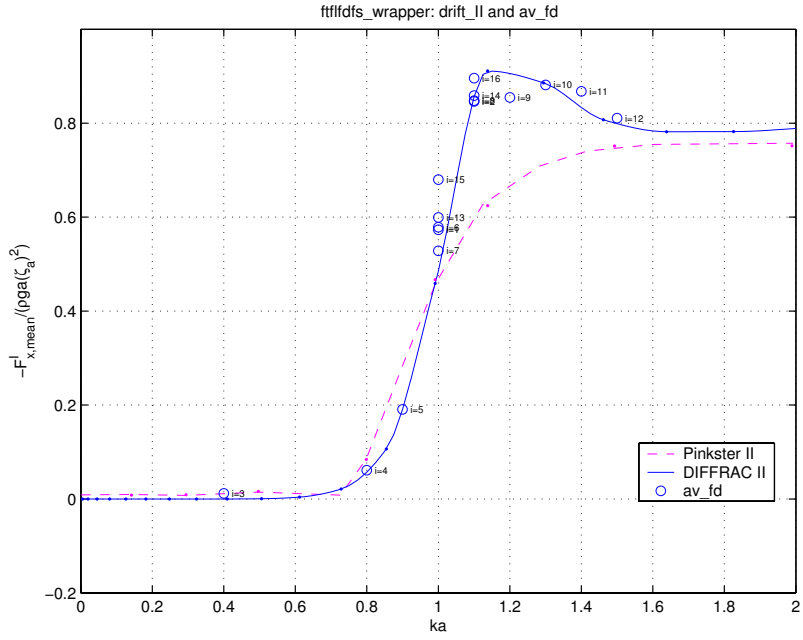

(b) Component II in the thesis of Pinkster and of DIFFRAC. The term depending on the velocities squared.

Figure 4.10: The drift in the horizontal direction.

i	ka	h	a	drift	drift_ft	xamp	zamp	xphase	zphase	drift_I
1	1.0	0.25	12	-7.7 %	-1.7 %	1.1 %	8.9 %	1.4 %	-0.1 %	5.7 %
2	1.1	0.25	12	-19.9 %	-20.5 %	0.6 %	-0.1 %	0.8 %	-1.0 %	3.5 %
3	0.4	0.50	8	8112.7 %	7247.6 %	1.1 %	-1.7 %	1.7 %	-0.0 %	-79.5 %
4	0.8	0.50	8	17.5 %	23.7 %	-0.4 %	-3.9 %	0.6 %	-0.1 %	-23.9 %
5	0.9	0.50	12	-16.9 %	-9.6 %	0.1 %	2.2 %	1.5 %	1.4 %	-20.5 %
6	1.0	0.50	12	-7.0 %	-7.3 %	0.9 %	9.1 %	1.3 %	-0.2 %	6.7 %
7	1.0	0.50	8	-17.1 %	-15.3 %	-0.9 %	2.5 %	0.8 %	0.2 %	-6.6 %
8	1.1	0.50	12	-19.9 %	-22.2 %	0.5 %	-0.3 %	0.8 %	-1.3 %	3.7 %
9	1.2	0.50	12	-22.0 %	-21.3 %	-0.8 %	-8.5 %	0.3 %	0.5 %	-4.0 %
10	1.3	0.50	12	-17.0 %	-18.0 %	-2.1 %	2.5 %	0.5 %	1.3 %	0.2 %
11	1.4	0.50	12	-14.1 %	-14.5 %	-2.0 %	8.0 %	0.9 %	-0.2 %	3.9 %
12	1.5	0.50	12	-19.1 %	-24.9 %	-0.2 %	3.9 %	1.1 %	-1.8 %	2.4 %
13	1.0	1.00	12	-4.6 %	-4.1 %	0.3 %	9.9 %	1.1 %	-0.7 %	10.7 %
14	1.1	1.00	12	-19.7 %	-19.5 %	-0.2 %	-1.2 %	0.5 %	-1.9 %	4.6 %
15	1.0	2.00	12	3.4 %	3.7 %	-2.5 %	12.0 %	0.1 %	-3.0 %	26.0 %
16	1.1	2.00	12	-19.7 %	-20.4 %	-2.7 %	-4.6 %	-0.2 %	-4.4 %	7.3 %

Table 4.1: The differences between the DIFFRAC calculations and the results obtained with HYPAN, given in percentages. ka is the wave number times the radius of the sphere, h is the wave height in metres, and a is the radius of the sphere in metres. Drift is the drift obtained from the equilibrium position of the mooring system, drift_ft the drift obtained from the average total force, and drift_I is the relative wave height component of the drift force. xamp, zamp, xphase, and zphase are the (normalised) amplitudes and phases of the surge and heave motions respectively.

i	ka	h	a	amp_ft	amp_fl	amp_fd	amp_fs	amp_fpb	av_ft	av_fl	av_fd	av_fs	av_fpb
1	1.0	0.25	12	102.33	102.40	0.96	2.55	2.27	0.58	0.77	-0.57	1.84	-1.52
2	1.1	0.25	12	103.21	103.25	0.99	2.13	2.29	0.71	1.63	-0.85	2.06	-2.13
3	0.4	0.50	8	21.24	21.27	0.04	0.63	0.09	0.02	0.05	-0.01	-0.02	0.00
4	0.8	0.50	8	31.67	31.76	0.39	1.56	0.91	0.11	-0.01	-0.06	0.33	-0.16
5	0.9	0.50	12	49.45	49.54	0.64	2.06	1.51	0.24	0.17	-0.19	0.75	-0.49
6	1.0	0.50	12	51.12	51.26	0.96	2.56	2.28	0.57	0.80	-0.58	1.86	-1.54
7	1.0	0.50	8	33.60	33.79	0.92	2.32	2.09	0.53	0.75	-0.53	1.68	-1.40
8	1.1	0.50	12	51.57	51.64	0.99	2.13	2.29	0.70	1.62	-0.85	2.06	-2.14
9	1.2	0.50	12	51.05	51.10	0.91	1.55	2.03	0.68	1.99	-0.85	1.56	-2.00
10	1.3	0.50	12	50.17	50.21	0.88	1.23	1.92	0.65	2.25	-0.88	1.22	-1.94
11	1.4	0.50	12	49.74	49.78	0.81	0.97	1.76	0.62	2.36	-0.87	0.92	-1.79
12	1.5	0.50	12	49.89	49.95	0.72	0.73	1.53	0.51	2.25	-0.81	0.65	-1.58
13	1.0	1.00	12	25.47	25.75	0.98	2.57	2.32	0.58	0.86	-0.60	1.90	-1.60
14	1.1	1.00	12	25.72	25.86	0.99	2.10	2.30	0.72	1.69	-0.86	2.05	-2.16
15	1.0	2.00	12	12.49	13.05	1.03	2.60	2.46	0.62	1.05	-0.68	2.08	-1.84
16	1.1	2.00	12	12.77	13.01	1.01	2.02	2.31	0.73	1.84	-0.90	2.01	-2.23

Table 4.2: The amplitude and the average of all components of the hydrodynamic force as calculated by HYPAN. The normalisation is the same as in the drift figures: divided by $\rho g a (H/2)^2$.

i	ka	h	a	amp_ft_sd	amp_fl_sd	amp_fd_sd	amp_fs_sd	amp_fpb_sd	av_ft_sd	av_fl_sd	av_fd_sd	av_fs_sd	av_fpb_sd
1	1.0	0.25	12	0.02	0.03	0.01	0.00	0.00	0.01	0.00	0.00	0.00	0.00
2	1.1	0.25	12	0.01	0.02	0.02	0.00	0.01	0.00	0.00	0.00	0.00	0.00
3	0.4	0.50	8	0.00	0.01	0.00	0.00	0.00	0.00	0.00	0.00	0.00	0.00
4	0.8	0.50	8	0.01	0.01	0.01	0.01	0.00	0.00	0.00	0.00	0.00	0.00
5	0.9	0.50	12	0.00	0.01	0.01	0.01	0.00	0.01	0.00	0.00	0.00	0.00
6	1.0	0.50	12	0.01	0.01	0.03	0.01	0.01	0.01	0.00	0.00	0.00	0.00
7	1.0	0.50	8	0.01	0.01	0.04	0.01	0.01	0.01	0.00	0.00	0.00	0.00
8	1.1	0.50	12	0.01	0.01	0.03	0.01	0.01	0.00	0.00	0.00	0.00	0.00
9	1.2	0.50	12	0.01	0.01	0.03	0.02	0.02	0.00	0.00	0.00	0.00	0.00
10	1.3	0.50	12	0.01	0.01	0.03	0.02	0.03	0.00	0.00	0.00	0.00	0.00
11	1.4	0.50	12	0.01	0.01	0.03	0.02	0.03	0.00	0.00	0.00	0.00	0.00
12	1.5	0.50	12	0.01	0.01	0.02	0.02	0.04	0.00	0.00	0.00	0.00	0.00
13	1.0	1.00	12	0.00	0.01	0.06	0.01	0.02	0.01	0.00	0.00	0.00	0.00
14	1.1	1.00	12	0.00	0.00	0.06	0.02	0.02	0.00	0.00	0.00	0.00	0.00
15	1.0	2.00	12	0.00	0.00	0.13	0.01	0.08	0.01	0.00	0.00	0.00	0.00
16	1.1	2.00	12	0.00	0.00	0.13	0.05	0.08	0.00	0.00	0.00	0.00	0.00

Table 4.3: The standard deviation in the amplitude and the average of all components of the hydrodynamic force as calculated by HYPAN. The normalisation is the same as in the drift figures: divided by $\rho g a (H/2)^2$.

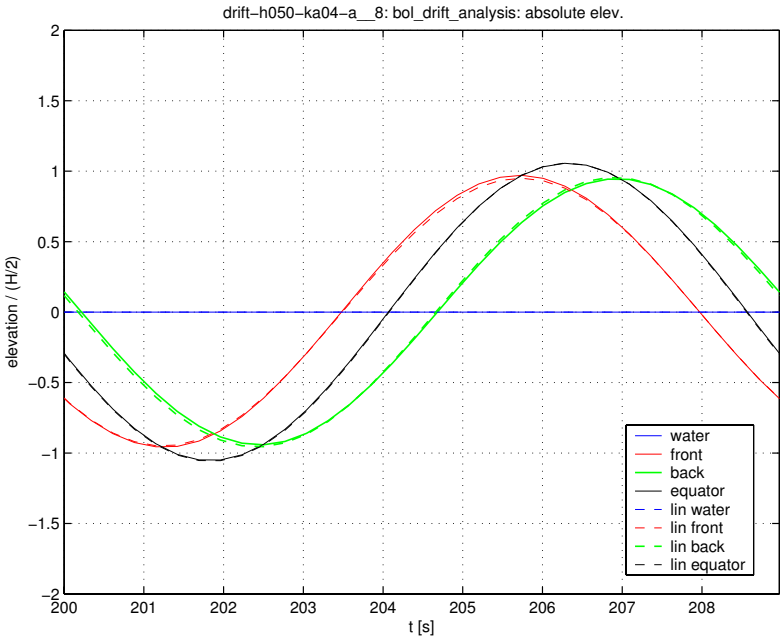

(a) Absolute wave elevations.

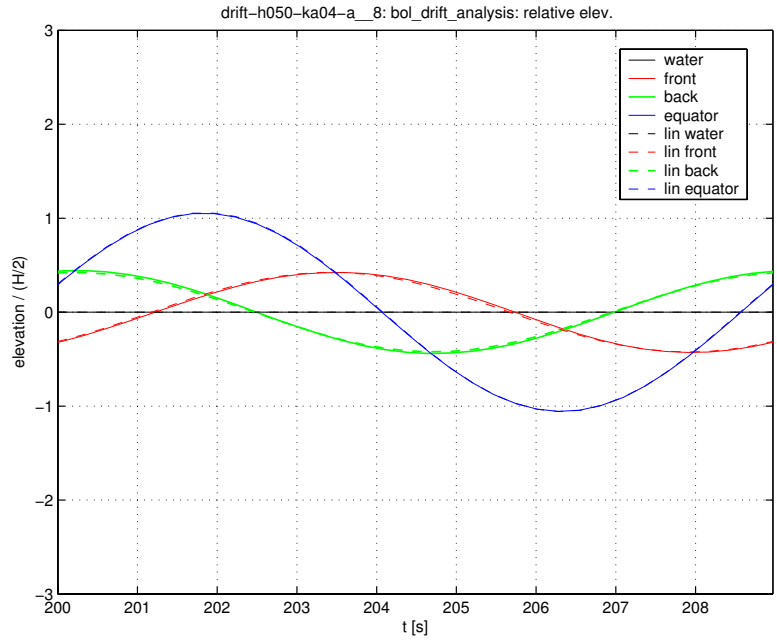

(b) Relative wave elevations.

Figure 4.11: Wave height at waterline: at the front and at the back of the sphere, together with the vertical position of the centre and the mean water level. Both absolute and relative to the postion of the centre.

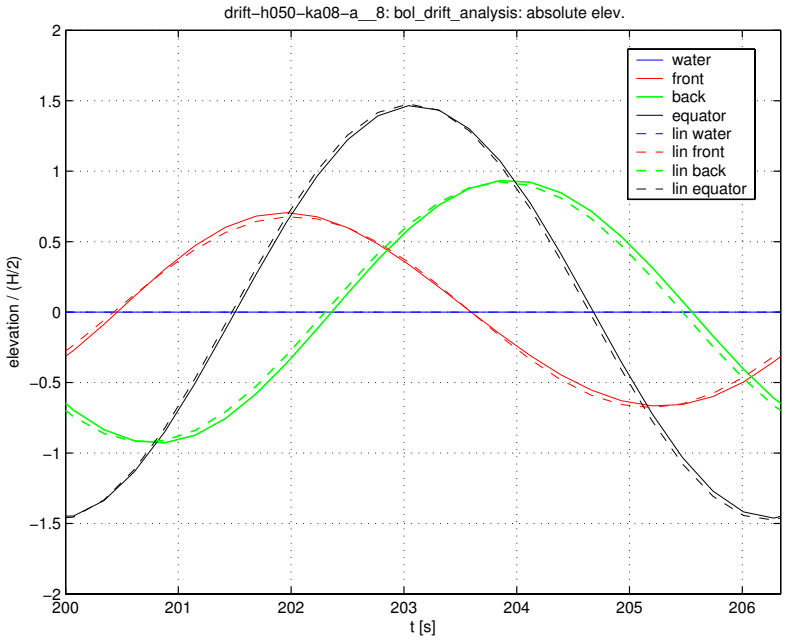

(a) Absolute wave elevations.

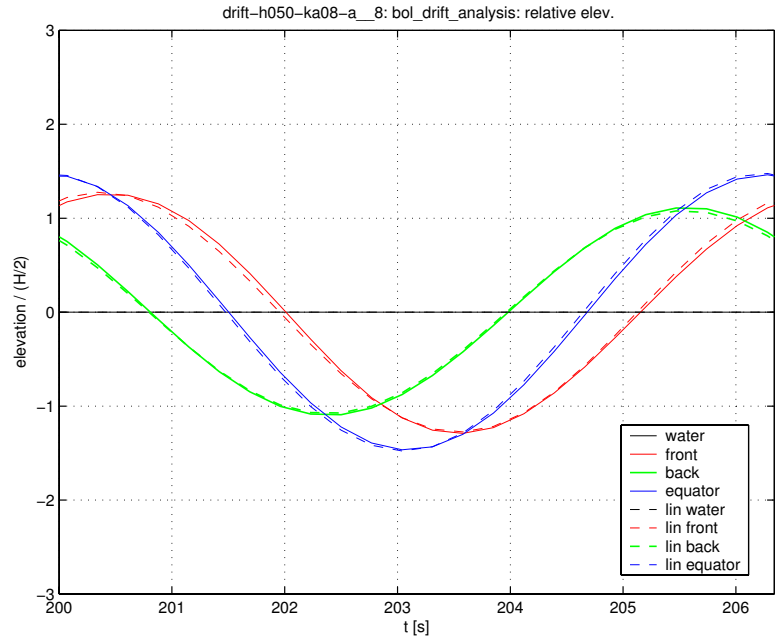

(b) Relative wave elevations.

Figure 4.12: Wave height at waterline: at the front and at the back of the sphere, together with the vertical position of the centre and the mean water level. Both absolute and relative to the postion of the centre.

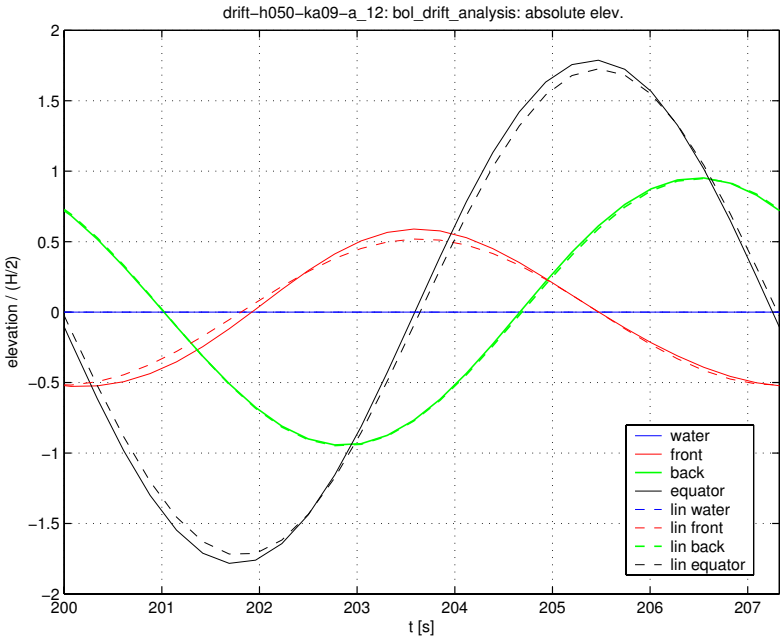

(a) Absolute wave elevations.

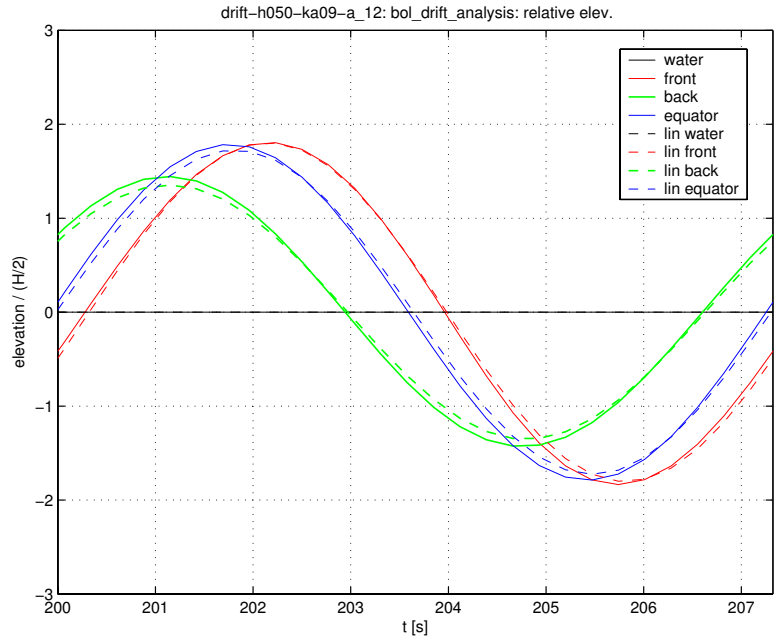

(b) Relative wave elevations.

Figure 4.13: Wave height at waterline: at the front and at the back of the sphere, together with the vertical position of the centre and the mean water level. Both absolute and relative to the postion of the centre.

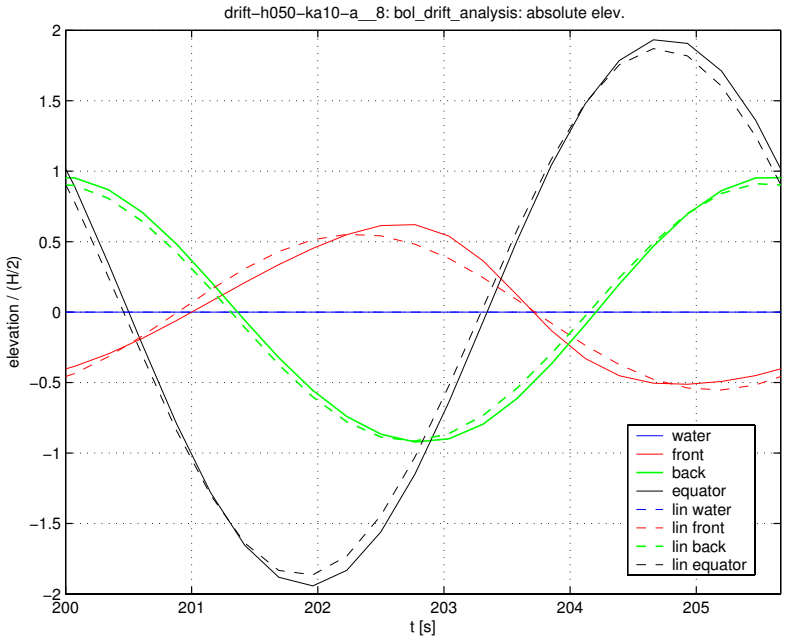

(a) Absolute wave elevations.

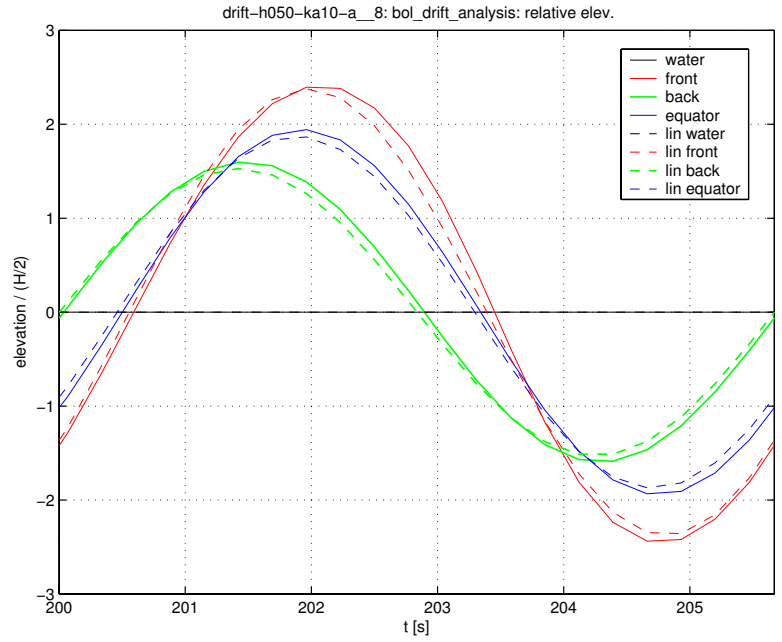

(b) Relative wave elevations.

Figure 4.14: Wave height at waterline: at the front and at the back of the sphere, together with the vertical position of the centre and the mean water level. Both absolute and relative to the postion of the centre.

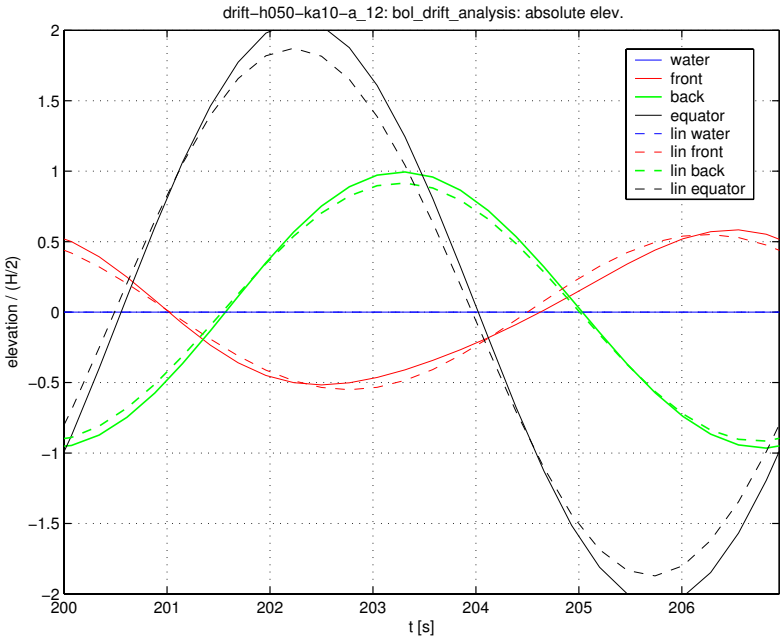

(a) Absolute wave elevations.

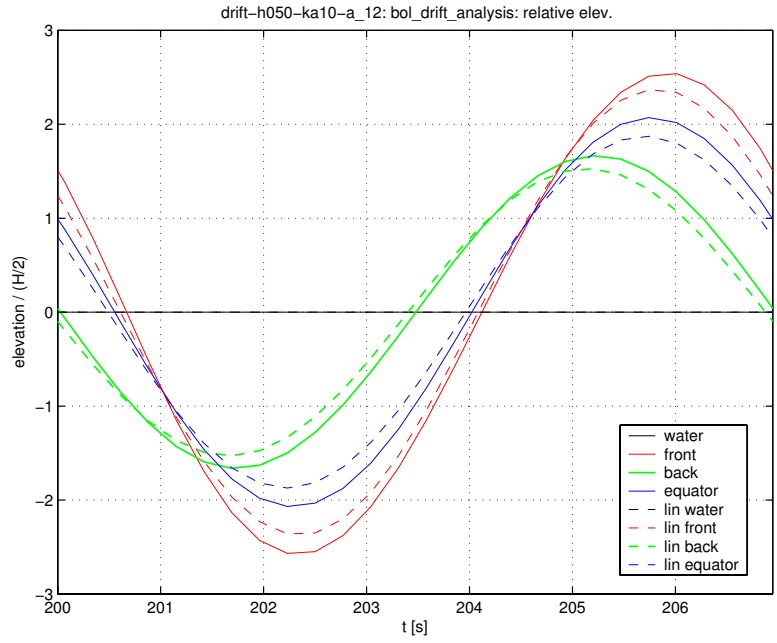

(b) Relative wave elevations.

Figure 4.15: Wave height at waterline: at the front and at the back of the sphere, together with the vertical position of the centre and the mean water level. Both absolute and relative to the postion of the centre.

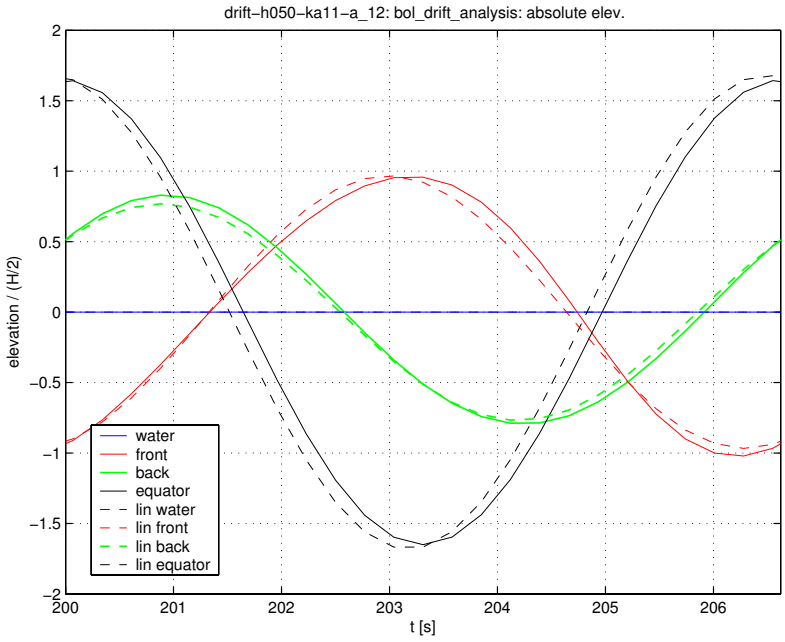

(a) Absolute wave elevations.

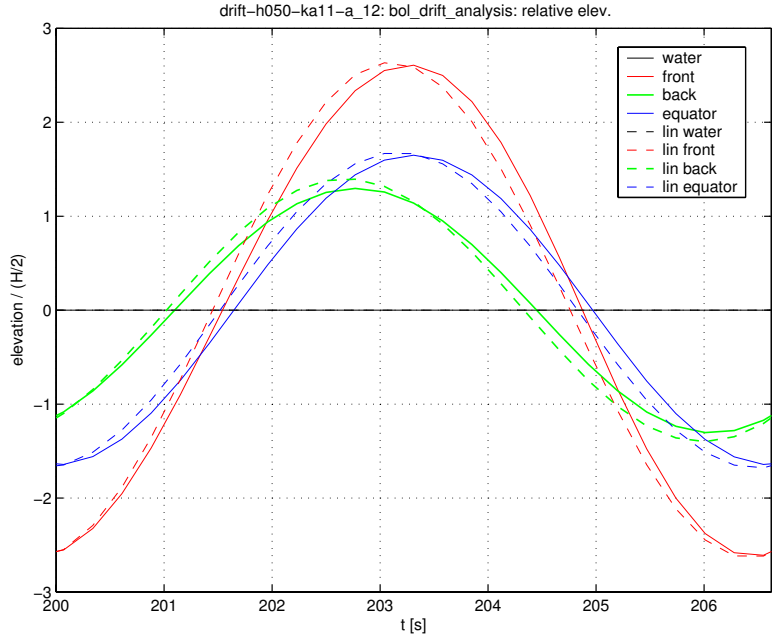

(b) Relative wave elevations.

Figure 4.16: Wave height at waterline: at the front and at the back of the sphere, together with the vertical position of the centre and the mean water level. Both absolute and relative to the postion of the centre.

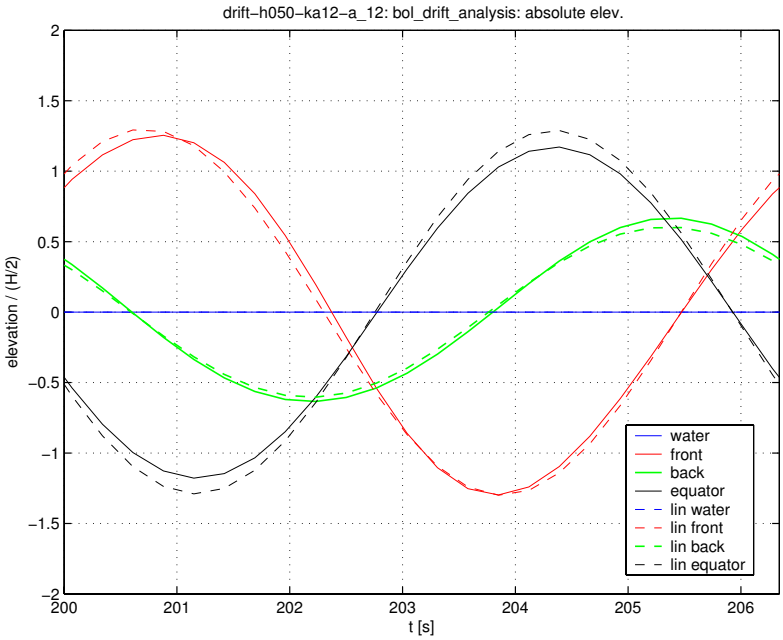

(a) Absolute wave elevations.

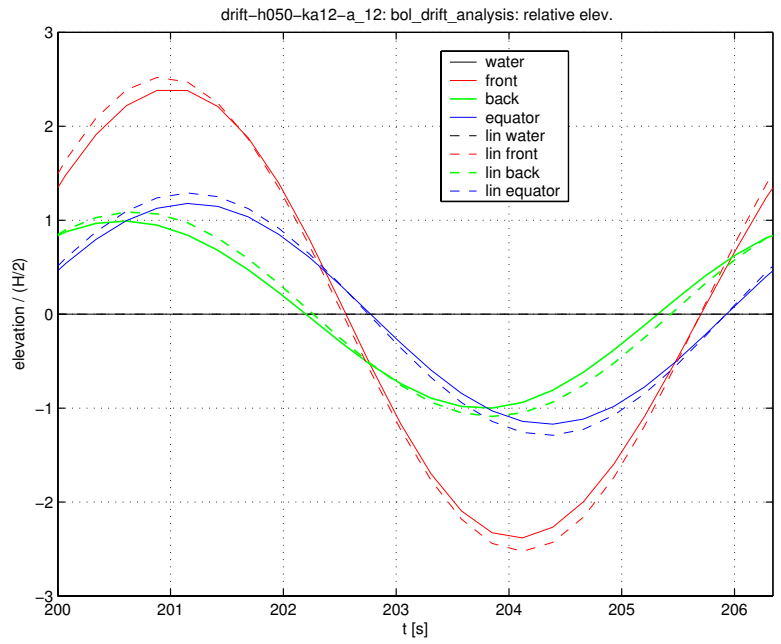

(b) Relative wave elevations.

Figure 4.17: Wave height at waterline: at the front and at the back of the sphere, together with the vertical position of the centre and the mean water level. Both absolute and relative to the postion of the centre.

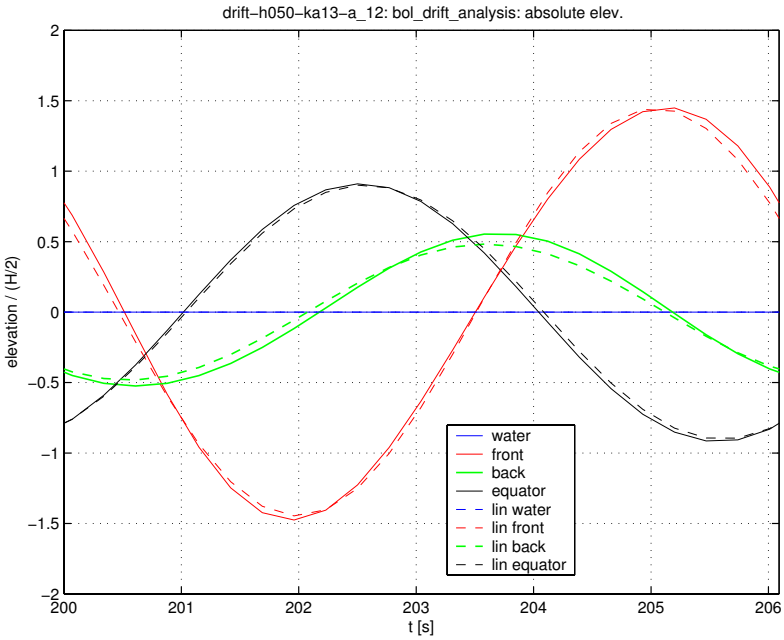

(a) Absolute wave elevations.

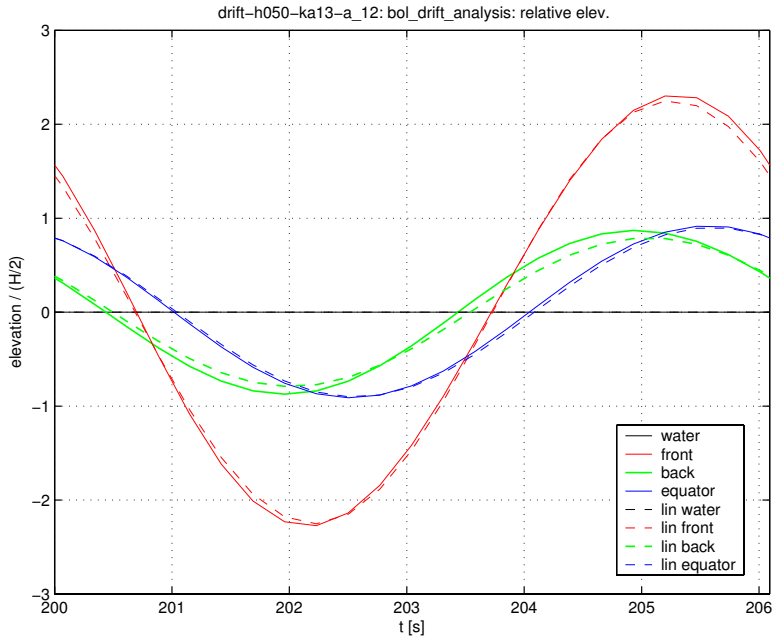

(b) Relative wave elevations.

Figure 4.18: Wave height at waterline: at the front and at the back of the sphere, together with the vertical position of the centre and the mean water level. Both absolute and relative to the postion of the centre.

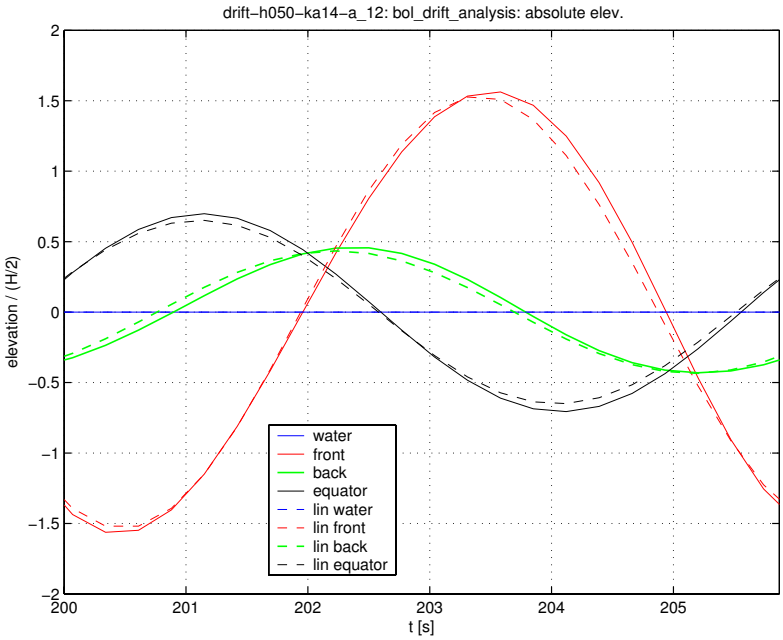

(a) Absolute wave elevations.

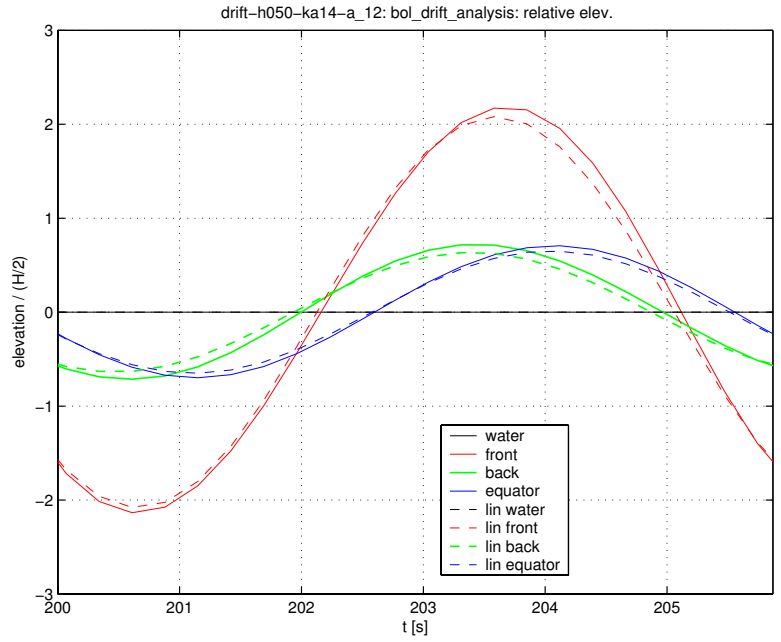

(b) Relative wave elevations.

Figure 4.19: Wave height at waterline: at the front and at the back of the sphere, together with the vertical position of the centre and the mean water level. Both absolute and relative to the postion of the centre.

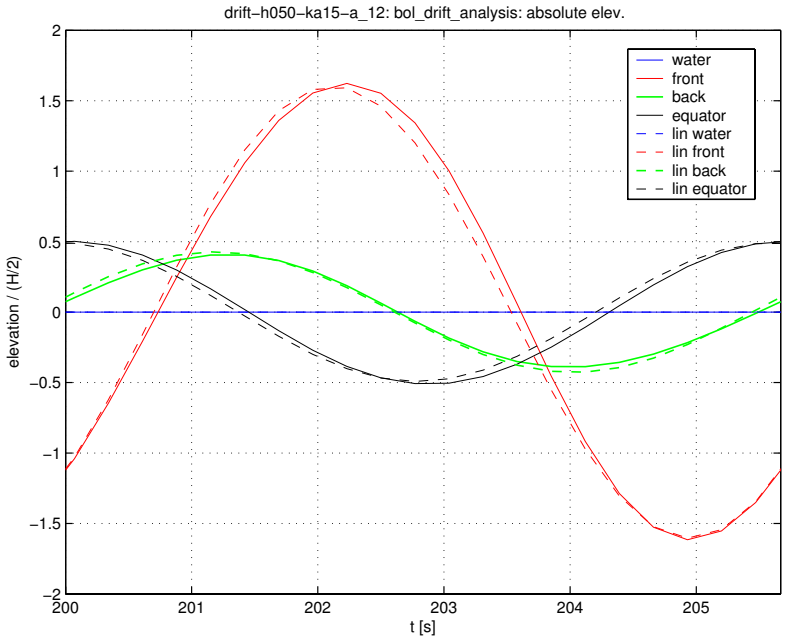

(a) Absolute wave elevations.

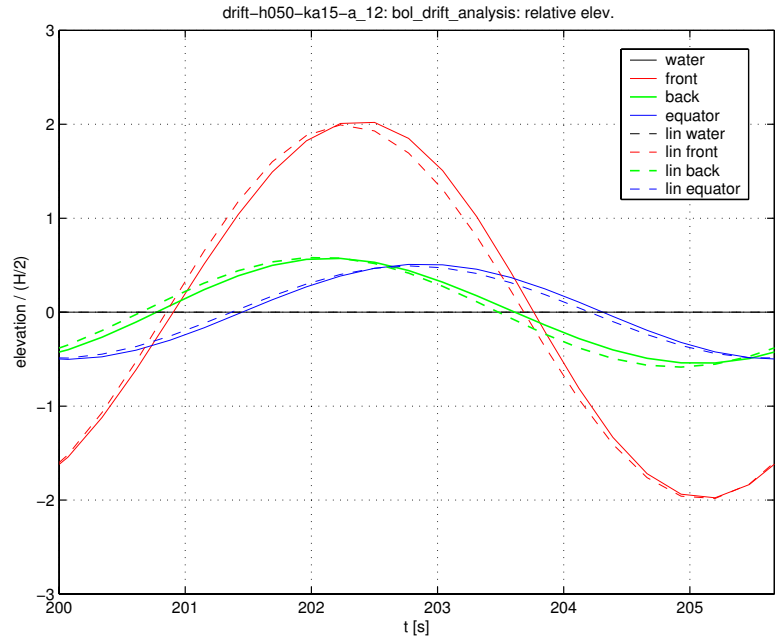

(b) Relative wave elevations.

Figure 4.20: Wave height at waterline: at the front and at the back of the sphere, together with the vertical position of the centre and the mean water level. Both absolute and relative to the postion of the centre.

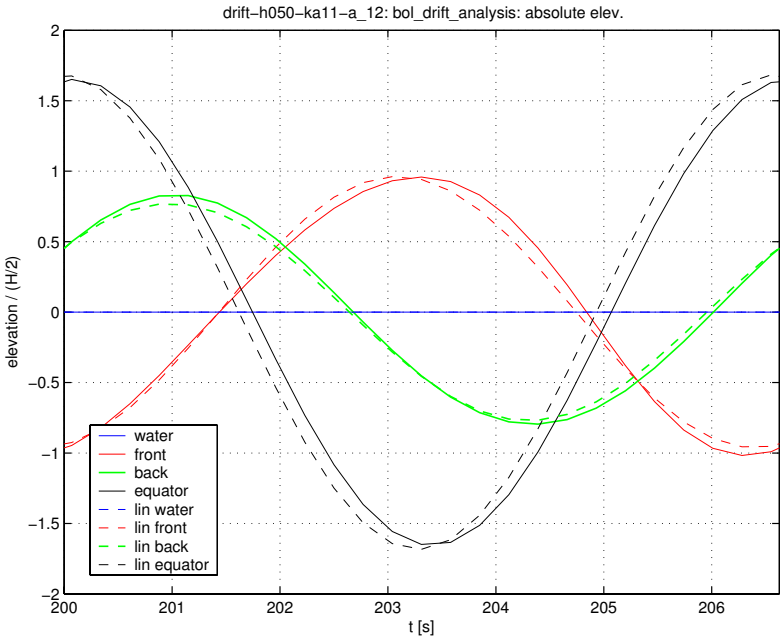

(a) Absolute wave elevations.

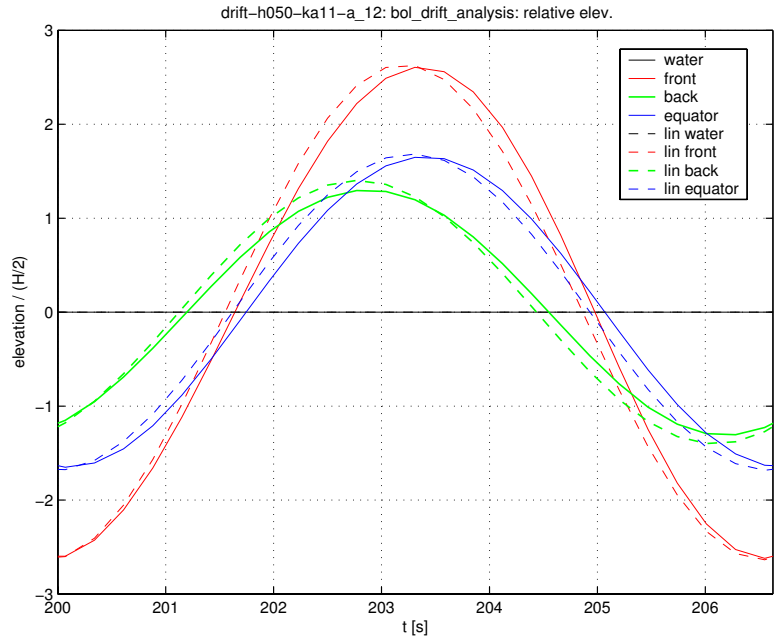

(b) Relative wave elevations.

Figure 4.21: Wave height at waterline: at the front and at the back of the sphere, together with the vertical position of the centre and the mean water level. Both absolute and relative to the postion of the centre. Drift-new-2: drift-h050-ka11-a_12.

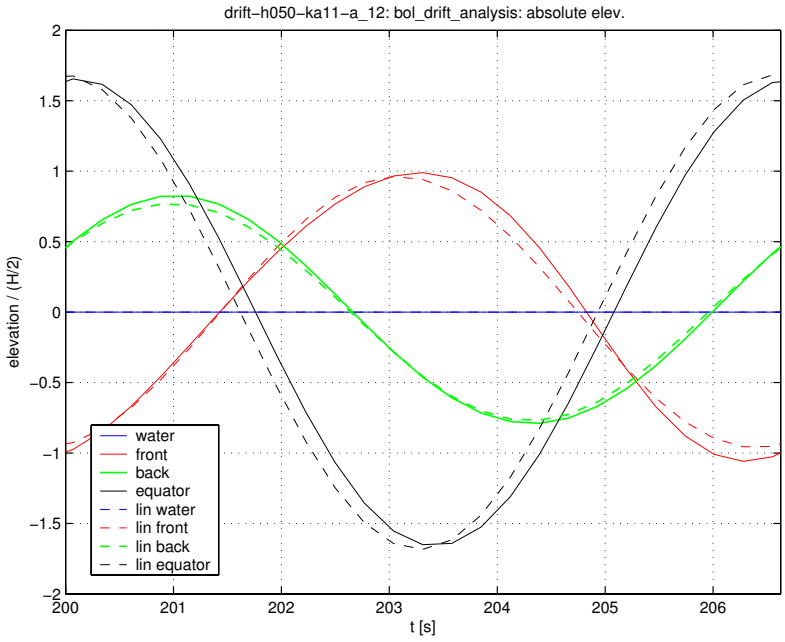

(a) Absolute wave elevations.

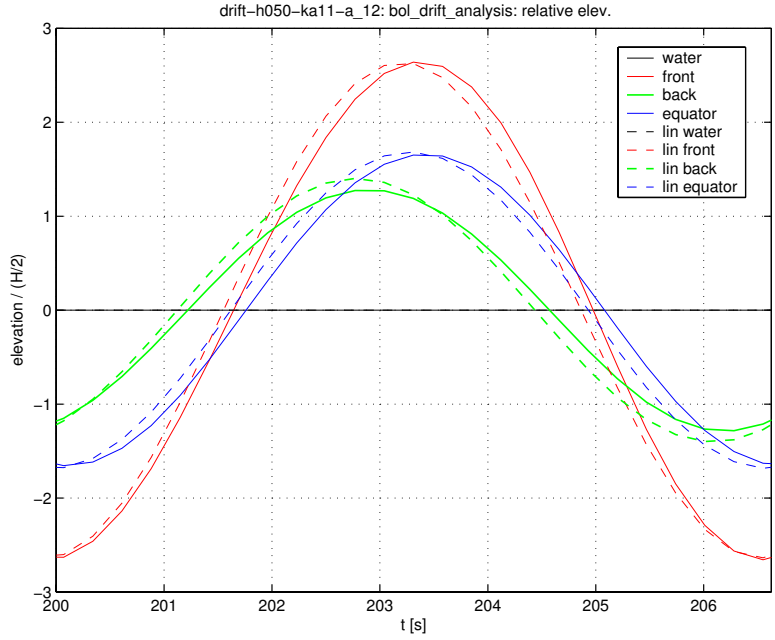

(b) Relative wave elevations.

Figure 4.22: Wave height at waterline: at the front and at the back of the sphere, together with the vertical position of the centre and the mean water level. Both absolute and relative to the postion of the centre. Drift-new-2-d0: drift-h050-ka11-a_12.

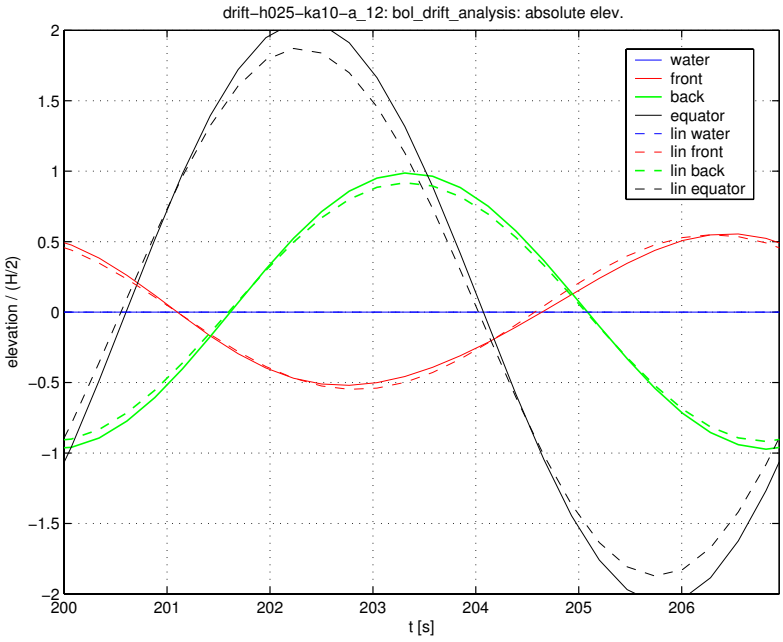

(a) Absolute wave elevations.

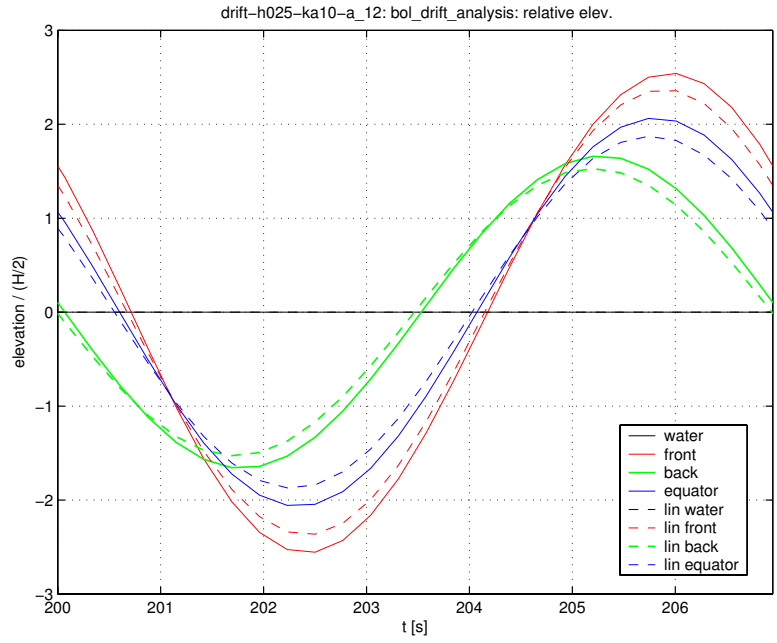

(b) Relative wave elevations.

Figure 4.23: Wave height at waterline: at the front and at the back of the sphere, together with the vertical position of the centre and the mean water level. Both absolute and relative to the postion of the centre.

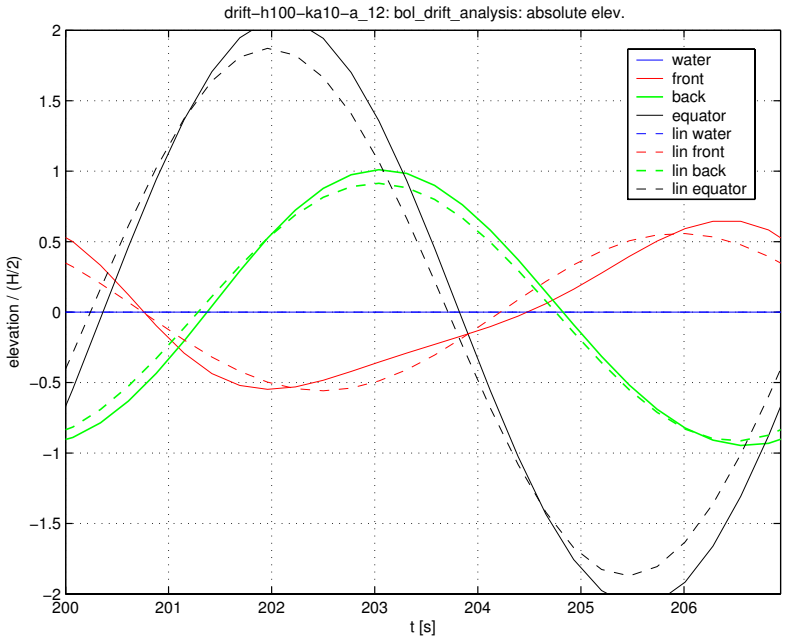

(a) Absolute wave elevations.

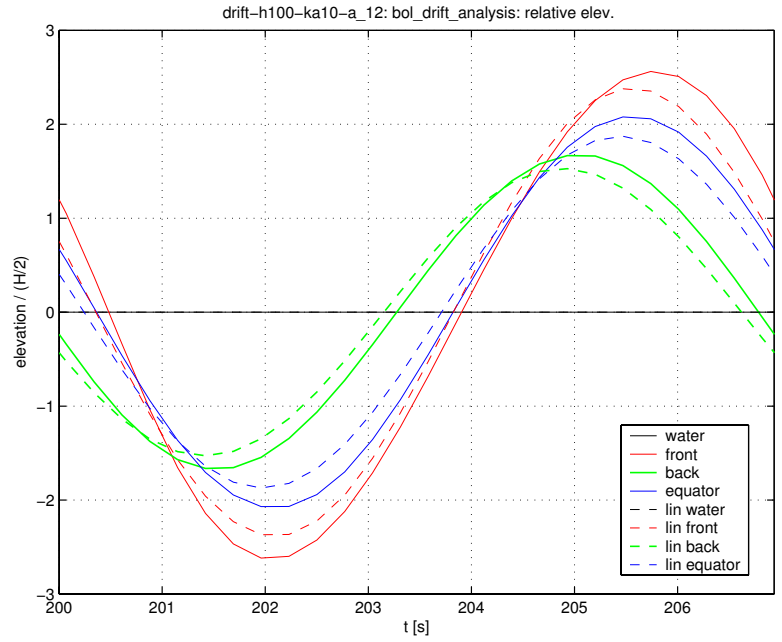

(b) Relative wave elevations.

Figure 4.24: Wave height at waterline: at the front and at the back of the sphere, together with the vertical position of the centre and the mean water level. Both absolute and relative to the postion of the centre.

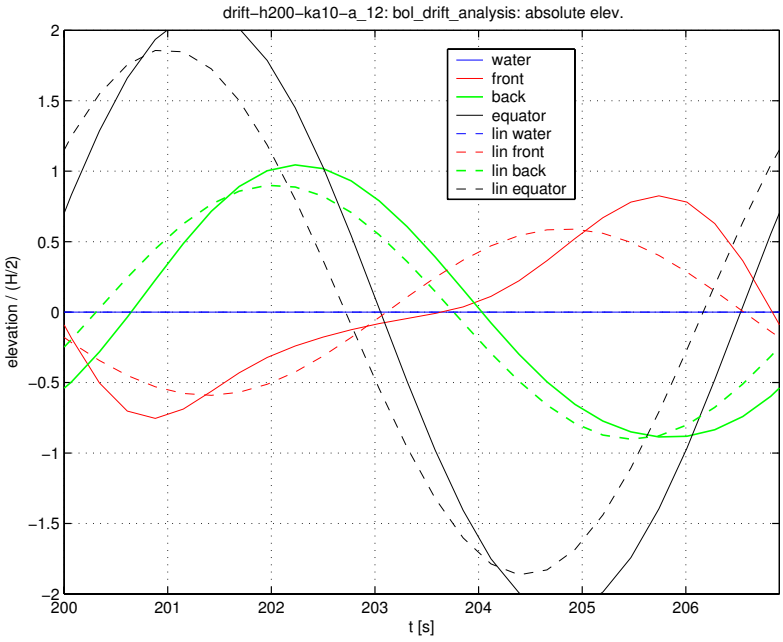

(a) Absolute wave elevations.

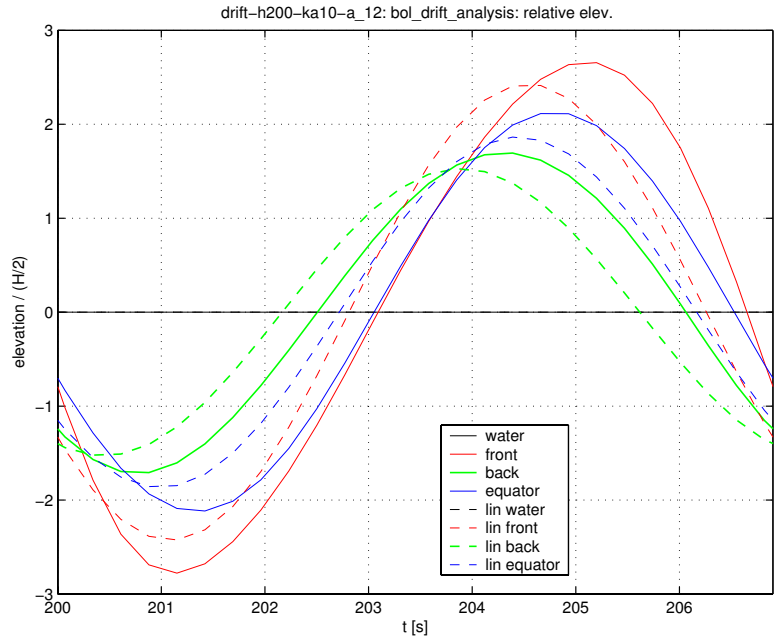

(b) Relative wave elevations.

Figure 4.25: Wave height at waterline: at the front and at the back of the sphere, together with the vertical position of the centre and the mean water level. Both absolute and relative to the postion of the centre.

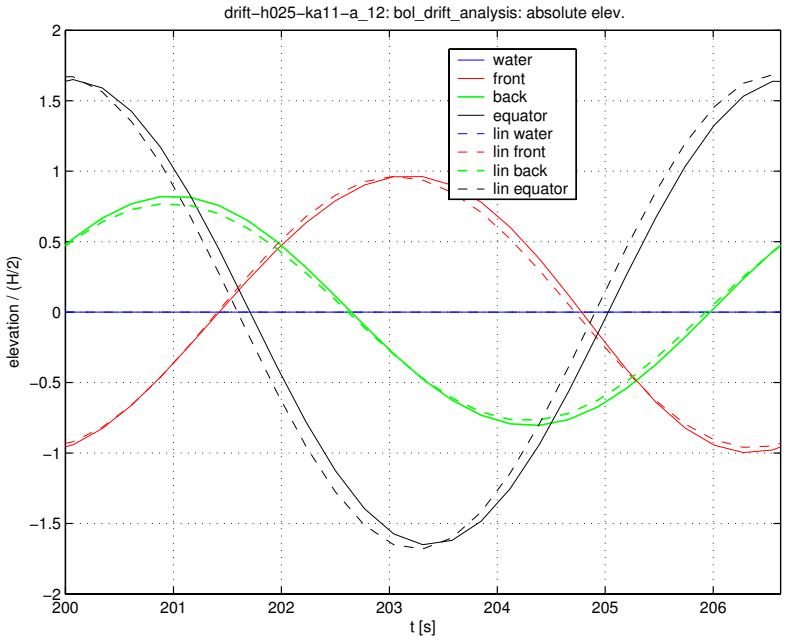

(a) Absolute wave elevations.

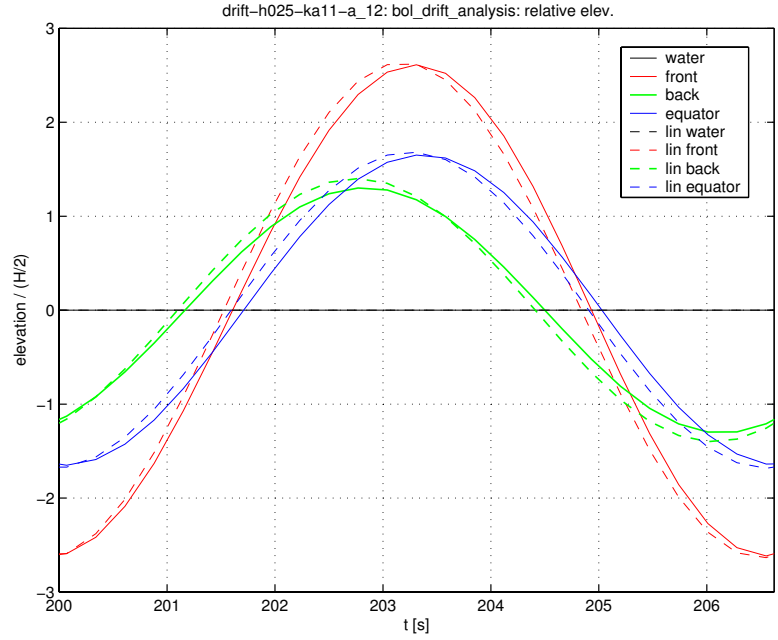

(b) Relative wave elevations.

Figure 4.26: Wave height at waterline: at the front and at the back of the sphere, together with the vertical position of the centre and the mean water level. Both absolute and relative to the postion of the centre.

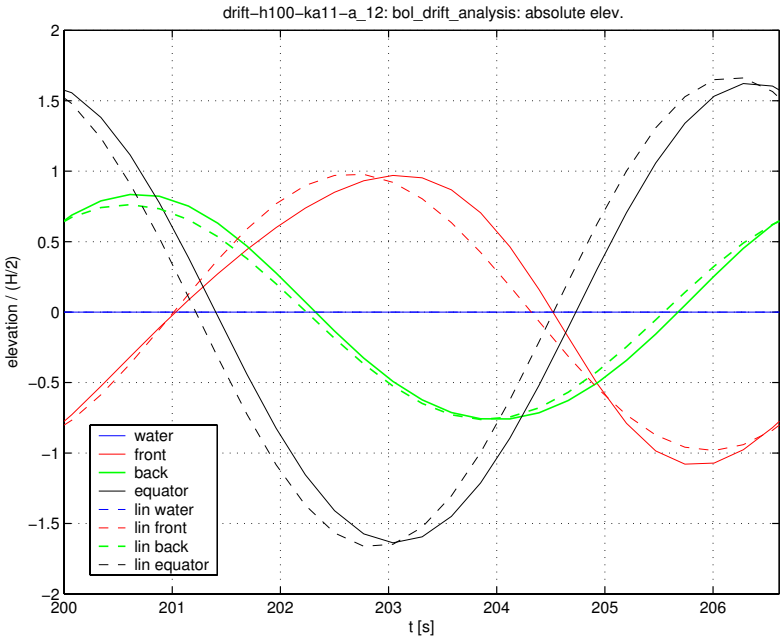

(a) Absolute wave elevations.

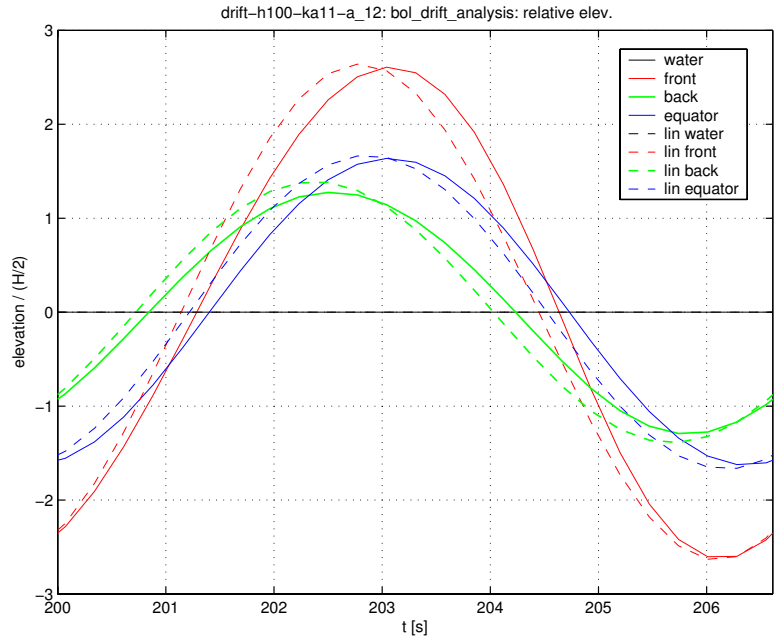

(b) Relative wave elevations.

Figure 4.27: Wave height at waterline: at the front and at the back of the sphere, together with the vertical position of the centre and the mean water level. Both absolute and relative to the postion of the centre.

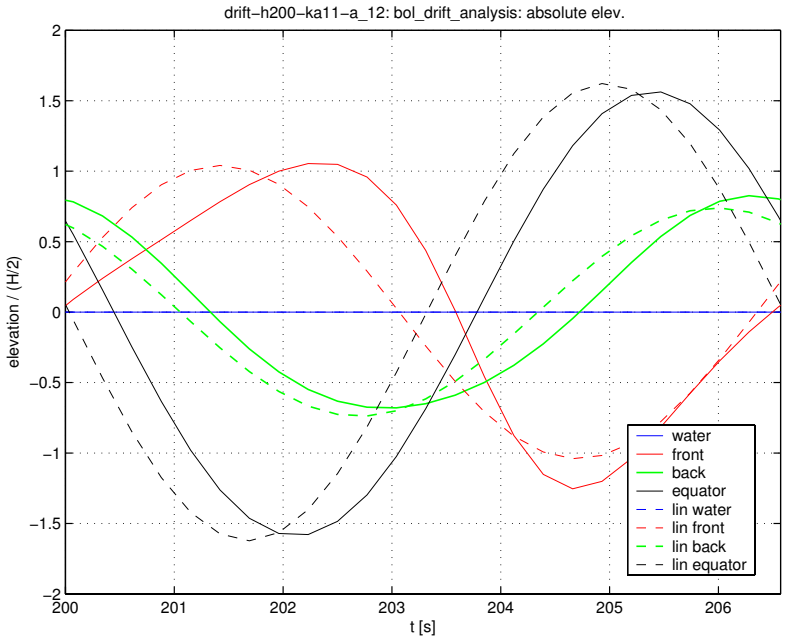

(a) Absolute wave elevations.

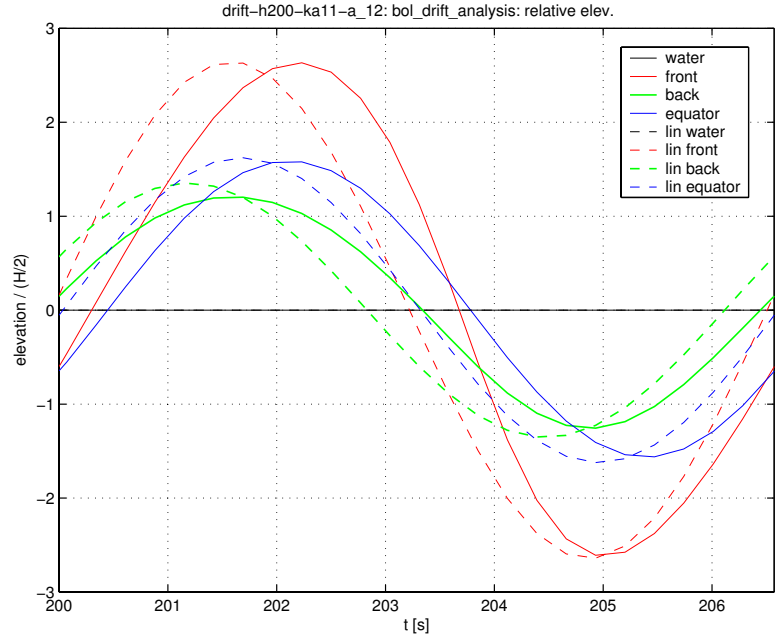

(b) Relative wave elevations.

Figure 4.28: Wave height at waterline: at the front and at the back of the sphere, together with the vertical position of the centre and the mean water level. Both absolute and relative to the postion of the centre.

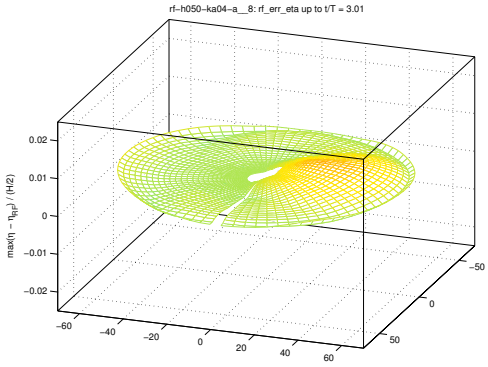

(a) Maximum deviation from the prescribed incoming wave elevation in the time period from $t/T = 0$ till $t/T = 3$.

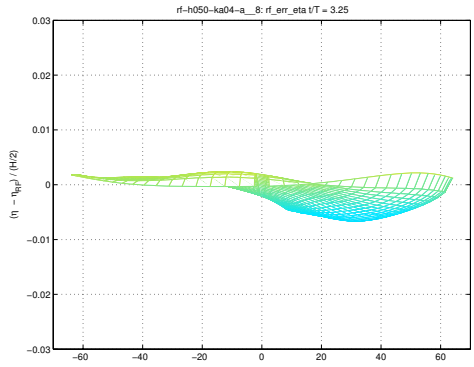

(b) The deviation from the prescribed incoming wave elevation at $t/T = 3.25$.

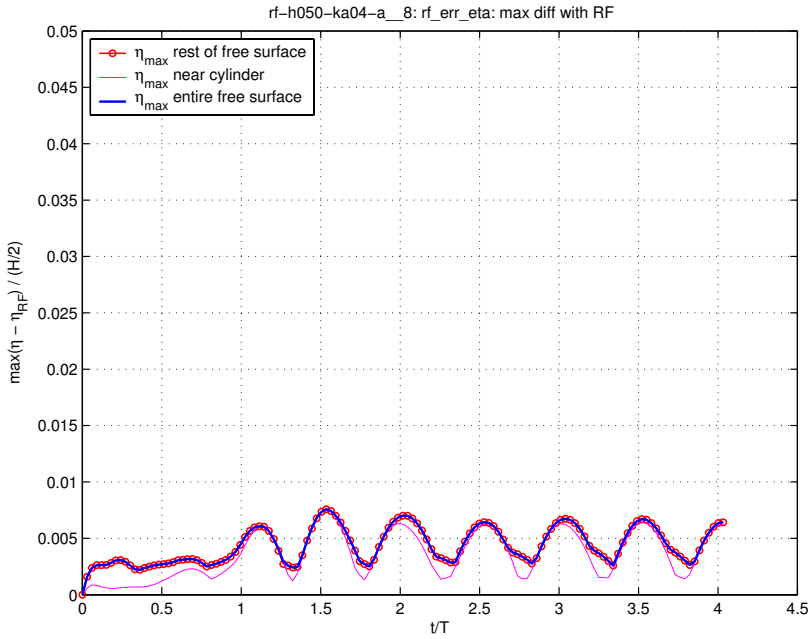

(c) Maximum deviation from the prescribed incoming wave elevation as a function of time for the whole free surface, for the part near the sphere, and for the rest of the free surface.

Figure 4.29: The incoming wave is prescribed also on the fixed sphere. There should be only the incoming wave then.

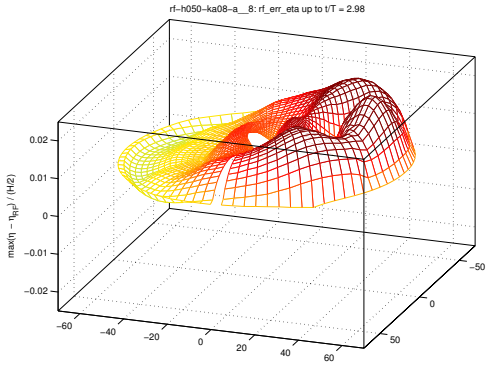

(a) Maximum deviation from the prescribed incoming wave elevation in the time period from $t/T = 0$ till $t/T = 3$.

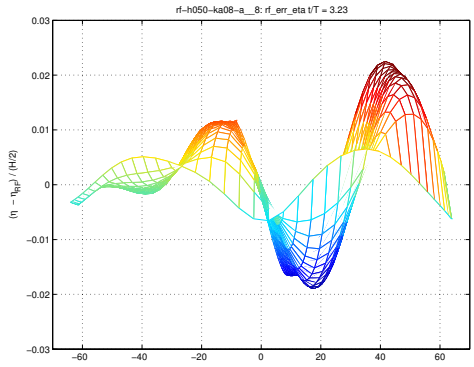

(b) The deviation from the prescribed incoming wave elevation at $t/T = 3.25$.

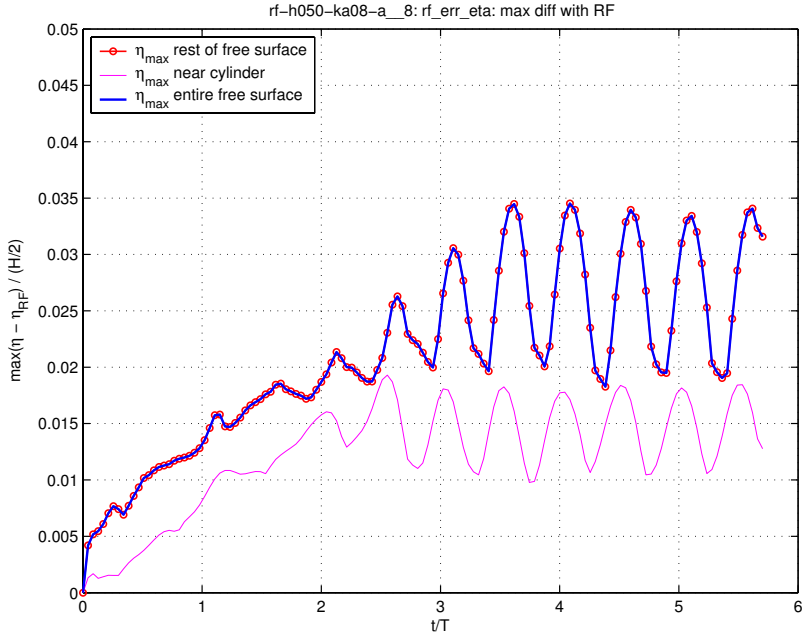

(c) Maximum deviation from the prescribed incoming wave elevation as a function of time for the whole free surface, for the part near the sphere, and for the rest of the free surface.

Figure 4.30: The incoming wave is prescribed also on the fixed sphere. There should be only the incoming wave then.

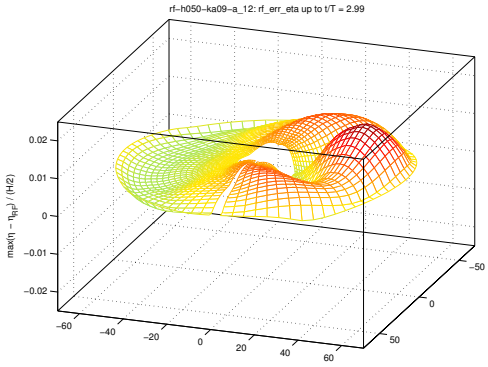

(a) Maximum deviation from the prescribed incoming wave elevation in the time period from $t/T = 0$ till $t/T = 3$.

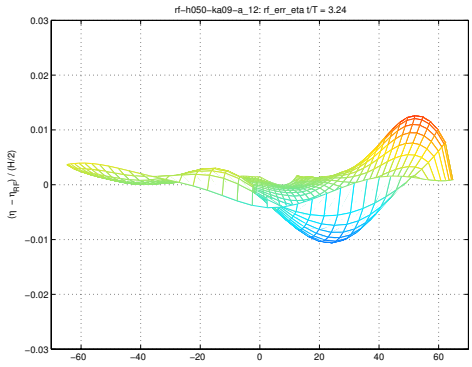

(b) The deviation from the prescribed incoming wave elevation at $t/T = 3.25$.

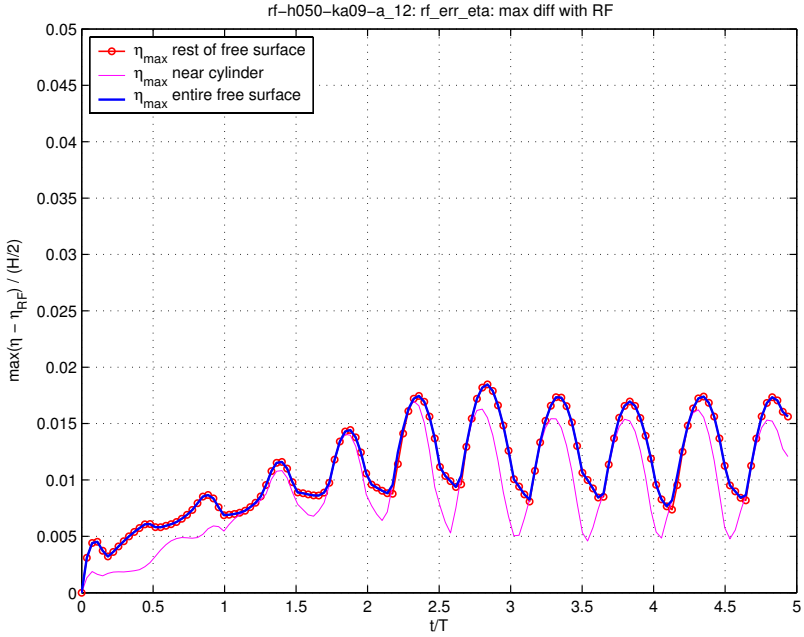

(c) Maximum deviation from the prescribed incoming wave elevation as a function of time for the whole free surface, for the part near the sphere, and for the rest of the free surface.

Figure 4.31: The incoming wave is prescribed also on the fixed sphere. There should be only the incoming wave then.

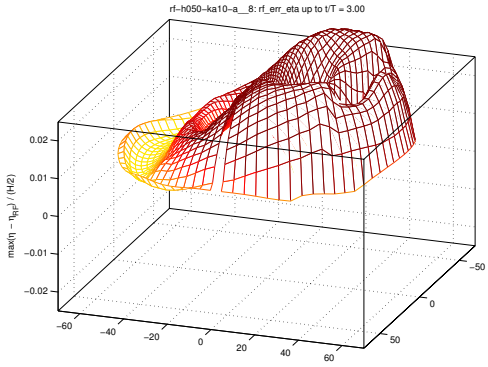

(a) Maximum deviation from the prescribed incoming wave elevation in the time period from $t/T = 0$ till $t/T = 3$.

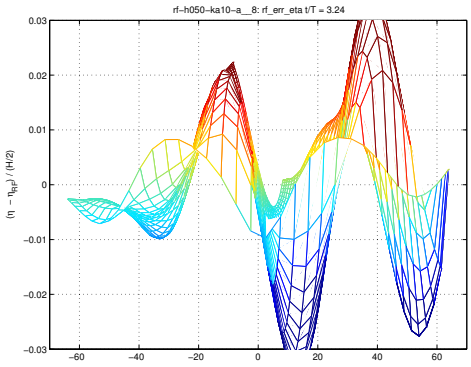

(b) The deviation from the prescribed incoming wave elevation at $t/T = 3.25$.

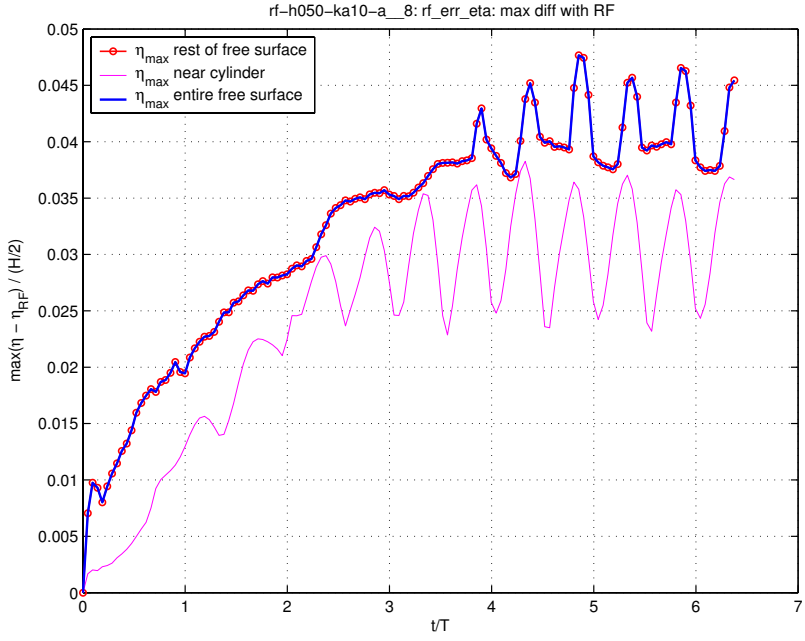

(c) Maximum deviation from the prescribed incoming wave elevation as a function of time for the whole free surface, for the part near the sphere, and for the rest of the free surface.

Figure 4.32: The incoming wave is prescribed also on the fixed sphere. There should be only the incoming wave then.

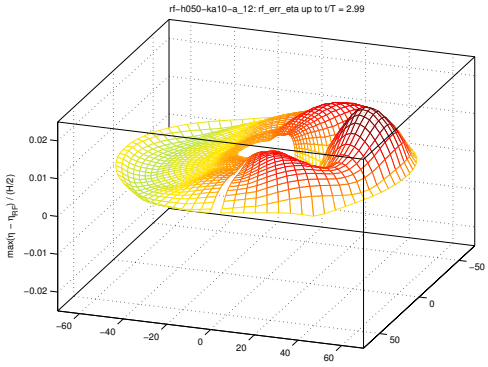

(a) Maximum deviation from the prescribed incoming wave elevation in the time period from $t/T = 0$ till $t/T = 3$.

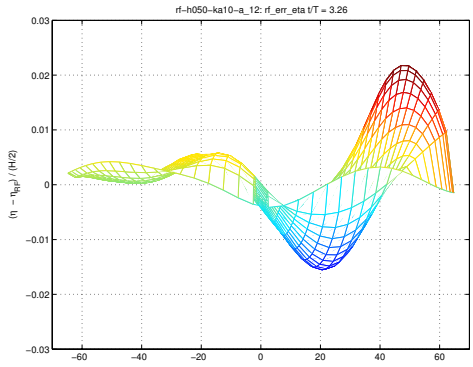

(b) The deviation from the prescribed incoming wave elevation at $t/T = 3.25$.

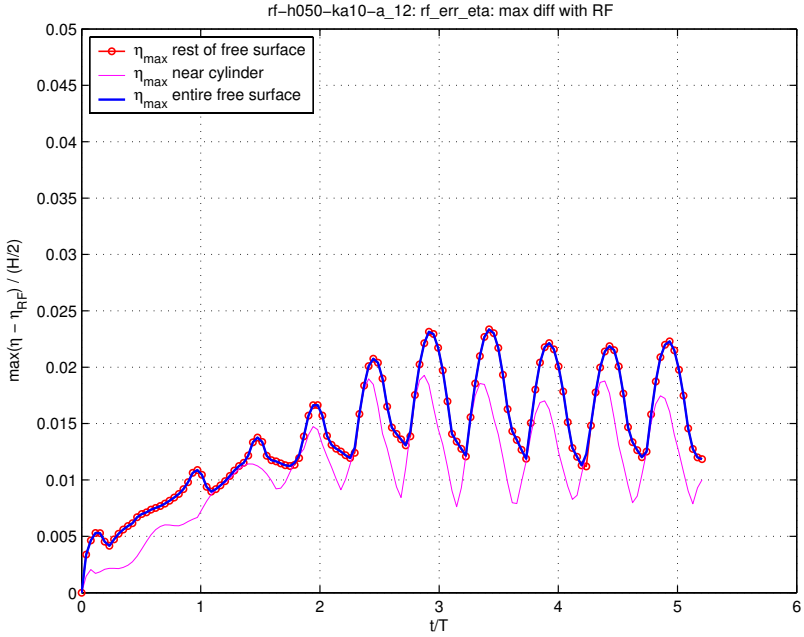

(c) Maximum deviation from the prescribed incoming wave elevation as a function of time for the whole free surface, for the part near the sphere, and for the rest of the free surface.

Figure 4.33: The incoming wave is prescribed also on the fixed sphere. There should be only the incoming wave then.

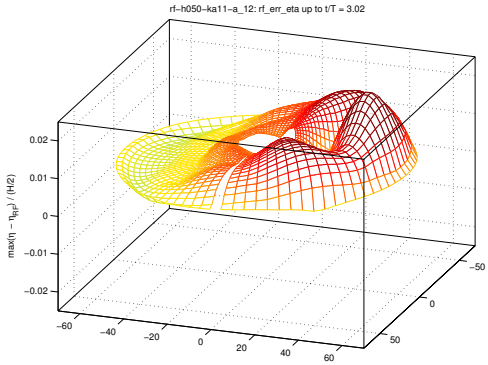

(a) Maximum deviation from the prescribed incoming wave elevation in the time period from $t/T = 0$ till $t/T = 3$.

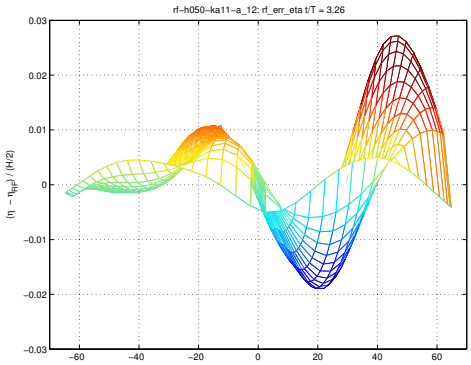

(b) The deviation from the prescribed incoming wave elevation at $t/T = 3.25$.

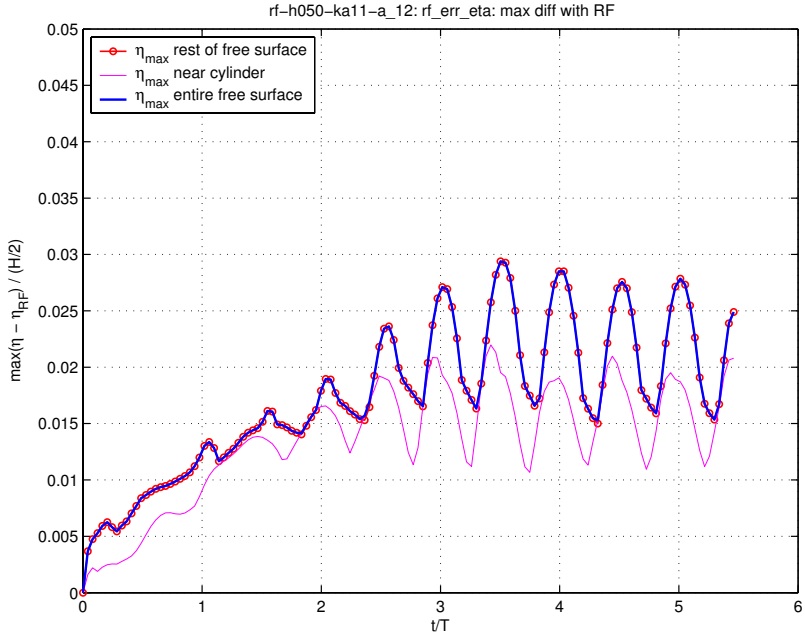

(c) Maximum deviation from the prescribed incoming wave elevation as a function of time for the whole free surface, for the part near the sphere, and for the rest of the free surface.

Figure 4.34: The incoming wave is prescribed also on the fixed sphere. There should be only the incoming wave then.

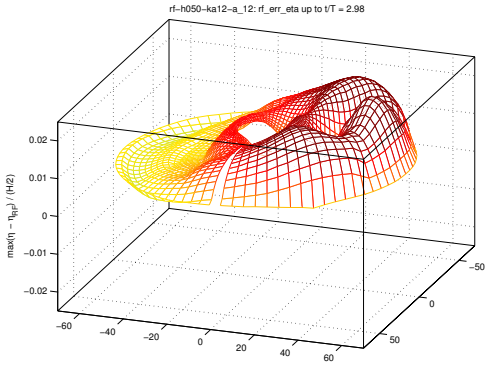

(a) Maximum deviation from the prescribed incoming wave elevation in the time period from $t/T = 0$ till $t/T = 3$.

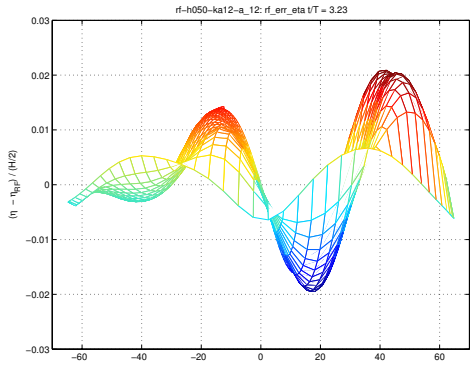

(b) The deviation from the prescribed incoming wave elevation at $t/T = 3.25$.

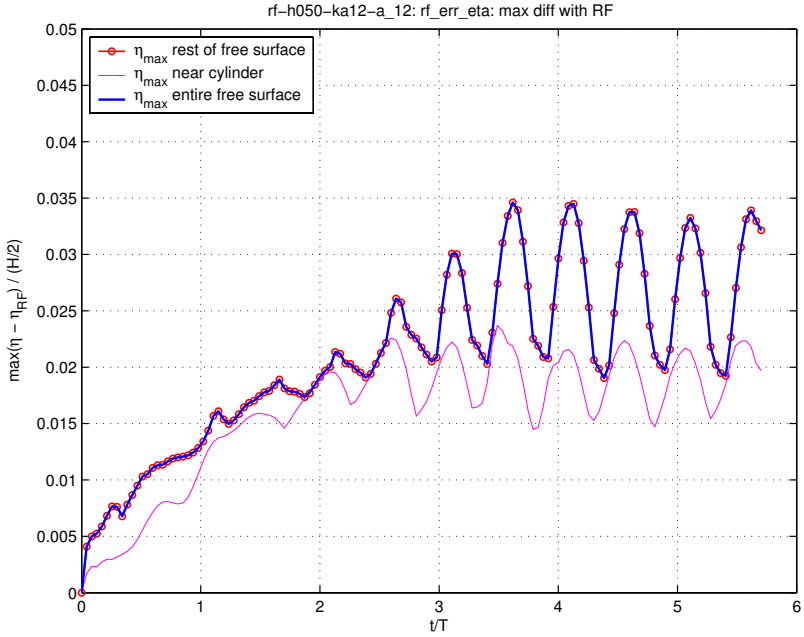

(c) Maximum deviation from the prescribed incoming wave elevation as a function of time for the whole free surface, for the part near the sphere, and for the rest of the free surface.

Figure 4.35: The incoming wave is prescribed also on the fixed sphere. There should be only the incoming wave then.

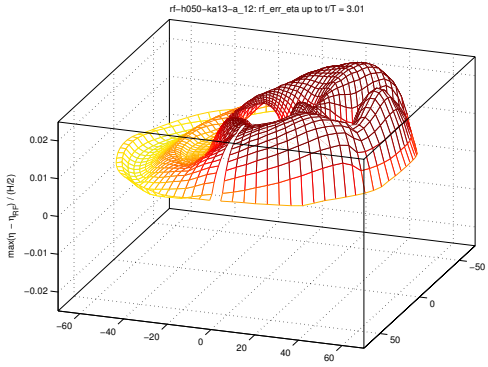

(a) Maximum deviation from the prescribed incoming wave elevation in the time period from $t/T = 0$ till $t/T = 3$.

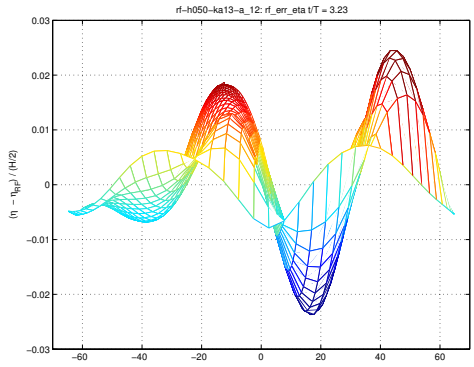

(b) The deviation from the prescribed incoming wave elevation at $t/T = 3.25$.

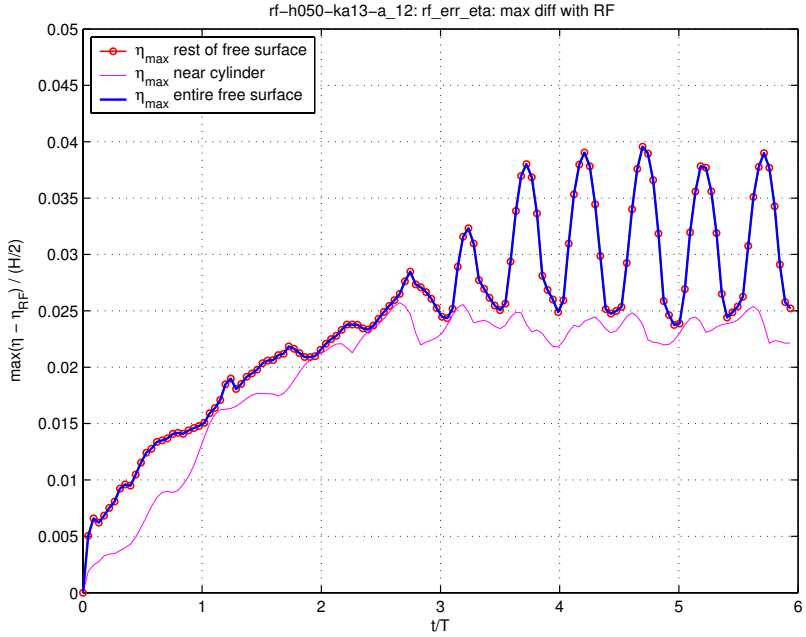

(c) Maximum deviation from the prescribed incoming wave elevation as a function of time for the whole free surface, for the part near the sphere, and for the rest of the free surface.

Figure 4.36: The incoming wave is prescribed also on the fixed sphere. There should be only the incoming wave then.

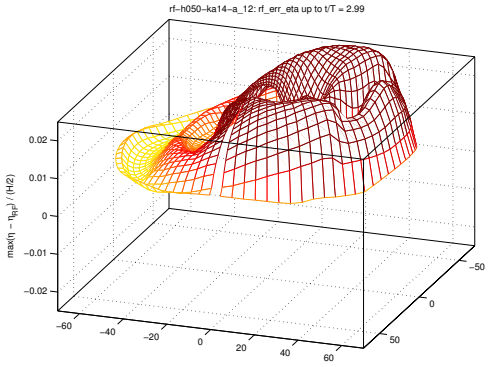

(a) Maximum deviation from the prescribed incoming wave elevation in the time period from $t/T = 0$ till $t/T = 3$.

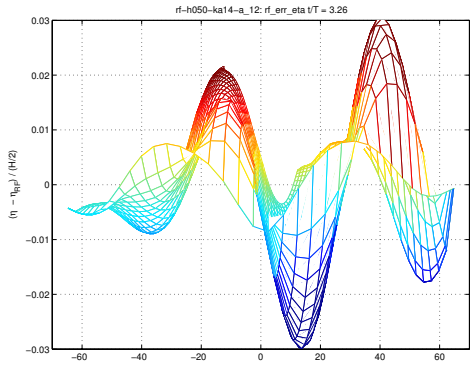

(b) The deviation from the prescribed incoming wave elevation at $t/T = 3.25$.

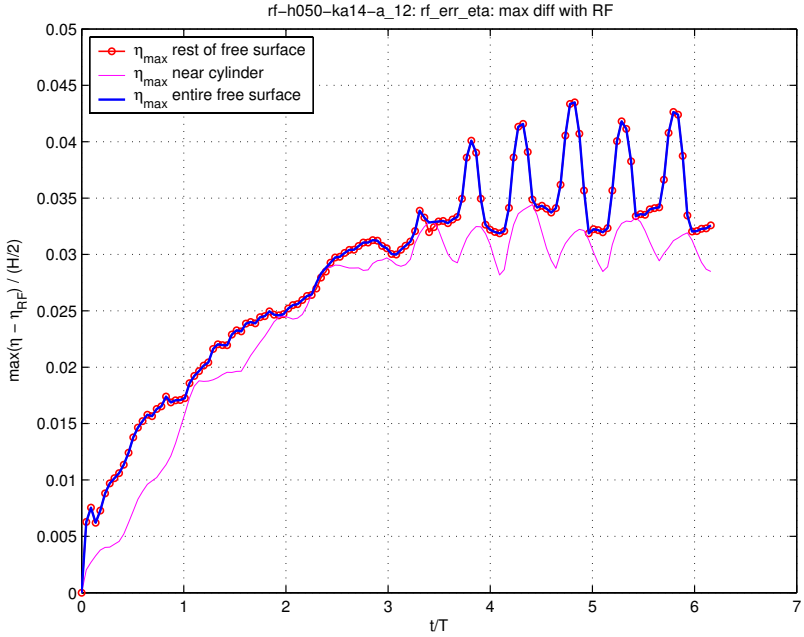

(c) Maximum deviation from the prescribed incoming wave elevation as a function of time for the whole free surface, for the part near the sphere, and for the rest of the free surface.

Figure 4.37: The incoming wave is prescribed also on the fixed sphere. There should be only the incoming wave then.

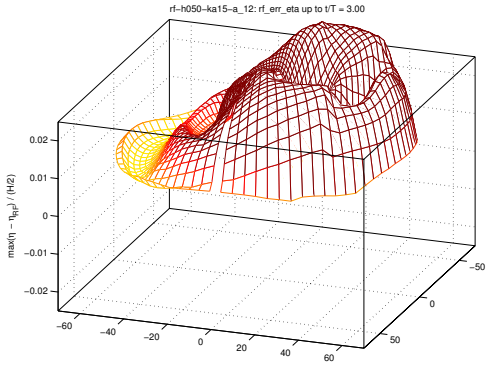

(a) Maximum deviation from the prescribed incoming wave elevation in the time period from $t/T = 0$ till $t/T = 3$.

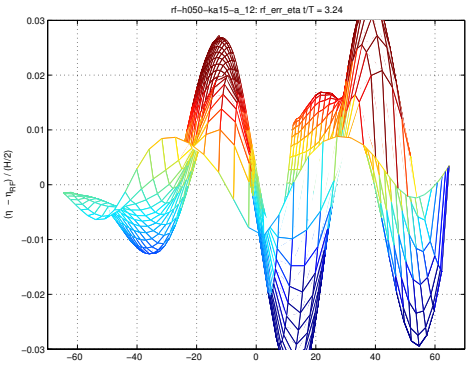

(b) The deviation from the prescribed incoming wave elevation at $t/T = 3.25$.

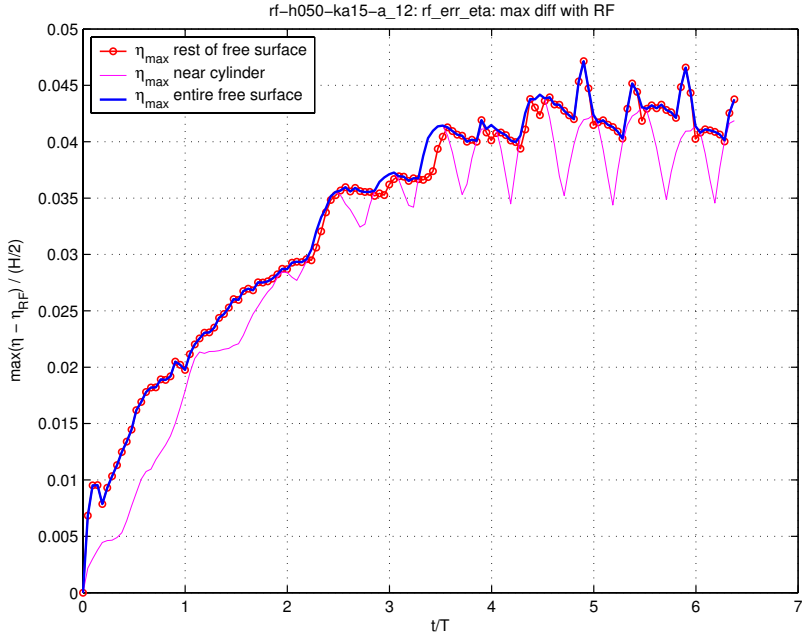

(c) Maximum deviation from the prescribed incoming wave elevation as a function of time for the whole free surface, for the part near the sphere, and for the rest of the free surface.

Figure 4.38: The incoming wave is prescribed also on the fixed sphere. There should be only the incoming wave then.

4.3 Conclusion

Although it is very difficult to have enough resolution for a range of incoming wave frequencies, the quality of the solutions obtained is reasonable. For the amplitudes of the heave motions the differences with the linear results are the largest. This can be attributed to the limited quality of the beach setup as indicated by the free decay experiments. In domains of this size doing any better is very difficult.

The difference between the HYPAN calculations and the linear[4] results for the mean horizontal drift force, of for example -20% at maximum drift, are not understood completely. An indirect calculation of the first linear drift component using the relative wave motions as calculated by HYPAN shows that a deviation of up to -10% in the total drift force can be attributed to the deviations for the wave elevation near the cylinder and to deviations in the motions of the sphere. The spread in the deviations for the first linear drift component is larger however then the spread in the deviations for the total drift force. It is therefore questionable whether these deviations for the first linear drift component and those for the total drift have the same origin. The calculation of the second linear drift component, using the velocity squared term in the total hydrodynamic force, suggests that the accuracy of the calculation of the total drift could be even better then suggested by the indirect calculation of the first linear drift component. This would explain the different spread in the deviations for the first linear drift component and in those for the total drift. This leaves a larger part of the difference between the HYPAN calculations and the linear results for the total drift unexplained however.

The effect of the different amplitudes of the incoming wave on the results strongly suggests that for the smaller wave heights the current calculations can be considered to be in the "linear" regime, which is compatible with the very small steepness of the smallest incoming waves. The fully nonlinear potential theory calculations should therefore coincide with the linear results used for reference which are exact up to second order in the incoming wave amplitude for the mean horizontal drift force. Since these are asymptotic error estimates, there is room for some scepsis however.

Future investigations should of course correct the implementation of the mooring forces, although that should have no significant effect. It is also a good idea to try to do a direct calculation of the first and the third linear components of the drift force from the quantities that determine the hydrodynamic force in HYPAN. But most importantly, the representation of the incoming waves should be improved and, to allow for a better beach, the size of the domain should be enlarged. See chapter 6 for suggestions on how to achieve this.

[4] The term linear is used here because the mean horizontal drift force, a second order quantity, is completely determined by first order quantities.

Chapter 5

Parallelisation and other computational aspects

HYPAN was originally written to be run on a vector computer, originally a Cray Y-MP and later a Cray C90. It used only one CPU on those machines. On the Cray C90 HYPAN was able to run at 500 Mflops of a peak of 1 gigaflops. At the end of 2000 the Cray C90 was taken out of production. It was replaced in the middle of 2001 by two 512 processor Origin 3800 systems from Silicon Graphics. It uses MIPS R14000 processors running at 500 MHz, with one gigabyte RAM per processor. The performance of HYPAN on one processor of TERAS, as the new supercomputer was called, was originally one-third of the performance on one CPU of the Cray C90. There was a clear need to parallelise our code. Using domain decomposition, already implemented in HYPAN, one could divide the total domain into several subdomains each running on their own CPU. However, splitting up the free surface into different domains results in one-sided differences along the boundaries of those domains. Domain decomposition is therefore only useful when the computational domain can be made up of relatively large blocks. For the diffraction calculations we planned to do, we needed at least one large domain that could not be split up into smaller domains. Parallelisation within a domain was needed. When several domains would be used, in principle, one would still be able to run them in parallel using MPI. A grant from NCF enabled Willem Vermin from SARA to work on this parallelisation of HYPAN [29].

In this chapter we will describe that parallelisation effort together with some related information. We start with a list of where what kind of work is done in HYPAN. Then we ask ourselves how we can do it faster, leading naturally to the parallelisation effort.

5.1 Computational work

Figure 5.1 gives a summary of the computational work that HYPAN has to do. Most of the program code deals with computations that are of linear order. Most of the computation time is spent in a few routines that do computations of quadratic order.

```
-----------------------------------------------------------------------

  Read input
  Allocate memory
  Determine initial boundary conditions

  RK-loop:

    Calculate geometry
    Calculate influence coefficients: dipole and source coefficients:
      CFD*phi + CFS*phn = 0; 2N unknowns, N equations
    Build system matrix AA from half of the columns of CFD and CFS
    Calculate RHS:
      multiply other columns of CFD and CFS with known phi and phn
    Precondition AA: diagonal scaling
    Solve the system: iterative solver: matrix vector products
    When free floating body:
      Calculate equations of motion matrix
      Extend system matrix AA
      Calculate RHS
      Precondition AA
      Solve the system
    Calculate new boundary conditions

-----------------------------------------------------------------------
```

Figure 5.1: Pseudo listing of main computational work.

Those few computations are:

1. Initialising the three N by N matrices: AA, CFD, and CFS.

2. Filling the two coefficients matrices (CFD and CFS): for the zeroth order of the dipole coefficients a number of `atan` function calls are needed for each matrix element. In a loop over all networks there is a loop over all panels of the network and for each of those panels there is a loop over all collocation points.

3. Building the linear system: half of the columns of the dipole and source coefficients matrices are copied into the system matrix AA, the other half is matrix vector multiplied with the known boundary conditions to form the right-hand side.

4. Preconditioning the linear system using diagonal scaling: multiply all elements of the system matrix with the applicable value.

5. Solving the linear system with an iterative Conjugate Gradient Squared (CGS) method. The work is done by two matrix vector multiplications per iteration, multiplying the rows of the system matrix with a vector.

6. Extending the system matrix in case of free floating bodies. This is of the order of N*MNFB and MNFB*MNFB, where MNFB is the number of panels on the body.

When there are free floating bodies an extra linear system has to be solved, $\nabla^2\phi_t = 0$. It uses the same system matrix except for some additions. On the wetted surface of the body not ϕ or ϕ_n is given, but the relationship between the two: the equations of motion. This means that for the panels on the body both ϕ and ϕ_n are unknown, but that there is an extra equation for each body panel. The system matrix used for $\nabla^2\phi = 0$ is thus extended with a column of dipole influence coefficients for every panel on the body. To compensate for these extra unknowns an extra row is added for every panel on the body to satisfy the equations of motion. The memory for this large system matrix is allocated in the beginning and the smaller system matrix is put in there in such a way that it does not need to be reshuffled to be part of the larger system matrix.

5.2 How to speed things up

We need to speed things up. The most thorough way to do this is to change the computational order of the construction and solving of the linear system. This has been done using domain decomposition and it can be done by using cluster decomposition. The problem with domain decomposition is how to connect the different sub domains without introducing a discontinuity to the waves, for example because of one-sided discretisations. This is why the already implemented domain decomposition in HYPAN was not able to solve our current speed problems. Introducing cluster decomposition or fast multipole acceleration into an existing higher order boundary integral method is complicated. It has recently been done by [13]. One of the problems is the accuracy, especially for very high waves it is necessary to force a total

solid angle of 4π, see Broeze. Whether it is necessary for more moderate waves is not clear. The far field approximations that are available in the current code show some undesirable effects for the current grid setup. Whether this is a problem with this specific implementation remains to be investigated. In the meantime all influence coefficients are calculated with the analytical expressions from Romate. This is on TERAS a factor of three more expensive than a typical mix of far field approximations and analytical expressions.

Dividing the available work between as many processors as possible is also an effective way to improve the turnaround time of your calculations. The most trivial form of parallelisation is to make sure that you have a large number of calculations to do and give them one processor each. However, for development work it is very preferable to have the results of one calculation as soon as possible. And of practical interest: single system images running on hundreds of processors tend to be very unstable, a calculation that takes a week has a large chance of being stopped. The main computational work in HYPAN consists of a loop over all panels which calculates for each iteration a loop over all collocation points. It should be easy to divide those last loops between several processors.

5.3 Parallelisation

5.3.1 Open MP or MPI?

Open MP (Open specifications for Multi Processing) is a specification for a set of compiler directives, library routines, and environment variables that can be used to specify shared memory parallelism in Fortran and C/C++ programs. Basically, you take a serial program code in which you insert compiler directives around the code that you would like to be run in parallel. These compiler directives can also be used to specify scheduling policy and to specify which variables are private to the threads.

MPI (Message Passing Interface) is a library specification for message passing. When using message passing all processes run from the beginning according to the same program code which includes statements about which process needs to do what. All data allocation is done per process, each process gets its own local collection of data and there is no global data. From this it is obvious that with MPI one has very precise control over where what data is stored and how and when processes communicate with each other to exchange results or data. This at the cost of having to think for every data structure about how to distribute it between the different processes and of having to specify explicitly how the processes exchange their data. In other words: there is very precise control, but you have to use it and you have to use it for the whole program.

Open MP on the other hand uses a shared memory programming model. If the underlying hardware needs message passing for this it is implemented, but hidden from the user. This means that one can start with one master thread running the program code and only start up more threads at the moments when they are useful. And only in those places one has to think about private variables, scheduling options, critical sections, locks, etc. This makes it possible to incrementally parallelise a serial program. If there are only changes in the source code in relatively few places, the readability and thus the maintainability of the code does not really change, especially

because these changes are mostly relatively small. Of course, this ease of use one gets at the expense of having less opportunities to optimise to perfection. But as long as that is not needed it is an excellent idea to use Open MP to parallelise an existing serial program.

In the case of HYPAN we use a boundary integral formulation which means that for N unknowns we get a dense system matrix of N*N elements. Most of the source lines are spent on manipulating data structures of order N and most of the time is spent on manipulating data structures of order N*N. This kind of situation is ideal for the Open MP approach.

5.3.2 Principles and problems

TERAS has a nonuniform memory access architecture. This means that each CPU (or better: node) has an amount of memory (one gigabyte in case of TERAS) placed nearby. The total main memory consists of all those local pieces of memory together. The nodes are connected in some hierarchical fashion so that all memory positions are reachable from each CPU within a few hops across the nodes. Because each hop takes time, the time to reach a memory location far away takes much longer than to reach a local memory location. These node dependent memory access times give this architecture its name. Open MP presents the user a global shared memory, access to the memory of other nodes is implemented transparently for the user, it only takes more time. To achieve reasonable performance it is necessary that each node has the data that it uses most nearby in its local memory. Open MP itself does not provide any facility for this however. Instead the manufacturer of a nonuniform memory access machine has to think of something. In case of TERAS there is a First Touch Principle: the node that references a particular page of memory first gets it into its local memory (as long as there is enough of it).

When several processors try to reach the same memory location at the same time there can be a problem. Just reading the value is not a problem, but if one of the processors wants to write to the memory location the results depend on which one was first. Even when both processors perform the same associative operation on the contents the results can still dependend on their relative timing. For updating a processor takes the current value from the memory location and after having performed the operation on it the processor puts it back, but if in the meantime an other processor took the value for processing the update of the first processor will be lost when the second processor writes its results back. Such a case, where the results depend on the relative timing of the different processors, is called a race condition.

Open MP provides several mechanisms to deal with such race conditions. The first one is a critical section. When a part of the code is declared as being a critical section there is at any one time only one thread allowed to be executing the code inside that section. This is very easy to use, but it is not very parallel. Another mechanism is the use of locks. A lock is a user declared variable which can be set by a special subroutine and unset by another special subroutine. When updating a matrix in an overlapping way one can for example associate each column of the matrix with a lock. Before updating part of such a column one first tries to set the associated lock, this only succeeds when the lock is free. If the lock is not free one can try to update another column. After finishing updating a certain column the associated lock is to

be unset again. This is less easy to use, but it can allow more than one thread to work in parallel on the same section, only blocking other threads where needed.

5.3.3 Implementation

Every processor needs to do his share of work on the three big N*N matrices CFS, CFD, and AA. To do that efficiently every processor needs to have his part of each matrix in his local memory. Using the First Touch Principle this is accomplished by letting each processor initialise his own part of those matrices to zero.

For the calculation of the influence coefficients matrices CFS and CFD the influence of every panel on each collocation point is calculated. Each panel has its own column in the CFS and CFD matrices. The calculation of those columns is distributed over all processors, each processor calculates its own columns. However, because of the higher order discretisation of the boundary integral every panel not only contributes to its own column, but also to the columns of his eight neighbours. This means that every column is possibly updated by several processors at once. This is an unacceptable race condition. To prevent this the influence coefficients per panel are first written to local scratch arrays, one for each coefficients matrix and both 9 columns wide. After that those local scratch columns are written to the coefficients matrices using locks per column. If a column is locked another column is tried until all columns have been done.

To solve the linear system first the system matrix and the right-hand side have to be constructed. The system matrix AA consists of those columns of CFD and CFS for which the associated ϕ of ϕ_n is unknown. Each processor copies his unknown columns into his part of the system matrix. The remaining columns of CFD and CFS are matrix vector multiplied with the known ϕ and ϕ_n to form the right-hand side. The matrix vector multiplies involve a summation along the rows of the matrix; unfortunately the elements in such a row are not neighbours in memory. All matrix vector multiplies in the code are parallelised as follows. Each processor multiplies his part in every row with the corresponding part of the vector and puts the results into a local scratch array. Every processor now has a contribution to every element of the the global right-hand side in his local scratch array. To add up all those contributions the global right-hand side is divided in as many pieces as there are processors. Each piece is protected with a lock. The processors try to update all pieces until the work is done. The system is solved using CGS as an iterative solver. The work is done by two matrix vector multiplies per iteration. Typically about 30 iterations are needed when using 9000 panels.

When there is a floating body not only $\nabla^2\phi = 0$ needs to be solved but also $\nabla^2\phi_t = 0$. The system matrix for the second equation is equal to the system matrix for the first equation except for MNFB extra columns from CFS and MNFB extra rows from the equations of motion coupling the 2*MNFB unknowns on the floating body. In the current implementation the largest matrix is divided over all processors, giving each processor a group of consecutive columns. When solving the large system all processors work on their part of the matrix, when solving the smaller system all processors still work on their part of the largest matrix and some will therefore be idle. This is not too much of a problem, because MNFB is typically less than 30 percent of the total number of panels. However, when building the system matrix some influence

coefficients columns will have to move across nodes, because a processor's part of the AA matrix does no longer correspond perfectly to the parts that the same processor holds of the CFS and of the CFD matrix. The results do not indicate that this has to change, but it can be changed if needed.

5.3.4 Results

To show the effect of the parallelisation four different cases are considered. The first two cases are based on the fixed cylinder calculations from chapter 3, one using 9000 panels and one using 30,000 panels. The other two cases are based on the floating sphere calculations from chapter 4, one using 7000 panels and one using 20,000 panels. The two calculations with the largest grids used one time step and the other two used 10 time steps. For each calculation there are plots giving the speed up as a function of the number of processors used. There are separate plots for the speed up of the whole calculation, of the calculation of the coefficients, of the solution of the linear system, and of the matrix vector multiplies. All runs were run in normal production time, but some runs were run in a more busy environment than the others. Some were run during the very quiet Easter holidays of 2003. On TERAS a job gets the number of processors it requests and the associated local memory. It is not guaranteed however that those processors are near to each other[1], especially when the system is almost full. It is also not guaranteed that others are not using parts of your local memory (but this should be considered to be a bug). When processors are not near to each other it is possible that the communication of others runs through your part of the system. All this means that even while in principle you get exclusive access to the requested processors the activity of others can disturb the efficiency of your calculations.

Figure 5.2 shows the 9000 panel cylinder case. With 60 processors we have a maximum total speed up of 40. For more than 60 processors the speed up flattens until it rises again when using more than 100 processors. Notice the large bandwidth of the results for more than 20 processors. The speed up of the calculation of the influence coefficients shows the same general picture, although the bandwidth is smaller and the speed up is slightly larger. The speed up of the iterative solver shows a very broad bandwidth. During the Easter holidays it reached a maximum speed up of 36 while using 64 processors; using more processors gave a lower speed up. In normal busy operation the speed up is very small: it has a maximum of around 10. Using more than 40 processors the minimum total speed up is about 20. In quiet times the solve and the calculation of the coefficients are in balance, in busy (normal) times the solve is the bottleneck.

Figure 5.3 shows the 30,000 panel cylinder case. Using 60 processors we have a maximum total speed up of 33, which is less than for the 9000 panels case. This is probably a cache effect. The bandwidth is slightly less, but that could be because of different circumstances. The speed up does not flatten using up to 128 processors. The speed up of the calculation of the coefficients shows the same picture. The maximum speed ups for the solve are lower than those for the 9000 panel case using the same number of processors. But because the speed ups are not flattening the

[1] In terms of the number of hops, or the number of CPU cycles, that are needed to reach each others local memory.

maximum speed up reached is almost 70. During quiet times and for these matrix sizes the solve is not the bottleneck any more.

Figure 5.4 shows the 7000 panel sphere case. When using 60 processors the total speed up is almost 30. But for more processors the maximum speed up stays more or less the same. The bandwidth is large. The speed up of the coefficients calculation shows a very small bandwidth. After almost flattening the speed up increases again to more than 50 using 128 processors. At 60 processors the speed up is slightly less than 40. The speed up of the solve reaches a maximum of almost 30 at 60 processors, but the bandwidth is very large: in busy times the speed up stays below 10. The solve is clearly the bottleneck, especially in busy times. The total speed up can be as low as 18 at 60 processors.

Figure 5.5 shows the 20,000 panel sphere case. The total speed up is 30 using 60 processors. For more processors the total speed up seems to flatten. The speed up of the calculation of the coefficients shows a similar picture except that the speed up is 40 when using 60 processors and that the flattening for higher numbers of processors is slightly less. The speed up of the solve is around 30 using 60 processors. In quiet times the speed up then continues to increase up to a speed up of almost 50 using 128 processors. In more busy times the speed up of the solve seems to have a ceiling of around 30.

Summarising we can say that when the system load on TERAS is low we can have a speed up of between 30 and 40 at 60 processors, but when the system load is normal the speed up can be around 20. For the calculations with the 30,000 panels and the fixed cylinder the calculation of the influence coefficients is the bottleneck, in the other cases the bottleneck is the solving of the linear system. When system load is low the speed up of the calculation of the influence coefficients and the speed up of the solving of the linear system are reasonably in balance, but on a busy system the speed up can be halved, mainly caused by a smaller speed up of the solve.

5.4 Conclusion

On the Cray C90, using one processor, the calculations using 9000 panels and the fixed cylinder as done in chapter 3 took one week for four periods or 400 times steps. It is obvious that then there is little room for trial and error. On the new Silicon Graphics Origin 3800 the same calculations can be done in 20 hours using 16 processors or between 6 and 10 hours for 64 processors. As already remarked in the previous chapters it would be very nice to be able to use even larger amounts of panels. An increase in the number of panels of about a factor of 4 will allow for a domain that is twice as large and a resolution near the cylinder that is also twice as large. This brings us to the calculations with the 30,000 panels and the fixed cylinder. This would take again almost one week to calculate 400 times steps. Probably the time step also needs to be reduced with a factor of two. This means that either new hardware is needed for this kind of calculations or better algorithms. The new Silicon Graphics Altix system at SARA consisting of 416 Itanium 2 processors could give some improvement, but at the moment the speed increase per processor of a factor of two till three for most applications is compensated by a less efficient implementation of Open MP. This should improve however in the near future.

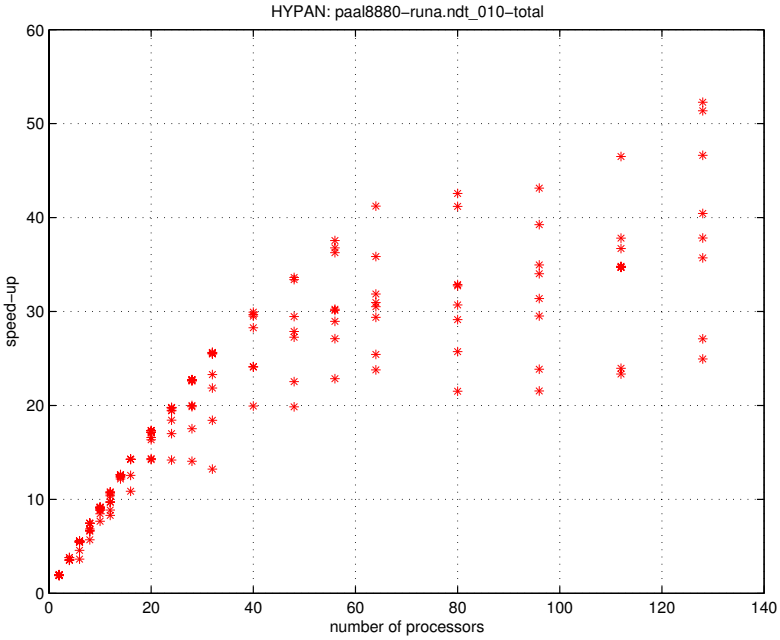

(a) speed up of the total calculation

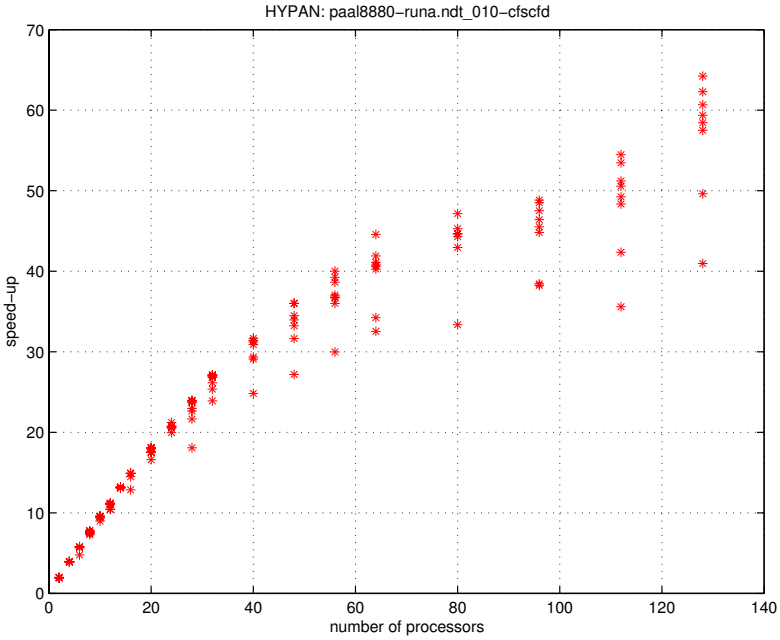

(b) speed up of the influence coefficients calculation

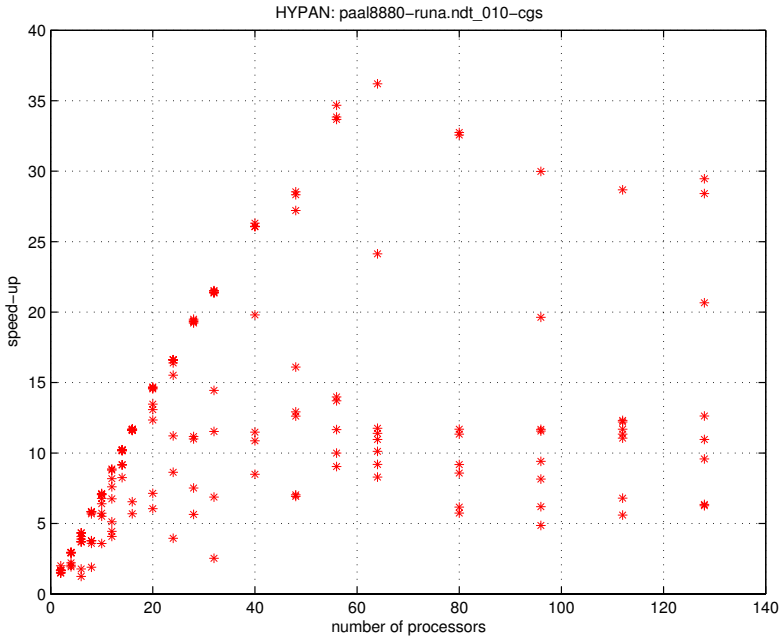

(c) speed up of the iterative solver

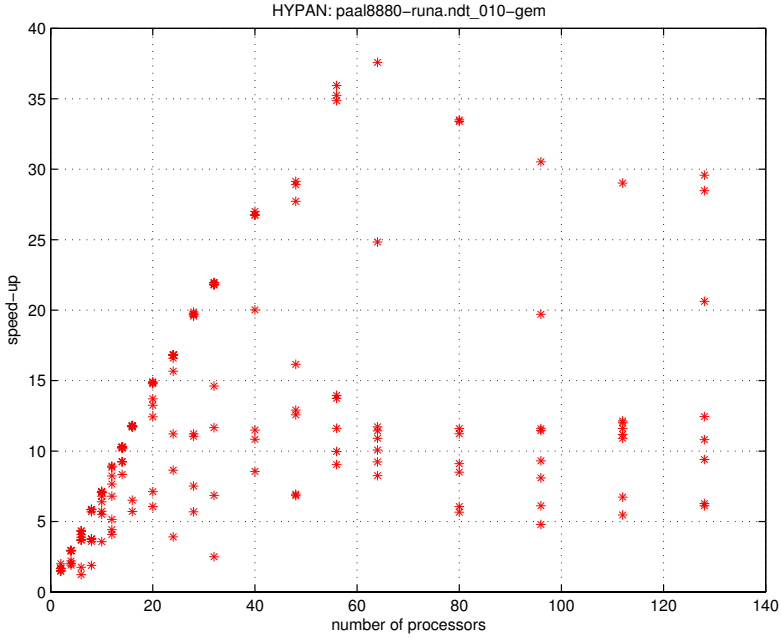

(d) speed up of the matrix vector multiplies

Figure 5.2: The speed up as function of the number of processors used for the calculations using 9000 panels and a fixed cylinder.

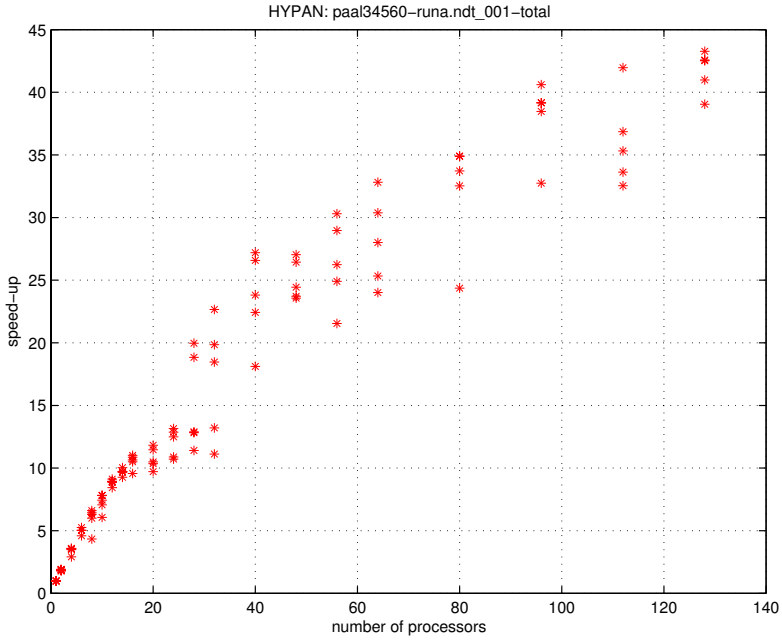

(a) speed up of the total calculation

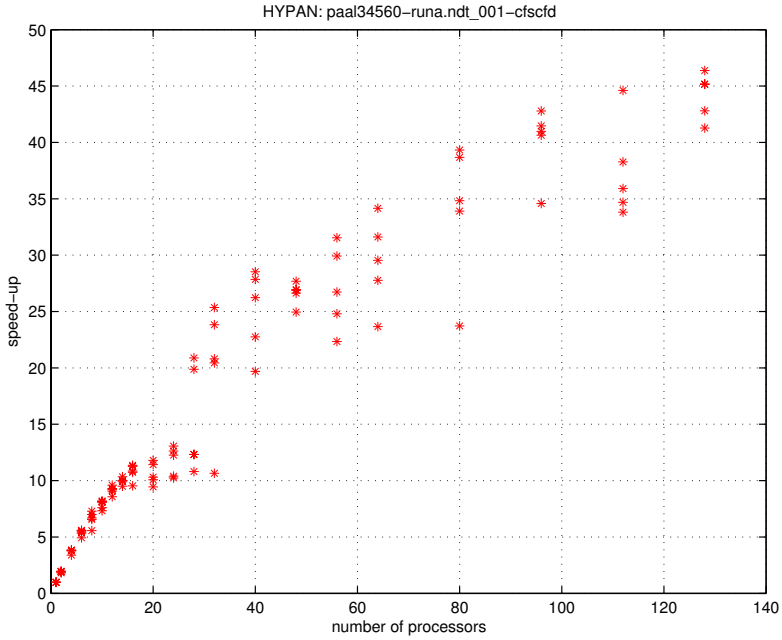

(b) speed up of the influence coefficients calculation

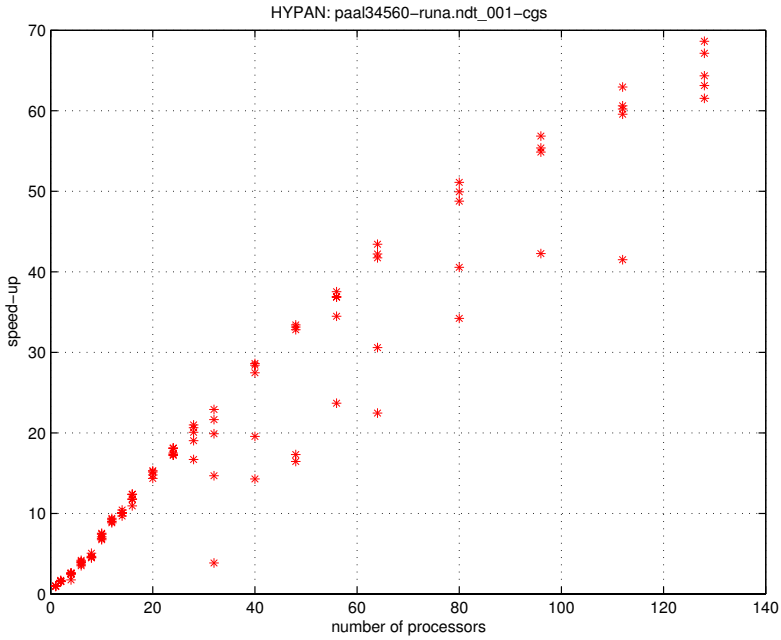

(c) speed up of the iterative solver

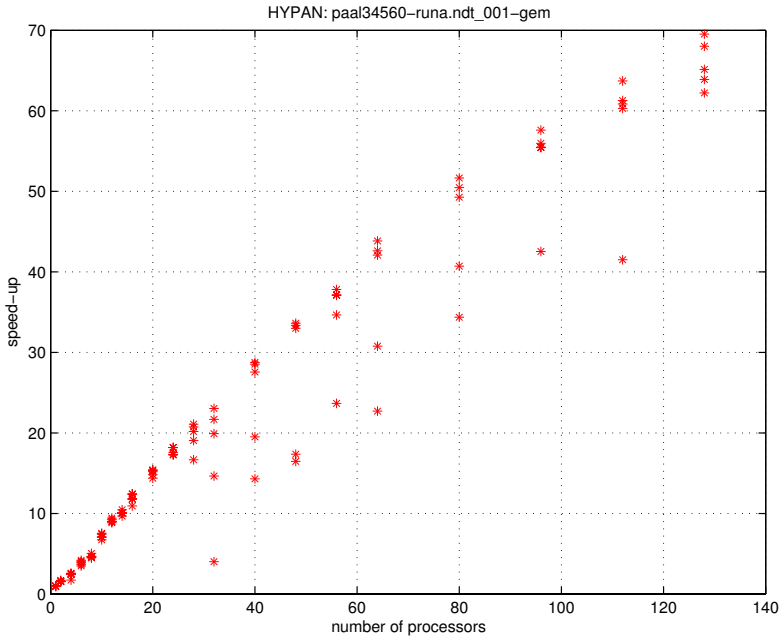

(d) speed up of the matrix vector multiplies

Figure 5.3: The speed up as function of the number of processors used for the calculations using 30,000 panels and a fixed cylinder.

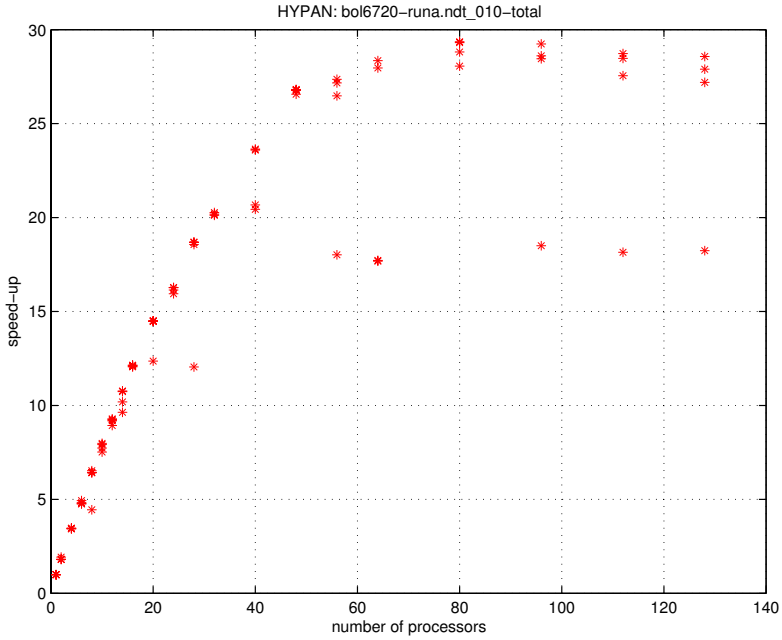

(a) speed up of the total calculation

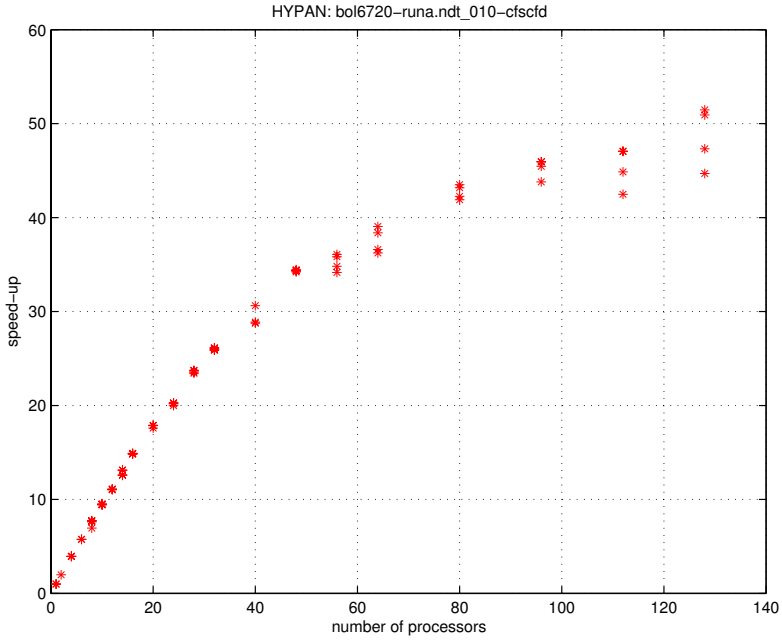

(b) speed up of the influence coefficients calculation

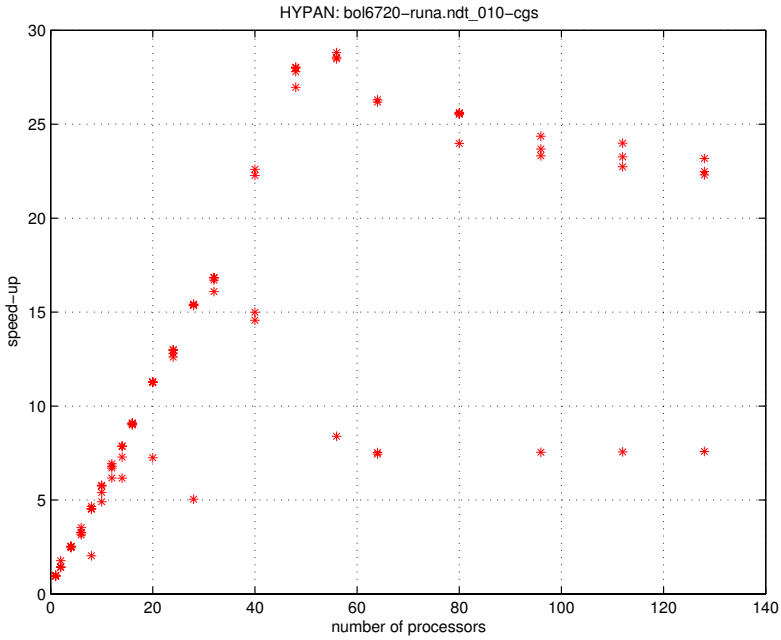

(c) speed up of the iterative solver

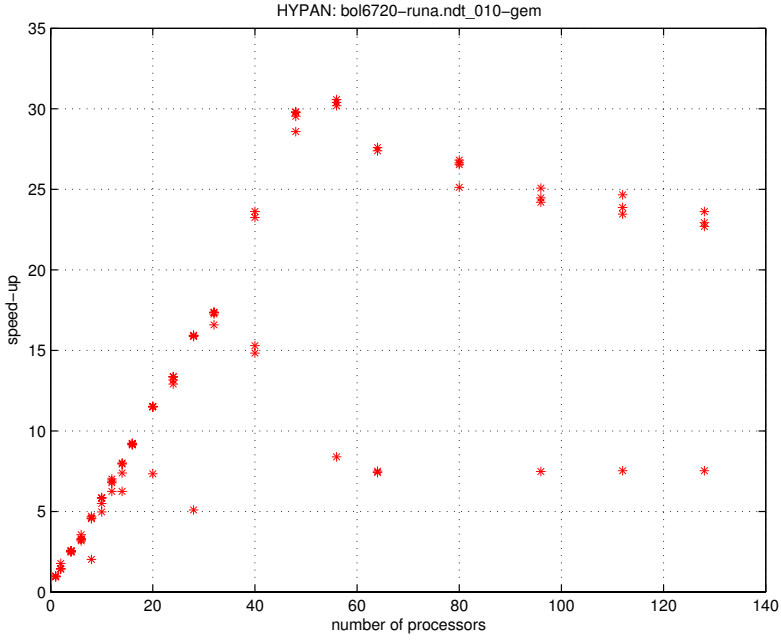

(d) speed up of the matrix vector multiplies

Figure 5.4: The speed up as function of the number of processors used for the calculations using 7000 panels and a floating sphere.

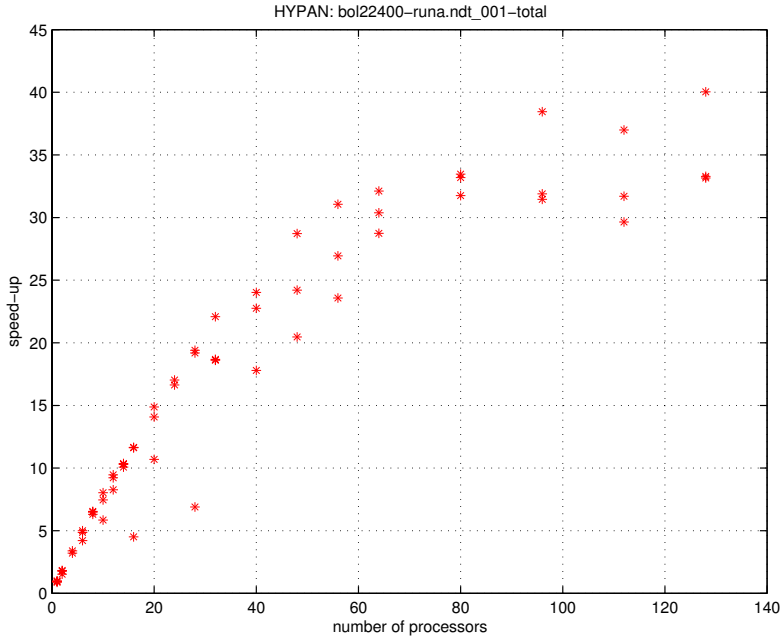

(a) speed up of the total calculation

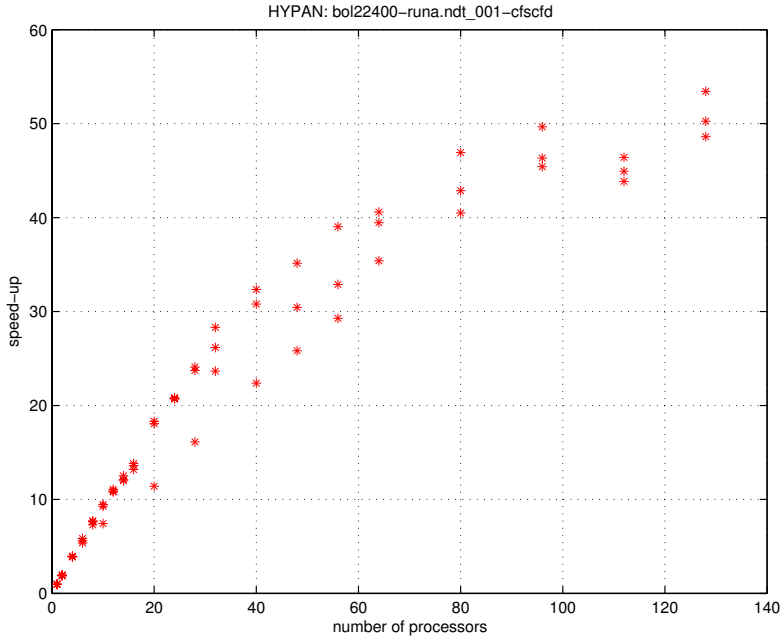

(b) speed up of the influence coefficients calculation

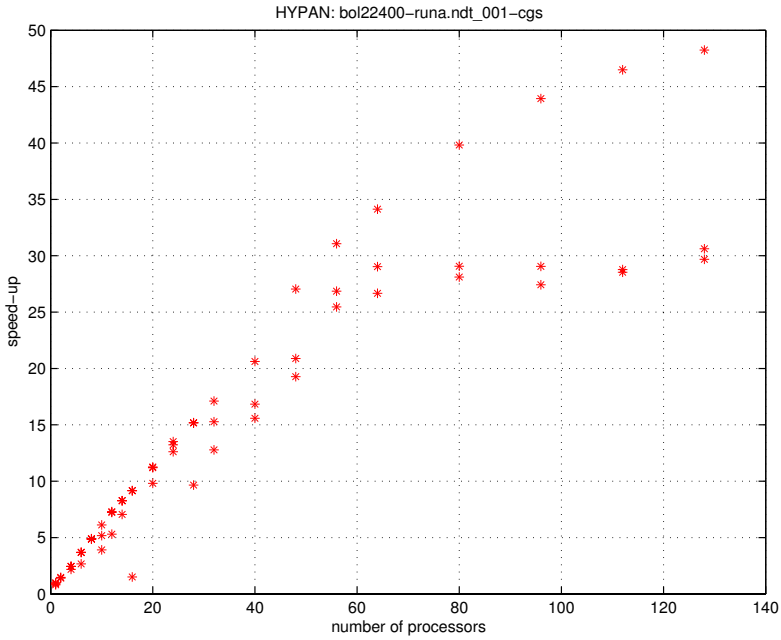

(c) speed up of the iterative solver

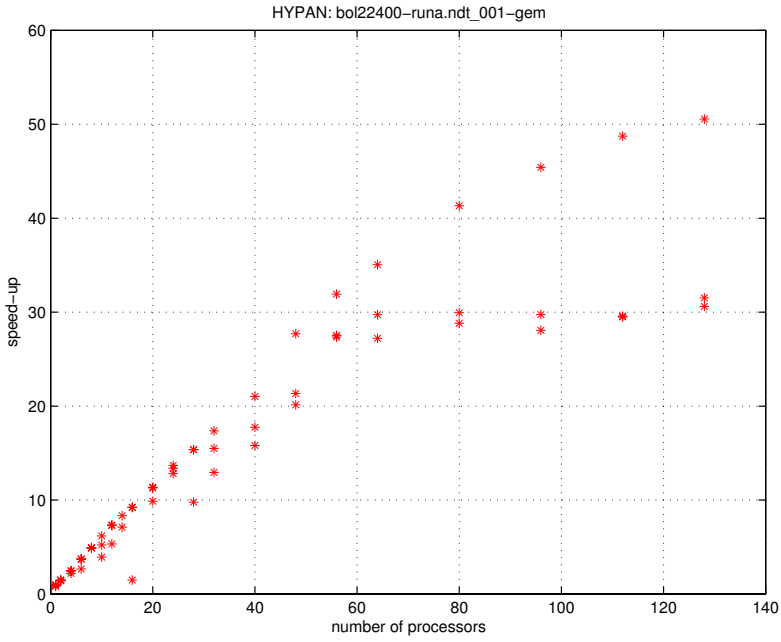

(d) speed up of the matrix vector multiplies

Figure 5.5: The speed up as function of the number of processors used for the calculations using 20,000 panels and a floating sphere.

Chapter 6

The future

The current capabilities of HYPAN for the calculation of diffraction problems follow from the contents of this thesis. The agreement of the results from HYPAN with theory and experiments is good. The main bottleneck for the accuracy and for the type of calculations that can be done is the grid that can be used. This is both limited by the number of panels that can be calculated in a reasonable amount of time and by the specific characteristics of the grid implementation.

As stated earlier in chapter 2, the number of panels in the circumferential direction is the same for all networks. The total number of panels needed depends therefore largely on the choice of this number. With 80 panels in the circumference the total number of panels will be between 5000 and 10,000. To give an indication, a calculation with a free-floating body using 6800 panels takes about 1500 seconds for one time step on one MIPS R14000 running at 500 MHz. It follows that using (much) more than 80 panels the circumference is not feasible. The memory requirements are relatively mild. Having 3 large matrices of size N^2 filled with doubles needing 8 bytes each, the amount of memory needed is to very good approximation $24N^2$ bytes. In case of 5000 panels the amount of memory needed is therefore 600 MByte. For 10,000 panels it is 2.4 GByte.

As an example, we calculate the minimum number of panels needed when using 80 panels in the circumference. The five bottom networks need 1 * (80/4)*(80/4) + 4 * (80/4)*4 = 720. For the height of the domain, in case of 'infinite' depth, at least 10 panels are needed. This results in 80*10 = 800 panels for the domain mantle. In the radial direction of the free surface you need 30 panels, which results in 80*30 = 2400 panels for the free surface. For an object the minimum amount of panels is a bottom set of networks, see above, but now with 1 * (80/4)*(80/4) + 4 * (80/4)*6 = 880 panels. This adds all up to a minimum total number of panels of 4800, say 5000 panels.

It is good to realise at this point that objects with water cross-sections having large aspect ratios are more difficult to deal with then objects that have a water cross-section with a small aspect ratio. This is because the piece in the middle takes extra grid points at the same resolution and because the beach and especially the Sommerfeld radiation condition prefer a point source as the origin of the diffracted waves.

Since the number of panels in the circumferential direction is limited, the size of the domain is limited by the number of panels per wavelength needed to resolve the smallest incoming wavelength, see equation (3.1). The length of the largest incoming wavelength is limited by the quality of the absorbing boundary conditions, or better how well you can simulate an infinite domain. Using a Sommerfeld radiation condition a domain radius of at least a quarter of a wavelength is needed and perhaps more. A domain radius of half a wavelength worked for the calculations in chapter 3. A beach without a Sommerfeld radiation condition needs at least half a wavelength to reduce the reflection to around 5 percent; the distance between the beach and the object should not be too small, almost a wavelength would be ideal, using less than a quarter of wavelength would mean solving a different problem, a problem with a different kind of water. The result of all this is that the range of incoming wave frequencies that can be calculated for a given object is limited. This was one of the problems with the calculations done in chapter 4.

The other main contributor to the computation time that is needed for the calculations, is the number of periods that needs to be calculated. For the regular waves in chapter 3 10 periods were enough. In chapter 4 we try to mimic a real mooring set up. Before the mooring system has settled down a large number of periods has passed, 20 periods should be enough, we took 30 periods to be certain. When using the average total force instead of the displacement of the mooring system the number of periods could probably be limited to around 10. When one wants to calculate irregular waves the number of smallest periods that needs to be calculated is much larger.

6.1 Solving only for the difference with the incoming wave

Ferrant, see e.g. [8], uses the analytical description of Rienecker & Fenton for the incoming wave to separate the velocity potential into one term for the incoming wave and one term for the rest. This does not put any restrictions on the total potential. As long as the velocity potential for the incoming wave satisfies the Laplace equation for arbitrary wave elevations the remaining velocity potential term can be solved separately. Start with the total potential written as the sum of the incoming wave potential and the remaining potential and then replace all references to the incoming wave potential with the analytical description. Do the same for the wave elevation. Evaluating all these references explicitly, including any derivatives, leads to a problem that only depends on the remaining or diffraction potential and on the extra wave elevation due to the diffraction. A discretisation of this problem only has to resolve that diffraction potential. This means that further away from the object the resolution in the circumferential direction becomes less and less important. Furthermore, the resolution in the radial direction further away from the object does only need to resolve the diffracted waves well enough to allow them to be damped away. This procedure would allow us to remove the limit on the domain size caused by having to resolve the incoming wave. The domain can be as large as is useful for absorbing the diffracted waves and the fixed circumferential resolution is much less of a problem. It would therefore be possible to calculate a larger range of frequencies. In principle, this approach can also be used in the presence of floating bodies, the implementation

however will be a major bookkeeping operation.

6.2 Lowering the computational complexity of the problem

As said earlier in chapter 5, the computational complexity of both the construction of the linear system and the solving of that system are of order N^2. Nowadays there are several methods to exploit the idea that to calculate the influence of a number of panels relatively far away from the field point, but close to each other, one can group those panels together neglecting the details within the group that will have a negligible influence at that distance. It is possible to construct such a hierarchical structure of groups that the calculation, the storage and the evaluation of the resulting influence coefficients are almost of order N. We will refer to this kind of methods as cluster decomposition methods. Domain decomposition can be seen as a simple form of cluster decomposition, because the idea is similar, although there is no real hierarchical structure. Normally we do not consider it as such however. The classic example is the Fast Multipole Algorithm, first developed by Greengard and Rokhlin [14] for the N-body problem with Coulomb or gravitational interactions. These ideas have also been applied to calculations of water waves using potential theory, for example by Kring, Korsmeyer, et al. [18]. Their higher order nonlinear version still had to be written however.

Having a computer code that is capable of performing stable calculations of highly nonlinear water waves, it is inconvenient to replace the whole Laplace solver, since that would imply new discretisations and new stability problems. Instead it would be better to keep the method the way it is, only replacing the matrix vector multiplies in the iterative solver (including the calculation of the influence matrices) by a more efficient approach to get approximately the same resulting vector. Recently such an approach has been taken by Fochesato and Dias [13] based on a three-dimensional boundary element method for calculating highly nonlinear water waves developed by Grilli et al. [15]. This is not a trivial undertaking, but they managed to decrease the computation time by a factor of 6 for a problem using 6000 nodes. They claim that their algorithm could be run in parallel. It remains to be seen whether this approach can be incorporated into HYPAN without sacrificing the current stability, but it seems to be worth the effort to try.

6.3 Dealing with irregular waves

After implementing the suggestions in the previous two sections one can start to think about calculating the fully non-linear diffraction of irregular wave fields. But even then the computational requirements will remain very high. The calculation of very long time series will not be feasible, instead only some small interesting time intervals of a complete time series should be considered. To represent an irregular incoming wave field the Rienecker & Fenton approach is not suitable. We do need however an incoming wave field built up out of analytical expressions satisfying the Laplace equation, because we have to be able to evaluate the velocity potential, the wave elevation, and their derivatives at arbitrary positions. The potential and its derivatives

even above the incoming wave elevation. One way of accomplishing this is to use a two-dimensional time-domain pseudospectral method like Ferrant et al. [12]. Using a three-dimensional pseudospectral method will even allow for diffraction calculations with short-crested wave systems.

6.4 Conclusion

The above suggestions can be implemented in the near future. This will enable the further exploration of the nonlinear effects in wave diffraction problems. Especially in more practical situations where the water waves are irregular, and where the fixed or floating objects have water cross-sections with larger aspect ratios and with more corners.

Appendix A

A.1 Broeze's equation 6.22

The errors near non-smooth boundaries caused by one-sided discretisations of terms in the time-dependent boundary conditions and by some ignored higher order terms in the expressions for the influence coefficients (see also Romate [25]) are instable in time for non-linear computations. To control these ill behaved errors an extra error is introduced that makes the total error well-behaved. This modified dynamic free surface boundary condition is described by Broeze's equation 6.22, only to be used in the first row of collocation points near a non-smooth boundary:

$$\phi_t = a\left[(\phi_{s_\perp})_{\text{lat.bound.}} - (\phi_{s_\perp})_{\text{free surf.}}\right] - \frac{1}{2}(\nabla\phi)^2 - g(z - z_0) \tag{A.1}$$

Here $s_\perp$ is the tangential coordinate on the free surface perpendicular to the intersection line. The parameter a should be positive, but small to prevent inaccuracies. We used a=0.05. For solutions of the continuous problem the velocities $\phi_{s_\perp}$ on the intersection line calculated using data from the free surface and calculated using data from the lateral boundary should be equal. For the discrete problem the difference is a measure of the truncation errors involved. The exact solution is not influenced, but possible numerical deviations are suppressed.

A.2 Calculation of α and β from free decay tests

The equation for free heave motion is

$$(m + a)\ddot{z} + b\dot{z} + cz = 0 \tag{A.2}$$

with a the added mass coefficient and b the damping coefficient for heave. This can be rewritten into the following convenient form:

$$\ddot{z} + 2\nu\dot{z} + \omega_0^2 z = 0 \tag{A.3}$$

with the damping parameter

$$\nu = \frac{b}{2(m + a)} \tag{A.4}$$

and the characteristic angular frequency in the absence of damping

$$\omega_0 = \sqrt{\frac{c}{m+a}} \tag{A.5}$$

The solution for equation (A.3) is

$$z(t) = Ae^{-\nu t}\cos(\omega t + \varphi) \tag{A.6}$$

where

$$\omega = \sqrt{\omega_0^2 - \nu^2} \tag{A.7}$$

It is convenient to normalise a and b and to call the result α and β:

$$\alpha = \frac{a}{m} \tag{A.8}$$

$$\beta = \frac{b}{m\omega} \tag{A.9}$$

We can express α and β in terms of ω and ν for a sphere of radius r and mass $m = \frac{1}{2}\rho\frac{4}{3}\pi r^3$:

$$\alpha = \frac{3g}{2r}\frac{1}{\omega^2+\nu^2} - 1 \tag{A.10}$$

$$\beta = \frac{3g}{r}\frac{\nu}{(\omega^2+\nu^2)^{\frac{3}{2}}} \tag{A.11}$$

A.3 Implementation of the mooring system

In the implementation of the mooring system an error was made. It is shown below however that the effect on the results presented in chapter 4 is negligible. In equation (2.37), giving the body boundary condition, the mooring force was not included. It wás included in the calculation of the acceleration:

$$\vec{a}_b = m^{-1}\vec{F}_p - g\hat{z} + a_{mooring}\hat{y} \tag{A.12}$$

with

$$a_{mooring} = -\omega_{0,m}^2(y - y_0) - 2D\omega_{0,m}\dot{y} \tag{A.13}$$

$$D = 0.33 \qquad \text{(crit. damp. coeff.)} \tag{A.14}$$

$$\omega_{0,m} = 0.01\,\text{rad/s} \qquad \text{(eigenfreq. mooring)} \tag{A.15}$$

and with $\vec{F}_p$ following from the integration of the pressure. This pressure depends on ϕ_t which follows from the solution of $\nabla^2\phi_t = 0$. But, as said before, the body boundary condition used to solve this equation did not include the mooring force and the resulting ϕ_t therefore does not include the reaction forces of the water in response to that mooring force. In equilibrium we should have had

$$< a_{total} > = < m^{-1}F_p > + < a_{mooring} >= 0 \tag{A.16}$$

$$= m^{-1} < F_{drift} > + m^{-1} < F_{F_m} > + < a_{mooring} >= 0 \tag{A.17}$$

where the average reaction forces $m^{-1} < F_{F_m} >$ due to the mooring force F_m were negligible. Therefore

$$F_{drift} = m < a_{mooring} >= -m\omega_{0,m}^2(< y > -y_0) \tag{A.18}$$

But if the average reaction forces would have been negligible if the mooring system had been implemented correctly, then also the absence of those forces in the current implementation should be negligible. This means that equation (A.18) is still valid.

A.4 Components of the mean horizontal drift force

From the thesis of Pinkster [22] we have the following expressions for the contributions to the mean horizontal drift force for a sphere submerged down to its middle. These expressions depend only on the mean first order quantities and are accurate up to second order. The superscript $^{(1)}$ denotes first order quantities, ζ_r is the relative wave height with respect to the centre of mass of the sphere, S_0 is the mean wetted surface, and $\vec{X}$ is the displacement vector from the equilibrium position.

$$F_I^{\text{mean}} = \oint_{\text{mean WL}} \frac{1}{2}\rho g(\zeta_r^{(1)})^2\,(\hat{n}\cdot\hat{k})\,dl_{\text{mean}} \tag{A.19}$$

$$F_{II}^{\text{mean}} = \iint_{S_0} -\frac{1}{2}\rho(\nabla\phi^{(1)})^2\,(\hat{n}\cdot\hat{k})\,dS_{\text{mean}} \tag{A.20}$$

$$F_{III}^{\text{mean}} = \iint_{S_0} -\rho(\vec{X}^{(1)}\cdot\vec{\nabla}\phi_t^{(1)})\,(\hat{n}\cdot\hat{k})\,dS_{\text{mean}} \tag{A.21}$$

$\vec{k}$ is the wave vector of the incoming wave, thus $(\hat{n}\cdot\hat{k})$ has the opposite sign as the longitudinal direction cosine used by Pinkster, resulting in the same overall sign convention.

Bibliography

[1] Ballast, A., Eggermont, M., Zandbergen, P.J., Huijsmans, R.H.M.: "Free Surface Elevation near Round and Square Cylinders in Moderate Non-linear Deep Water Waves", 2002, Proceedings of the 17th International Workshop on Water Waves and Floating Bodies, Cambridge, p.p. 9 - 12.

[2] Berkvens, P.J.F.: "Floating bodies interacting with water waves", PhD-thesis, 1998, University of Twente, Enschede, The Netherlands.

[3] Broeze, J.: "Numerical Modelling of Non-Linear Free Surface Waves with a 3D Panel Method", PhD-thesis, 1993, University of Twente, Enschede, The Netherlands.

[4] Contento, G., Francescutto, A., Lalli, F.: "Nonlinear Wave Loads on Single Vertical Cylinders: Pressure and Wave Field Measurements and Theoretical Predictions", Proceedings of ISOPE '98, Vol. 3, p.p. 526 - 534.

[5] Daalen, E.F.G. van: "Numerical and Theoretical Studies of Water Waves and Floating Bodies", PhD-thesis, 1993, University of Twente, Enschede, The Netherlands.

[6] De Kat, J.O., Thomas, W.L.,: "Broaching and capsize model tests for validation of numerical ship motion predictions", 1998, Procedings of the 4th International Workshop on Ship Stability.

[7] Fekken, G.: "Numerical Simulations of Free-Surface Flow With Moving Rigid Bodies", PhD-thesis, 2004, University of Groningen, The Netherlands.

[8] Ferrant, P.: "Time Domain Computation of Non-Linear Diffraction Loads Upon Three Dimensional Floating Bodies", Proceedings of ISOPE '95, Vol. 3, p.p. 280-288.

[9] Ferrant, P.: "Nonlinear wave-current interactions in the vicinity of a vertical cylinder", 1997, Proceedings of the 12th International Workshop on Water Waves and Floating Bodies, Marseilles, Molin, B.(ed.), p.p. 65-69.

[10] Ferrant, P.: "Run-up on a Cylinder due to Waves and Current Potential Flow Solutions with Fully Non-Linear Boundary Conditions", Proceedings of ISOPE '98, Vol. 3, p.p. 332-339.

[11] Ferrant, P.: "Seakeeping simulations in non linear waves", 1999, Proceedings of the 7th International Conference on Numerical Ship Hydrodynamics, Nantes.

[12] Ferrant, P., Le Touzé, D., Pelletier, K.: "Non-linear time-domain models for irregular wave diffraction about offshore structures", 2003, International Journal for Numerical Methods in Fluids, 43, p.p. 1257-1277.

[13] Fochesato, C., Dias, F.: "Numerical model using the Fast Multipole Algorithm for nonlinear three-dimensional free-surface waves", submitted 2004.

[14] Greengard, L., Rokhlin, V.: "A fast algorithm for particle simulations", 1987, Journal of Computational Physics, 73, p.p. 325-348.

[15] Grilli, S., Guyenne, P., Dias, F., "A fully nonlinear model for three-dimensional overturning waves over arbitrary bottom", 2001, Int. J. Num. Meth. Fluids, 35, p.p. 829-867

[16] Haas, P.C.A. de: "Numerical simulation of nonlinear waves using a panel method; Domain decomposition and applications", PhD-thesis, 1997, University of Twente, Enschede, The Netherlands.

[17] Huijsmans, R.H.M., Westhuis, J., Ballast, A.: "Non-linear diffraction around heeled ship sections", 1999, Proceedings of ISOPE '99, Vol. 3, p.p. 651 - 657. See also [20].

[18] Kring, D., Korsmeyer, T., Singer, J., Danmeier, D., White, J.: "Accelerated, Nonlinear Wave Simulations for Large Structures", 1999, 7th International Conference on Numerical Ship Hydrodynamics, Nantes, France.

[19] MacCamy, R.C., Fuchs, R.A.: "Wave Forces on Piles: a Diffraction Theory", 1954, U.S. Army Beach Erosion Board, Technical Memorandum No. 69.

[20] Meskers, G.: "Realistic Inflow Conditions for Numerical Simulation of Green Water Loading", Master's thesis, 2002, Delft University of Technology, The Netherlands.

[21] Nielsen, F.G.: "Comparative Study of Airgap under Floating Platforms and Run-up on Platform Columns", report of the ISSC 2000 Committee 1.2.

[22] Pinkster, J.A.: "Low Frequency Second Order Wave Exciting Forces on Floating Structures", PhD-thesis, 1980, Technische hogeschool Delft, The Netherlands.

[23] Rienecker, M.M., Fenton, J.D.: "A Fourier Method Approximation Method for Steady Water Waves", 1981, Journal of Fluid Mechanics, Vol. 104, p.p. 119-137.

[24] Romate, J.E.: "Local error analysis in 3-D panel methods", 1988, Journal of Engineering Mathematics, 22, p.p. 187-207.

[25] Romate, J.E.: "Numerical Simulation of Nonlinear Gravity Waves in Three Dimensions using a Higher Order Panel Method", PhD-thesis, 1989, University of Twente, Enschede, The Netherlands.

[26] Romate, J.E.: "Local error analysis of three-dimensional panel methods in terms of curvilinear surface coordinates", 1990, SIAM Journal of Numerical Analysis, 27, 2, p.p. 529-542.

[27] Shirakura, Y., Tanizawa, K., Naito, S.: "Development of 3-D Fully Nonlinear Numerical Wave Tank to Simulate Floating Bodies Interacting with Water Waves", Proceedings of ISOPE 2000, Vol. 3, p.p. 253-262.

[28] Tanizawa, K.: "A nonlinear simulation method of 3-D body motions in waves", 1995, Journal of the Society of Naval Architects of Japan, 178, p.p. 179-191.

[29] Vermin, W.J., Ballast, A.: "Report on the parallelization of HYPAN", 2002, SARA report.

[30] Westhuis, J.: "The Numerical Simulation of Nonlinear Waves in a Hydrodynamic Model Test Basin", PhD-thesis, 2001, University of Twente, The Netherlands.

Acknowledgements

The work on this thesis has been made possible by the support of the Dutch Technology Foundation STW, of the National Computing Facilities foundation NCF, of the Institute of Mechanics, Processes and Control of the University of Twente IMPACT, of the Maritime Research Institute Netherlands MARIN, and of WL-Delft Hydraulics.

Nawoord

Het onderzoek voor dit proefschrift is verricht op het MARIN (Maritime Research Institute Netherlands) onder de vlag van het TIM (Twente Institute of Mechanics), later IMPACT (Institute of Mechanics, Processes and Control of the University of Twente). Het werd gefinancierd door Technologie Stichting STW. Het rekenwerk gebeurde op de nationale supercomputer, eerst op de Cray C90, later op de Silicon Graphics Origin 3800 (TERAS). Voor het gebruik van deze supercomputer-faciliteiten bij het SARA in Amsterdam is subsidie verleend door de Stichting Nationale Computer Faciliteiten (NCF). Ik wil Willem Vermin bedanken voor de prettige samenwerking bij de parallellisatie van de computercode. Van de leden van de STW gebruikers-commissie wil ik vooral Mart Borsboom (WL-Delft Hydraulics), Johan Romate (SHELL) en Jan Broeze (ATO-WUR) even noemen. De halfjaarlijkse gebruikers-commissie vergaderingen en de halfjaarlijkse werkgroep vergaderingen waren erg nuttig.

Paul de Haas (WL-Delft Hydraulics), Johan Romate (toen tijdelijk UT) en Patrick Berkvens wil ik bedanken voor het op gang helpen in het begin van het onderzoek. Douwe Dijkstra, vooral ook je relativeringen hier en daar tijdens de drie-wekelijkse besprekingen heb ik op prijs gesteld. Professor Zandbergen, de promotor, wil ik in het bijzonder bedanken voor het in mij gestelde vertrouwen en de mij gegeven vrijheid. Als het onderzoek enigszins stokte werd het op de drie-wekelijkse besprekingen, af en toe onder het genot van een anekdote, vrijwel altijd weer vlot getrokken. Ook de rustige aanmoediging in de laatste fase heeft goed gewerkt. Natuurlijk wil ik ook Michiel Eggermont bedanken. Als 'mede-AIO's' zijn wij al die jaren samen naar de Twentse werkbesprekingen geweest, jij vanuit Delft, ik vanuit Wageningen. Ook het debuggen van een grote, niet door jezelf geschreven computercode is veel minder frustrerend als je een lotgenoot kunt bellen. Michiel, je hebt een belangrijke bijdrage aan dit proefschrift geleverd.

Op het MARIN werd ik begeleid door René Huijsmans. René, bedankt voor de aansporingen richting de floating body workshops en voor de prettige sfeer. Verder heb ik in de jaren op het MARIN welgeteld 10 verschillende kamers gedeeld met andere studenten en promovendi, altijd met veel plezier. Met een aantal van die mensen heb ik relatief lang een kamer gedeeld. Allereerst met Robert Otto, het is al lang geleden, maar ik heb er goede herinneringen aan. Ook samen met Jaap-Harm Westhuis, Jie Dang en Anne Boorsma op één kamer was een hele bijzondere ervaring. Samen met Geert Meskers heb ik onder het genot van uitzicht op de Grebbeberg genoten van ballen, koffiepotten, sjoelen, strandjes en Google-en. Ook alle andere afstudeerders en promovendi wil ik bedanken voor de bij tijd en wijle hilarische lunches!

Curriculum vitae

The author was born on December 19, 1973, in Groningen, The Netherlands. After attending secondary school from 1986 till 1992 at the 'Wessel Gansfort College' in the same town, he studied Theoretical Physics at the University of Groningen (RuG). His Master's Thesis was titled "Forest wetness detection using radar, a theoretical study". After obtaining his Master's degree in the autumn of 1997, he started with the work for his PhD at the University of Twente under the supervision of prof. dr. ir. P. J. Zandbergen at the beginning of 1998. This research work was carried out at MARIN in Wageningen under the supervision of dr. ir. R. H. M. Huijsmans.